UNIVERSIDADE DE SANTIAGO DE COMPOSTELA

FACULTADE DE FÍSICA

DEPARTAMENTO DE FÍSICA DE PARTÍCULAS

Determination of the Pionium Lifetime in the DIRAC Experiment at CERN

JOSÉ LUIS FUNGUEIRIÑO PAZOS

Bernardo Adeva Andany

Catedrático da área de Física atómica, molecular e nuclear

Máximo Pló Casasús

Catedrático da área de Física atómica, molecular e nuclear

e

Antonio Romero Vidal

Doutor en Ciencias Físicas

INFORMAN

que a memoria titulada

Determination of the Pionium Lifetime in the DIRAC Experiment at CERN

foi realizada por D. José Luis Fungueiriño Pazos no **Departamento de Física de Partículas** da **Universidade de Santiago de Compostela** e na **Organización Europea para a Investigación Nuclear (CERN)** baixo a súa dirección, e constitúe o traballo de tese que presenta para optar ó Grao de Doutor en Ciencias Físicas.

Santiago de Compostela, 3 de Febreiro de 2012.

Asdo. Bernardo Adeva Andany   Asdo. Máximo Pló Casasús

Asdo. Antonio Romero Vidal   Asdo. José Luis Fungueiriño Pazos

A miña nai

.

Conan's Father: Fire and wind come from the sky, from the gods of the sky. But Crom is your god, Crom and he lives in the earth. Once, giants lived in the Earth, Conan. And in the darkness of chaos, they fooled Crom, and they took from him the enigma of steel. Crom was angered. And the Earth shook. Fire and wind struck down these giants, and they threw their bodies into the waters, but in their rage, the gods forgot the secret of steel and left it on the battlefield. We who found it are just men. Not gods. Not giants. Just men. The secret of steel has always carried with it a mystery. You must learn its riddle, Conan. You must learn its discipline. For no one - no one in this world can you trust. Not men, not women, not beasts. [Points to sword]. This you can trust.

("Conan The Barbarian", John Milius, 1982)

El hombre de negro huía a través del desierto, y el pistolero iba en pos de él.

No apunto con la mano;
El que apunta con la mano ha olvidado el rostro de su padre.
Apunto con el ojo.

No disparo con la mano;
El que dispara con la mano ha olvidado el rostro de su padre.
Disparo con la mente.

No mato con la pistola;
El que mata con la pistola ha olvidado el rostro de su padre.
Mato con el corazón.

[Alzó la mirada hacia ellos.]
Rolando Deschain: ¿Veis el punto donde se cruzan las líneas en el centro?
[Eddie sintió que se le ponían los pelos de punta. La boca se le secó de repente.]
Eddie Dean: ¿Es ahí, Rolando? ¿Es ahí donde...?
[Rolando asintió. Su cara surcada de arrugas tenía una expresión grave.]
Rolando Deschain: En este nexo se halla el Gran Pórtico, la llamada Decimotercera Puerta, que gobierna no sólo éste sino todos los mundos. [Dio unos golpecitos en el centro del círculo]. Aquí está la Torre Oscura que he buscado durante toda mi vida.

("La Torre Oscura", Stephen King, 1982-2012?)

Batman: *You either die a hero or live long enough to see yourself become the villain. I can do those things. Because I'm not a hero, not like Dent. I killed those people. That's what I can be.*

Lt. James Gordon: *No, no, you can't! You're *not*!*

Batman: *I'm whatever Gotham needs me to be.*

[cut to Gordon at Dent's funeral]

Lt. James Gordon: *A hero. Not the hero we deserved but the hero we needed. Nothing less than a knight. Shining.*

[Gordon is shown on top of Gotham Central. An axe is in his hand. He is being watched by an assortment of reporters and police officers. The next lines are heard in voiceover]

Lt. James Gordon: *They'll hunt you.*

Batman: *You'll hunt me. You'll condemn me. Set the dogs on me.*

[Gordon takes the axe to the bat light]

Batman: *Because that's what needs to happen.*

Batman: *[Alfred is shown burning the note from Rachel] Because sometimes the truth isn't good enough. Sometimes people deserve more.*

[We see Lucius Fox type his name into the sonar machine. The machinery around him sparks and the sonar screen fades out. Lucius smiles and walks away]

Batman: *Sometimes people deserve to have their faith rewarded.*

[last lines]

James Gordon Jr.: *Why's he running, Dad?*

Lt. James Gordon: *Because we have to chase him.*

James Gordon Jr.: *He didn't do anything wrong.*

Lt. James Gordon: *Because he's the hero Gotham deserves, but not the one it needs right now. So we'll hunt him because he can take it. Because he's not our hero. He's a silent guardian, a watchful protector. A dark knight.*

("The Dark Knight", Christopher Nolan, 2008)

Agradecementos

Cada vez que se consegue un obxectivo na vida ou se rebasa unha meta, cada vez que un se impón á adversidade ou simplemente cando por fin acada algo que levaba tempo perseguindo, un bota a vista atrás e deixa que o mecanismo da súa memoria invada de recordos o seu consciente. Lembra deste xeito todo polo que tivo que pasar, todos os malos momentos e todos os puntos febles que foron atacados ao longo do seu camiño. Aínda que só o fai durante un instante, xa que inmediatamente despois só pode e quere recordar os bos momentos, e con eles ás persoas coas que os compartiu, para agradecer de forma sincera e de todo corazón todo aquilo que aportaron todas e cada unha das persoas que comparten a victoria que finalmente ve conquistada.

Por suposto as primeiras persoas ás que debo agradecer todo e canto poderei ser na vida, todo e canto poida acadar polos meus propios medios e, en definitiva, todo aquilo que son e que poida chegar a ser algún día, son os meus pais; eles son os verdadeiros artífices deste logro, xa que sen eles eu nin sequera podería ter comezado esta nin outras moitas andainas.

A miña nai non só foi capaz de darme unha vez a vida, senón que se atreveu a desobedecer a médicos e enfermeiras, agasallándome por segunda vez co ben máis preciado, para que eu hoxe puidese estar aquí dándolle as gracias. Ela foi tamén quen me dou a educación e as ferramentas necesarias que me permiten ser mellor persoa cada día que o intento. Bótote de menos e durante o que me queda de vida maldicirei ó ceo por levarte antes de tempo.

O meu pai nunca entendeu moi ben en que diaño estaba a traballar o seu fillo maior, pero nunca permitiu que iso condicionase en xeito algún o seu poder de sacrificio polos seus fillos, traballando a reo para poder darlles educación e benestar, así como a oportunidade da que el nunca puido servirse. Gracias por todo, meu pai.

Quero por suposto agradecer a Bernardo Adeva a posibilidade que me brindou de traballar día a día nun grupo de investigación en Física de Partículas, confiando en min dende o principio, algo que non foi doado e que sen dúbida foi unha arriscada aposta. Gracias por saber conducir esta nave a bo porto.

Toño é unha desas persoas á que lle debo tantas e tantas cousas que nunca lle podería facer xustiza por moito que escribise del. Dicir simplemente que este traballo NUNCA podería ver a luz sen a súa inestimable, inconmensurable e paciente axuda. Toño, meu rei, tes o ceo gañado.

Debo agradecerlle a Otón aquel primeiro pulo inicial que me dou alá pola temporada 2005/2006 e que constitúe a orixe da miña actividade investigadora.

Foi unha mágoa non poder compartir máis tempo xuntos, pero o pouco que temos en común foi moi gratificante para min. Gracias Otto.

Moitos e moitas compañeiras de traballo, despacho e facultade sodes tamén protagonistas de tantos bos momentos e de tantos instantes de reflexión, apoio e mutua afirmación, sen os cales hoxe en día estariamos a falar doutro resultado completamente distinto. Entre todos permitide que escolla un par de nomes, deixando que aqueles que non figurades hoxe aquí sexa por mor unicamente da miña preguiza e non doutra cousa. Entre os que traballáchedes comigo no día a día, deixade que mencione a Mariñas, Diego, Cris, Xabier, os Pablos e Antonio. Anabel, Iago, Georgui e Martín foron moito máis que compañeiros de despacho e departamento. A todos gracias por intentar cambiar o mundo ao meu lado.

Mención aparte merecen os señores Eliseo e Daniel. Se todo o mundo tivese alomenos un par de persoas como estas ao seu carón, as cousas resultaríanlle moito máis doadas e tamén moito máis levadeiras. Tanto Daniel como Eliseo foron compañeiros de excepción e espero simplemente poder algún día devolver parte do que tanto o un como o outro me deron a cambio de nada. Gracias.

A pesares de non ter traballado nunca con Abraham —é algo que me encantaría poder facer, incluso sen estar á altura das circunstancias— debo recoñecerle o exquisito trato que sempre tivo comigo, sendo ademais unha das persoas coas ideas máis claras que endexamais coñecín, a non ser por suposto o propio señor Esperante, que constitúe un caso aparte.

Na parte técnica, como se de premios do espectáculo se tratase, debo recoñecer a desinteresada labor que tanto Marcos Seco como Juan Saborido levaron a cabo, este último incluso exercendo labores de conselleiro. A Marcos teño que agradecerlle que sempre tivese un momento que poder adicarme, ben para explicarme algo ou ben para perder comigo incontables tardes de software e paciencia, sen amosar nunca nin o menor dos xestos de cansancio ou desacougo. Quero agradecer asimesmo as moitas horas que perdeu Cibrán lendo o tostón que tedes diante, corrixindo incluso ata o menor dos erros tipográficos. Como dicía o outro, "Escribir é humano; corrixir divino".

Agora que un bota a vista atrás dáse conta de que a cousa non foi para tanto, pero non pode deixar de pensar que todo puido ter ido bastante peor e ser moito máis incómodo, de non ser polo traballo de persoas como Bea, Charo ou Mercedes. Olga, Conchi, Isabel e Josefa sempre me trataron como se fose da familia e a todas lles dou as gracias. Mención especial merece Mari Carmen, que non só destacou por ofrecerme unha e mil veces a súa axuda en infinidade de problemas, senon que tamén se convertiu nunha amiga e colaboradora.

Gustaríame tamén agradecerlle aos rapaces do CESGA a súa gran contribución neste traballo, especialmente a todos os que traballaron comigo, pero deixade que mencione simplemente a Carlos, Pablo, Javier e Sergio. Gracias a todos pola aportación.

Narciso, David, Ana, Koté, Mario, Víctor, Mó Ni Ka e moitos outros e outras fúchedes un grande apoio no último ano da miña vida e sempre vos agradecerei o voso bon humor, as vosas ganas de pasalo sempre ben, as interminables e deliciosas conversas, o voso saber facer e as vosas ganas de vivir, que se me contaxiaron; pero sobre todo agradezo a vosa calor cando máis o necesitaba. Gracias a todos e a todas.

Debo agradecer asimesmo todo o que me brindaron Kalerio, Fontal e Ferro, sempre de forma desinteresada, sempre co mellor dos seus sorrisos, e sempre traballando no que son amistades que sen ningún tipo de dúbida han durar toda a vida. Gracias rapaces por darme todo o que me déchedes.

A Carretero lle corresponde un lugar especial no meu corazón, pois así debe ser para os mellores amigos. Non recordo recibir nunca unha negativa súa, e debe ser porque nunca endexamais nada me negou. Quero agradecerlle todo o que fixo e que seguirá facendo por min, que non é pouco, senón moito máis do que moita xente fixo. Gracias Xosé María, por todo.

A meu irmán Alonso teño que agradecerlle que sempre coñeza o modo de facer que os meus problemas semellen menores do que realmente son —poida que simplemente me ensinase a velos como realmente son, sen máis— cada vez que nos xuntamos, botando unhas risas como somentes nós podemos facelo. Por moitos anos e moitas aventuras e desventuras que poidamos vivir, sei que poderei seguir contando con el para calquera cousa, como sempre fixen, e por iso se merece moito máis que o meu agradecemento. O merece todo.

A Esther lle debo tantas e tantas cousas que simplemente sería unha loucura intentar mencionar nin sequera parte delas, supoñendo incluso que me dese tempo a mencionar as máis importantes. Durante moitos anos fuches capaz de facerme mellorar día a día, construindo en grande medida o home que hoxe son. Sempre che estarei agradecido por todo o tempo que estivemos xuntos e por todas as cousas que compartimos. Gracias, nena.

¿Que podo dicir de ti, Anne? Moitas son as sensacións que se agolpan no meu corazón e que loitan por emerxer, pero poucas son as palabras que son capaz de articular cando penso no moito que che debo e no moito que me gustaría poder deberche. Poida que deba deixar que outros plasmen con verbas unha pequena parte do que me encantaría poderche dicir, cielo: "Nunca quise tanto a nadie en mi vida, nunca a un ser extraño le llamé mi familia".

Contents

Resumo

O traballo realizado nesta tese doutoral presenta os resultados finais da análise da vida media do pionium (estado ligado $\pi^+\pi^-$) sobre datos tomados no experimento DIRAC (Di-meson Relativistic Atom Complex), emprazado na Organización Europea para a Investigación Nuclear (CERN).

A vida media do pionium é demasiado pequena como para poder ser medida de forma directa, e polo tanto DIRAC propón unha medida indirecta da mesma. As colisións protón-núcleo producen pares cargados mediante desintegracións fortes de hadróns intermediarios. Algúns destos pares forman átomos $\pi^+\pi^-$ gracias á interacción coulombiana do estado final, e unha vez producidos, propáganse no branco con velocidade relativista. Antes de aniquilarse en dous pións neutros, os pares atómicos interactúan cos átomos do branco, o cal pode facer que se exciten (ou se desexciten) ou que se ionicen.

Os pares procedentes da ruptura dos átomos $\pi^+\pi^-$ presentan características cinemáticas específicas, que permiten a súa identificación experimental. Resolvendo a ecuación de transporte para os pares excitados, desexcitados e os ionizados, obtemos unha relación específica, para un determinado branco, entre a probabilidade de ruptura e a vida media do pionium, determinada a través das seccións eficaces inclusivas da dispersión $\pi\pi$.

O obxectivo do experimento é a medida da vida media do pionium cunha precisión do 10%, que á súa vez implica unha precisión do 5% na determinación da diferencia das lonxitudes de dispersión pión-pión $|a_0 - a_2|$, para isospin I=0 e I=2, a través da relación:

$$\Gamma_{1s} = \frac{1}{\tau_{1s}} = \frac{2}{9}\alpha^3 P |a_0 - a_2|^2 (1 + \delta) \tag{1}$$

A determinación de $|a_0 - a_2|$ avalía de forma trascendental a Teoría de Perturbacións Quiral (ChPT). Cando as masas dos quarks u e d son nulas a simetría quiral é exacta no marco da Cromodinámica Cuántica (QCD), pero cando m_d e m_u son finitas, prodúcese a rotura espontánea da simetría quiral, debendo introducirse un lagranxiano efectivo en termos de campos físicos —as masas dos pións— que dea conta dos parámetros da dispersión $\pi\pi$. En tal marco, a Teoría de Perturbacións Quiral predí unha vida media para o pionium de $\tau_{1s} = 2.9 \pm 0.1\ fs$ e un valor de $|a_0 - a_2|\,M_\pi = 0.265 \pm 0.004$, en termos de M_π, a masa dun pión cargado.

O método de detección está baseado na identificación de pares $\pi^+\pi^-$ procedentes da ionización do pionium nun branco de Níquel onde incidiron os feixes de protóns de 20 ou 24 GeV/c producidos polo acelerador PS do CERN.

Os átomos que se producen en ditas interaccións poden sufrir varios procesos:

- Aniquilarse entre sí para producir un par de pións neutros segundo a reacción $\pi^+\pi^- \rightarrow \pi^0\pi^0$.

- Excitación (desexcitación) a niveis atómicos enerxéticamente superiores (inferiores).

- Ionización (ruptura) ao interaccionar cos átomos do branco.

Para os propósitos do experimento cómpre separar prefectamente estes pares de pións procedentes da ionización dun átomo piónico no branco de Níquel doutros pares $\pi^+\pi^-$ tamén producidos nas interaccións protón-Níquel, xa que poderían interferir na correcta extracción da probabilidade de ionización do pionium, tales como:

- *Pares Coulombianos* (CC). Producidos na mesma interacción pNi a partires dunha resonancia de vida media curta. Estes pares posúen interacción coulombiana no seu estado final.

- *Pares Non Coulombianos* (NC). Producidos na mesma interacción pNi, onde polo menos un dos pións procede dunha resonancia de vida media longa. Estos pares non posúen interacción coulombiana no estado final.

- *Pares Accidentais* (AC). Producidos en diferentes interaccións pNi. Non exhiben interacción coulombiana no seu estado final.

O espectrómetro DIRAC foi deseñado e orquestrado co propósito de separalos pares atómicos do fondo de pares $\pi^+\pi^-$ recentemente descritos. Os pares atómicos presentan un moi pequeno ángulo de apertura ($\theta < 3\ mrad$) debido ao baixo momento relativo no seu centro de masas ($Q < 3\ MeV/c$) no instante no que o átomo é ionizado, que DIRAC pode desentrañar sen problemas gracias aos 0.55 MeV/c e 0.10 MeV/c de resolución no momento lonxitudinal (Q_L) e transversal (Q_T) no sistema centro de masas, respectivamente.

O camiño que percorrerán os pares atómicos ao longo do dispositivo experimental de DIRAC comeza no punto de interacción onde son creados, cando os feixes de protóns de 20 ou 24 GeV/c inciden sobre un branco de Níquel de 98 ou 94 micras atravesando de seguido o detector GEM/MSGC —deseñado e construido de forma íntegra polo Grupo de Altas Enerxías (GAES) do Instituto Galego de Física de Altas Enerxías (IGFAE) da Universidade de Santiago de Compostela (USC).

Inmediatamente despois, os pares $\pi^+\pi^-$ franquean un sistema de fibras de centelleo (SFD), que axudan na reconstrucción espacial e temporal das trazas, e hodoscopios de ionización (IH), que axudan na selección de trazas a moi baixo ángulo, non resoltas polos detectores de trazado (GEM/MSGC e SFD), mediante un criterio de doble ionización (o cal significa que dúas partículas pasaron polo IH). A continuación os pares $\pi^+\pi^-$ deixan atrás a zona *upstream* do experimento para adentrarse na zona *downstream*, separadas pola presenza do imán de 1.65 T de campo magnético, que curva as partículas cargadas no plano horizontal, segundo a dirección de propagación do par $\pi^+\pi^-$.

A partires dese momento os pións continúan o seu percorrido a través do espectrómetro por cadanseu brazo *downstream*, segundo a súa carga eléctrica. Un pión cargado positivamente (negativamente) seguirá o seu camiño polo brazo esquerdo (dereito) do espectrómetro, atopando ao seu paso despois do imán unhas cámaras de deriva (DC) que serven para a reconstrucción de trazas, e son indispensables para a medida do momento das partículas, para seguidamente atravesar un sistema de hodoscopios verticais[1] e horizontais (VH e HH).

O VH é usado para a selección de sucesos que chegan a el en coincidencia temporal nos dous brazos *downstream*. Os pares que acceden a este detector dentro dunha venta temporal $\Delta t \leq 0.5$ ns son denominados pares *prompt*, e conteñen tanto pares atómicos como pares accidentais, coulombianos e non coulombianos. O HH é usado como criterio de coplanariedade, o cal garantiza que os pares de partículas teñen unha compoñente pequena en Q_Y, definida como a compoñente transversal do momento do par $\pi^+\pi^-$ no centro de masas ao longo do eixo Y, perpendicular á dirección de propagación do pionium. A continuación os pións cargados seguen a súa andaina atopándose cos detectores Cherenkov (CH) e Preshower (PSH), que se encargarán basicamene de rexeitar electróns ou muóns que puidesen ser confundidos cos pións.

---

[1]Os hodoscopios verticais proporcionan información temporal básíca e por iso reciben o nome de Detector de Tempo de vóo —Time-Of-Flight, ToF—. Foron ademais construidos e instalados de forma íntegra polo GAES.

Finalmente os pións rematarán o seu percorrido polo espectrómetro DIRAC ao seren detidos por unha grosa capa de ferro absorvente, encargada de parar todo tipo de hadróns. As únicas partículas que sobrepasarán este absorvente serán muóns, que poderán ser detectados no seguinte e último detector que conforma o espectrómetro, o detector de muóns (MU). Os sucesos rexistrados por este detector serán, por suposto, rexeitados da mostra de pares $\pi^+\pi^-$, elemento de estudo despois de toda a reconstrucción.

O proceso de selección de trazas comeza na zona *downstream*, e prolóngase en sentido inverso ao avance das partículas cargadas a través do espectrómetro. Os tres últimos detectores (MU, PSH e CH) deben determinar a posible existencia dun par $\pi^+\pi^-$, rexeitando os impactos producidos por electróns; unha vez feito isto, a traza correspondente será unha posible traza obxecto de estudo. O tempo de vóo invertido polas partículas cargadas entre o detector IH da zona *upstream* e os detectores de tempo de vóo (VH) da zona *downstream* debe estar comprendido nunha ventá de $|\Delta t| < 5$ *ns*, podendo levarse entón a cabo a selección de trazas candidatas a ser finalmente pares $\pi^+\pi^-$.

As trazas *downstream* que pasen os cortes, e sexan consideradas pares de pións, serán extrapoladas dende as cámaras de deriva ata o imán, onde serán propagadas cara atrás no tempo gracias a un mapa que describe o campo magnético dentro do imán. Máis tarde estas trazas deberán ser extrapoladas buscando o punto de interacción do feixe de protóns co branco de Níquel, e serán axustadas con aquelas trazas reconstruidas polos detectores *upstream* (GEM/MSGC e SFD). Falaremos entón dun candidato a traza final.

A probabilidade de ionización do pionium no branco de Níquel defínese como a razón n_A/N_A entre o número de pares observados pola ionización do pionium causada polos átomos do branco (n_A) e o número de átomos piónicos formados dentro do branco (N_A). Aínda que N_A non pode ser medido de forma directa, si o poden ser tanto n_A^{rec} como N_C^{rec}, que son respectivamente o número de pares átomicos e de pares coulombianos reconstruidos polo espectrómetro, para momentos relativos do sistema centro de masas $\pi^+\pi^-$ menores que un determinado corte. A probabilidade de ionización pode ser entón escrita da forma:

$$P_{br} = \frac{n_A}{N_A} = \frac{n_A^{rec}}{N_C^{rec}} \cdot \frac{1}{K^{exp}} \tag{2}$$

onde

$$K^{exp} = K^{th} \frac{\epsilon_A}{\epsilon_C} \tag{3}$$

sendo ϵ_A e ϵ_C as eficiencias de reconstrucción e aceptancia do detector para os pares n_A e N_C, respectivamente. O factor K experimental, K^{exp}, pode ser facilmente calculado, xa que os valores de K^{th} son coñecidos e están tabulados.

O método utilizado para avaliar a probabilidade de ruptura do pionium consiste en determinar por un lado o espectro de datos reais, a partires de sucesos procedentes da reconstrucción de DIRAC, e por outro lado o espectro do Monte Carlo con todos os tipos de pares $\pi^+\pi^-$ citados anteriormente: coulombianos, non coulombianos, atómicos e accidentais. O Monte Carlo úsase para reconstrui-los datos experimentais mediante unha combinación lineal dos pares mencionados que, ao minimizar un axuste χ^2, proporciona n_A^{rec} e N_C^{rec}.

A fracción de pares accidentais presente na mostra de sucesos *prompt* debe ser determinada de forma precisa, xa que a cantidade de pares accidentais é un parámetro fixado na análise χ^2 dos distintos espectros dos pares descritos con anterioridade. Gracias ás precisas medidas do detector de tempo de vóo, esta cantidade pode ser facilmente determinada en función do momento, para cada un dos tres anos de toma de datos do experimento.

Na análise de datos, un novo xerador foi usado no presente traballo, que utiliza como input unha función do momento do par $\pi^+\pi^-$ plana en θ, que producirá un arquivo de 50000 sucesos coa posición e trimomento de cada un dos pións. Este arquivo cinemático será o input de GEANT-DIRAC, que xerará un suceso para cada un dos eventos contidos no arquivo cinemático, facéndoo pasar por cada un dos detectores do espectrómetro, gardando a información de cada un deles nun arquivo chamado *buffer file*. GEANT-DIRAC é o nome que recibe a versión modificada dun paquete de simulación suministrado polo CERN, GEANT3, que foi convenientemente reformado para os propósitos do experimento, e que contempla tanto a xeometría única de DIRAC como a súa aceptancia, así como a simulación da resposta dos detectores (resolución, eficiencia, etc.).

Estes *buffer files* serán entregados a ARIANE, un programa con deceas de subrutinas e miles de liñas de código que os procesará, dixitalizando os sucesos e gardando a resposta dos detectores, xerando os impactos en cada un deles, así como as súas eficiencias de detección e as súas resolucións. O output do programa ARIANE será unha colección de *n-tuplas* (matrices) que máis tarde serán procesadas por un pequeno programa chamado *readnt* no que se van aplicar uns pesos ás propias *n-tuplas* coa finalidade de que o espectro (p, θ) teña a mesma forma para datos e para Monte Carlo. Este último programa producirá todos e cada un dos histogramas necesarios para o axuste final da probabiliade de ionización do pionium.

Actualmente existen dúas determinacións previas de τ_{1s} no experimento DIRAC levadas a cabo cun tracking no que participou activamente o detector GEM/MSGC. A primeira medida foi determinada únicamente con datos pertencentes ao ano 2001, mentras que a segunda medida inclúe xa os anos 2002 e 2003, sendo as vidas medias respectivamente $\tau_{1s} = 2.58^{+0.30}_{-0.26} \ fs$ e $\tau_{1s} = 2.58^{+0.19}_{-0.18} \ fs$.

- O primeiro traballo centrouse principalmente no sistema de rastreo dos detectores *upstream*, no seu alineamento e na simulación Monte Carlo do detector GEM/MSGC.

- O segundo dos traballos estudiou con maior profundidade os erros sistemáticos na análise da probabilidade de ruptura do pionium, dando así conta da contaminación de pares K^+K^-, levando a cabo unha simulación máis precisa da resposta dos detectores e incluindo toda a estatística tomada polo experimento durante os anos 2001, 2002 e 2003.

O presente traballo non constitúe unha nova revisión do método de análise senon que propón un método máis preciso e introduce dúas novas correccións, como son a simulación do trigger e a resolución do momento, que fan que o Monte Carlo sexa sensiblemente diferente aos utilizados previamente. Dende un primeiro instante se procedeu á selección de datos cuns criterios distintos, onde só foron incluidos arquivos de datos onde o detector GEM/MSGC funcionase correctamente.

Un antigo criterio na selección de trazas foi eliminado, unha vez se demostrou a validez das trazas eliminadas. Dito criterio de selección estaba baseado nuns valores máximos permitidos dos χ^2 calculados para as trazas das cámaras de deriva. Tanto os traballos recentes, arriba mencionados, como todos os traballos levados a cabo con este restrictivo criterio de selección de trazas estaban obviando máis do 30% da estatística total de átomos.

O Monte Carlo descrito nesta tese inclúe a simulación de varios aspectos da análise que ata o de agora eran inéditos. A simulación de certas peculiaridades orixinais fai deste novo Monte Carlo unha ferramenta moito máis potente e poderosa do que o foron os seus antecesores, axudando enormemente a unha mellor comprensión do experimento. Os aspectos máis novedosos e importantes do actual Monte Carlo son a simulación da acción do trigger e a degradación da resolución no momento de laboratorio nunha pequena cantidade (0.066%), que foi necesaria introducir para que a resolución do pico da masa invariante da partícula Lambda (1116) fose igual nos datos e no Monte Carlo. Esta degradación coñécese como *smearing* en momento.

Foi absolutamente necesario introducir a simulación do trigger para dar unha descripción fidedigna á simulación tanto da compoñente lonxitudinal como transversal do momento, que anteriormente non puideron ser todo o perfectamente descritas na chamada zona de extrapolación (para $Q_L > 2\ MeV/c$ non existe sinal do pionium). Datos e Monte Carlo presentaban diferentes pendentes para $Q_L > 10\ MeV/c$ e unha corrección en Q_L era totalmente necesaria, levada a cabo en forma de polinomio lineal. A simulación do trigger resolveu o problema inmediatamente, deixando patente a relación entre unha mellor simulación do Monte Carlo e unha mellor descripción e entendemento do experimento.

A introducción do *smearing* en momento foi motivada pola resolución do momento estudiada con sucesos Lambda (1116). Realizouse un axuste de máxima verosimilitude a datos reais e ao Monte Carlo de lambdas, no que se reconstruiron as masas dos lambdas. Observouse nun primeiro instante que a resolución do Monte Carlo era menor que a dos datos reais, e a degradación da resolución do Monte Carlo voltouse necesaria para que a anchura dos lambdas reconstruidos fose idéntica tanto para datos como para Monte Carlo. Esto por suposto aseguraría unha mellor comunión entre datos e Monte Carlo, evitando unha diferente resolución que podería chegar a falsear o sinal do pionium.

Ideouse un método para degradar lixeiramente a resolución do Monte Carlo, introducindo unha pequena función Gaussiana na distribución da resolución de momento, que a ensanchaba moi lixeiramente (0.066%). A implementación de tal degradación lévase a cabo no último estadio da análise, a través do programa *readnt*, e por tanto a distribución de momento vese modificada debido a esta corrección. Q_L e Q_T tamén se ven afectadas polo efecto desta minúscula degradación, provocando un cambio do 2% na probabilidade de ruptura do pionium.

Utilizouse un método con dúas Gaussianas para determinar con extrema precisión a resolución da masa dos lambdas. A primeira das Gaussianas dá conta dos parámetros físicos da distribución, mentras que a segunda Gaussiana foi introducida para dar conta dunha asímetría na forma da masa reconstruida polo axuste. Unha vez que os parámetros foron extraídos para os datos reais, foron impostos para o Monte Carlo, probando distintos valores do *smearing* en momento ata que por fin se dou co valor óptimo para o que as resolucións para datos reais e Monte Carlo concordaban.

Antes de acometer definitivamente a análise do pionium, algúns aspectos da mesma deben ser estudiados con detalle e atención. Débese conceder especial relevancia, por exemplo, á contaminación de pares K^+K^- dentro da mostra $\pi^+\pi^-$, ao aliñamento de Q_L, á resolución de dobre traza e ó problema do PSC (Peak Sensing Circuit) das fibras de centelleo.

A contaminación de pares K^+K^- foi determinada para valores baixos e altos do momento, mediante un estudo da masa invariante reconstruída polos detectores _upstream_ SFD e IH. Para resolver a contaminación a baixo momento, utilizouse un método que leva a cabo un veto na masa do pión, corroborado por un método alternativo que propón a parametrización da masa cadrada en función duns cortes de selección. O cálculo da contaminación de pares K^+K^- levouse a cabo utilizando un axuste de máxima verosimilitude, practicado sobre funcións Gaussianas que describen distintos pares de partículas baixo a mesma hipótese de K^- na masa negativa (brazo dereito do espectrómetro).

Q_L debe ser simétrico por construcción, pero o alineamento dos detectores _upstream_ con respecto ás cámaras de deriva da zona _downstream_ non sempre asegura esta característica. O xeito de facer Q_L simétrico conséguese mediante o desplazamento do branco, nunha determinada dirección, que corrixe o desalineamento existente entre estas dúas zonas do espectrómetro. Nun primeiro paso se corrixe este desalineamento de forma groseira e a ollo, pero nunha etapa final debe facerse un alineamento moito máis fino, que involucra a dependencia de Q_L co momento. Cando finalmente teñamos alineado Q_L, poderemos asegurar a invariancia CP.

Cando os seis detectores _upstream_ GEM/MSGC e SFD non son capaces de resolver unha traza, debido á cercanía de dúas series de impactos, buscamos sinais de dobre ionización nos detectores IH, que serán capaces de determinar a dobre natureza dunha traza non resolta polos detectores _upstream_. Falaremos en tal caso de trazas colapsadas (nunha ou noutra proxección) ou dobremente colapsadas, se a traza é colapsada en ambas proxeccións X e Y. Datos e Monte Carlo piden distintos cortes de dobre ionización para distinguir entre trazas colapsadas, xa que debe crumprirse un criterio que asegure a mesma porcentaxe entre trazas colapsadas e non colapsadas tanto para datos reais como para Monte Carlo.

A simulación do detector de fibras de centelleo debe levarse a cabo tendo en conta o problema do PSC (Peak Sensing Circuit). Dito problema radica na imposibilidade da electrónica de describir de forma eficiente pares $\pi^+\pi^-$ a moi curtas distancias. Cando dúas fibras contiguas son atravesadas de forma simultánea por dúas partículas, o algoritmo de reconstrucción do PSC produce unha supresión de entre o 20 e o 40 por cento de tales eventos. A electrónica do dispositivo e o seu algoritmo non poden ser reemplazados, pero si debe simularse de forma eficiente semellante carencia.

Os erros sistemáticos involucrados na determinación da probabilidade de ruptura do pionium foron tamén analizados con extremo detalle, sufrindo moitos deles unha severa regresión na súa magnitude. Esto, xunto co incremento do 30 por cento de estatística, permitiu levar a cabo a máis precisa medida da vida media do pionium no seu estado fundamental, cunha precisión do $\sim 9\%$, onde máis de 22000 átomos foron reconstruidos polo espectrómetro. Á súa vez, $|a_0 - a_2|$ puido ser determinada cunha precisión do $\sim 4\%$.

Os datos reais foron divididos en cinco grupos distintos, atendendo aos distintos grosores dos brancos utilizados e da enerxía do feixe de protóns. Cada un destos grupos de datos foi asimesmo dividido en sete intervalos de momento, e levouse a cabo un axuste dependente do momento. Estas 35 medidas independentes da probabilidade de ruptura do pionium foron analizadas mediante un axuste de máxima verosimilitude, onde se tiveron en conta tanto a incertidume estatística como a sistemática, producindo unha vida media:

$$\tau = \left(3.15^{+0.20}_{-0.19}\Big|_{\text{stat}} \ ^{+0.20}_{-0.18}\Big|_{\text{syst}} \right) \times 10^{-15} \ s \tag{4}$$

Como medida de precaución levouse a cabo un test χ^2 para comprobar os resultados obtidos polo método de máxima verosimilitude. O resultado corroborou o valor obtido para a vida media do pionium, con practicamente a mesma precisión: $\tau = (3.15 \pm 0.20) \times 10^{-15}$ s. En consecuencia, a robustez do método de análise vese reforzada por esta constatación.

A través da relación (1) podemos obter a medida final da diferencia de lonxitudes de dispersión da dispersión $\pi\pi$:

$$|a_0 - a_2| = \left(0.2533^{+0.0080}_{-0.0078}\Big|_{\text{stat}} \ ^{+0.0078}_{-0.0073}\Big|_{\text{syst}} \right) M_{\pi^+}^{-1} \tag{5}$$

Conclusións

Este traballo presenta os máis precisos e modernos resultados obtidos na determinación da vida media do pionium, levados a cabo polo Experimento DIRAC no CERN, como producto do novo método de análise adoptado, que permitiu incrementar en máis dun 30 por cento a estatística de sucesos estudiados, debido á inclusión de eventos previamente non utilizados, gracias ao detector GEM/MSGC.

Levouse a cabo unha comparación detallada dos dous métodos numéricos existentes para describir a propagación dos átomos dentro do branco, no capítulo (3) desta tese, demostrando que as diferencias na probabilidade de ionización para un valor dado do momento son despreciables. Ademais, introduciuse un novo Monte Carlo (baseado no DIRAC PAIRS Generator - DIPGEN) ampliamente utilizado na colaboración DIRAC, que contén unha descripción detallada da aceptancia dos pares $\pi^+\pi^-$ no espectrómetro. O novo Monte Carlo tivo que ser mellorado e posto a punto con algunhas melloras e correccións non consideradas previamente, tales como a simulación do sistema de trigger de DIRAC e a adaptación da resolución en momento.

O presente traballo reporta a máis precisa e completa descripción dos erros sistemáticos que interveñen na determinación da probabilidade de ruptura do pionium, drásticamente reducidos con respecto a traballos anteriores. Semellante descripción e comprensión dos erros sistemáticos, xunto coa inclusión de sucesos obviados ata o de agora (ata o 30 por cento da estatística total de sucesos reconstruidos polo espectrómetro, que ascende a un total de 22000 átomos), permitiu acometer a máis precisa medida da vida media do pionium no seu estado fundamental, cunha precisión do ~9%, propiciando que as lonxitudes de dispersión $\pi\pi$ fosen determinadas cunha precisión do ~4%.

Os datos reais foron separados en cinco grupos distintos, segundo os diferentes grosores dos brancos empregados e atendendo ademais ás distintas enerxías dos feixes de protóns, de 20 e 24 GeV. Un axuste dependente do momento foi levado a cabo para cada un dos cinco grupos de datos, onde finalmente 35 diferentes valores da probabilidade de ruptura do pionium foron obtidas mediante un axuste de máxima verosimilitude, onde se tiveron en conta as incertidumes estatísticas e sistemática, producindo unha vida media:

$$\tau = \left(3.15^{+0.20}_{-0.19}\Big|_{\text{stat}} \; {}^{+0.20}_{-0.18}\Big|_{\text{syst}} \right) \times 10^{-15} \; s \tag{6}$$

Levouse a cabo un test χ^2 para comprobar os resultados obtidos polo método de máxima verosimilitude, como medida comprobativa. O resultado confirmou totalmente o valor obtido de forma previa, producindo un resultado: $\tau = (3.15 \pm 0.20) \times 10^{-15}$ s. Consecuentemente, a robustez do método de análise vese reforzada por esta constatación.

Nunha publicación previa da Colaboración DIRAC, informábase dunha vida media de:

$$\tau = \left(2.91^{+0.45}_{-0.38}\Big|_{\text{stat}} \; {}^{+0.19}_{-0.49}\Big|_{\text{syst}} \right) \times 10^{-15} \; s \tag{7}$$

onde tanto as incertidumes estatística como sistemática eran maiores que na presente medida. A pesares de ter en conta fontes de erro non consideradas anteriormente, puidemos reducir o erro sistemático nun factor 1.7, demostrando deste xeito o grandísimo esforzo feito durante os últimos anos. O erro estatístico tamén foi reducido en case que un factor 2, e finalmente, logo de engadir todos os erros en cadratura, o erro relativo que acompaña á nosa medida previa é dun 19 por cento, mentras que a presente medida ten un erro relativo menor do 9 por certo, o que implica unha reducción de máis do dobre.

Tendo todo isto en conta, obtemos a medida final da diferencia de lonxitudes de dispersión da dispersión $\pi\pi$:

$$|a_0 - a_2| = \left(0.2533^{+0.0080}_{-0.0078}\Big|_{\text{stat}} \; {}^{+0.0078}_{-0.0073}\Big|_{\text{syst}} \right) M_{\pi^+}^{-1} \tag{8}$$

Esta diferencia das lonxitudes de dispersión pión-pión pode debe ser comparada coa medida publicada anteriormente pola Colaboración DIRAC:

$$|a_0 - a_2| = 0.264^{+0.033}_{-0.020} \; M_{\pi^+}^{-1} \tag{9}$$

en relación á cal se reduciron os erros sistemáticos e estatísticos nun factor 2.5, tal e como pode ser observado na Fig. (1).

A medida actual de $|a_0 - a_2|$ é totalmente compatible coas medidas obtidas pola Colaboración NA48/2 a través dos experimentos $K_{3\pi}$ e K_{e4}. A medida de $|a_0 - a_2|$ obtida por $K_{3\pi}$ é:

$$(a_0 - a_2)M_{\pi^+} = 0.2571 \pm 0.0048 \text{ (stat)} \pm 0.0029 \text{ (syst)} \pm 0.0088 \text{ (theo)} \quad (10)$$

mentras que as medidas da diferencia de lonxitudes de dispersión $\pi\pi$ obtidas polos experimentos $K_{3\pi}$ and the K_{e4} de forma conxunta son:

$$(a_0 - a_2)M_{\pi^+} = 0.2639 \pm 0.0020 \text{ (stat)} \pm 0.0015 \text{ (syst)} \pm 0.0088 \text{ (theo)} \quad (11)$$

A nosa medida actual da diferencia de lonxitudes de dispersión pión-pión inclúe a incertidume teórica nos erros sistemáticos, e combinando todos os erors das medidas en cadratura, podemos finalmente comparar os valores obtidos pola Colaboración DIRAC cos obtidos polos experimentos de NA48/2. A Fig. (1) e a Táboa (1) resumen as medidas de $|a_0 - a_2|$ levadas a cabo por DIRAC e NA48/2, onde se pode observar o excelente acordo entre ambos experimentos e a Teoría de Perturbacións Quiral, ChPT.

Medida de $|a_0 - a_2|$	$|a_0 - a_2| \times M_{\pi^+}$	Erro combinado
ChPT	0.2650	$\pm$ 0.0040
DIRAC	0.2533	$\pm$ 0.0109
$K_{3\pi}$	0.2571	$\pm$ 0.0104
$K_{3\pi}$ & K_{e4}	0.2639	$\pm$ 0.0091
World Average	0.2581	$\pm$ 0.0058

Table 1: *Valores actuais da diferencia das lonxitudides de dispersión $\pi\pi$.*
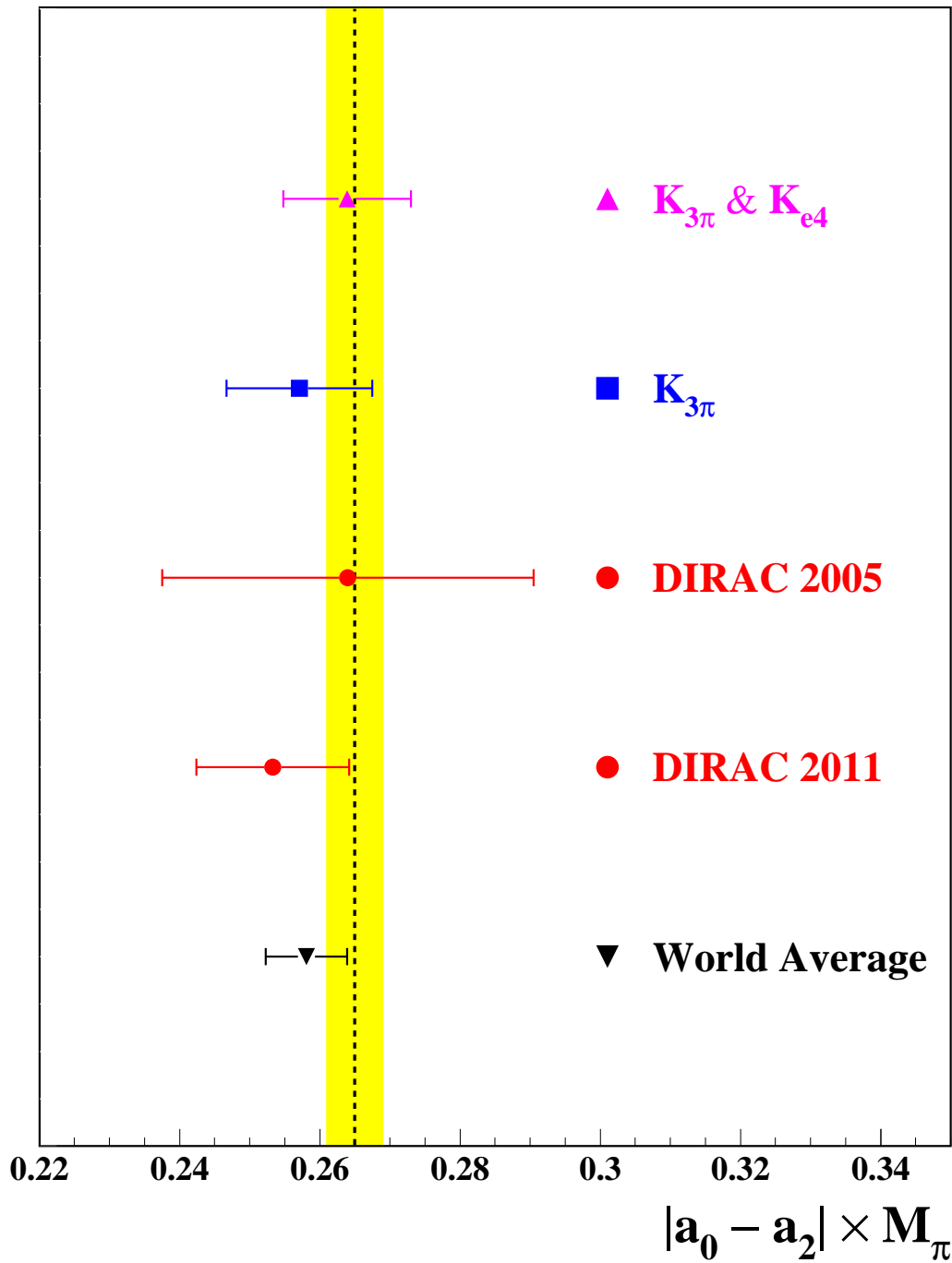
Figure 1: *Valores experimentais de* $|a_0 - a_2|$ *obtidos por DIRAC e por NA48/2. A liña negra discontinua representa a predicción da Teoría de Perturbacións Quiral, e o seu erro ven representado pola banda amarela. O valor da* World Average *foi calculado a través da media ponderada pesada polos valores individuais dos erros implicados; os dous valores proporcionados por NA48/2 e a medida de DIRAC publicada en 2011.*

Summary

The work presented in this PhD dissertation represents the latest and most accurate measurement of the pionium lifetime, tackled within the framework of the DIRAC experiment at the European Organization for Nuclear Research (CERN).

The goal of the DIRAC experiment is to measure the pionium breakup probability in a Nickel target, and then extract the pionium lifetime after precise simulation of the atom interactions with matter, leading to the result:

$$\tau = \left(3.15^{+0.20}_{-0.19}\Big|_{\text{stat}} \ {}^{+0.20}_{-0.18}\Big|_{\text{syst}} \right) \times 10^{-15} \ s \tag{12}$$

Through the pionium lifetime, the pion-pion scattering lengths difference for Isospin $I = 0, 2$, $|a_0 - a_2|$, can be determined.

Much previous activity has been devoted to the determination of the pionium lifetime in DIRAC, but the present work has accomplished a new selection method using the upstream position detectors yielding an enhanced data sample, and a refined simulation of the detector and trigger response. As a consequence of the latter, a most complete and meticulous description of the systematic errors involved in the lifetime measurement has been provided. The result has been a reduction of the systematic uncertainties with respect to our previous publication.

The pionium lifetime measurement leads to the following $\pi\pi$ scattering lengths difference:

$$|a_0 - a_2| = \left(0.2533^{+0.0080}_{-0.0078}\Big|_{\text{stat}} \ {}^{+0.0078}_{-0.0073}\Big|_{\text{syst}} \right) M_{\pi^+}^{-1} \tag{13}$$

fully compatible with other experiments in agreement with the predictions by the Chiral Perturbation Theory.

Chapter 1

The DIRAC Experiment

1.1   Introduction

The aim of the DIRAC experiment at CERN [1] is to measure the lifetime of the $\pi^+\pi^-$ hydrogen-like atom (pionium)in the ground state with 10% precision [1, 2, 3, 4, 5, 6, 7]. This lifetime is essentially determined by the reaction $\pi^+\pi^- \to \pi^0\pi^0$. Annihilation into two photons amounts to less than 0.3% [8, 9] and is neglected here. This allows to determine the S-wave isospin dependent $\pi\pi$ scattering length difference $|a_0 - a_2|$ at a 5% accuracy, in a model independent way [10, 11, 12, 13, 14, 15] by means of the relation:

$$\Gamma_{1S} = \frac{1}{\tau_{1S}} = \frac{2}{9}\alpha^3 p \left|a_0 - a_2\right|^2 (1 + \delta) \tag{1.1}$$

with τ_{1S} the lifetime of the atomic ground state, α the fine-structure constant, p the π^0 momentum in the atomic rest frame, and a_0 and a_2 the S-wave $\pi\pi$ scattering lengths for isospin 0 and 2, respectively. The term δ accounts for QED and QCD corrections [12, 13, 14, 15]. It is a known quantity ($\delta = (5.8 \pm 1.2) \times 10^{-2}$) ensuring a 1% accuracy for Eq. (1.1) [14]. The $\pi\pi$ scattering lengths a_0, a_2 have been calculated within the framework of Standard Chiral Perturbation Theory (ChPT) [16, 17] with a precision better than 2.5% [18]:

$$a_0 \ M_{\pi+} = 0.220 \pm 0.005, \qquad a_2 \ M_{\pi+} = -0.0444 \pm 0.0010 \tag{1.2}$$

$$\left|a_0 - a_2\right| \ M_{\pi+} = 0.265 \pm 0.004 \tag{1.3}$$

where $M_{\pi+}$ is the mass of the charged pion. These a_0 and a_2 values lead to the prediction $\tau_{1S} = (2.9 \pm 0.1) \times 10^{-15}s$.

The Generalized Chiral Perturbation Theory allows for larger a-values [19]. Model dependent measurements of a_0 have been done using K_{e4} decays [20, 21].

DIRAC proposes a method to measure the lifetime of the pionium whose underlying idea is the following: high-energy proton-nucleus collisions produce pairs of oppositely charged pions via strong decays of intermediate hadrons. Some of these pairs form $\pi^+\pi^-$ atoms through Coulomb final state interaction. Once produced, the $\pi^+\pi^-$ atoms propagate in the target with relativistic velocity. Prior to their decay into pairs of neutral pions, the atoms interact with the target atoms. This interaction excites/de-excites or breaks them up. The $\pi^+\pi^-$ pairs from the breakup exhibit specific kinematical features, which allow their experimental identification. Excitation/de-excitation and breakup of the atom compete with its decay. Solving the transport equation for excitation/de-excitation and breakup [22, 23, 24, 25, 26, 27, 28, 29, 30, 31, 32, 33, 34] leads to a target-specific relation between breakup probability and lifetime, which is known at the 1% level [6, 25, 35, 36]. Therefore, measuring the breakup probability allows to determine the lifetime of pionium [26, 37, 38], thereby subjecting Chiral Perturbation Theory to a very sensitive test.

1.2 $\pi\pi$ Scattering

The study of $\pi\pi$ scattering is a classical subject in the field of strong interactions. The properties of the pions are intimately related to an approximate symmetry of QCD. In the chiral limit, where the masses of the quarks u and d (m_u and m_d) vanish, this symmetry becomes exact, the Lagrangian being invariant under the group $SU(2)_R \times SU(2)_L$ of chiral rotations. The symmetry is spontaneously broken to the isospin subgroup $SU(2)_V$. The pions represent the corresponding Goldstone bosons of the theory.

A second symmetry breakup, explicit in this case, arises from the fact that the quarks are not massless. The theory only possesses an approximate chiral symmetry, because m_u and m_d happen to be very small. The consequences of the smallness of the symmetry breaking may be used to propose an effective field theory [16]. The various quantities of interest are expanded in powers of the momenta and quark masses. In the case of the charged pion mass, for instance, the expansion starts with [39]:

$$M_{\pi^+}^2 = (m_u + m_d)B + O(m^2), \quad B = \frac{1}{F_\pi^2}|\langle 0|\bar{u}u|0\rangle| \qquad (1.4)$$

F_π is the pion decay constant in the chiral limit, $m_u, m_d \to 0$. The formula shows that the square of the pion mass is proportional to the product of $m_u + m_d$ with the order parameter $\langle 0|\bar{u}u|0\rangle$. The two factors represent quantitative measures

for explicit symmetry and spontaneous symmetry breaking, respectively.

If the explicit symmetry breaking is turned off, the pions become massless. The $SU(2)_V$ symmetry is then exact, so that the spectrum contains three massless Goldstone bosons, while all other levels form massive, degenerate isospin multiplets.

For a given pion pair interacting strongly, being r the finite size of the interaction range and k the momentum of the pion in the center of mass frame, at low energy ($kr << 1$) the S-wave dominates the total cross section. The isospin state of a pion pair with zero angular momentum could only be $I = 0$ or $I = 2$ because of Bose-Einstein statistics. The scattering produces a phase shift in the wave function so that the scattering matrix can be parametrised in terms of two phases

$$|\pi\pi\rangle = e^{2i\delta_{0,2}}|\pi\pi\rangle, \quad \delta_{0,2} = a_{0,2}k + O(k^3) \tag{1.5}$$

where the subscripts 0,2 refer to the isospin state. If natural units are used, a_0 and a_2 are dimensioned as length and therefore are called scattering lengths. The first prediction for a_0 and a_2 is due to S.Weinberg (1966) [40]

$$a_0 M_\pi = \frac{7M_\pi^2}{32\pi F_\pi^2} = 0.16, \quad a_2 M_\pi = -\frac{M_\pi^2}{16\pi F_\pi^2} = -0.045 \tag{1.6}$$

where M_π and F_π are the mass and decay constant of the charged pion. $\pi\pi$ scattering at low energy is a fundamental process for ChPT, particularly sensitive to the mechanism of spontaneous chiral symmetry breaking.

The two low energy expressions (1.6) are valid only at tree level in a series expansion in powers of the quark masses: the next-to-leading order corrections were calculated in [17], and the next-to-next-to-leading order corrections in [41].

The upshot of that analysis is that a_0 and a_2 are the essential low energy parameters. Once these are known, the available experimental data determine the low energy behaviour of the $\pi\pi$ scattering amplitude with remarkably small uncertainties.

Only data sufficiently close to the threshold mass of two pions can provide significant precision bounds on the scattering lengths determination. The DIRAC experiment at CERN [1] uses that $\pi^+\pi^-$ atoms decay into a pair of neutral pions through the strong transition $\pi^+\pi^- \to \pi^0\pi^0$. Since the momentum transfer nearly vanishes, only the scattering lengths are relevant. DIRAC is of particular interest, since it tests the hypothesis of the quark condensate representing the leading order parameter of the spontaneously broken symmetry. If the theoretical predictions should turn out to be in contradiction with DIRAC outcome, the commonly accepted picture would require a thorough revision.

1.3   QCD Standard Model and ChPT

The non-perturbative regime of the strong sector of the Standard Model (Quantum Chromo Dynamics, QCD) presents a formidable challenge at low energies ($E < 1GeV$), due to our limited calculation capability. A solution for this inconvenient is the replacement of the fundamental QCD Lagrangian with an effective one. Chiral Perturbation Theory (ChPT) is an effective field theory introduced in the late seventies [16] and soon thereafter developed [42, 43] into a powerful tool able to overcome the mentioned limitation. At the cost of a certain number of free parameters to be determined from experimental data, ChPT can quantitatively account for effects due to mesons structure and form factors. Quantitative predictions on low energy processes involved in Standard Model tests are in general dependent on the corrections provided by ChPT and, as a consequence, the interpretation of possible traces of new physics in the confinement regime requires ChPT. Measurements testing the coherence of ChPT and its assumptions are of fundamental importance.

The most precise determination of the pionium scattering lengths difference is achieved using a combination of the Chiral Perturbation Theory at two loops and the Roy equations [44]. In ChPT the quark condensate $\langle 0|\bar{q}q|0\rangle$ determines the relative size of mass and momentum terms in the perturbative expansion. The value of this fundamental parameter must be determined experimentally. ChPT relates the quark condensate to S-wave $\pi\pi$ scattering lengths in isospin states $I = 0$ and $I = 2$, a_0 and a_2, which are predicted with 2% precision [45] through Eq. (1.4). The Roy equations determine the $\pi\pi$ scattering amplitude in terms of the imaginary parts at intermediary energies, except for two subtraction constants: the S-wave scattering lengths a_0, a_2. At low energies, the contributions from the imaginary parts are small, as well as the current experimental information about these suffices, but the contributions about the scattering lengths is subject to comparatively large uncertainties.

Chiral symmetry does not fully determine the higher order contributions, because it does not predict the values of the coupling constants appearing in the effective Lagrangian. There are two categories of coupling constants: terms that survive in the chiral limit and symmetry breaking terms proportional to a power of M_π. The former show up in the momentum dependence of the scattering amplitude, therefore these couplings can be determined phenomenologically. For the coupling constants of the second category, which describe the dependence on the quark masses, we need to rely on experimental input sources other than $\pi\pi$ scattering. A detailed discussion can be found in [19, 46].

1.4 Photonic Decays of Pionium

The strong interaction partial decay width of the desintegration $\pi^+\pi^- \to \pi^0\pi^0$ can be written in terms of the scattering lengths as follows:

$$\Gamma_{\pi^0\pi^0} = \frac{16\pi}{9}\frac{p*}{M_\pi}\left(a_0 - a_2\right)^2 \left|\Psi_n^{(C)}(0)\right|^2 \tag{1.7}$$

where $\Psi_n^C(r)$ is the atomic wave function and n the pionium principal quantum number[1].

The annihilation into two photons via the reaction $\pi^+\pi^- \to \gamma\gamma$ competes with the strong decay, and its partial decay width is described by the relation:

$$\Gamma_{\gamma\gamma} = \frac{\pi\alpha^2}{8M_\pi^2}\left|\Psi_n^{(C)}(0)\right|^2 \tag{1.8}$$

In contrast to scalar QED, one is concerned here with two coupled channels of non-relativistic particles, $\pi^+\pi^-$ and $\pi^0\pi^0$, which are separated by a mass gap $M_\pi - M_{\pi^0} << M_\pi$. As a result of this, the ground state of pionium dominantly decays into $\pi^0\pi^0$, while its decay into $\gamma\gamma$ is suppressed by a factor $\sim 4 \times 10^3$ [8].

1.5 Pionium Production

Oppositely charged pions emerging from a high energy proton-nucleus collision may be either produced directly from the nucleus fragmentation or stem from intermediate hadron resonances. These resonances can be classified into "short-lived" and "long-lived" sources, attending to their decay path length, compared to the Bohr radius of the pionium, $a_\pi = 2/(M_\pi\alpha) = 387.5$ fm.

- The "long-lived" resonances have a lifetime long enough to fly a distance much larger than the Bohr radius of the pionium, as happens to Λ, K_0^S and η, which present decay path lengths of 7.89 cm, 2.2 cm and 1.7 Å, respectively. The pions from these resonances will not form bound states with other pions coming from resonances of very short lifetime.

- The "short-lived" resonances exhibit a decay path length very small compared to the pionium Bohr radius. The Coulomb interaction between pions coming from these resonances can establish a correlation, increasing the double inclusive cross section, allowing the formation of bound states.

---

[1]The pionium is only produced in S states, since the wavefunction in other states happens to be zero at the origin for higher values of l $(l > 0)$

After the interaction, a spectrum emerges with different types of $\pi^+\pi^-$ pairs, with well differentiated characteristics, as shown in Figs. (1.1, 1.2,1.3, 1.4):

- Atomic pairs (AT). These $\pi^+\pi^-$ pairs come from the pionium ionization.
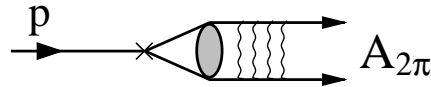
Figure 1.1: *Atomic pairs creation diagram.*

- Coulomb pairs (CC). $\pi^+\pi^-$ pairs coming from the same proton-nucleus interaction or from short-lived sources. Regardless they exhibit Coulomb interaction in the final state, they do not form atoms.
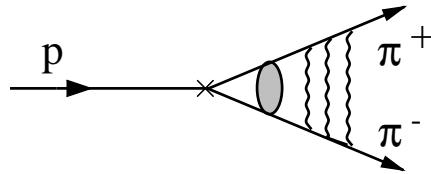
Figure 1.2: *Coulomb pairs creation diagram.*

- Non-Coulomb pairs (NC). These $\pi^+\pi^-$ pairs are originated in the same proton-nucleus interaction, but at least one pion comes from a long-lived source. They do not exhibit Coulomb interaction in the final state.
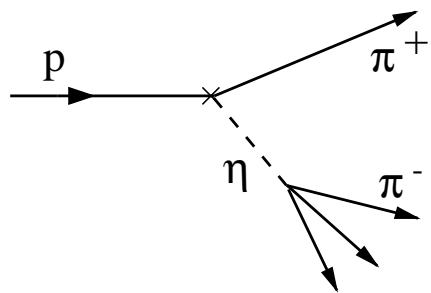
Figure 1.3: *Non-Coulomb pairs creation diagram.*

- Accidental pairs (ACC). $\pi^+\pi^-$ pairs coming from different proton-nucleus interaction, without Coulomb interaction in the final state.
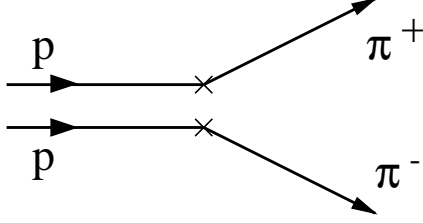
Figure 1.4: *Accidental pairs creation diagram.*

Pion pairs from "short-lived" sources undergo Coulomb final state interaction and may form atoms. If the strong final interaction is neglected, and since the region of production is small as compared to the Bohr radius of the atom, the cross section σ_A^n for production of atoms with principal quantum number n is related to the inclusive production cross section for pion pairs from "short-lived" sources without Coulomb correlation (σ_s^0) [38]:

$$\frac{d\sigma_A^n}{d\vec{p}_A} = (2\pi)^3 \frac{E_A}{M_A} |\Psi_n^C(\vec{r}^* = 0)|^2 \frac{d^2\sigma_s^0}{d\vec{p}_+ d\vec{p}_-}\bigg|_{\vec{p}_+ = \vec{p}_-} \qquad (1.9)$$

with $\vec{p}_A, E_A$ and M_A the momentum, energy and mass of the atom in the lab frame, respectively, and $\vec{p}_+, \vec{p}_-$ the momenta of the charged pions. The square of the Coulomb atomic wave function for zero distance $\vec{r}^*$ between them in the c.m. system is $|\Psi_n^C(0)|^2 = \delta_{l0}\,\delta_{m0}\,p_B^3/\pi n^3$, where $p_B = M_\pi\alpha/2$ is the Bohr momentum of the pions and M_π the pion mass. The production of atoms occurs only in S-states [38], since the l, m functions are zero in the origin, for $l, m \neq 0$.

Final state interaction also transforms the "unphysical" cross section σ_s^0 into a real one for Coulomb correlated pairs, σ_C [47, 48]:

$$\frac{d^2\sigma_C}{d\vec{p}_+ d\vec{p}_-} = |\Psi_{-\vec{k}^*}^C(\vec{r}^*)|^2 \frac{d^2\sigma_s^0}{d\vec{p}_+ d\vec{p}_-} \qquad (1.10)$$

where $\Psi_{-\vec{k}^*}^C(\vec{r}^*)$ is the continuum eigenstate of the hydrogenlike hamiltonian wave function and $2\vec{k}^* \equiv \vec{q}$ with $\vec{q}$ being the relative momentum of the π^+ and π^- in the c.m. system[2]. $|\Psi_{-\vec{k}^*}^C(\vec{r}^*)|^2$ describes the Coulomb correlation and

---

[2]For the sake of clarity we use the symbol Q for the experimentally reconstructed and q for the physical relative momentum.

at $r^* = 0$ coincides with the Gamow-Sommerfeld-Sakharov[3] factor $A_C(q)$ with $q = |\vec{q}|$ [48]:

$$A_C(q) = \frac{2\pi M_\pi \alpha / q}{1 - exp(-2\pi M_\pi \alpha / q)} \qquad (1.11)$$

One can approximate in (1.10) $\frac{d^2\sigma_s^0}{d\vec{p}_+ d\vec{p}_-} \approx \left.\frac{d^2\sigma_s^0}{d\vec{p}_+ d\vec{p}_-}\right|_{q=0}$ and then relate the number of produced pionium atoms, N_A, to the number of Coulomb correlated pion pairs, N_{CC} [49]:

$$\frac{N_A}{N_{CC}} = \frac{\sigma_A^{tot}}{\sigma_C^{tot}|_{q \leq q_0}} = \frac{(2\pi\alpha M_\pi)^3}{\pi} \frac{\sum\limits_{n=1}^{\infty} \frac{1}{n^3}}{\int_0^{q_0} A_C(q)\, d^3q} = k_{th}(q_0) \qquad (1.12)$$

Eq. (1.12) defines the theoretical k-factor. Throughout this thesis we will use $q_0 = 2 MeV/c$ and $k_{th}(q_0) = 0.615$.

In order to account for the finite size of the pion production region and of the two-pion final state strong interaction, the squares of the Coulomb wave functions in Eqs. (1.9) and (1.10) must be substituted by the square of the complete wave functions, averaged over the distance $\vec{r}^*$ and the additional contributions from $\pi^0\pi^0 \to \pi^+\pi^-$ [50]. It should be noticed that these corrections essentially cancel each other in the k-factor (Eq. 1.12) and lead to a correction of only a fraction of a percent. Thus finite size corrections can be neglected for k_{th}.

For a Ni target and a 24 GeV/c proton beam, $\sim 7 \times 10^{-7}$ atoms are produced per proton interaction, of which, only $\sim 1 \times 10^{-9}$ are detectable in the experiment, due to momentum and angular acceptance of the DIRAC apparatus.

---

[3]$A_C(q)$ factor establishes the Coulomb interaction of the pairs, discovered by Gamow-Sommerfeld and Sakharov. We refer to Coulomb factor to unify the nomenclature.

1.6   Propagation Inside the Target

The method for observing pionium atoms and measuring its lifetime has been proposed in [38]. Pairs of $\pi^+\pi^-$ are produced mainly as unbound ("free") pairs, but sometimes also as pionium. Once produced, the pionium atoms propagate in the target with relativistic velocity (average Lorentz factor $\gamma \approx 17$ in our case) and may annihilate into two neutral pions or interact with target atoms, whereby they become excited/de-excited or break up. Figs. (1.5, 1.6, 1.7) show the possible interactions to be suffered by the pionium.
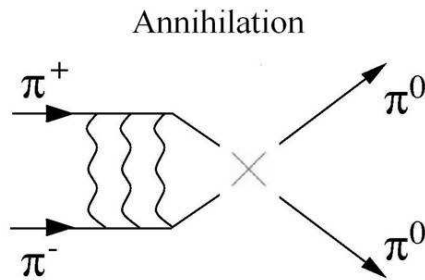
Figure 1.5: *Pionium annihilation diagram.*
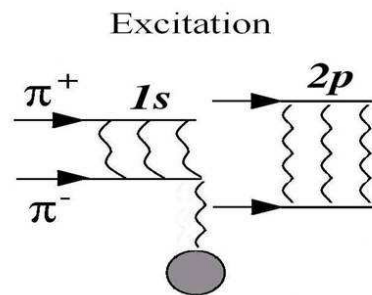
Figure 1.6: *Pionium excitation diagram.*
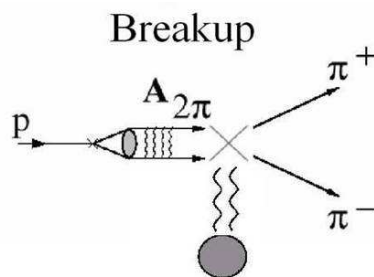
Figure 1.7: *Pionium breakup diagram.*

The $\pi^+\pi^-$ pairs from breakup (atomic pairs) exhibit specific kinematic features which allow to identify them experimentally [38], namely very low relative momentum q and q_L (the component of $\vec{q}$ parallel to the total momentum $\vec{p_+} + \vec{p_-}$) as shown in Fig. (1.8). After breakup, the atomic pair traverses the target and, to some extent, loses these features by multiple scattering, essentially in the transverse direction, while q_L is almost not affected. This is one reason for considering distributions in $Q_{L,T}$ as well as in Q when analyzing the data
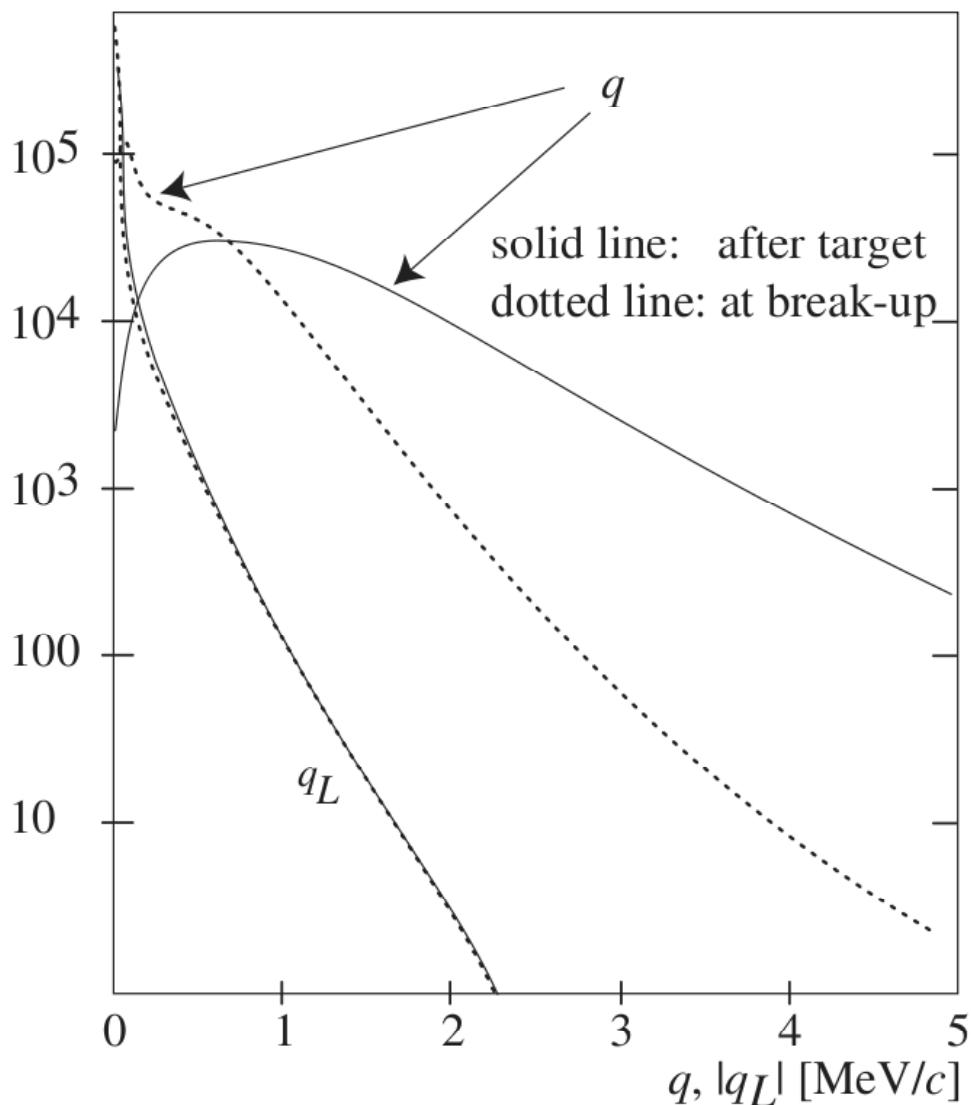
Figure 1.8: *Relative momentum distributions (q, q_L) for atomic $\pi^+\pi^-$ pairs at the breakup point and at the exit of the target. Note that q_L is almost not affected by multiple scattering in the target.*

Excitation/de-excitation and breakup of the atom are competing with its decay. Solving the transport equations with the cross sections for excitation and breakup, [22, 23, 24, 25, 26, 27, 28, 29, 30, 31, 32, 33, 34] leads to a target-specific relation between breakup probability and lifetime which is estimated to be accurate at the 1% level [25, 35, 36]. Measuring the breakup probability thus allows to determine the lifetime of pionium [38].

The first observation of pionium [51] was achieved in the interaction with Tantalum at the Serpukhov U-70 synchrotron. In that experiment, the atoms were produced in collisions of 70 GeV/c protons inpinging on a 8 μm thick Ta target. With only 270 ± 50 observed atomic pairs, it was possible to set a lower limit on the pionium lifetime [37, 49]: $\tau > 1.8 \times 10^{-15}s$ (90% CL).

1.7   Pionium Lifetime

The breakup probability is a function of the atom momentum and depends on the dynamics of the pionium interaction with the target atoms and on the pionium lifetime. For a given target atomic number and thickness, the theoretical breakup probability for pionium is calculated [28] with a relative error of less than 1% [35] thanks to the detailed knowledge of the cross-sections involved in the process, which is purely electromagnetic, in which Born and Glauber approximations are used [24, 27, 32]

This breakup probability is uniquely linked to the atom lifetime [38]. In Fig. (1.9) the P_{br} as a function of the lifetime is displayed for Ni targets with 94 μm and 98 μm. These were the foil thicknesses installed in DIRAC during the 2001-2003 data taking period.

Measuring P_{br} thus allows to determine the lifetime of pionium. In DIRAC the breakup probability can be measured experimentally as the ratio of the detected number of atomic pairs (n_A) over the total number of produced atoms (N_A):

$$P_{br} = \frac{n_A}{N_A} \tag{1.13}$$

As explained before, the total number of produced $\pi^+\pi^-$ atoms is related by an exact expression to the number of free pion pairs with low relative momenta, so the breakup probability can be measured with DIRAC experimental method.
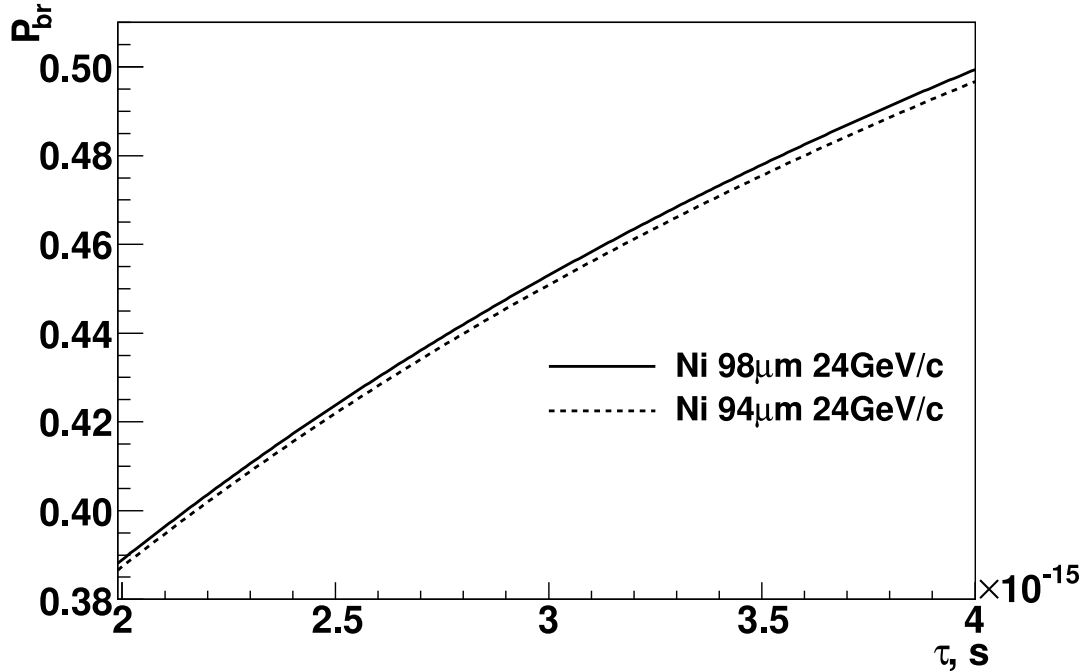
Figure 1.9: *Breakup probability as a function of pionium lifetime for Nickel targets with thicknesses of 94 μm and 98 μm. Only the 24 Gev/c proton beam momentum is shown here.*

1.8 The NA48/2 Experiment

The NA48/2 experiment at CERN [52] has been in the race for the $|a_0 - a_2|$ determination, simultaneously to DIRAC. In the NA48/2 facility, Kaons are produced by impinging 400 GeV protons from the SPS on a Beryllium target, then decay strongly via the reaction $K^\pm \to \pi^\pm \pi^+ \pi^-$ or in a semileptonic way by means of the breakdown $K^\pm \to \pi^+ \pi^- e^\pm \nu$.

In the former case the pion scattering lengths are extracted from the phase shift, requiring the use of Roy equations [44]. In addition to a 2 parameter fit with the pion scattering lengths a_0 and a_2 as free parameters, the Universal Band approach, corresponding to a 1-dimensional fit of the phase shift with a fixed relation between a_0 and a_2, is also applied. Supplementary constraints from ChPT and isospin breaking are invoked to determine the pion scattering lengths.

In the latter case, one has to face one more disadvantage. The measurement of the $\pi\pi$ phases in the range $\sim[300, 400]$ MeV/c^2 needs a model dependent extrapolation method to obtain the $\pi\pi$ scattering lengths in the pion-pion system at rest. Therefore measurements carried out in both cases present undesirable model-dependency and might never be as reliable as those performed by DIRAC.

The latest results provided by the NA48/2 experiment will be discussed in Chapter (7), comparing them with those obtained by the DIRAC Collaboration.

Chapter 2

The DIRAC Experimental Setup

The main features of the DIRAC apparatus can be found in Ref. [2]. In this chapter we will follow literally the narration of the mentioned source, paying special attention to those detectors made entirely by the Experimental High Energy Physics Group (GAES) of the Galician Institute of High Energy Physics (IGFAE) of the University of Santiago de Compostela: the VH and the GEM/MSGC detectors. Some technical characteristics will be intentionally omited, since they do not contribute to the comprehension of the present work. In addition, some aspects unreported in [2] will be addressed here, such as the T0, T2 and T3 trigger. The chapter will conclude with a historical review of the $K\pi$ atom detection.

2.1 Technical Characteristics

The DIRAC experiment is designed to detect oppositely charged pion pairs of a low relative center-of-mass momenta with high precision. The DIRAC spectrometer consists of a magnetic double arm spectrometer placed at a 24 GeV/c extracted proton beam of the CERN PS, impinging on a 94 or 98 μm thick Nickel target. The spectrometer setup is shown in Figs. (2.1) and (2.2). A detailed description can be found in [2]. Since its start-up, DIRAC has accumulated about 22000 atomic pairs.

The proton beam intensity during data taking was 0.9×10^{11} per spill with a spill frequency of 400÷450 ms. The beam line was designed to keep the beam halo negligible [53]. The beam intersection with the target plane reveals a Gaussian shape in the transverse and horizontal planes. The horizontal and vertical widths of the beam spot were $\sigma_{hor} = (0.80 \pm 0.08)$ mm and $\sigma_{vert} = (1.60 \pm 0.07)$ mm [54].
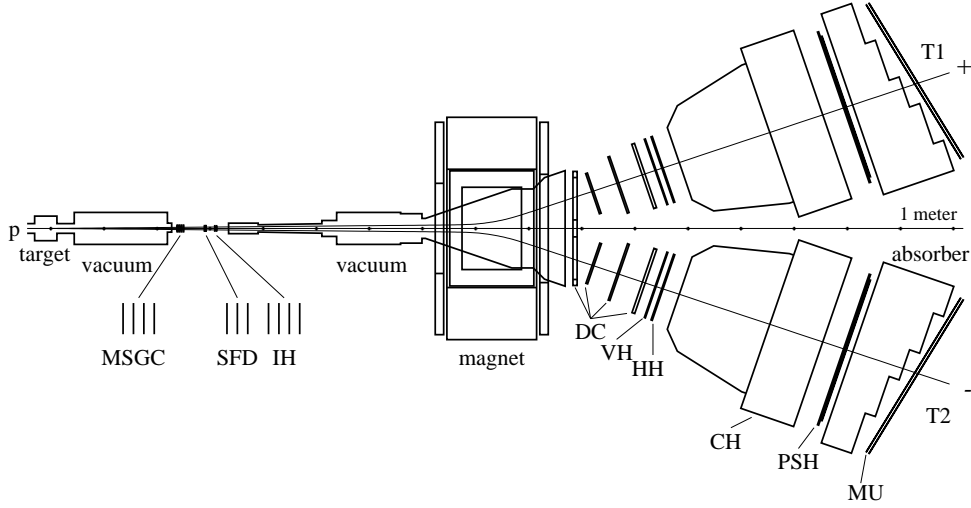
Figure 2.1: *Schematic top view of the DIRAC spectrometer. Upstream of the magnet: Target, Microstrip Gas Chambers (GEM/MSGC), Scintillating Fiber Detectors (SFD), Ionization Hodoscopes (IH) and iron shielding. Downstream of the magnet: Drift Chambers (DC), Vertical and Horizontal Hodoscopes (VH, HH), gas Cherenkov Counter (Ch), Preshower detectors (PSh) and, behind the iron absorver, Muon detectors (Mu).*

The targets we report here were 94 and 98 μm thick Ni foils, corresponding to a nuclear interaction probability of $\sim 6.4 \times 10^{-4}$ [55] or 6.7×10^{-3} radiation length. The transverse dimensions of the circular targets (4.4 cm diameter) were sufficient to fully contain the proton beam and to exclude possible interactions of the beam halo with the target holder.

The spectrometer axis is inclined upward by 5.7° with respect to the proton beam. Particles produced in the target propagate in a vacuum pipe to the upstream (with respect to the magnet) detectors. Afterward they enter into a vacuum chamber which ends at the exit of the magnet. The exit window is made of a 0.68 mm thick Al foil. The angular aperture is defined by a square collimator and is 1.2 msr ($\pm 1^{\circ}$ in both directions). DIRAC is equiped with a central dipole magnet whose field is B=1.65 T and with a bending power BL=2.2 Tm, capable to separate positively and negatively charged particles: positive (negative) particles are deflected to the left (right).

The upstream detectors are 2.5 to 3 m away from the target and cover an area of roughly 10$\times$10 cm^2. There are three upstream detectors: the Microstrip Gas Chambers (GEM/MSGC), the Scintillating Fiber Detector (SFD) and the Ionization Hodoscopes (IH). After the magnet, in the downstream region, the two
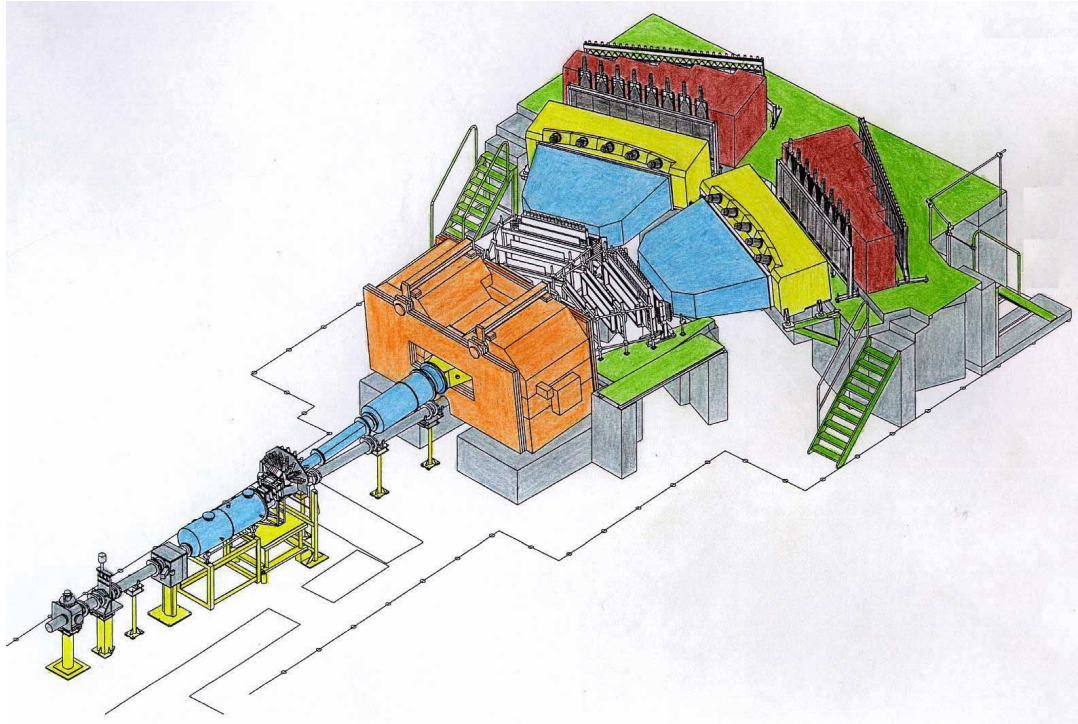
Figure 2.2: *Isometric artistic view of the DIRAC experimental setup.*

arms of the spectrometer are identically equipped with Drift Chambers (DC), the Vertical Hodoscopes (VH), the Horizontal Hodoscopes (HH), the threshold Cherenkov detectors (Ch), the Preshower detector (Psh) and the Muon detector (Mu).

2.2   Spectrometer Performance

The momentum range covered by the spectrometer is $1.2 \div 8$ GeV/c. The relative resolution on the lab-momentum is dominated by the multiple scattering downstream the vertical SFD detector and the spatial resolution of the drift chambers. While the former leads to a momentum independent resolution, the later aleads to a slight increase with momentum. Studies of the Λ signal in $\pi^- p$ track pairs [56] result in $\sigma(p)/p = 2.8 \times 10^{-3}$ increasing to 3.3×10^{-3} at 8 GeV/c (Figs. (4.12) and (4.14)). The resolutions on the relative c.m. momentum of $\pi^+\pi^-$ pairs from atomic break up, $\vec{Q} = (Q_X, Q_Y, Q_L)$, are in the plane transverse to the total momentum $\vec{p}_{\pi^+\pi^-}^{Lab}$, $\sigma_{Q_x} \approx \sigma_{Q_Y} \leq 0.49$ MeV/c and

longitudinally $\sigma_{Q_L} = 0.50$ MeV/c [57][1]. The setup allows to identify electrons (positrons), protons with $p \leq 4$ GeV/c (by Time-Of-Flight) and muons (cf. Fig. 23 in [2]). It cannot distinguish π- from K-mesons, but kaons constitute a negligible contamination [58, 75]. This contamination will be studied in section 3.9.

The trigger system [59] reduces the event rate down to a level acceptable for the data acquisition system. The on-line event selection keeps almost all events with $Q_L < 22$ MeV/c, $Q_T = \sqrt{Q_x^2 + Q_y^2} < 10$ MeV/c and rejects events with $Q \geq 15$ MeV/c progressively [60]. In the first level trigger [61] a coincidence of VH, HH and PSh signals and anticoincidence with Ch signals in both arms is treated as a pion-pair event. A condition on the HH of the positive and negative arms, $|HH_1 - HH_2| \leq 2$ slabs, rejects events with $Q_y > 10$ MeV/c. Fast hardware processors [59, 62, 63, 64] are used to decrease the first level trigger rate by a factor 5.5. The trigger rate in standard conditions was around 700 per spill. The trigger accepts events in a time window ± 20 ns with respect to the positive arm and thus allows for collecting also accidental events. The trigger system provides parallel accumulation of events from several other processes needed for calibration such as e^+e^- pairs, $\Lambda \rightarrow p\pi^-$ or $\pi^\pm \pi^+ \pi^-$ final states.

Dead times were studied in a run with 30% higher intensity than nominal and depend on the average beam intensity as well as on the micro duty cycle of the beam. An overall dead time of 33% was found for triggers and data acquisition, with an additional 10% due to front-end electronics [65]. At normal intensities, dead times are lower. Biases due to dead times could not be found. When selecting data offline for further analysis, some run periods have been eliminated, those where problems with detectors, spill structure or micro duty cycle were found.

The full setup, including detectors, detector responses, read-outs, triggers and the magnet has been implemented into the detector simulation DIRAC-GEANT [66] and into the DIRAC analysis package ARIANE [67] such that simulated data can be treated in the same way as real measurements.

---

[1]A momentum dependence of $\sim 0.016 [MeV/c] \times p_{\pi^+\pi^-}^{Lab}$ (p in GeV/c) is included in these numbers

2.3   The GEM/MSGC Detector

The University of Santiago de Compostela has been responsible for the conception [1] and full construction of this detector. The GEM/MSGC detectors of DIRAC are the first active planes of the spectrometer, at a distance of 2.4 m from the target foil. The four planes take part of the upstream tracking procedure of the experiment, developing the main task of direct measurement of particle trajectories upstream the magnet. Its excellent spatial resolution allows to improve the double track resolution for close lying tracks.

The DIRAC GEM/MSGC chambers are gas detectors working in proportional mode based on the principle of the Gas Electron Amplifier (GEM) [68, 69], complemented with a second amplification and readout stage provided by Micro Strip Gas Chambers. Each chamber has active an area of 10.24×10.24 cm^2, and its active gas volume is limited by two planes, a drift electrode and a microstrip sensor plane. A GEM foil is placed between them, evenly spaced from the other two with an uniform gap of 3 mm, as indicated in Fig. (2.3).
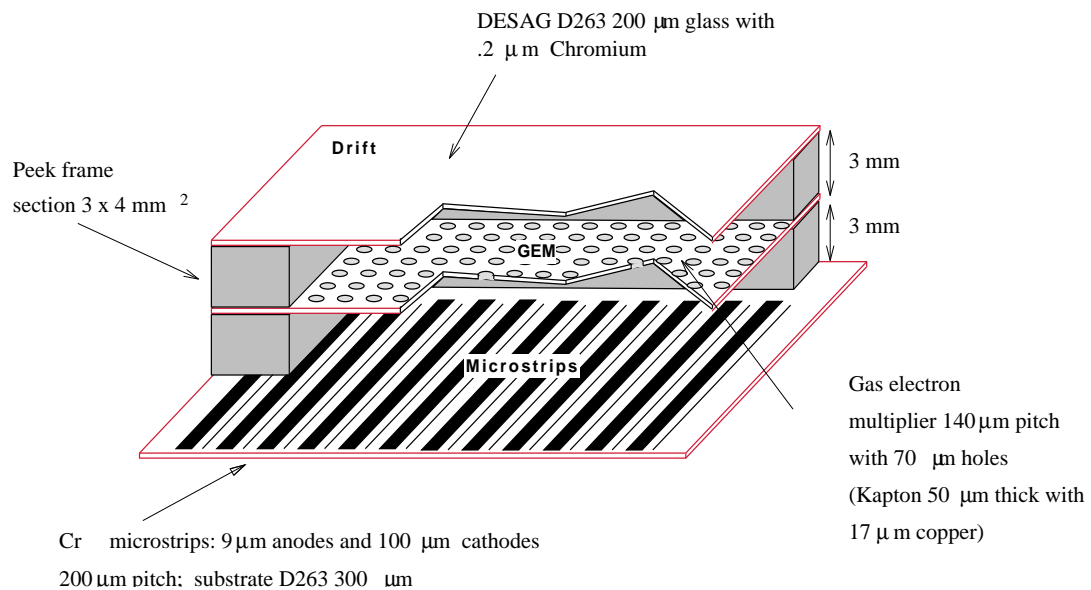
Figure 2.3: *Layout of the GEM/MSGC detector.*

The drift electrode is made of a Chromium-coated thin glass (200 μm) methalized in one side connected to a negative voltage. The GEM is a kapton film of 50 μm double-sided methalized with 4 μm of Cu. It presents a perforated pattern with 80 μm diameter holes, 140 μm apart from each other.
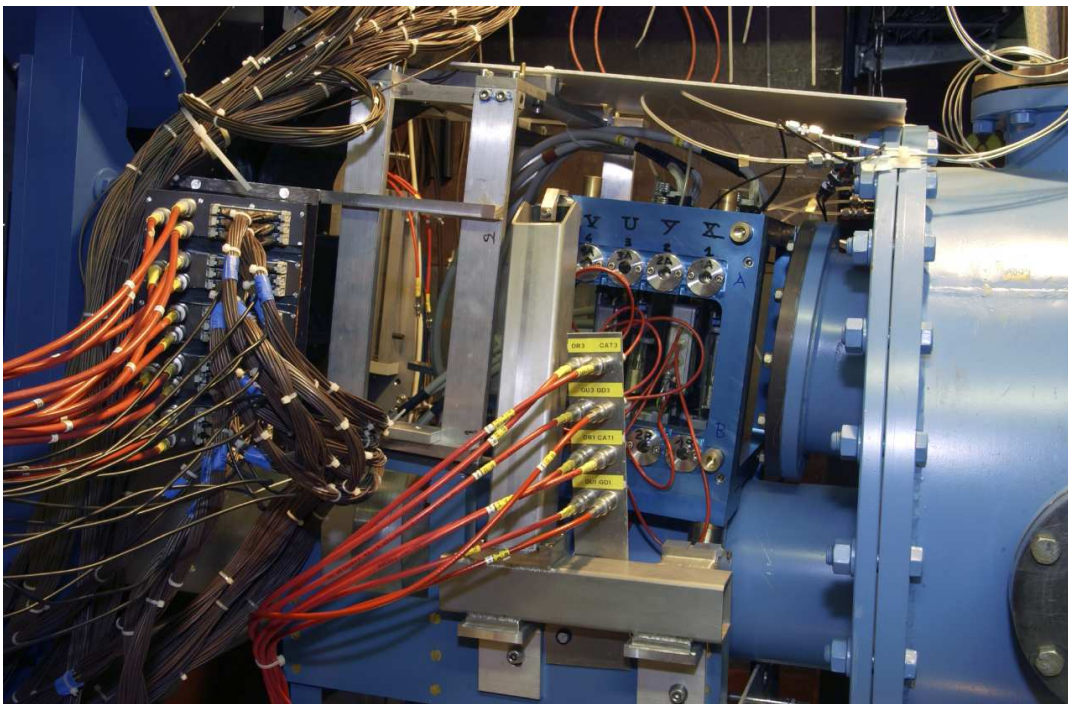
Figure 2.4: *Photography of the three detectors installed upstream the magnet, between the first vacuum chamber (right-hand side) and the secondary particle channel. From right to left, the GEM/MSGC, SFD and IH detectors can be found. The primary proton beam line can be appreciated at the bottom.*

The microstrip plane consists of alternating Chromium strips mounted over a subtract DESAG D263 of 300 μm thick ionic glass. Anodes are 9 μm wide, cathodes 100 μm and pitch between anodes is 200μm. In the bottom side of microstrips plane a methalic film is used as electrode (backplane).

The planes are mounted on a Stesalit frame chemically inert with respect to the gas admixture. The gas used for operation is an admixture with Argon and Di-metil-eter (DME, C_2H_6O) in a 60/40 proportion. The entry hole in the frame of the detector has a diameter greater than the output one, ensuring a light overpressure necessary for detector operation.

With the introduction of the GEM foil —a potential difference of $\sim$ 400 V is applied between the two metal layers with an amplification by a factor of 30—, the primary electrons signal becomes doubly amplified, allowing lower values of High Voltage (HV) and consequently a more stable operational mode.

A primary electron produced in the first gas volume, defined by the drift plane (with applied voltage of $\sim$ 400 V) and GEM, will ionize the atoms of the gas producing an initial electron avalanche when entering the GEM electric field. At a later stage, a new multiplication takes place in the region next to

the microstrips. The electrons produced in the avalanche are collected by the anode (ground) nearest to the position of original electron.

Electrons are atracted by the positive electric field of the strips, developing a second avalanche, so electron signal becomes doubly amplified. The cloud of positive ions tends to cluster around adjacent cathodes, with applied voltage of ~ -3000 V. An overall detector gain of approximately 3000 is achieved. HV values are limited by sparks inside the gas volume, that may occur when the charge collected by the strips is over a threshold value, usually produced under high particle irradiation conditions.

The GEM/MSGC measures particle coordinates in 4 planes along the direction of the incoming particle: X, Y, XP, YP, with orientations 0, 90, 5, 85 degrees, respectively, where the 0 degrees are defined by microstrip disposed vertically (X-coordinate). The distances to the target plane in Z coordinates are 2.246, 2.338, 2.464 and 2.502 m. The stereo angles allow resolution of ghost ambiguities for two or more particles. With a single-hit space resolution close to 50 μm, this detector provides a precise measurement of the pion pair opening angle, ultimately limited by multiple scattering in the thin target. The four planes installed in the DIRAC spectrometer can be seen in Fig. (2.4).

The GEM/MSGC permits to reduce the effect of the multiple scattering in the target foil. It performs a direct measurement of the transverse momentum (Q_T) by measuring the distance between π^+ and π^-. Together with the Scintillating Fiber Detector (SFD), to be described in next section, it also allows to improve the resolution of the longitudinal component Q_L, by providing the impact point at the magnet entrance. Because of its standalone tracking capability with stereo angles, it also monitors the beam position coordinates. GEM/MSGC's allows to resolve tracks with the same hit in SFD, improving double track resolution form 4 mrad to 0.4 mrad. The precise spatial resolution from GEM/MSGC together with TDC information from SFD allows an effective rejection of background particles crossing the detectors from secondary interactions or particle decays along the channel. As an additional merit, they do not affect negatively to the global setup, adding a low quantity of matter and being practically transparent to the radiation.

Single hit resolution was determined by setting 4 GEM/MSGC planes parallel to each other, all measuring the same coordinate. The resolution was defined using in each case 3 detectors to define the track, and typical vales of 54 μm were found, as shown in Fig. (2.5). The average efficiency for a standard detector is 90%. When at least 4 signals among 6 detectors are required to construct a track, this is sufficient to provide 97% overall upstream tracking efficiency.
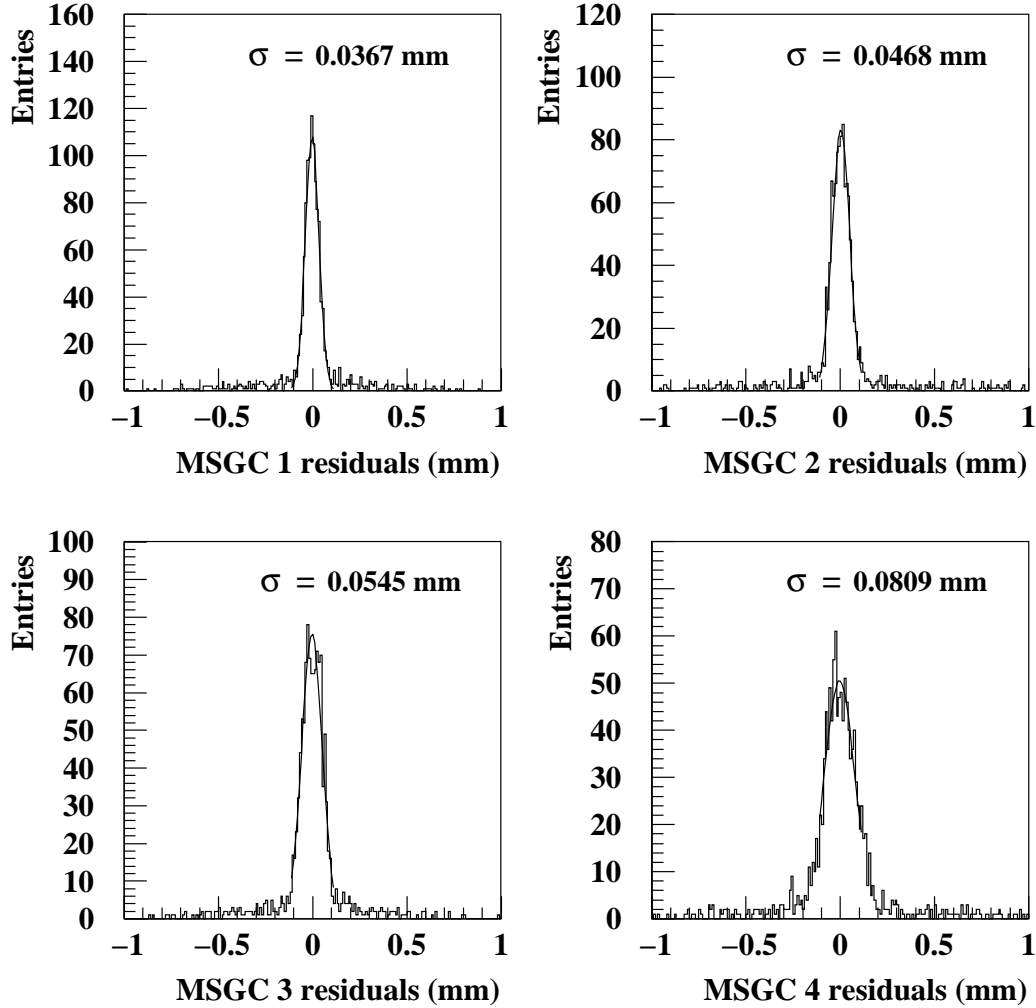
Figure 2.5: *Space resolution of the GEM/MSGC detector measured in a dedicated beam-test with 4 planes parallel to each other. Please notice the influence of the multiple scattering in the detector resolution.*

2.4   The Scintillating Fiber Detector

The Scintillating Fiber Detector (SFD) is used together with the GEM/MSGC detector, for upstream tracking, and provides topological trigger capabilities [70] for rejection of pairs with relative distance larger than 9 mm. It can also capture time information for trigger purposes.

The SFD consists of two perpendicular fiber planes to measure the X and Y coordinates of incident particles[2], as the deposited energy from the particles is transformed into light. Every single fiber is built in a nucleus of scintillating

---

[2]A third upgraded SFD-U plane rotated 45º relative to X and Y was added for 2002 and 2003 periods.

material surrounded by a coating with a lower refraction index, allowing the total reflexion phenomenon for a solid angle given by:

$$\Omega = 2\pi(1 - n_2/n_1) \qquad (2.1)$$

where n_1 and n_2 are the refraction index of the scintillating material and the coating, respectively. The light produced by an incident particle will be retained in the fiber with a high probability, once the total reflexion is produced.

The SFD covers a 105×105 mm^2 area. Each detector plane is composed of 240 column channels with 440 μm pitch, consisting of a stack of 5 fibers in depth, measuring each one from 70 to 150 mm, as seen in Fig. (2.6). Fibers forming one sensitive column are connected via a light guide into one channel of position-sensitive photomultiplier (PSPM), with a total of 15 photomultipliers of 16 channels each.
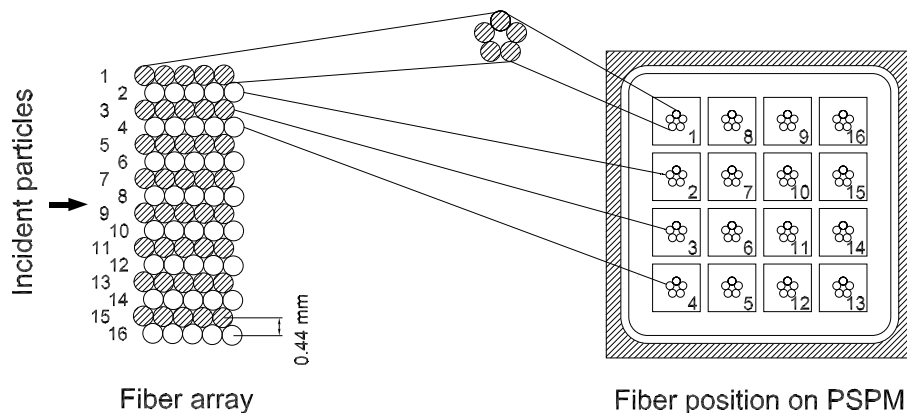
Figure 2.6: *The SFD principal structure. A 16-channel fragment is shown.*

A dedicated electronic circuit Peak Sensing Circuit (PSC) has been custom developed to provide signal discrimination with dynamic rejection of cross-talk in adjacent channels using the peak-sensing technique [71]. Discrimination of a channel is given by the condition $2A_i - A_{i-1} - A_{i+1} > A_{thr}$, where A_i are channel signal amplitudes and A_{thr} defines the threshold value.

For time correlated particle pairs (up to $\sim$ 5 ns time difference) with distance more than one fiber pitch, the PSC algorithm provides efficient detection, avoiding cross-talk and rejecting noise. However, when adjacent fiber columns are crossed by two particles simultaneously, then the PSC algorithm leads to a suppression (with 50% probability) of the detected yield of double track events, and one of the hits is lost. For time difference greater than 5 ns the PSC behaves as an ordinary leading edge discriminator.

The level of optical cross talk among the PSPM channels due to escape of ultraviolet light from one fiber column to the adjacent one, together with noise was found to be $\sim 2\%$. Readout supplies time information in digital form TDC. The detection efficiency is high (larger than 97% as we shall see) and the average hit multiplicity is near 5 in the 50 ns time window of TDC. Each detector fiber is equipped with a TDC channel which provides time tagging essential for upstream tracking. The raw time spectra, obtained from e^+e^- and $\pi^+\pi^-$ events, are shown in Fig. (2.7) for two arbitrary SFD channels. After off-line deconvolution of the trigger time jitter the resolution of the SFD is found to be σ=0.8 ns, obtained for e^+e^- triggers. Single track resolution is defined by the fiber column pitch of 440 μm.
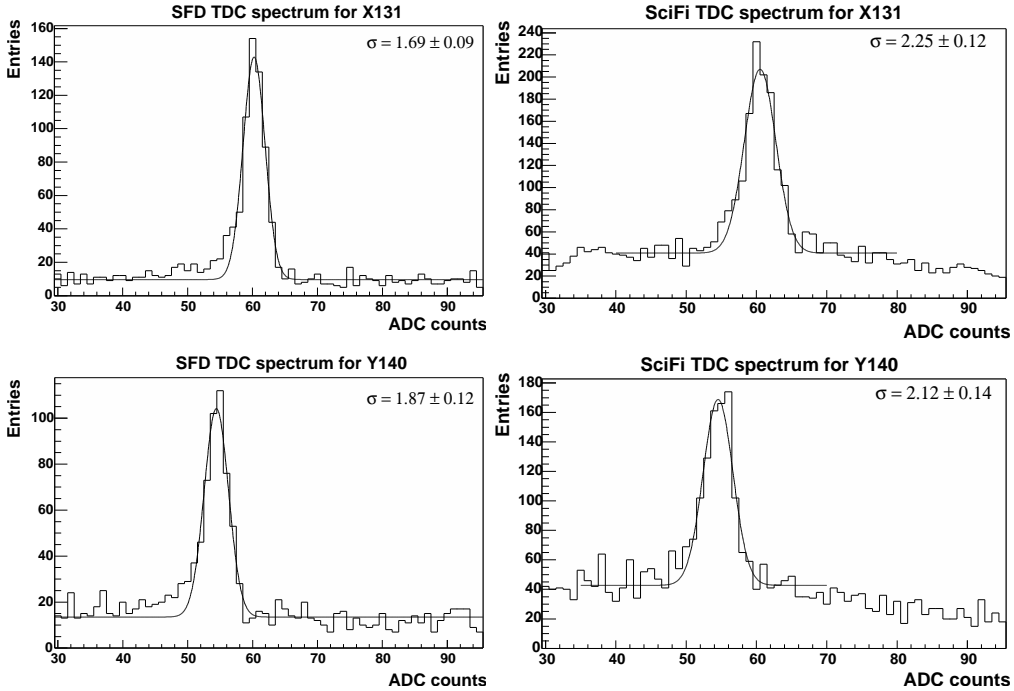
Figure 2.7: *SFD raw time spectra for e^+e^- (left) and for $\pi^+\pi^-$ (right) trigger data. The horizontal scale is in TDC channels, the channel width is 0.5 ns.*

2.5   The Ionization Hodoscope

Since charged pions originated from pionium breakup cross the upstream detectors at rather small relative distances, a dedicated Ionization Hodoscope [72] has been built to separate the double ionization signal produced by close pion pairs incident on the same scintillating slab, from single ionization signals produced by one particle. This way, uncertainties resulting from pairs with

relative distance less than the double track resolution are significantly reduced. In addition, the IH takes part of the trigger system of DIRAC, to be described in section (4.2.3).

The IH detector is a scintillation hodoscope consisting of 4 planes of 11×11 cm^2 sensitive area (Fig. 2.8) placed 3 m downstream the target. Two planes (X-A and X-B) are vertically oriented, and the other two (Y-A and Y-B) are horizontally oriented, shifted by a half-slab-width to mutually cover the gaps between slabs. Each plane is assembled from 16 scintillating plastics. The slabs are 11 cm long, 7 mm wide and 1 mm thick. They are connected to the PM photocathodes via 2 mm thick and 7 mm wide lucite light guides.
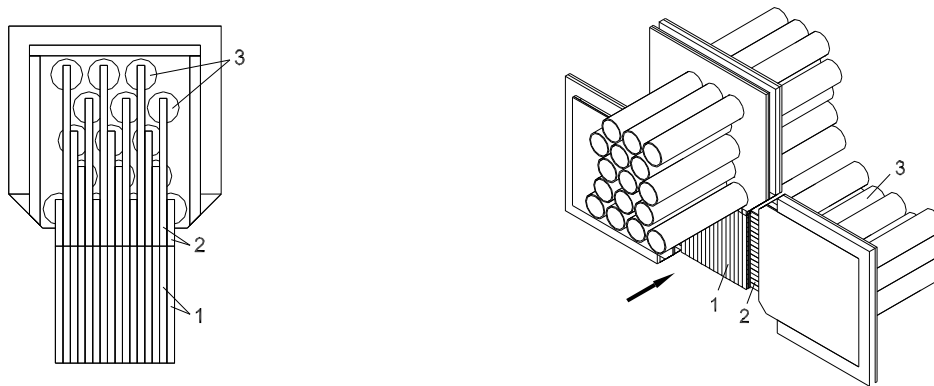
Figure 2.8: *Design and isometric view of the IH scintillation plane (1.— scintillators, 2-— light-guides, 3.— photomultipliers).*

The front and rear surfaces of a slab are covered by a millipore film [73] for efficient light collection. At the lateral surface of the slab, light is reflected by a 30 μm mylar film in order to minimize the gaps between adjacent slabs, which is less than 70 μm wide.

Scintillation light is detected by photomultipliers. The photocathodes are in optical contact with the wide side of a light guide instead of the traditional butt-end readout, improving the light collection efficiency.

Signal amplitude and time are digitized by ADC and TDC modules, respectively. The time resolution of the IH detector is better than 1 ns. The typical response of one IH channel to close particle pairs incident on one scintillating slab and to single particle is shown in Fig. (2.9). If a threshold is set to retain 95% of the double ionization signal from pairs, the contamination from single particle amplitudes is less than 15% (Fig. 2.10).
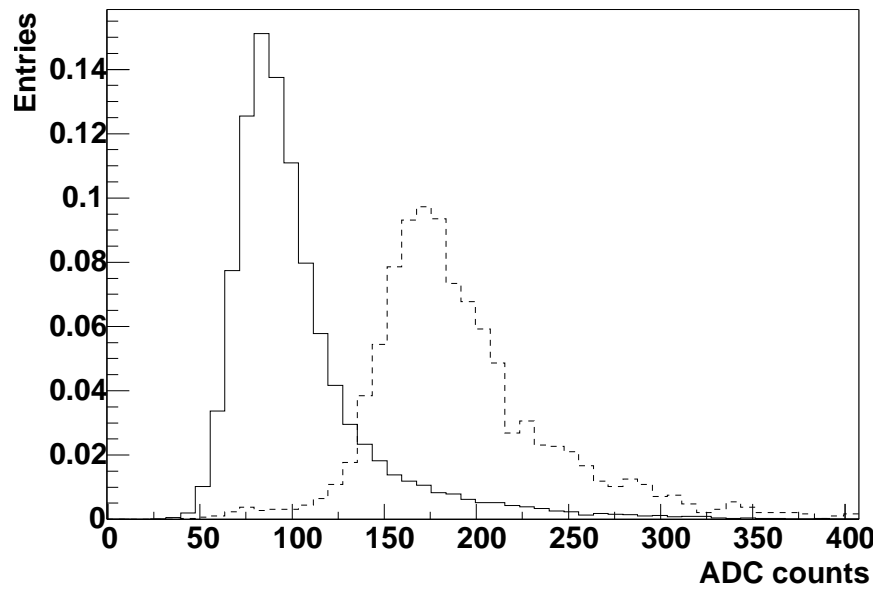
Figure 2.9: *Typical ADC spectra for single (solid line) and double (dashed line) ionization loss from particles crossing one IH scintillating slab.*
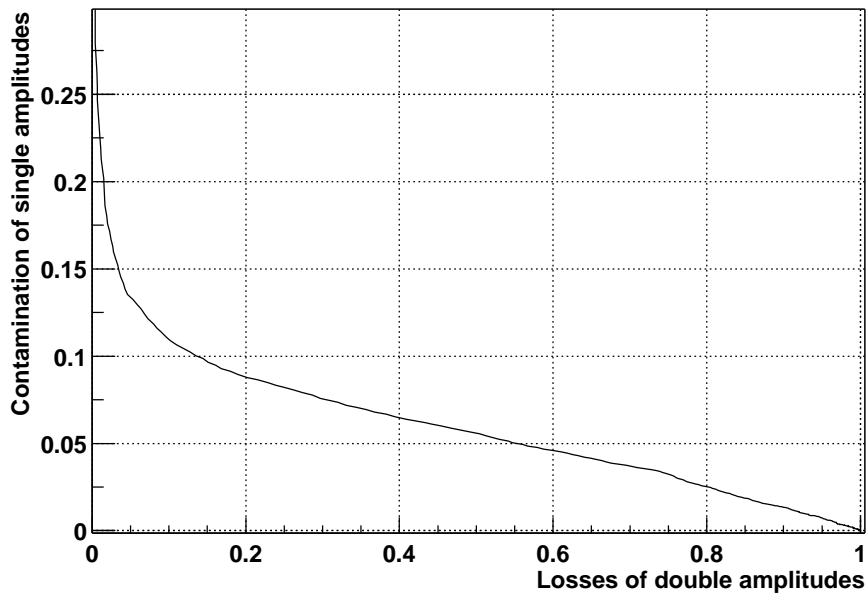
Figure 2.10: *Contamination of single ionization amplitudes as a function of losses of double ionization as obtained from the analysis of the spectra of Fig. (2.9).*

2.6 The Magnet

The magnet is located 8.3 m away from the target, and separates positive and negative particles coming from upstream, converting the spectrometer in a double-arm telescope. The two downstream arms are placed at $\pm 19^\circ$ relative to the central axis. The magnetic field ($B =$1.65 T, bending power $BL =$2.2 Tm) has been parametrized. The dipole magnet has an aperture of 1.55×0.50 m^2 ($W \times H$) and measures 0.5×1.5×1.1 m^3. To reduce the stray field, two magnetic screens are fixed near its entrance and exit.

2.7 The Drift Chambers

The drift chamber system is used to perform particle tracking downstream the dipole magnet. These are gas detectors with a periodic cell structure giving spatial and timing (by means of the drift time) information, used also in the T4 trigger level.

Despite the choice of a two-arm solution, the first chamber (DC-1) covers both left and right arms of the spectrometer (see Fig. (2.1)) and it is designed with two separated sensitive areas. This chamber provides 6 successive measurements of the particle trajectory along the coordinates X, Y, W, X, Y, W, where W is a stereo angle with inclination 11.3^0 with respect to the X-coordinate.
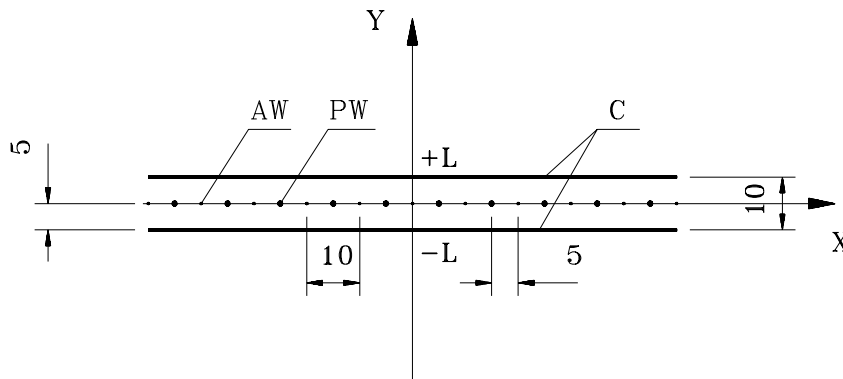
Figure 2.11: *Schematic view of the wire chamber electrodes: AW – anode wires, PW – potential wires, C – cathode foils. Dimensions are in mm.*

Each of the two arms consists of 3 chamber modules, of identical design, measuring coordinates X,Y (DC-2), X, Y (DC-3) and X, Y, X, Y (DC-4) following the direction of the outgoing particle. The dimensions of the DC modules are 0.8×0.4 m^2 for each DC-1 sensitive area, 0.8×0.4 m^2 for DC-2, 1.12×0.4 m^2

for DC-3, and 1.28×0.4 m^2 for DC-4. DC-1 is instrumented with 800 electronic channels, and both arms together contain 1216 electronic channels.

The distance between the center of the first half of DC1 and the center of DC4 provides a lever-arm of 1.6 m along the average particle path, having uniform spacing of chambers DC-2 and DC-3 along this path. Six measurement points, together with the 1.6 m lever arm, allow to accurately reconstruct the downstream tracks.

A schematic drawing of the sensitive element is shown in Fig. (2.11). As seen in the figure, a sensitive area, corresponding to each anode wire and limited by the cathode planes and potential wires, has a square (10×10 mm^2) shape. Cathode plane foils provide stable chamber operation and add only small amount of material along the particle path. A rather large diameter of the anode wires has been chosen in order to operate the chambers at high current avalanche amplification mode.

The chamber design is shown in Fig. (2.12) for the case of the DC-2 module. The module is a stack of aluminium and fiberglass frames fixed by screws with rubber o-rings glued to provide gas tightness.
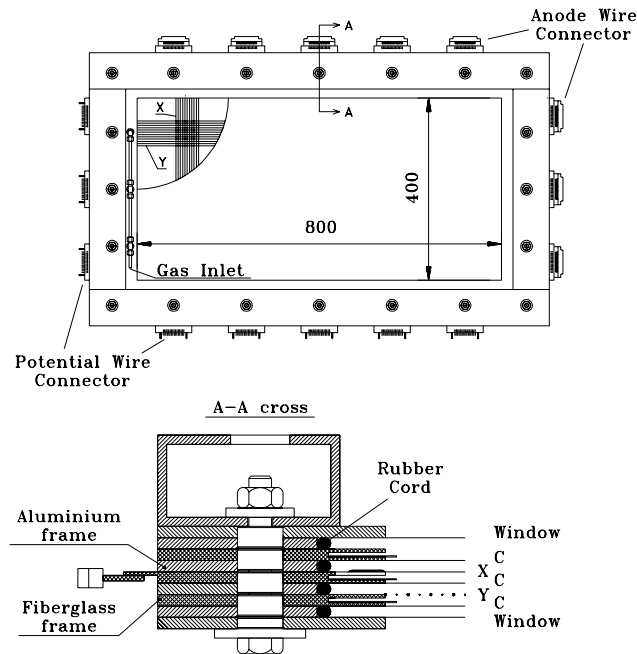
Figure 2.12: *Design of the DC-2 module. Top: general view. Bottom: structure of the frame stack; X − X-plane, Y − Y-plane, C − cathode foils.*

The design of module DC-1 differs from the former DC-2 description. The main difference, illustrated in Fig. (2.13), consists of the DC-1 comprising, in a single gas volume, two sets of sensitive planes, placed symmetrically to the left and right hand side of the spectrometer axis. The middle zone, strongly irradiated, is built insensitive to the particle flux. The limiting edge of the sensitive zones can be varied. This design of the DC-1 module ensures little amount of material, by avoiding frames in the small angle region.

The readout electronics of the drift chambers, which is a custom-made system [74], provides data transfer into the buffer collection memories and input to the trigger processor. The sensitive wire signals are digitized by TDC counters, which are plugged in the connectors mounted onto the chamber frames, and are subsequently linked to the Drift Chamber Proccessor (DCP) and VME buffer memory. This solution results in reduced number of electronic units, small number of cables and high noise immunity. The data of an event are stored in local buffers until the higher level trigger decision is issued.
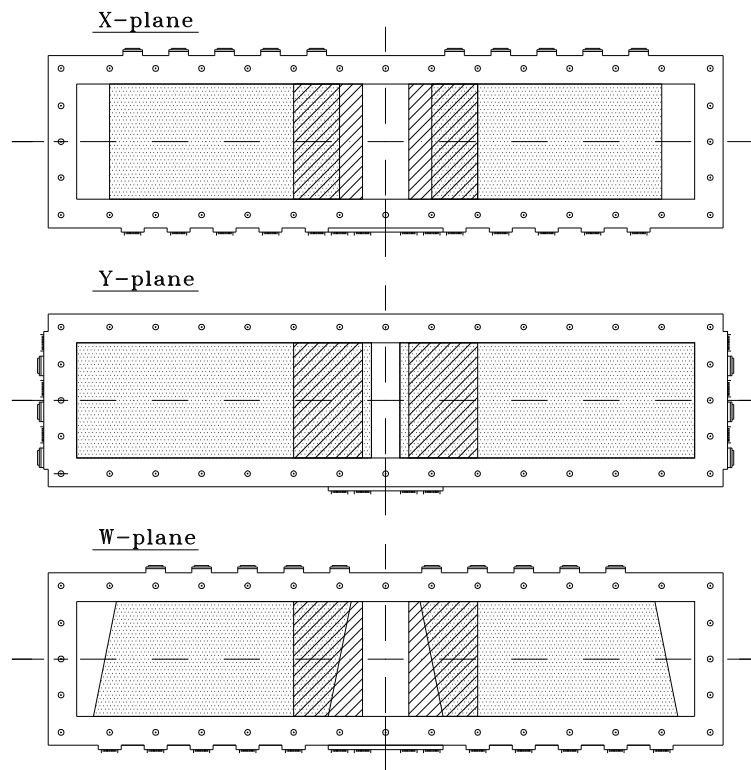
Figure 2.13: *Schematic view of the DC-1 module. Dotted areas show the sensitive regions of the X-, Y- and W-planes. Hatched areas mark the zones of the cathode strips which allow to change the width of the insensitive area in the central region.*

The drift chambers operate in a high current avalanche mode. The single hit efficiency is above 96% when the particle flux along the gas mixture $(Ar(\sim 50\%) + iC_4H_{10}(\sim 50\%) + H_2O(0.5\%))$ is about 10 kHz/cm^2. The tracking efficiency of the drift chamber system as a whole is about 99%, since the requested number of hits per reconstructed track is less than the total number of sensitive planes crossed by a particle. A space-to-time relationship was extracted from the time spectrum and its integral distribution shown in Fig. (2.14), for a sample of clean events with a small amount of background hits. Study of the drift function parameters for different chamber planes at different beam intensities shows good stability of the above relation.
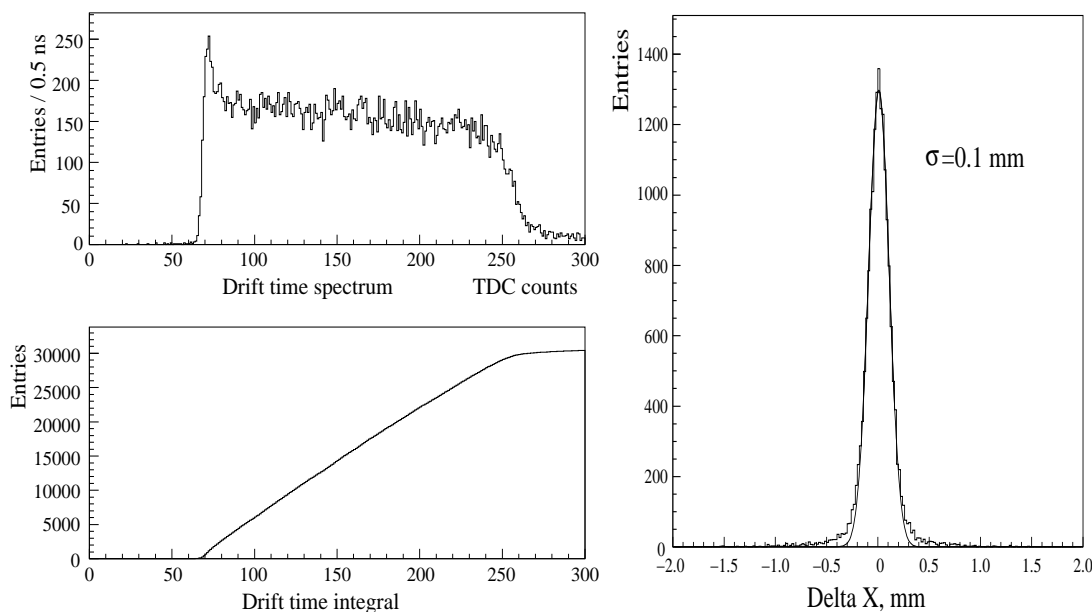
Figure 2.14: *Distribution of the drift time (left upper) and its integral spectrum (lower), horizontal scale is in TDC channels, bin width is 0.5 ns. On the right-hand side distribution of differences between the measured and predicted X-coordinate is displayed. Plots from X4 plane.*

The coordinate resolution of the DC system is also illustrated in Fig. (2.14), where the distribution of differences between the predicted and measured coordinates in one of the planes is shown (X4-plane right arm). The measured standard deviation, $\sigma = 100$ μm, is defined not only by the intrinsic chamber plane resolution, but also by the accuracy of the predicted track coordinates. Taking the latter into account the measured intrinsic space resolution of one plane is better than 90 μm.

2.8 The Time-Of-Flight Detector

A hodoscope system consisting of vertical scintillation slabs has been placed downstream the drift chambers. It has the overall purpose of providing fast coincidence signals between both spectrometer arms, necessary for the first level trigger and for events selection, as well as for DC timing also.

The TOF detector, also called Vertical Hodoscopes (VH) consists of two identical telescopes matching the acceptance of the DC system. Each telescope contains an array of 18 vertical scintillation counters. The slab dimensions are 40 cm length, 7 cm width and 2.2 cm thickness. Scintillation light is collected at both ends by two 12-dynode Hamamatsu R1828-01 photomultipliers coupled to fish-tail light guides. The front-end electronics was designed to minimize the time jitter, providing a position independent time measurement.
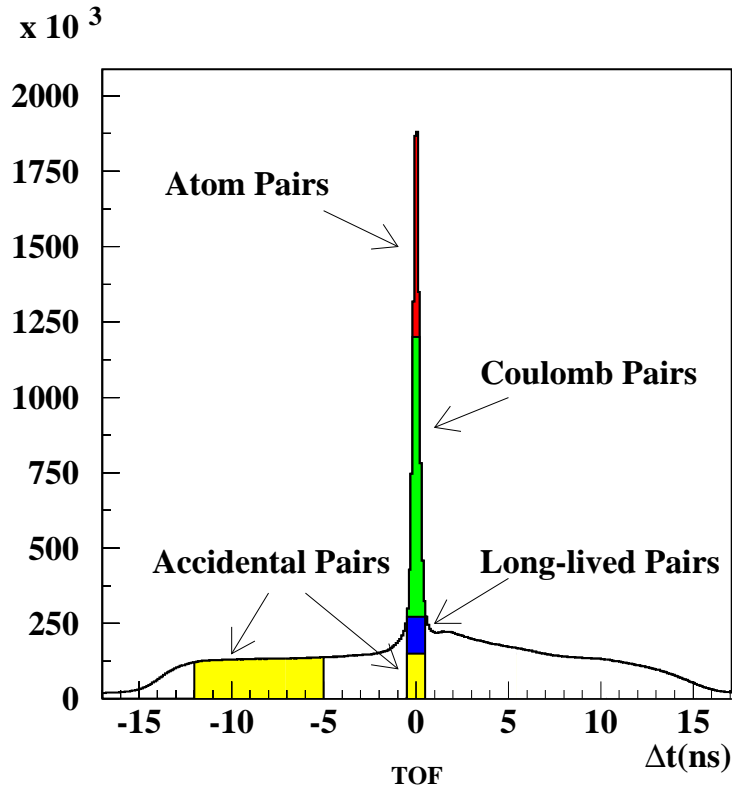
Figure 2.15: *Time difference between charged positive and negative particles obtained from standard hadron trigger data. The central peak has a Gaussian width of 193 ps, and the shaded area represents a 2σ cut used to select prompt $\pi\pi$ events. The flat background is originated from accidental pairs, not belonging to the same beam interaction. Note the shoulder on the right-hand side of the peak, due to $\pi^{-}p$ prompt pairs.*

The vertical array of scintillation counters is used, in correlation with other detectors, in the definition of dedicated triggers for calibration purposes and in a higher level trigger for the selection of low Q events (see trigger section). A key function of this detector, which motivated its special design, is to provide a very accurate time definition of pion pairs originated from the same proton-nucleus interaction (**prompt** pairs), in order to perform a clean separation (in off-line analysis) with respect to pairs formed in separate proton-nucleus interactions (**accidental** pairs). Used as a Time-Of-Flight detector it also allows to identify $p\pi^-$ pairs in prompt pairs, as they might constitute a significant source of background to the $\pi^+\pi^-$ signal.
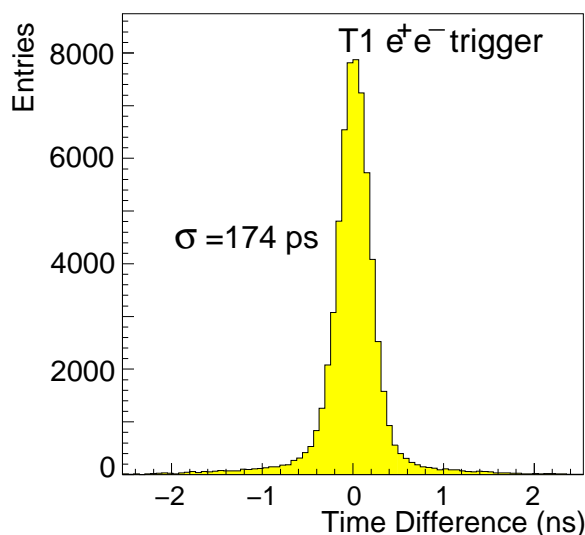
Figure 2.16: *Time difference spectrum for e^+e^- pairs detected by the vertical hodoscopes, after path length correction. Data come from e^+e^- triggers.*

The VH single-hit detection efficiency is 99.5% for the positive, and 98.8% for the negative hodoscope arms. In Fig. (2.15) the distribution of the time difference between positive and negative pions in the spectrometer is shown, where two distinct regions are clearly seen. The events in the peak correspond to the $\pi^+\pi^-$ prompt pairs that enter the VH in time coincidence, and apart from an small fraction, they represent the $\pi^+\pi^-$ pairs coming from the ionization in the target or from short-lived resonances. The region out of the peak is populated by accidental $\pi^+\pi^-$ pairs coming from different interactions or long-lived resonances, which do not enter the VH detector in time coindidence.

The observed ratio between prompt and accidental pairs in the 2σ cut region around the peak is about 16. The overall time resolution of the system has been measured with e^+e^- pairs to be 127 ps per counter [75], which corresponds to

174 ps resolution for the time difference between positive and negative arms (Time-Of-Flight resolution). The latter is shown in Fig. (2.16). The dedicated e^+e^- calibration trigger selects e^+e^- pairs from γ conversions and Dalitz decays of π^0 which are almost synchronous in time, as the time of flight of e^+e^- pairs is momentum independent in the available setup range of momenta.
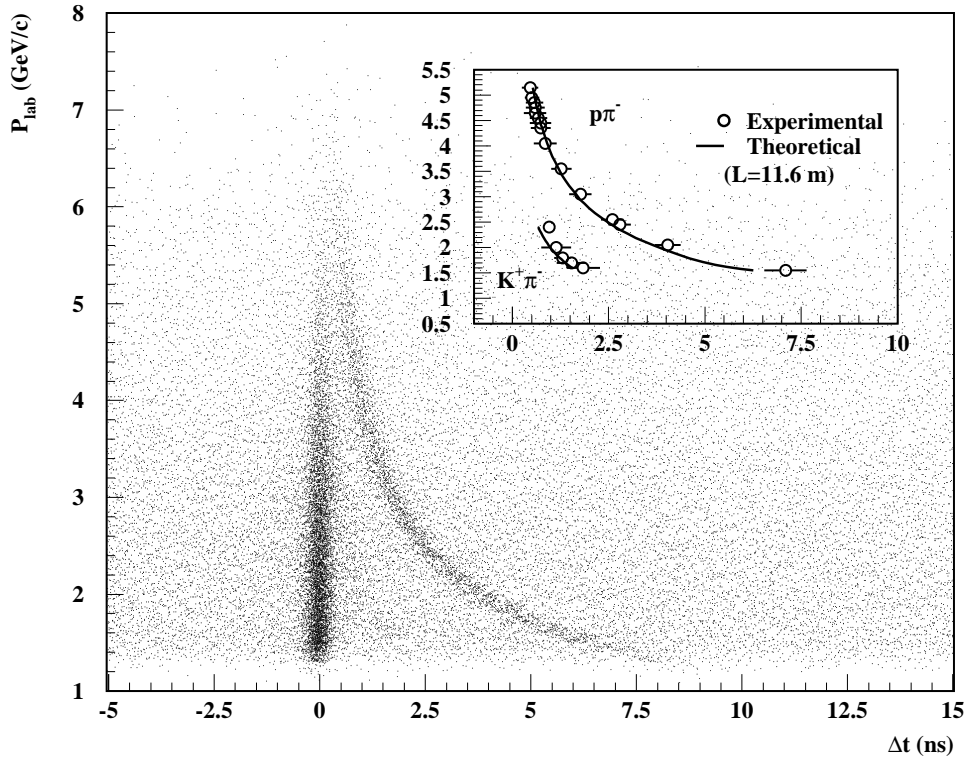
Figure 2.17: *Correlation between the measured momentum of the positive particle and the VH time difference between the positive and negative spectrometer arm, taking into account the correction for the difference in path length. The accumulation bands correspond to $\pi^-\pi^+$ (vertical band) and π^-p (curved band) pairs.*

This timing capability allows to separate $\pi^+\pi^-$ from π^-p pairs in the momentum range from 1 to 5 GeV/c, and from $\pi^\mp K^\pm$ pairs in the range from 1 to 2.5 GeV/c, as illustrated in Fig. (2.17).

2.9   The Horizontal Hodoscopes

The horizontal hodoscope (HH) system is similar to the VH in its design and implication on the definition of the first level trigger. In addition its response is used to apply a coplanarity criterion for triggering pairs hitting both detector

arms. This trigger requirement selects oppositely charged particles with relative vertical displacement, Δy, less than 7.5 cm. Its response is used to select events with small relative angle in the Y direction, and to support the reconstruction with spatial track information.

The HH is also separated into two arms, each covering an area of 40×130 cm^2. Each hodoscope consists of 16 horizontal extruded scintillating slabs of dimensions 130×2.5 cm^2, with a thickness of 2.5 cm. Both ends of each slab are coupled to specially shaped light-guides as illustrated in Fig. (2.18). With these specifications the coplanarity requirement corresponds to $\Delta y = 2$ slabs maximun.

The photomultipliers are equipped with a voltage divider allowing high counting rate capability. The front-end electronics system is the same as those for the vertical hodoscopes. The single hit detection efficiency of HH is greater than 96.6 % on both arms, and the time resolution is 320 ps.
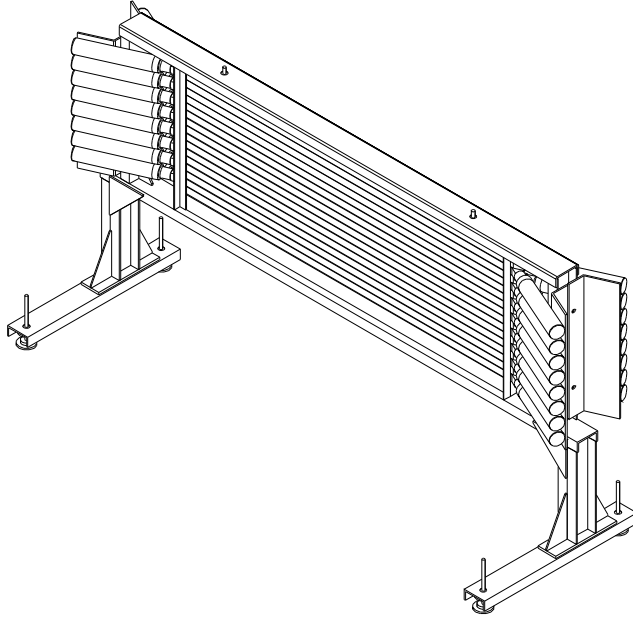
Figure 2.18: *General layout of the horizontal hodoscopes.*

2.10   The Cherenkov Counters

A pair of Cherenkov threshold detectors provides the strong e/π separation capability needed by the experiment. This detector is essential for rejection of the main background of electron-positron pairs from photon conversion, Dalitz pairs, and to a minor extent from resonance decays. It is used in the first level $\pi^+\pi^-$ main trigger, in the calibration trigger to select e^+e^- pairs and its signals are available for offline analysis.

The Cherenkov radiation occurs when the velocity of a charged particle exceeds the velocity of light in a dielectric medium, usually a gas, and it polarizes atoms resulting in emission of coherent radiaton. DIRAC's Cherenkov detector is structured in two identical threshold Cherenkov counters [76], each covering one spectrometer arm (Fig. 2.19). The radiator gas is enclosed in a volume defined by the entrance and exit windows, with dimensions 143×56 cm^2 and 336×96 cm^2, respectively. The chosen radiator is N_2 at normal temperature and pressure ($\theta_c = 1.4°$) and the counter length is 285 cm. Each counter is equipped with 20 mirrors and 10 photomultipliers arranged on two rows. Cherenkov light reflected by pairs of adjacent mirrors is focused onto the same photomultiplier. The analog signals from the PM are fed into two custom-made summing modules, discriminated and used for trigger purposes.
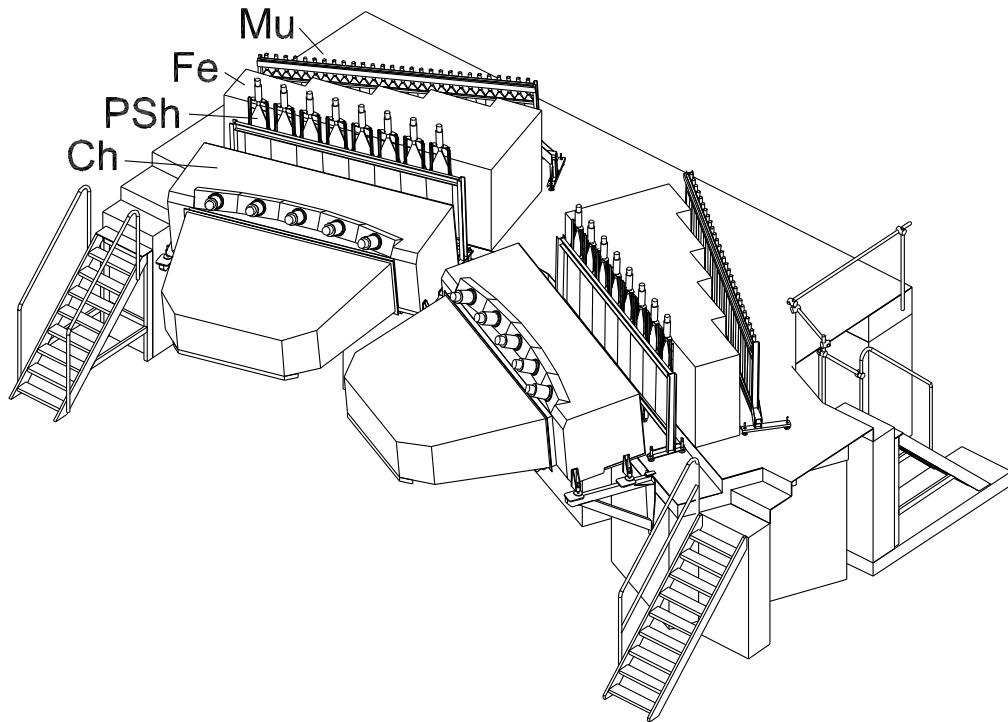
Figure 2.19: *The far end part of the DIRAC setup, comprising threshold Cherenkov counters (Ch), preshower detector (PSh), iron absorber (Fe) and muon counters (Mu).*

A single photoelectron peak is clearly observed in all channels as shown in Fig. (2.20), where we can see the ADC spectra from pions (a) and from single electrons (b). The number of photoelectrons detected by each counter is shown in Fig. (2.21), and from it we infer that both counters have an efficiency greater than 99.8% when operated at a threshold slightly less than 2 photoelectrons.
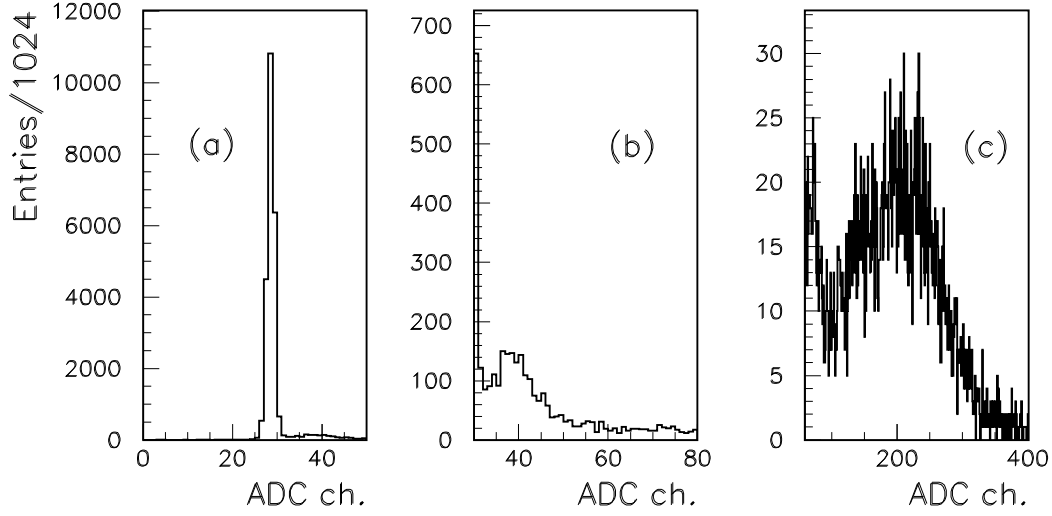
Figure 2.20: *ADC spectrum from one Cherenkov photomultiplier: (a) spectrum from pions (practically equal to the ADC pedestal distribution), (b) amplitude signal from single photoelectron, (c) spectrum from electrons.*
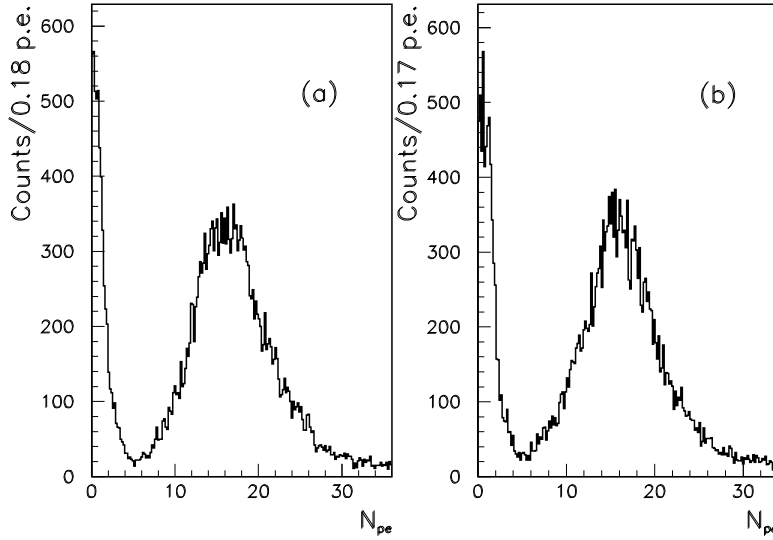
Figure 2.21: *Distribution of the number of photoelectrons detected from the (a) positive and (b) negative Cherenkov detector arms.*

The pion contamination above the detection threshold is estimated to be less than 1.5%. Such contamination arises from pions with momenta above the Cherenkov threshold and from accidental electron coincidences occurring within the trigger time-window. A general picture of the installed detectors described so far, looking into the magnet, with the Cherenkov counter in first plane, can be appreciated in Fig. (2.22).
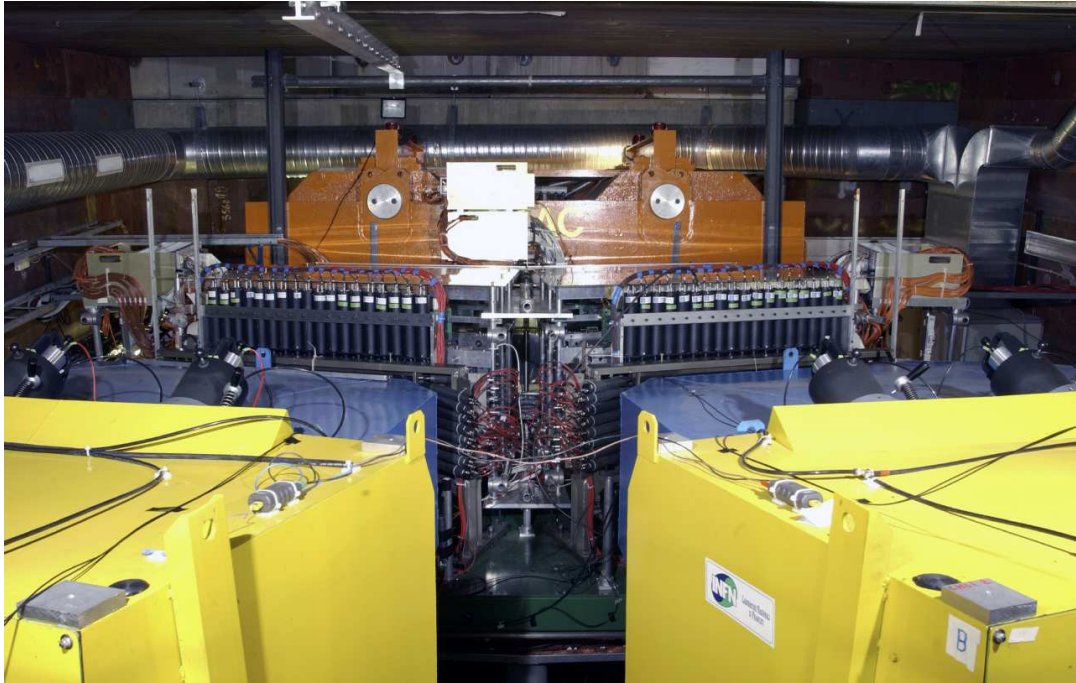
Figure 2.22: *General picture of the spectrometer installed downstream the magnet, taken from a reference plane close to the Cherenkov counters, which can be appreciated in the bottom part of the picture. The magnet can be seen at the far end, and in between we see the vertical and horizontal hodoscope photomultiplier layout. The drift chamber system is installed behind it.*

2.11 The Preshower Detector

The purpose of the Preshower (PSH) detector is two-fold: it provides additional electron/pion separation power in the off-line analysis and it is used in the trigger generating logic (T1).

The PSH is based on an array of lead converters followed by scintillation detectors [78]. Electrons (positrons) initiate in the converters electromagnetic showers which are sampled in the scintillation counters while pions behave as minimum ionising particles. For trigger purposes, a signal is released regardless a pion or an electron crossing a PSH counter.

The PSH consists of 16 detector elements placed symmetrically in two arms, as seen in Fig. (2.19). Each element has a Pb converter and a scintillation counter, Fig. (2.23). The converters of the two outermost elements of each arm (low momentum region) are 10 mm thick, whereas the rest are 25 mm thick (around 2 and 5 units of radiation length, respectively).

The scintillator slab dimensions are 35×75 cm^2 and 1 cm thickness. The detector signals are linearly split into two branches; the online readout is used for trigger purposes and the offline is used for ADC analyis, in particle separation. In the former, a leading edge discriminator is used with a threshold corresponding to efficient detection of minimum ionising particles.
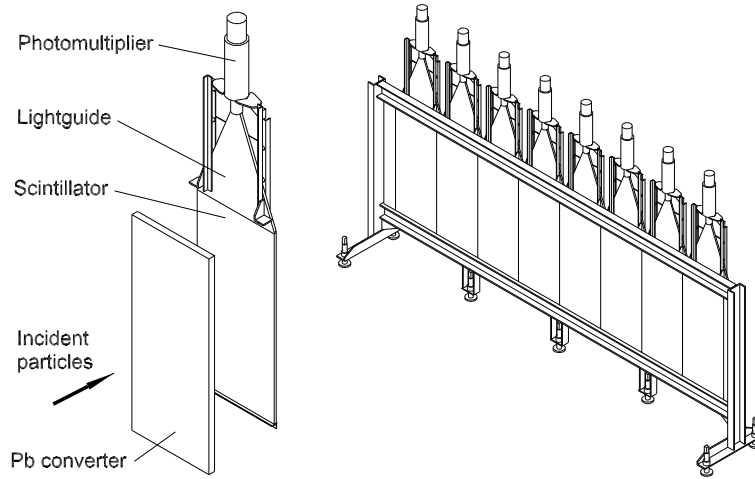
Figure 2.23: *PSH element and PSH array on one spectrometer arm.*

The single arm detector efficiency is 99.5% for pions. Fig. (2.24) shows the pulse-height spectra from one element of the PSH for pions and electrons selected by the trigger system (this selection is based on the Cherenkov detector response). The pion spectrum has a tail (originating from nuclear interaction of pions in the converter) extending to the electron amplitude region. Offline study showed that rejection of electrons reaches 85% with less than 5% losses of pions, what combined with Cherenkov on-line identification yields almost 100% electron rejection (e/π ratio better than 10^{-4}).
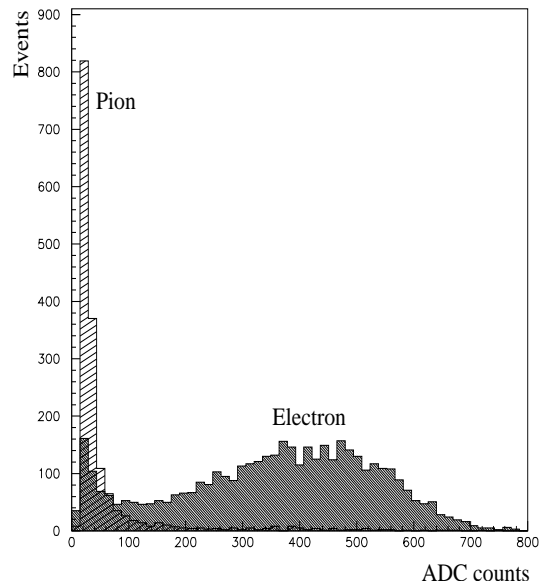
Figure 2.24: *Pulse-height spectra for pions and electrons in one element of PSH.*

2.12   The Muon Detector

Contamination of decay muons in the $\pi\pi$ events can be a serious source of background. For this reason a muon detection system is implemented to provide efficient muon tagging in the off-line analysis. Muons come almost entirely from pion decays with a small admixture from other decays and direct $\mu^+\mu^-$ pair production.

The muon detector consists of a double layer structure of scintillation counters (28 counters with equal scintillating slabs of 75×12 cm^2 front area and 0.5 cm thickness per arm) placed behind a thick (from 60 to 140 cm, see Fig. (2.19)), iron absorber which almost entirely eliminates hadrons and related hadronic showers. The thickness is larger in the region close to the spectrometer symmetry axis, in order to compensate for the harder pion momentum spectrum. This detector is placed at the downstream end of the DIRAC apparatus, few meters from the intense primary proton beam dump. As a result, the muon scintillation counters may undergo a high flux of background radiation from the beam dump area, which has required a special design of the counter arrays and electronics.

Figure 2.25: *Readout scheme of the muon detector element.*

To reduce this background, data from muon detector are read out only if simultaneous signals from a pair of corresponding counters in the two layers are detected, as shown in Fig. (2.25). Fig. (2.26) shows the measured time difference between the signals of the muon detector and the VH, for an individual muon element of the positive arm, showing a global time resolution of 1.3 ns.

Figure 2.26: *Time difference between the signals of the muon detector and the vertical doscope.*

Off-line use of muon counters has been chosen to avoid suppression of useful pion events on-time with background signals in this detector, which cause the suppression of events by 30%. From experimental data we have inferred that the fraction of events containing at least one muon is about 10% [79].

2.13   The Trigger System

The trigger system was designed to provide a reduction of the event rate to a level acceptable to the data acquisition which is around 700 events/spill. Pion pairs are produced in the target mainly in a free state with a wide distribution over their relative momentum Q, whereas atomic pairs from pionium desintegration have very low Q, typically below 3 MeV/c. The on-line data selection rejects events with pion pairs having approximately $Q_L > 30$ MeV/c or $Q_X > 3$ MeV/c or $Q_Y > 10$ MeV/c, keeping at the same time high efficiency for detection of pairs with Q components below these values.

A sophisticated multilevel trigger is used in DIRAC [59]. It comprises a very fast first level trigger and two higher level trigger processors. As explained before, due to the requirements of the data analysis procedure, not only time correlated (prompt) pion pairs are selected but also a large number of uncorrelated, accidental, pion pairs.

The statistical error of the pionium lifetime measurement depends on the number of both prompt and accidental detected pairs so events are collected inside a coincidence time window ($\pm$ 20 ns) between the times measured in the left (VH1) and right (VH2) vertical hodoscopes, centered around the peak of prompt events

A block diagram of the trigger architecture is presented in Fig. (2.27). At first, the pretrigger T0 starts higher level triggers and the first level trigger T1 starts digitization of the detector signals in the data acquisition (DAQ) modules (ADC, TDC, etc.). A positive response from T1 starts a powerful drift chamber trigger processor T4. At the next level the neural network trigger DNA/RNA rejects the events with high Q values, and a positive decision from it in coincidence with positive decision of T1 is used again in coincidence with T4 decision, which imposes additional constraints to the relative momentum and takes the final decision to accept or reject the event, start the readout of all electronics or clear the buffer. In addition to the main trigger designed to detect pionic atoms, several calibration triggers are run in parallel.
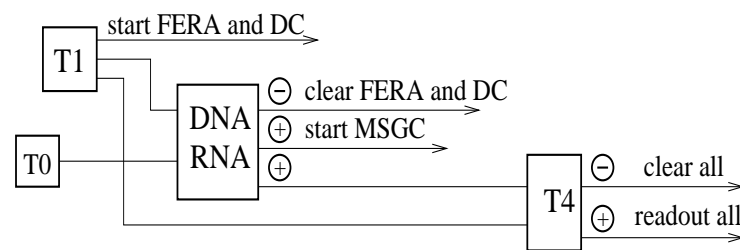
$\oplus$ and $\ominus$ denote positive and negative decisions of the corresponding trigger level

Figure 2.27: *General block diagram of the DIRAC multilevel trigger, since 2002, when the Neural network trigger, DNA, supplanted the Third level trigger, T3.*

2.13.1 Fast Zero Level Trigger (T0)

A fast zero level trigger T0 is aimed to provide the electronics of the ionization hodoscope with a gate of acceptable rate and as low as possible delay. The preshower detectors Pr_1 and Pr_2 placed behind the Cherenkov counters are also used at off-line data handling for additional suppression of electrons. The logic formula for this T0 is constructed from a coincidence of the OR signals of the vertical hodoscopes V_1 and V_2, together with the preshower detector, to decrease the secondary interactions, by means of:

$$(V_1 \cdot Pr_1) \cdot (V_2 \cdot Pr_2) \qquad\qquad (2.2)$$

This fast zero level trigger can be operated in different configurations, depending on the (OR, AND) configurations of (V_1, Pr_1) and (V_2, Pr_2) [80]. In this way, if V_1 and Pr_1 are arranged separately with V_2 and Pr_2 in an AND structure, the T0 trigger can be operated alone, while if V_1, V_2, Pr_1 and Pr_2 are organized in a common OR configuration, the T0 trigger output serves as the second level trigger T2 input, whose description will be given in subsection (2.13.3).

2.13.2 First Level Trigger (T1)

The first level trigger (a detailed description is given in [61]) accomplishes the following tasks:

- Selects events with signals in both detector arms.

- Classifies the particle in each arm as $\pi^{\pm}$ or $e^{\pm}$ depending on the presence of the Cherenkov counter signal. Protons, kaons and muons are equally included in the "pion" class (the discrimination is done offline). For the pion signature the requirements are: a coincidence of a hit in VH, HH, no signal in Cherenkov counters and a signal coming form PSH in arm i:

$$(VH_i \cdot HH_i \cdot \overline{C_i} \cdot PSH_i)$$

  Meanwhile for $e^+ e^-$ signal in Cherenkov is requested:

$$(VH_i \cdot HH_i \cdot C_i \cdot PSH_i)$$

  The signal from both arms are combined to produce the final decision.

- Restricts the coincidences between the signals detected in the two arms for a time window of ± 20 ns in Vertical Hodoscopes.

- Applies a coplanarity (Copl) criterion to particle pairs: the difference between the hit slab numbers in the Horizontal Hodoscopes in the two arms (HH1 and HH2) should be ≤ 2. This criterion forces a selection on the Q_y component of the relative momentum and reduces the rate by a factor of 2.

- Defines streams for events from several physics processes needed for the setup calibration with desired rate: e^+e^- pairs, Λ decaying into a proton and a negative pion (see Chapter (4)), $K^\pm$ decays to three charged pions.

The electronics of T1 gives a decision within 120ns. For Ni-2001 the data physical pion trigger is set to $(T1 \cdot \pi^+ \pi^- \cdot \text{Copl})$.

2.13.3   Second Level Trigger (T2)

The aim of DIRAC T2 trigger is to select events with at least one pair of charged particles with relative x–distance less than 9 mm, using for that purpose the SFD and IH information. The second level trigger signal can be operated in the following modes:

- MODE I. A pure IH mode looking for double ionization hits in both planes of the IH detector. The corresponding algorithm is $(A_i^{**} B_i^{**})\ OR\ (A_{i+1}^{**} B_i^{**})$.

- MODE II. Performes a single adjacent IH detector information through the algorithm: $(A_i^* A_{i+1}^*)\ OR\ (B_i^* B_{i+1}^*)$.

- MODE III. A pure SFD mode looking for events with at least a pair with relative distance < 9 mm.

These three modes can be arranged into seven different operation combinations, *types*, as shown in Table. (2.1).

	type 1	type 2	type 3	type 4	type 5	type 6	type 7
MODE I	yes	no	yes	no	yes	no	yes
MODE II	no	yes	yes	no	no	yes	yes
MODE III	no	no	no	yes	yes	yes	yes

Table 2.1: *Correspondence between T2 modes and all their possible combinations, t2-types.*

The ratios of the T2-types in relation with the T1 triggers are shown in Fig. (2.28). Note that the T2-types 1, 2 and 3 must be ignored, since they are not operated under the MODE-III, the pure SFD detector working mode. As it can be appreciated, the average efficiency is very low, around $\sim 65\%$, and the small distance in the SFD-X fibers is not appropriately described, due to the inaccuracy of the PSC (Peak Sense Circuit) problem simulation[3].

---

[3]The PSC problem will be object of study in section (4.2.2)

The PSC electronics generates a bias at low Q_T, eliminating very close pairs, which becomes too risky for the experiment understanding, so it was decided to remove the T2 trigger. At the end of 2001, also the third level trigger was removed, despite its perfect running, and replaced by the DNA/RNA trigger, due to a lack of maintenance. From 2001 only the T0, T1, DNA/RNA and the T4 trigger were running in the DIRAC experiment.
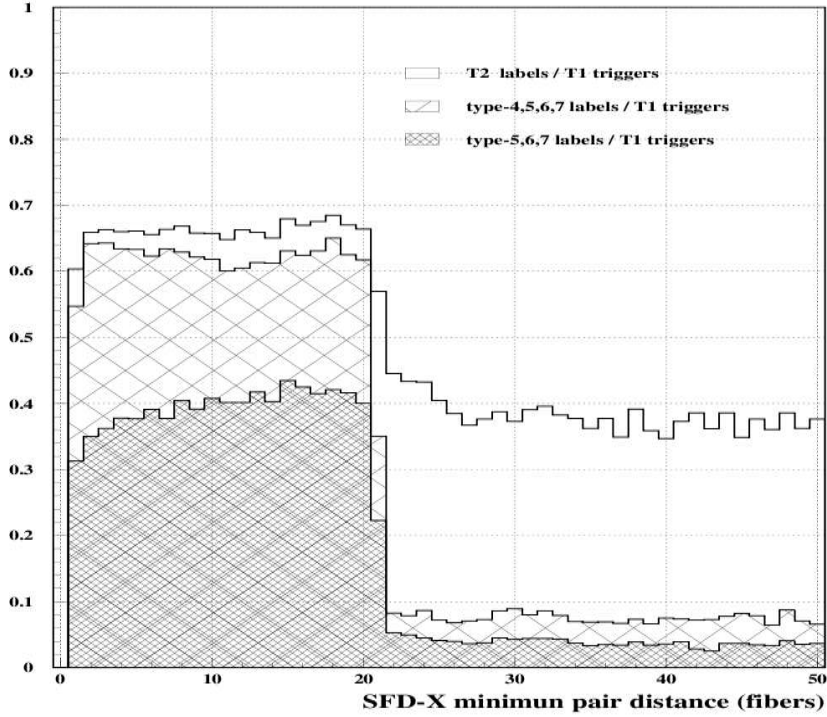
Figure 2.28: *Ratio between T2-labels number and T1-triggers number, function of SFD minimum pair x-distance, ratio T2 type(4+5+6+7)/T1, T2 type(5+6+7)/T1.*

2.13.4   Third Level Trigger (T3)

The third level trigger, T3, performs mainly a selection on the longitudinal relative momentum component $Q_L \leq 30$ MeV/c using the information from the Vertical Hodoscopes and the Ionization Hodoscopes. Fig. (2.29) shows its situation in the DIRAC multilevel trigger scheme.

The topological trigger T3 is applied after T1 or after T1 and T2 triggers. In the first case, the $\pi^+\pi^-$-signature is already known and a Q_Y selection (coplanarity cut) is applied. T2 trigger, started by T0, adds to the T1 trigger a low Q_X selection criterion.
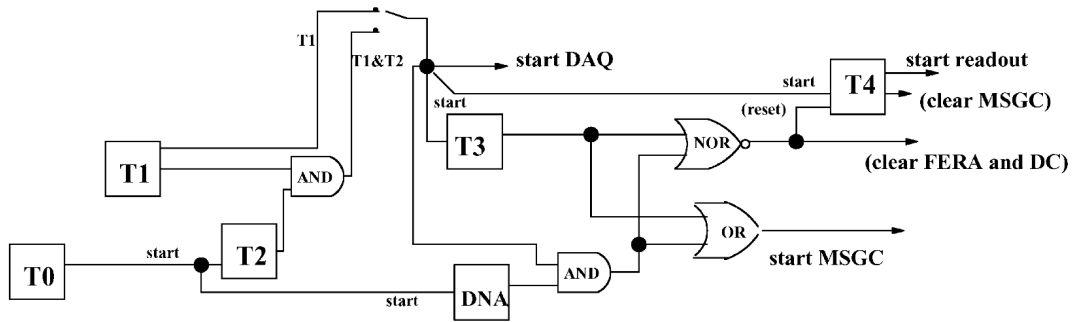
Figure 2.29: *General scheme of the DIRAC multilevel trigger utilized until 2001. T3 processor can be started with T1 trigger or T1 and T2 coincidences. The OR of T3 and DNA decisions starts the GEM/MSGC readout, while the NOR stops the T4 processor and produces a clear one for FERA and DC.*

For $\pi^+\pi^-$ events with low Q_L, the topological correlation between the numbers of slabs hit in VH1 (left), and VH2 (right) is exploited: for any slab hit in VH1 there is an allowed range of slabs in VH2, where a corresponding hit can be found (see Fig. (2.30)).

The input data for T3 are signals from VH1 and VH2 vertical hodoscopes, (2×18)-inputs, plus 16-inputs from IH logic pattern. The VH scintillator signals from top and bottom photomultipliers are sent to a Constant Fraction Discriminator (CFD) and to a CAEN C561 Mean Timer module. The output of the Mean Timer is an ECL signal which is independent of the particle impact point along the scintillator. The IH logic-signals correspond to hit slab where a double ionization or two hits in adjacent slabs have been detected, and this means that two particles at a small relative x distance (small Q_X) cross the IH detector.

The decision time of T3 is fixed and the strobe signal to T3 is given by T1 (or T1*T2) trigger signal, 120 ns later, while the T3 module issues the signal of either a positive or a negative decision. The positive decision is sent to the T4 trigger processor and simultaneously enables the readout of GEM/MSGC data onto buffer memories.

The T3 logic is implemented in a Field Programmable Gate Array (FPGA) technology. The full programmability of FPGA technology is a useful option for the fast and complex trigger systems. The T3 logic was created after extensive training with Monte Carlo simulation of the DIRAC apparatus and further checked with real T1 triggered data.
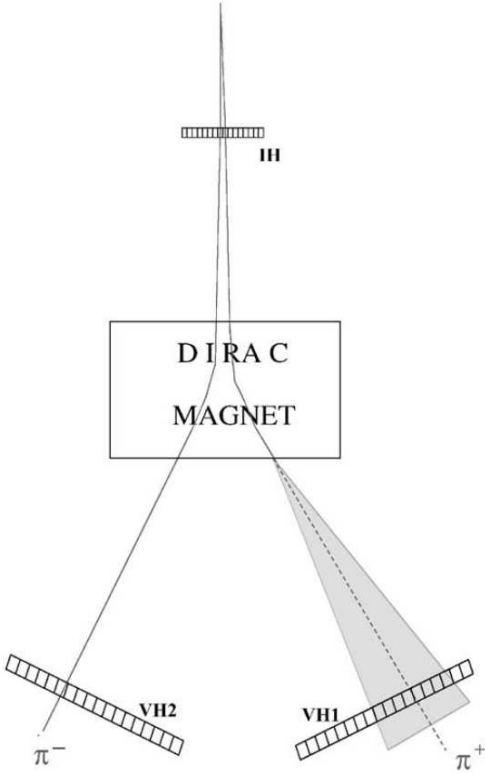
Figure 2.30: *T3 selection: a $\pi^+\pi^-$ pair that hits the same slab or two adjacent slabs in IH detector is accepted by T3 if there exists, in the VH detector, an allowed (low Q_L) combination between the hit slabs in the two arms.*

With a 94 μm thick Ni target and an incident flux of 7×10^{10} protons per spill ($\sim$450 ms), the secondary charged particle rate in the detectors upstream the magnet is $\sim2\times10^6$ per spill. In these conditions, the initial rate of 5×10^3 $\pi^+\pi^-$ T1 triggers (coincidence signals in the downstream arms) is reduced to 2.5×10^3 $\pi^+\pi^-$ after a coplanarity cut (T1-coplanarity involves a cut in Q_Y component [61]) and further T3 trigger performs a rejection of pairs with large Q_L by a factor 2.

The selected $\pi^+\pi^-$ pairs are those with $Q_L \leq 30$ MeV/c; the efficiency of the selection is high and unbiased in the accidental time window. Q spectra is shown in Fig. (2.31). Here, ratios between relative c.m.s momentum components Q_X, Q_Y and Q_L for T1-coplanarity trigger data and T1-coplanarity trigger data selected by T3 are shown for the kinematic region of interest for DIRAC, namely: $Q_X \leq$ 3, $Q_Y \leq 3$ and $Q_L \leq 30$ MeV/c. The ratio of Q_X distributions shows a central enhancement due to the double ionization criterion in the IH detector used by the T3 logic. In the Q_Y component, there is no such selection and the ratio is completely uniform. Finally, Q_L-ratio shows the major T3 effect: the selection of pairs with low Q_L. Pion pairs with $Q_L \leq 30$ MeV/c are accepted with high constant efficiency (97$\pm$1% in the interesting kinematic region), whereas pairs with $Q_L > 30$ MeV/c are rejected and they correspond to the tails of the ratio distribution on both sides of the central uniform region.

The Third level trigger was used during standard data taking and it has shown an extremely good performance stability during all the run time and beam conditions, until 2002, when it was replaced by the DNA/RNA trigger. The T3 trigger can be applied in OR/AND with the Neuronal Network trigger, which performs a task similar to T3.

Figure 2.31: *Ratios between distributions of relative $\pi^+\pi^-$ momentum components for T1-coplanarity triggers and T1-coplanarity triggers labelled with T3. Solid line histogram is the expected T3 answer by software simulation of the hardware implemented logic, while points with error bars are the experimental results.*

2.13.5   Neural Network Trigger (DNA/RNA)

The DNA/RNA (Dirac Neural Atomic and Revised Neural Atomic triggers)
is a processing system [63, 81] that uses a neural network algorithm. The
DNA/RNA can be operated in OR/AND mode together with the Third Level
Trigger, and fulfills a very similar task. In the beggining of the 2002 data-taking
year, the DNA/RNA supplanted the T3 trigger, due to a lack of maintenance
of the latter.
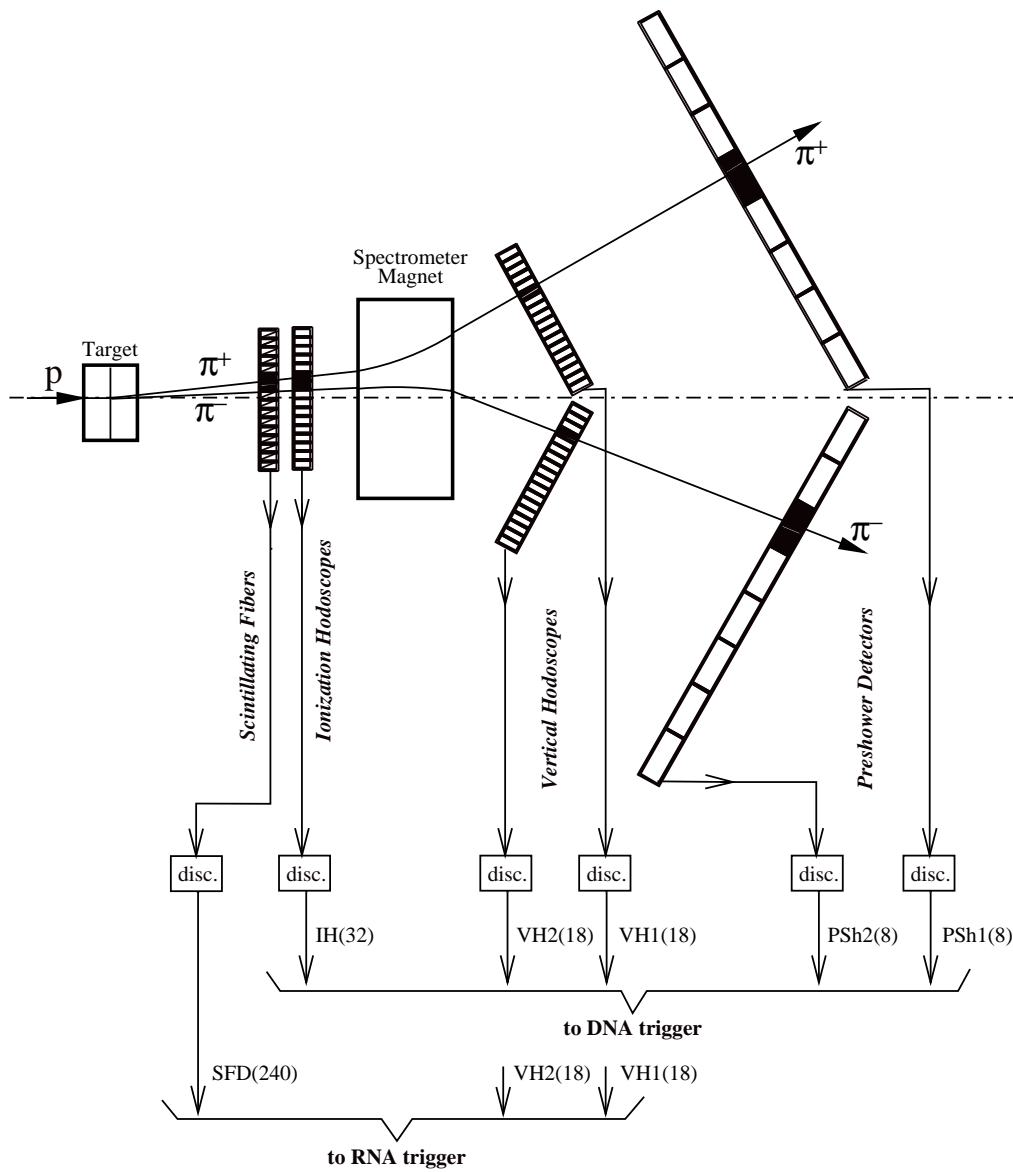
Figure 2.32: *DIRAC detectors used for the neural network triggers DNA and
RNA. Numbers of signal channels from each detector are given in parentheses.*

Pretrigger T0 provides fast initial signal to the DNA (coincidence of hit slab in VH1, VH2, PSH1 and PSH2). The DNA/RNA receives the hit patterns from VH1, VH2 and the X-planes of IH and the SFD (see Fig. (2.32)), that are analyzed for the two arms, programmed in OR($\wedge$) relation with the following logic:

$$(VH_1 \cdot VH_2 \cdot IH_{x,1}) \wedge (VH_1 \cdot VH_2 \cdot IH_{x,2})$$

The neural network was trained with Monte Carlo and real data to select particle pairs with low relative momenta: $Q_x < 3$ MeV/c, $Q_y < 10$ MeV/c and $Q_L < 30$ MeV/c. The events that do not satisfy any of those conditions are rejected. DNA needs a positive decision from T1 for the event to be executed.

With DNA/RNA a rate reduction of 2.3 with respect to T1 is achieved. It evaluates an event in 250 ns with an efficiency in low $\vec{Q}$ region of 94%.

2.13.6   Drift Chamber Processor (T4)

T4 is the final trigger stage and it requires DNA or T3 positive as input. The T4 processor reconstructs straight tracks in the X-projection of the drift chambers allowing to select pairs with low relative momentum (the algorithm is described in [59]). Fig. (2.33) shows the block diagram of the T4 operation.

The drift chamber processor includes two stages: the track finder and the track analyser.

- The **track finder** uses the hit wires information from all DC X-planes (drift time values are not used in the T4 logic). For each combination of hits in two edge base planes defines hit windows for the intermediate planes and the number of hits inside it are counted and required to be more than 4.

- An identical processor is used for each arm. If tracks are found in both arms, the **track analyser** continues the event evaluation. Track candidates are compared to the contents of a look-up memory table obtained with Monte Carlo methods containing all possible combinations of track identifiers for pion pairs with $Q_L < 30$ MeV/c and $Q_x < 3$ MeV/c and allows the start of data transfer to the detector electronics if a coincidence is found.
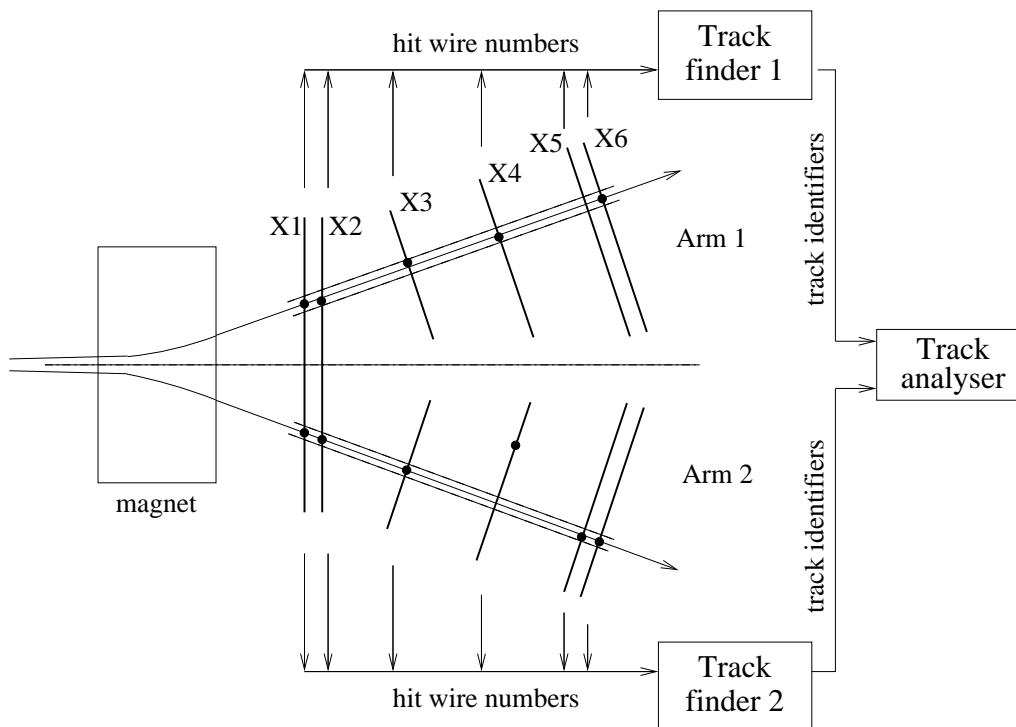
Figure 2.33: *T4 operation block diagram.   Only the drift chamber X-planes involved in T4 are shown.*

The T4 decision time depends on the complexity of the event and is around 3.5 μs on average, being forced a positive response if the processing time exceeds a limit in order to reduce the dead-time. T4 reduces the output of DNA/RNA by a factor of 5, and the efficiency for $Q < 30$ MeV/c exceeds 99%.

The whole trigger system is fully coamputer controlled: no hardware intervention is needed in order to modify the trigger configuration. With all selection stages enabled the event rate at the typical experimental conditions is around 700 per spill, that is well below the 7% limit of the DAQ rate capability and calibration triggers.

2.13.7 Trigger Performances

The performance of the trigger system as a whole in selecting low-Q events is illustrated in Fig (2.34), where the magnitude of the relative momentum of pion pairs Q is shown (in their center-of-mass frame), after DNA/RNA and T4 trigger selection. The trigger efficiency as a function of Q is flat in the low-Q region, as illustrated in Fig. (2.34). This is considered an important figure of merit of the spectrometer, for a precision study of the $\pi^+\pi^-$ Coulomb interaction.
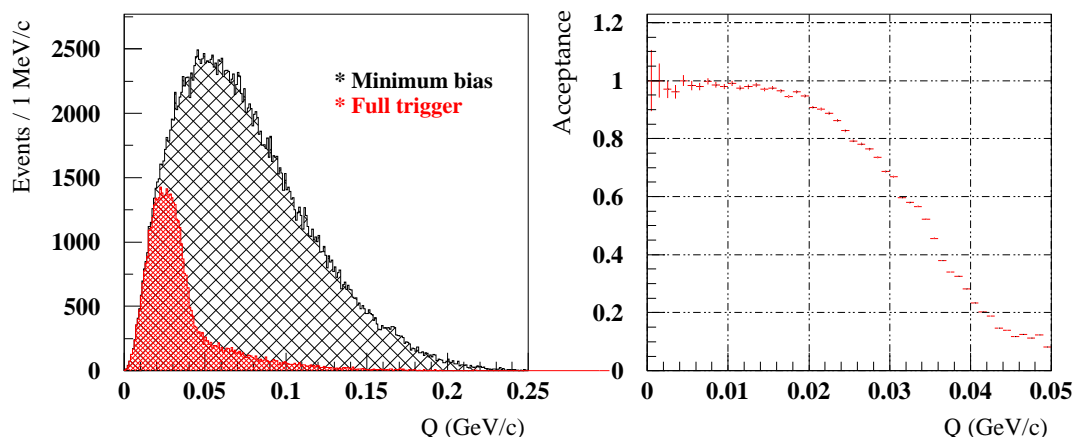
Figure 2.34: *Left: Distribution of Q for accepted $\pi^+\pi^-$ pairs after the full DIRAC trigger system, and for minimum bias pairs. Right: trigger acceptance, determined as the ratio between the previous two distributions.*

Pions from ionization of pionium entering the apparatus have momenta below 4 GeV/c. The apparatus momentum acceptance for time-correlated pairs is flat for pions with momenta between 1.6 GeV/c and 3 GeV/c, and decreases for higher momenta.

For the sake of completeness we also show the laboratory momentum (P) and its transverse projection (P_T) for a single π^- in Fig. (2.35), superimposing a parameterization of the inclusive yield based on the analytic representation [82], adapted to the DIRAC center-of-mass energy ($\sqrt{s}$=6.84 GeV) [83].
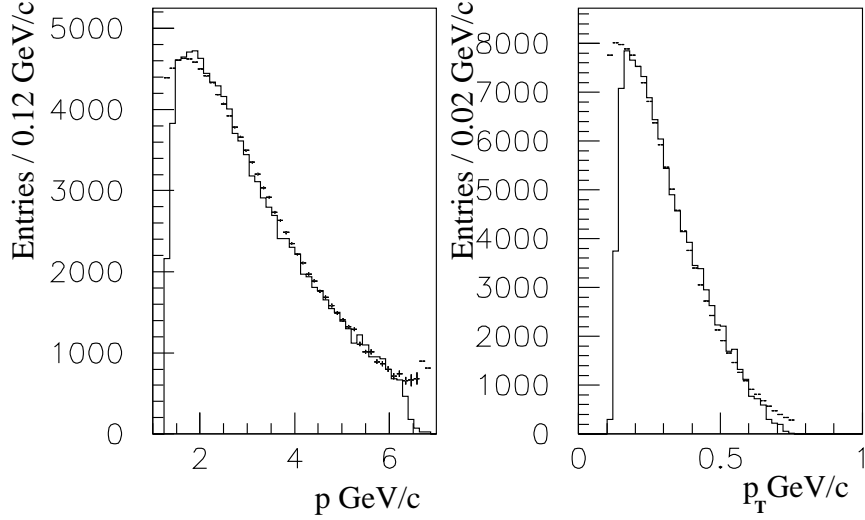
Figure 2.35: *Experimental laboratory momentum (P) and its transverse projection (P_T) of π^- corrected for apparatus acceptance (histogram). Superimposed, the results of the parameterization [82, 83].*

2.14   The DIRAC-II Experimental Setup

Since 2005 the DIRAC experiment has suffered some substantial modifications which allow the collaboration not only to keep studying the pionium signal and its physics, but also for the bound state formed by a π meson and a K meson [84] investigating the predictions of the Chiral Perturbation Theory in the quark s sector.

The most distinctive feature of the πK system with respect to the pionium is that the kaon is a strange particle, so the scattering lengths calculations must be accomplished taking this into account. Therefore the chiral symmetry breaking must be checked in $SU(3)_L \times SU(3)_R$. In addition, the larger mass of the strange quark slows down the convergency of the theoretical calculations in the ChPT.

The changes implemented to the spectrometer include: the installation of the MDC (Micro Drift Chambers), which replaces the GEM/MSGC detector and the inclusion of two new detectors in the *downstream* region, both assembled to the Cherenkov detector: the Heavy Gas Cherenkov and the Aerogel.

These two detectors are introduced in the DIRAC-II setup to accomplish the πK and the K-proton separation, respectively. In addition, an extension and re-arrangement of the Vertical Hodoscopes, the Preshower and the Muon
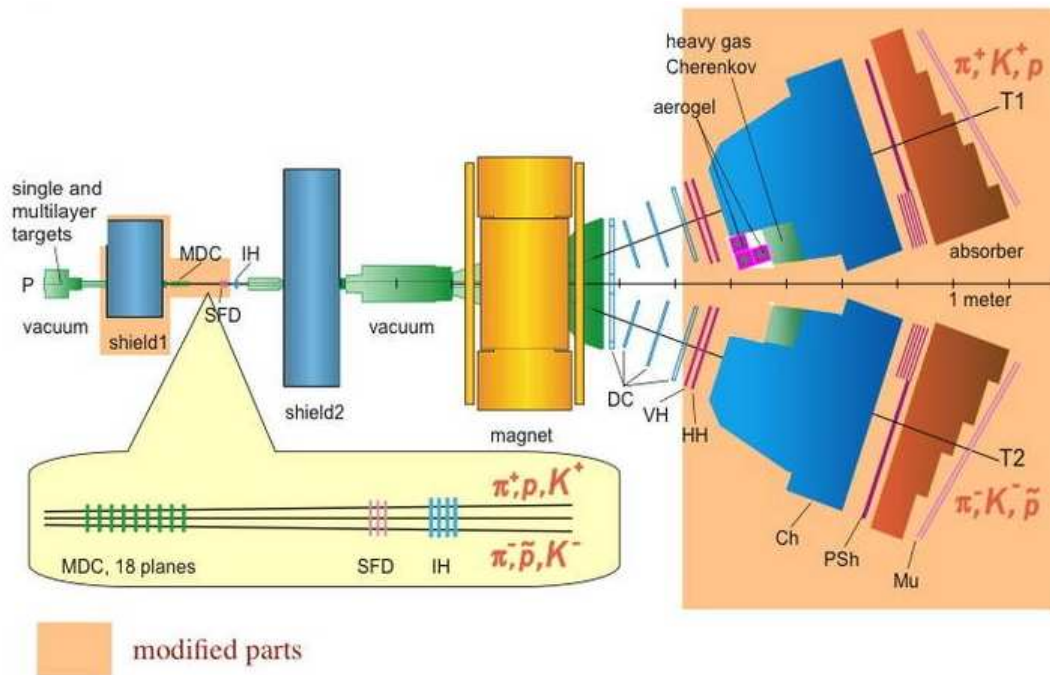
Figure 2.36: *Schematic top view of the DIRAC-II setup. The new detectors installed, the Micro Drift Chambers and the Aerogel Cherenkov counters, just as the modified detectors, the heavy gas Cherenkov counters, the Preshower and the Horizontal Hodoscopes are highlighted here.*

detector was done to allow the kaon detection in the region very close to the longitudinal axis of the spectrometer and to improve the πK detection efficiency for high momenta.

The author of this thesis was in charge of the VH detector, owned by his home institute, during the data taking period 2007 and 2008 in DIRAC-II, at the same time as he performed the final analysis of the pionium lifetime.

The DIRAC-II experimental setup including these new and modified detectors is shown in Fig. (2.36).

2.14.1 Modification of the Setup Geometry

The mass difference between the π and the K is very asymmetric, leading kaons to emerge from the magnet in a region very close to the longitudinal axis of the spectrometer. According to our calculations of the $\pi^+ K^-$ and $K^+ \pi^-$ yields in different geometrical configurations of the experimental setup, it is

possible to optimize the setup geometry to maximize the detection of such atoms. The geometry which has the maximal yield of either $\pi^+ K^-$ or $K^+ \pi^-$ consists of a rotation of detectors and of the secondary particles channel by $+4.0°$ and $-1.5°$, respectively, as shown in Fig. (2.37). The new geometry is not going to be implemented, since the collaboration has reported a pionium lifetime measurement with less than 10% of uncertainty [85]. The current setup represents a compromise solution between $\pi\pi$ and $K\pi$ detection.
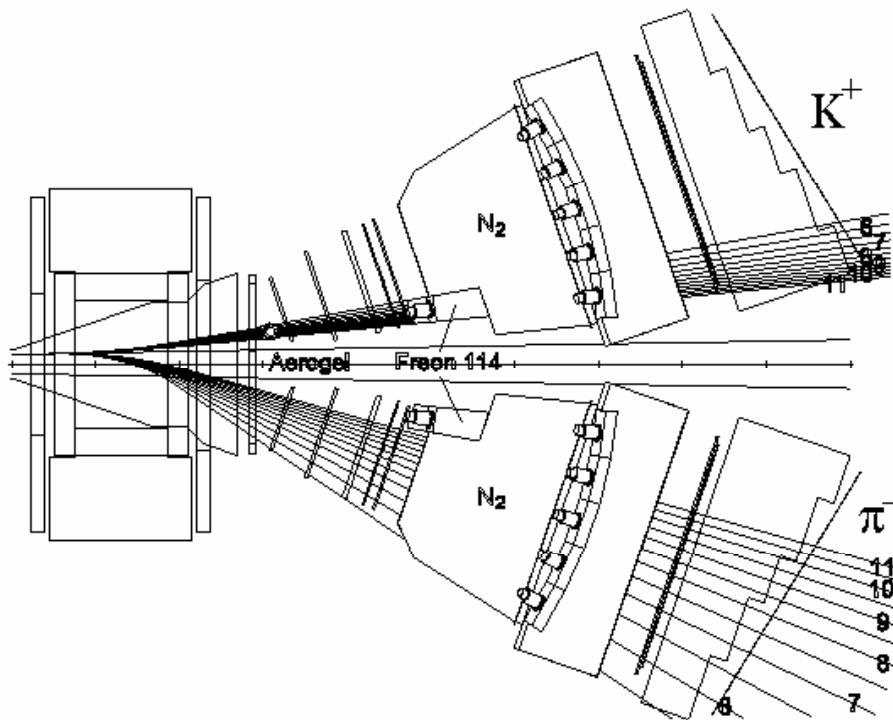
Figure 2.37: *Trajectories of π^- and K^+ from the $K^+\pi^-$ breakup for the existing geometry with Freon 114 Cherenkov counter and with Silica Aerogel threshold Cherenkov detector. The labels on the trajectory lines are the $K^+\pi^-$ momenta in GeV/c.*

2.14.2   The Micro Drift Chambers

The production rate of the $K\pi$ atom[4] is lower than the pionium and the proton beam had to increase its intensity for the new setup (from 0.9×10^{11} to 1.5×10^{11}. The micro drift chambers are the main tracker upstream the magnet, and were installed at the end of the 2007 run replacing the GEM/MSGC detector, unable to operate at the increased proton beam intensities.

---

[4] $\pi^+ K^-$ pairs present a lower rate production compared to $\pi^- K^+$ pairs but they have the disadvantage of the proton contamination at high momentum.
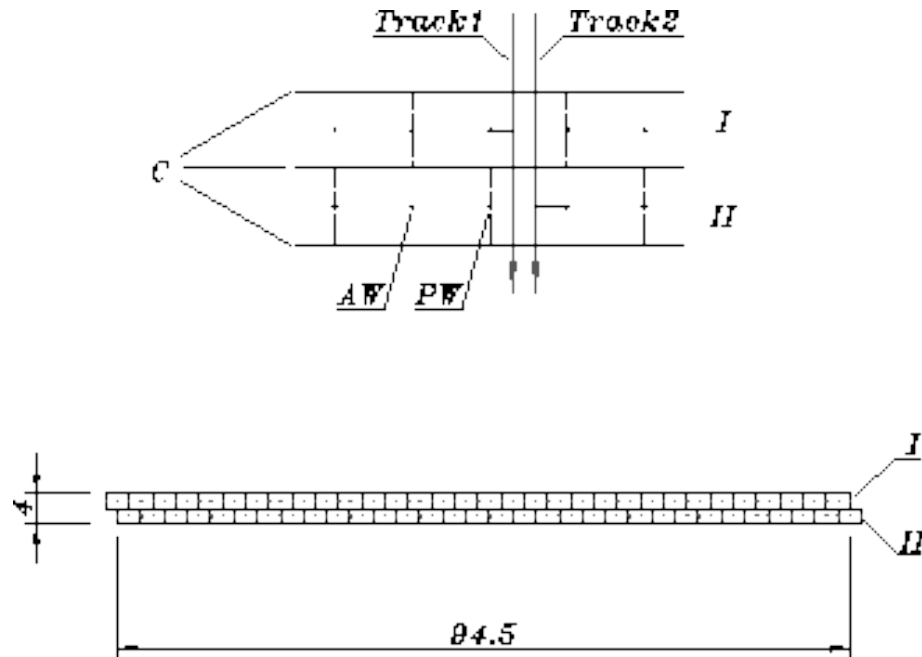
Figure 2.38: *Schematic layout of a double-plane drift chamber: AW —— anode wires, 50 μm in diameter; PW —— potential wires, 100 μm in diameter; C —— cathode, Mylar foil, 20 μm thick. Sizes are measured in mm.*

Drift chambers play a very important role in the DIRAC-II experiment. They provide track reconstruction with high efficiency and spatial resolution. Rigid mechanical design, rather simple production technology and precise features of read-out electronics make the drift chamber technique also attractive for particle tracking between the target and the magnet.

Let us consider how particles are detected in a drift chamber cell. In the case of one particle, primary ionisation electrons drift to an anode wire and initiate the avalanche process. This avalanche occupies part of the anode wire (dead zone) and inhibits the detection of another particle close-by in space. An additional limitation arises from read-out electronics. Even if two particles are detected on the anode wire, a later signal may not be accepted by the multi-hit TDC due to a finite double-hit resolution. These limitations are fatal in the case of a single plane chamber. An additional plane, shifted by half a cell width, eliminates not only a left-right ambiguity, but also the double track resolution problem, as can be appreciated in Fig. (2.38). If two tracks cross one cell, one particle is detected by the first plane and the other by the second plane.

Fig. (2.38) also shows a schematic layout of a double plane chamber. Each plane consists of 32 cells. The cell size is 3×2 mm^2, and the sensitive area is 94.5×94 mm^2. The chamber is operated in a high current avalanche mode with the gas admixture $Ar(0.33) + iC_4H_{10}(0.66) + H_2O(0.01)$. This permits to use the present drift chamber read-out electronics, which has demonstrated perfect operating features.

Drift parameters, time and space resolution of the chamber have been investigated with help of the GARFIELD simulation package [86], and the counting rate capability has been estimated from our dead zone measurement.
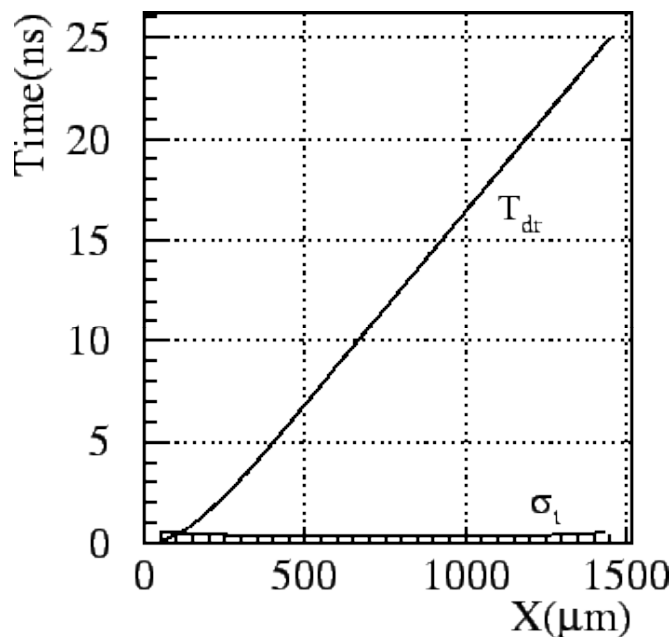
Figure 2.39: *Time features of the drift chamber simulated with help of the GARFIELD package. Gas mixture is* $Ar(0.33) + iC_4H_{10}(0.66) + H_2O(0.01)$.

Drift times (T_{dr}) and spreads of arrival time (σ_t) as a function of drift distance are shown in Fig. (2.39). The drift time T_{dr} exhibits rather linear dependence, what is very convenient for track reconstruction procedures. The maximum drift time is 26 ns. The σ_t value never exceeds 0.5 ns, thus the spatial resolution is better than 30 μm.

The double track resolution of the double plane chamber is illustrated in Fig. (2.40). The histograms correspond to two tracks separated by 100 μm in space. The left histogram corresponds to tracks detected by the first plane, and the right one to tracks detected by the second plane. The TDC bin width, of 0.5 ns, has been taken into account.

The micro drift coordinate detector, consisting of three double plane chambers, is installed along each coordinate (X and Y) in the region, where the upstream detectors are located. A full track reconstruction near the target should be achievable. The same DIRAC drift chamber readout electronics is utilized.
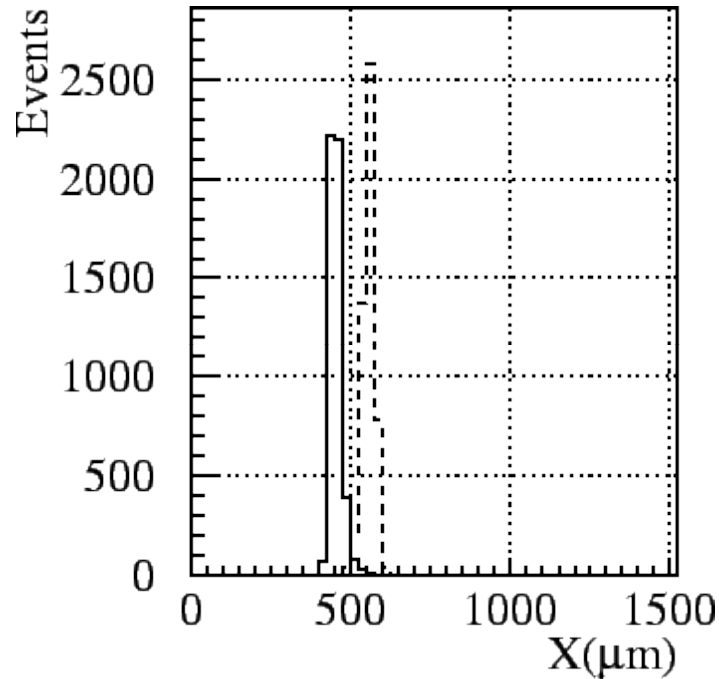
Figure 2.40: *The double track resolution of the double-plane drift chamber. The solid histogram corresponds to track position 450 μm and the dashed one to 550 μm with respect to the anode wire.*

The most important features of the detector are:

- a total of 18 planes,

- a spatial accuracy $\sigma = 30$ μm,

- a double track resolution $\sigma = 200$ μm,

- one plane efficiency $> 98\%$, working at a beam intensity I $= 2 \times 10^{11}$ protons per spill,

- a time resolution $\sigma = 1$ ns,

- a very low integral material budget.

2.14.3   The New Vertical Hodoscopes

The 36 scintillators of the Vertical Hodoscopes, which constituted the preceeding Time-Of-Flight detector of the DIRAC experiment, were fully reformed and they have been used to construct the TOF of the new experimental setup, as shown in Fig. (2.41). A simulation was done to determine the area destinated to house the πK atom signal, and the TOF was consequently modified to cover it. Two new scintillators were added to each arm of the spectrometer, with identical characteristics to the previously used in the TOF.
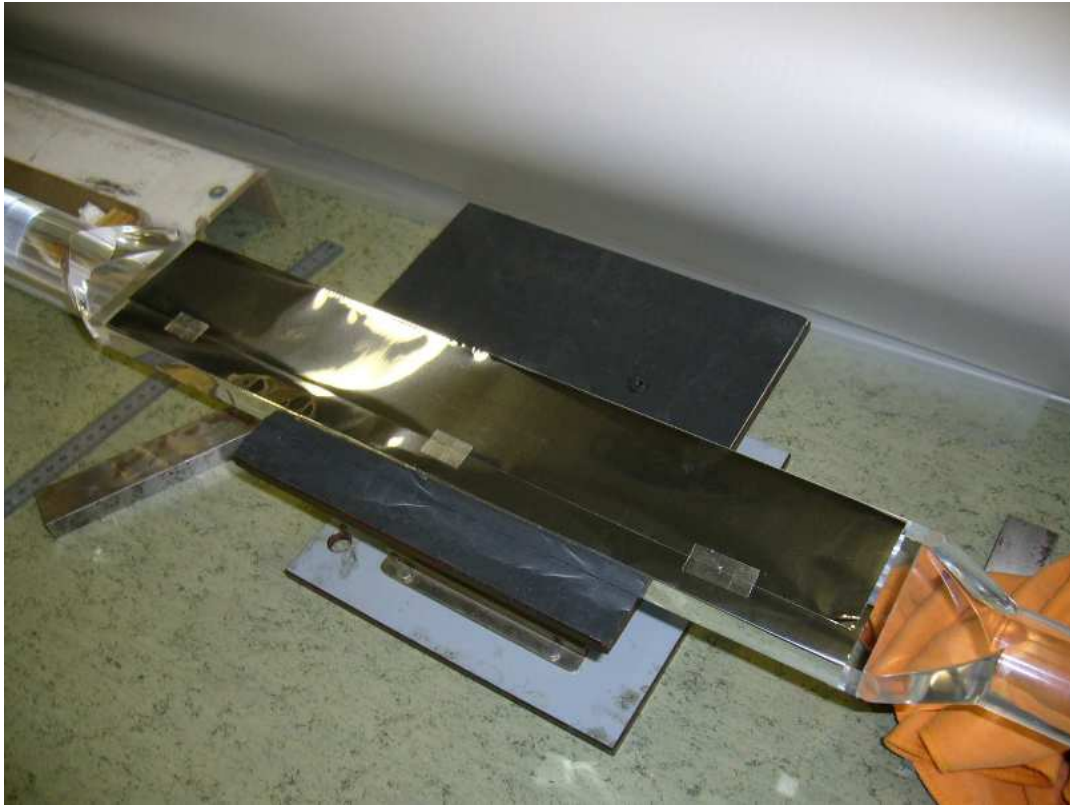
Figure 2.41: *One of the 36 reformed scintillators utilized in the new TOF detector, showing the aluminium coating of the scintillator.*

The 40 scintillators have been exhaustively tested before their definitive arrangement in the experimental setup. The main study parameters have been the luminical isolation and the shape and characteristics of the output signal, using cosmic rays. Fig. (2.42) shows the experimental setup for the cosmic rays test.
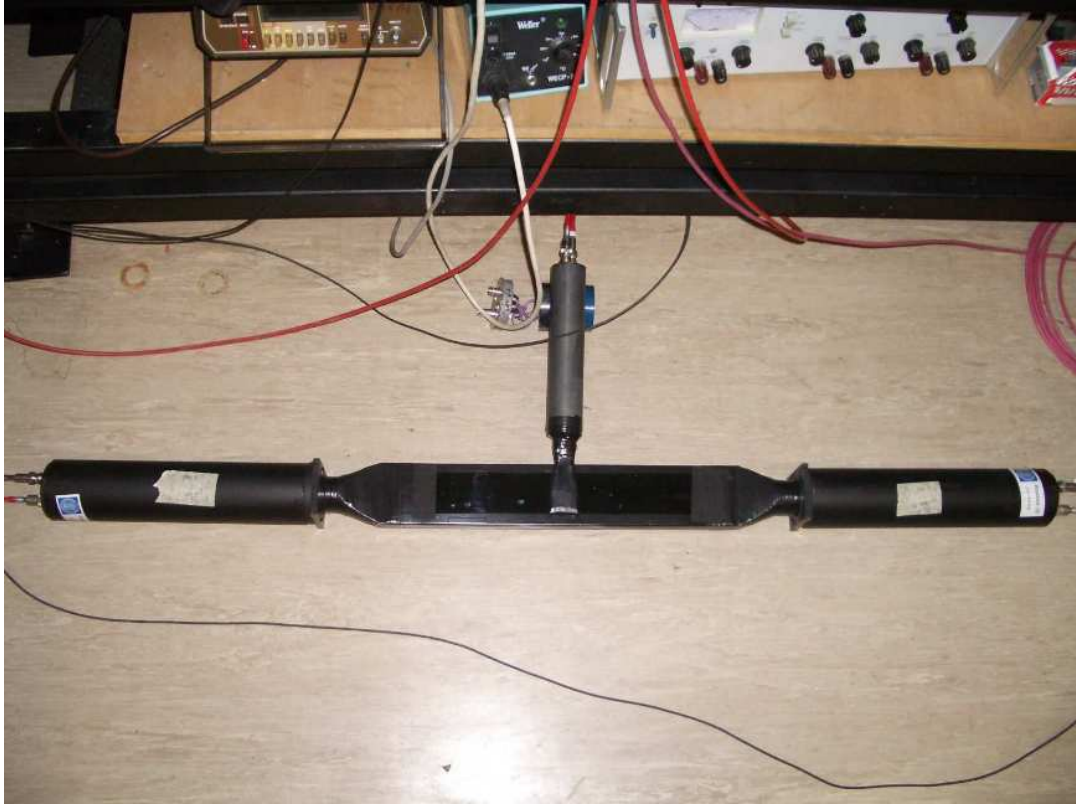
Figure 2.42: *Experimental setup utilized for the cosmic rays test applied to the TOF.*

In Figs. (2.43) and (2.44) we can observe the hits distribution for the left and right arm hodoscope system, respectively, calculated for a e^+e^- trigger. The lower particle rate for the scintillators close to the beam direction is explained by the inclusion of the Aerogel and the Heavy Gas Cherenkov in the DIRAC experimental setup, which have been introduced very close to the beam direction to discriminate electrons, thus decreasing the electron detection efficiency for the mentioned scintillators.
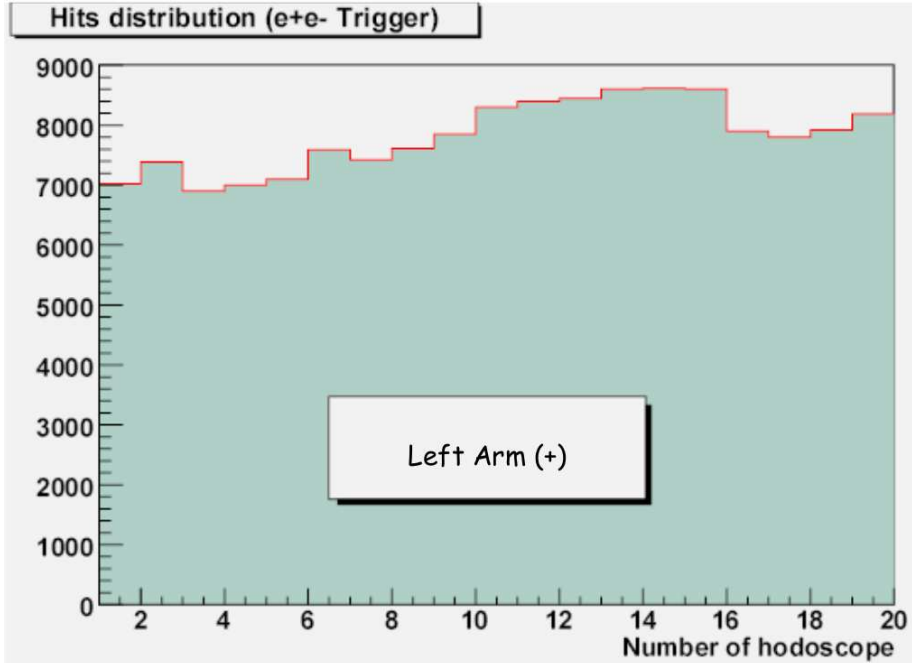
Figure 2.43: *Particle rate for each scintillator in the left arm of the spectrometer, for e^+e^- triggers. Note the lower particle rate for the hodoscopes close to the beam direction.*
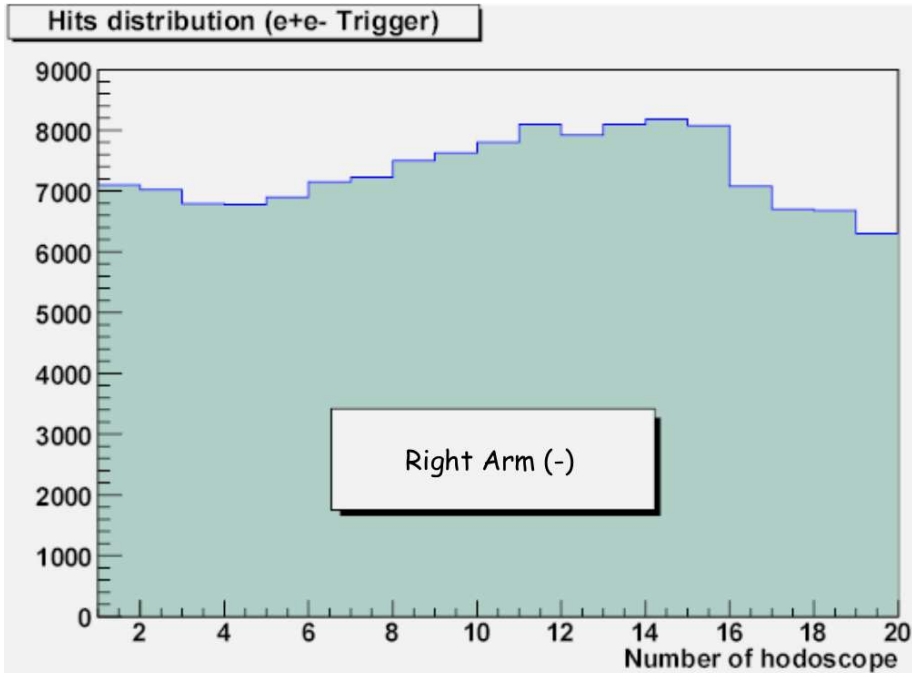
Figure 2.44: *Particle rate for each scintillator in the right arm of the spectrometer, for e^-e^- triggers. Note the lower particle rate for the hodoscopes close to the beam direction.*

2.14.4 The Cherenkov Counters

The Cherenkov detectors upgrade consists of two steps. The first upgrade is aimed at detecting π^+K^- and π^-K^+ pairs with the original DIRAC geometry, simultaneously to pionium detection. This upgrade has been described in section (2.14.1). The second upgrade, after completion of pionium measurement, is foreseen to optimize the setup geometry for detection of either π^+K^- or $K^+\pi^-$, according to the results the first upgrade measurements.

Figure 2.45: *Downstream detectors installed in the DIRAC-II experimental setup. The modified Cherenkov detector can be seen in light blue. The heavy gas Cherenkov detector is represented in yellow, while the aerogel Cherenkov counter is coloured in dark blue, in the left arm.*

In the case of π^+K^- detection, we have to discriminate in the negative arm negative kaons from other particles (electrons, muons and pions). It is necessary to employ in the existing threshold Cherenkov counter a gas with an index of refraction higher than that of N_2. The radiator replacement is necessary only for the counter placed on the negative spectrometer arm, maintaining the N_2 gas radiator in the counter on the positive arm, devoted to the selection of positive pions.

For the proposed setup geometry (Figs (2.37)) and the accepted πK momentum range (from 5 to 10 GeV/c), the momentum of negative kaons associated to the πK breakup will range between 3.9 and 7.8 GeV/c. Moreover, such kaons traverse only the central region of the counter. On the opposite arm the correlated positive pions cover a momentum range from $\sim$ 1.0 to 2.2 GeV/c. Fig. (2.45) shows the new downstream detectors installed in the DIRAC-II setup.
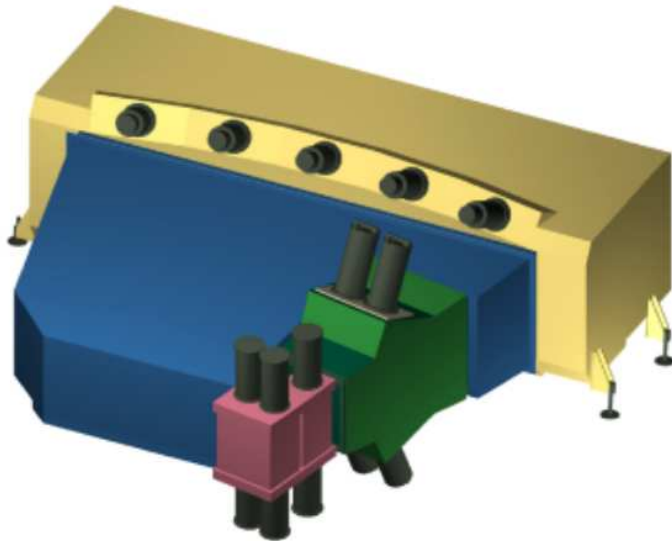
Figure 2.46: *The modified Cherenkov counter detector. The N_2-Cherenkov detector is shown in blue. Its tank has been modified to clear space for the two new Cherenkov detectors: in green the heavy gas and in red the aerogel modules.*

The heavy gas counter separates kaons from pions while the aerogel counter separates kaons from protons. Due to the strong suppression of antiprotons compared to protons, only the positive arm is equipped with an aerogel counter. The original N_2-tank had to be reduced to clear space for the two new Cherenkov detectors, as can be seen in Fig. (2.46). This modification reduces the electron/positron rejection efficiency, which can be compensated by the preshower detector.

A suitable radiator choice for the Cherenkov counter on the negative arm is sulfur hexafluoride (SF_6) gas, which has an index of refraction n = 1.00072 and corresponding threshold on pion and kaon momenta at $\sim$ 3.7 GeV/c and $\sim$ 13.0 GeV/c, respectively. It allows to discriminate pions (also muons and electrons) from kaons because only the former will produce Cherenkov light in the appropriate momentum range (3.9÷7.8 GeV/c).

Pions and kaons with momenta below the Cherenkov threshold and outside the interval of momenta of typical πK breakup products, namely $p_\pi < $ 3.7 GeV/c and 7.8$< p_K <$13 GeV/c, however, enter the counter acceptance and contribute to the trigger yield when operating the counter in anticoincidence. The trajectories of such particles intersect the mirrors located at both extremes of the counter exit window. To reject such a background we reduce the trigger acceptance of the negative arm by excluding the response of photomultipliers located at the edges of the counter.

SF_6 is known to have excellent transparency to light with wavelength above 190 nm [87], comparable to that of N_2, and a scintillation intensity 6.6 times less than in nitrogen [88], it is inert and non-flammable, and can be operated at normal temperature and pressure conditions. The maximum Cherenkov e-mission angle is 2.17° to be compared with 1.39° for N_2. Since the optics of the counter is optimized to focus light emitted at a maximum Cherenkov angle of 1.4° we expect a partial loss of Cherenkov photons falling outside the mirror acceptance. This loss does, however, correspond to a negligible diminishment of efficiency since the expected light yield in SF_6 is larger than in N_2, for the same radiator path length.

In case we choose $K^+\pi^-$ detection, we need to discriminate K^+ from π^+ and p in the positive arm. The π/K discrimination can be achieved with the same Cherenkov counter filled with SF_6 gas as in the π^+K^- case. To discriminate kaons from protons an aerogel threshold Cherenkov counter with n = 1.01 is used, to be described in section (2.14.6).

2.14.5   The Heavy Gas Cherenkov

The heavy gas Cherenkov counter shown in Fig. (2.47) detects pions and can be used in coincidence for the $\pi\pi$-atoms measurement to reduce contamination from other particle types, or in anti-coincidence for $K\pi$-atom observation. The C_4F_{10} gas used as radiator is cleaned permanently by a complex system, to achieve a very high purity [89]. Each module is read out by four Hamamatsu R1584 5-inch PMTs.

Fig. (2.48) shows the integrated pulse height of the analogue sum of the four PMTs as a function of the momentum for the ChF module installed in the right arm of the spectrometer. Electrons are rejected using the Ch in anti-coincidence. Anti-protons and kaons are strongly suppressed so that mainly pions are contributing to Fig. (2.48). The associated ADC spectrum for p > 4 GeV/c is also shown in Fig. (2.48). The average number of photoelectrons for pions is between 20 and 25 depending on the momentum.
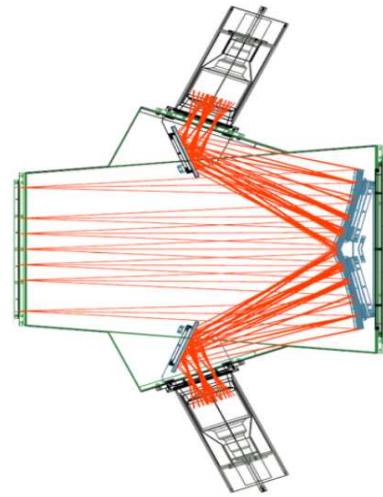
(a)   (b)

Figure 2.47: *(a): One of the heavy gas Cherenkov detector installed in the negative spectrometer arm. (b): Sketch of the inner part of the heavy gas detector illustrating the Cherenkov light propagation. The photons are first reflected backwards by a set of four spherical mirrors and then focused on the photocathode by flat mirrors.*
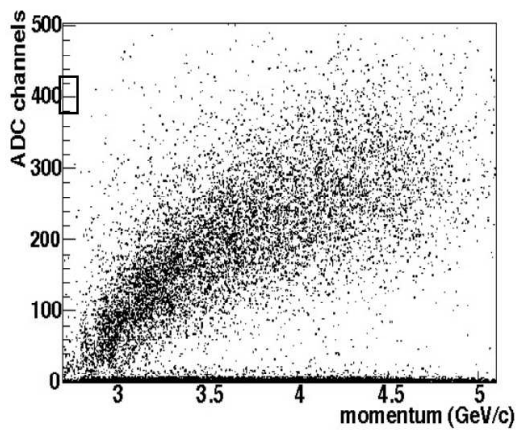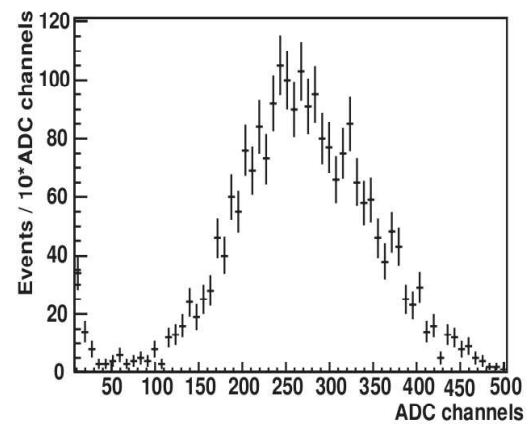
(a)   (b)

Figure 2.48: *Integrated pulse height of the analogue sum of the four PMTs as a function of momentum for pions (a) and the associated ADC spectrum for $p > 4$ GeV/c (b).*

2.14.6   The Aerogel Cherenkov Detector

To measure the distribution of πK-atoms in the DIRAC-II experiment, one needs to identify kaons in the momentum range between 4 to 8 GeV/c. The detection of $\pi^- K^+$ pairs is a more complex task in comparison with $\pi^+ K^-$ because in this case, in addition to π^+, a large admixture of protons to positive kaons is also expected.

The time of flight technique is not adequate for the separation of kaons and protons at such energies. Silica aerogel is the only material with a refractive index in the proper range required for a precise kaon identification. Due to the wide momentum range a duplex design has been chosen. The counter consists of overlapping modules with two different refractive indices n = 1.015 and n = 1.008. Since the large spatial kaon distribution at the location reserved for the Cherenkov counter in DIRAC-II experiment, a sensitive area of 440×340 mm^2 is needed.
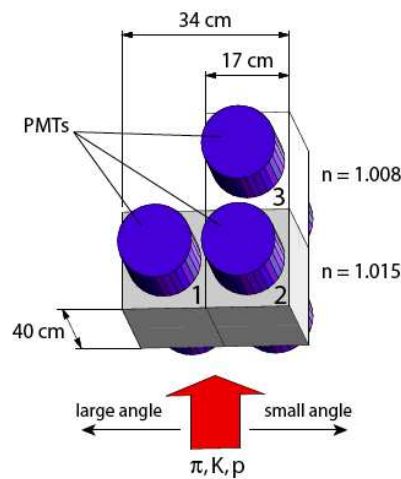
Figure 2.49: *Sketch of the aerogel design. The modules H1 and H2 (n = 1.015) cover the momentum range 4-5.5 GeV/c and the module H3 (n = 1.008) covers the range from 5.5 to 8 GeV/c. The PMTs are mounted on the top and bottom surfaces of each module. The sensitive area is 420×170 mm^2.*

The transverse dimensions of the aerogel counters are sufficient to collect all trajectories of K^+ from πK breakup. The thickness of the aerogel radiator is 90 mm. Thicker radiators have no advantages because the optical transmittance length is rather small ($25 \div 50$ mm). The longitudinal dimension of the boxes containing aerogel tiles is $200 \div 250$ mm. This space will be needed for light collection (mirror or diffuse). Each module is viewed by four 5-inches photomultipliers (Hamamatsu R1587) attached to the top and bottom sides.

The three Aerogel Cherenkov counters are shown in Figs. (2.49) and (2.50). The aerogel detectors are placed in front of the fourth (DC4) drift chamber modules, see Fig. (2.46).
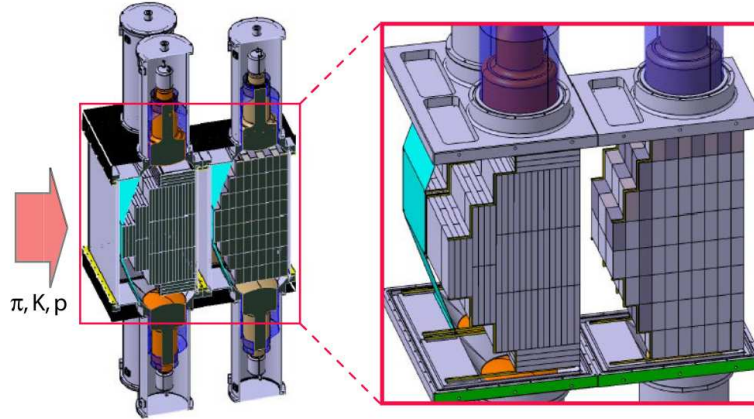
Figure 2.50: *Drawing of the aerogel final setup. The aerogel tiles are arranged in a pyramidal geometry in a steel box that also supports the housing of the PMTs and their mu-metal shields. The steel box is shielding the PMTs from the fringe field of the DIRAC dipole magnet.*

The counter was studied at the CERN PS T11 test beam with the momentum of 3.6 GeV/c (88% of pions and 12% of electrons). The number of photoelectrons detected with diffuse light collection was ∼5, with mirror collection ∼10. The geometry of the aerogel consists of:

- 2 modules with refractive index n = 1.015 and aerogel thickness = (147 ± 7) mm on the top and bottom of the counter and (231 ± 11) mm in the center of the counter. The active area is (417 ± 7) × (166 × 2) mm^2.

- 1 module with refractive index n = 1.008 and aerogel thickness = (163. ± 1.4) mm on the top and bottom of the counter and (233 ± 2) mm in the center of the counter. The active area is (424 ± 1.6) × (159 ± 0.6) mm^2.

- 6 PM photonics XP4570R, selected for high sensitivity.

The aerogel pion trigger rejects electrons and positrons using Ch in anti-coincidence and selects symmetric tracks with the same aperture in each spectrometer arm. Mainly pions and protons are present in the left arm as well as a few kaons. For tracks crossing H1, the scatterplot Fig. (2.51) clearly shows the presence of pions in the green ellipse. Protons above threshold are shown in the red ellipse, while protons below threshold are in the pedestal. Nevertheless, a few protons give some light due to accidental tracks, thermal photoelectrons or δ-electrons produced in the aerogel.
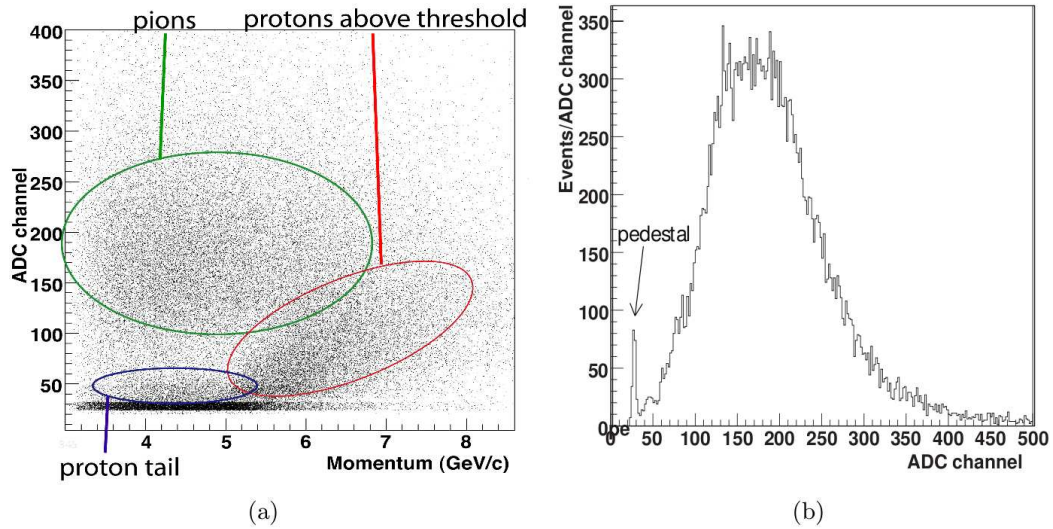
Figure 2.51: *(a): Scatterplot for H1. The pions are surrounded in green, the protons in red and the tail from pedestal in blue. Due to the low production rate, kaons are not visible in this plot. (b): Integrated pulse height spectrum measured with H1 for pions selected with the ChF in coincidence.*

To extract the proton signal using the aerogel Cherenkov, one can perform a TOF analysis or employ Λ decays. In the first case, since the negative particles are dominated by pions, we attribute the mass of the pion to the negative particle in a squared mass distribution. In the second case the lambda intermediate particle is used, which decays into one proton and one negative pion.

Using these two techniques to select protons, one obtains the resulting proton spectrum measured, as can be seen in Fig. (2.52). From left to right with H1, H2 and L1 respectively, The best fit is obtained with a Gaussian, plus a decreasing exponential for the positive tail of the distribution. This distribution provides a good way to estimate the proton rejection efficiency.

A cut of one photoelectron above the mean of the pedestal leads to $(94.6 \pm 8.4)\%$, $(93.2.6 \pm 7.6)\%$ and $(89.6 \pm 9.8)\%$ of rejected protons for H1, H2 and L1 respectively.

(a)   (b)   (c)
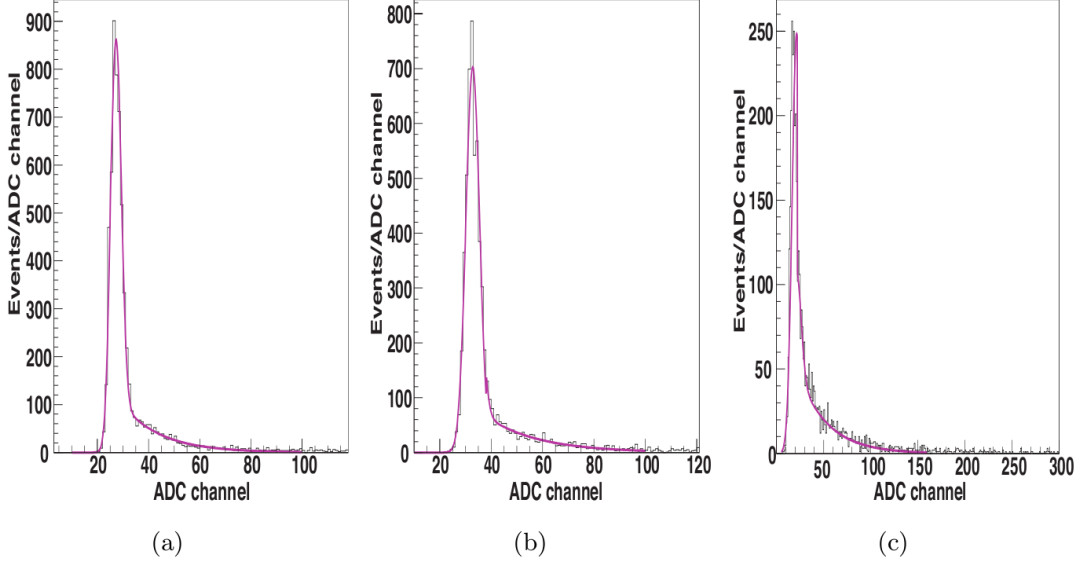
Figure 2.52: *From left to right: Proton ADC spectrum measured with the aerogel modules H1, H2 and L1, respectively. Protons are selected using TOF technique and Λ-decays. For a parameterization, the distribution is fitted in pink with a Gaussian and an exponential.*

2.15   DIRAC-II Performance

The DIRAC collaboration has reported the first experimental evidence of the $K\pi$ atom in 2009 [90], where 173 ± 54 $K\pi$ atoms were observed. From these first data, a lower limit for the lifetime was derived: $\tau_{1S} = 0.8$ fs at 90% confidence level. The $K\pi$ atoms are produced by the 24 GeV/c proton beam in a thin Pt target and the $\pi^{\pm}$ and $K^{\mp}$ mesons from the atom dissociation are analyzed by the spectrometer.

The momentum calibration was cross-checked with tracks from $\Lambda \rightarrow \pi^- p$ decays. Fig. (2.53) shows the invariant $\pi^- p$ mass distribution. A Gaussian fit is applied leading to a mass of 1115.35 ± 0.08 MeV/c^2 (statistical error) and a width of $\sigma = 0.58 \pm 0.01$ MeV/c^2, dominated by momentum resolution.
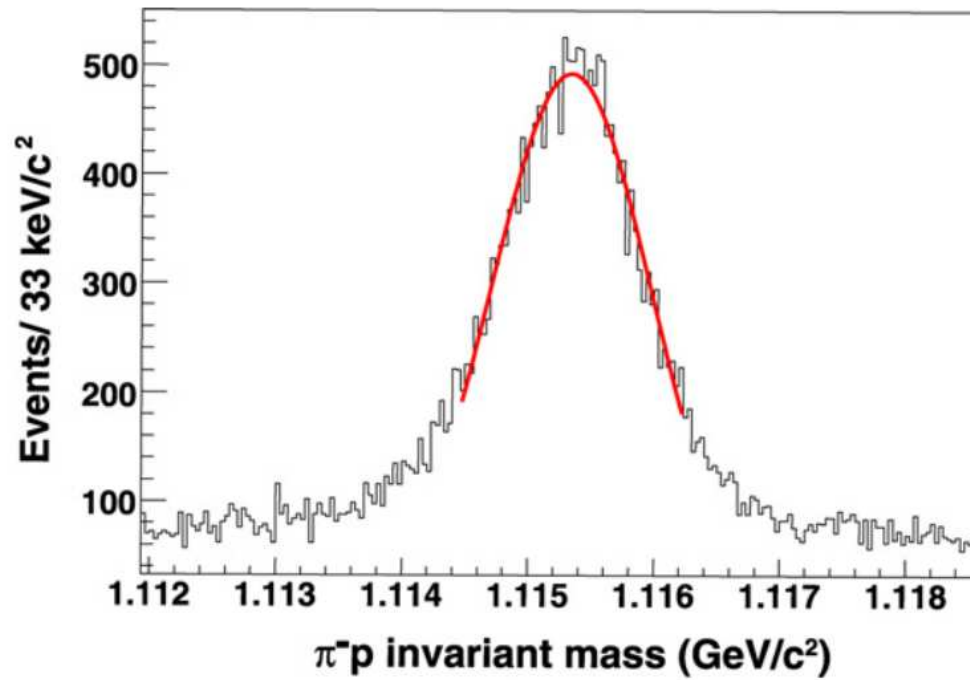
Figure 2.53: *$\pi^- p$ mass distribution in the Λ region. The line shows the Gaussian fit.*

A χ^2 minimization provides the number of $K\pi$ atoms found in the analysis. This minimization procedure will be explained in Chapter (3). Fig. (2.54) shows the MINUIT results for Coulomb and non-Coulomb contributions to $\pi^- K^+$ events. Since the shapes of both contributions are known, one can extrapolate into the $|Q_L| < 3$ MeV/c signal region. The difference between the data and the sum of both contributions is plotted in Fig. (2.55). Above $|Q_L| = 3$ MeV/c the residuals are consistent with zero, while the enhancement at low relative momentum is the first evidence for $\pi^- K^+$ atoms.
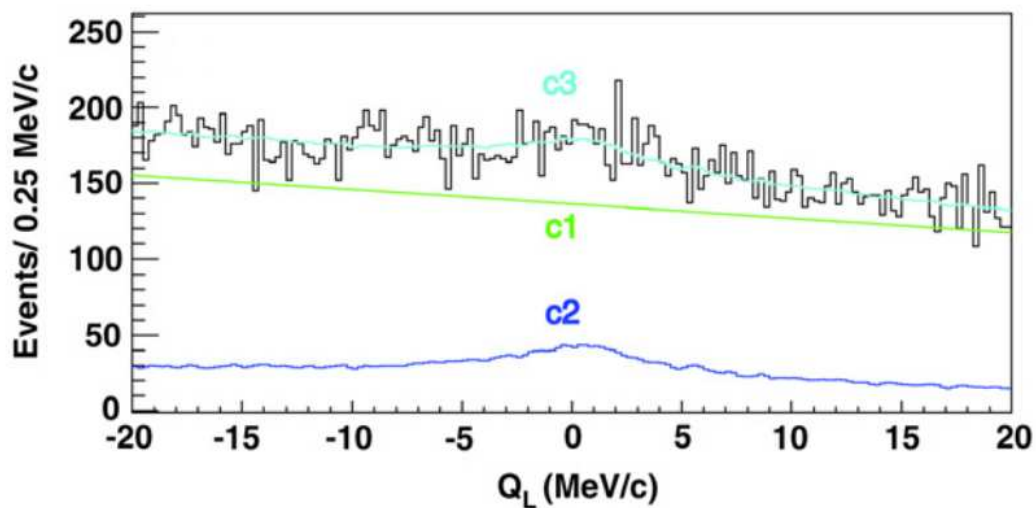
Figure 2.54: Q_L distributions for the $\pi^- K^+$ data sample (26 μm Pt target). The histogram shows the data. The fitted non-Coulomb and Coulomb pairs are in green (c1) and blue (c2) respectively, together with the total background in turquoise (c3).
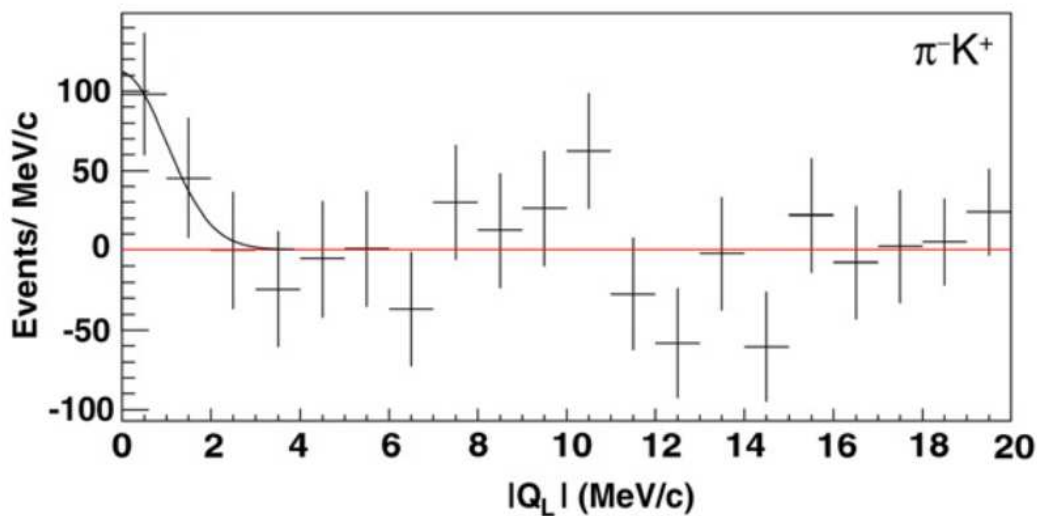
Figure 2.55: Residuals between data and fitted background. The solid line illustrates the distribution of atomic pairs.

2.16 Summary

This chapter has described in detail the DIRAC experimental setup and the detectors involved in the pionium lifetime determination, to be undertaken in the subsequent chapters. The DIRAC II experimental setup was also described, and its first physics publication [90], released in 2009, has reported the premier πK atom experimental evidence.

Chapter 3

Analysis Method

3.1 Data Selection

The analysis presented here has been carried out following the standard pre-selection procedure described in Appendix A for 2001-2003 Ni targets. This pre-selection applies a group of cuts that do not produce any significant bias in the shape of two-pion Coulomb interaction spectrum, further than shrinking the Q_T distribution to an approximate cut of $Q_T < 6MeV/c$. In particular, they are sufficiently general to not introduce biases in the upstream detector multiplicities.

The main advantage of this pre-selection arises from the strong data reduction, which improves the data processing time in the analysis. This is of course at the cost of having a slightly reduced range in the Q_T spectrum of the Coulomb interaction background.

3.2 Selection Cuts

The tracking procedures require the two tracks either to have a common vertex originated from the intersect of the beam with the target. The following cuts and conditions are applied to provide the cleanest possible event pattern [4]:

- "Prompt" events are defined by the time difference of the vertical hodoscopes in the two arms of the spectrometer to be $|\Delta t| \leq 0.5$ ns;

- "Accidental" events are defined by time intervals -15 ns $\leq \Delta t \leq -5$ ns and 7 ns $\leq \Delta t \leq 17$ ns, determined by the Time-Of-Flight measurements.

- Protons in "prompt" events are rejected by TOF in the vertical hodoscopes for momenta of the positive particle below 4 GeV/c.

- $e^{\pm}$ and $\mu^{\pm}$ are rejected by appropriate cuts on the Cherenkov, the preshower and the muon counter information;

- Cuts in the transverse and longitudinal components of Q are $Q_T \leq 5$ MeV/c and $|Q_L| < 15$ MeV/c. The Q_T cut preserves 98% of the atomic signal. The Q_L cut preserves data outside the signal region for defining the background;

3.3 Reconstruction Method

Charged pions pairs are reconstructed according to the method described and evaluated in [91, 92, 93], following a switchable option of the standard reconstruction program, ARIANE [94], which can work in two different modes:

- Only the SFD detector takes part in the tracking.

- All upstream detectors collaborate in the tracking.

This method has the distinct feature of having independent tracking in the upstream and downstream arms. This becomes possible when the full upstream spectrometer information is used, consisting (in 2002 and 2003) of 11 detector layers of GEM/MSGC (4), Scintillation Fiber Detector (SFD) (3), and Ionization Hodoscope (IH) (4) [2].

In a high radiation environment, it is important that the stray fields produced by the magnet do not play a significant role, just as happens in our tracking procedure, where straightline fitting allows unambiguous reconstruction of pion pairs pointing to the beam intersection with the target. Stray fields are negligible in the upstream detectors region.

The opening angle and the Q_T resolution are determined with very high precision by the tracking system, and are only limited in practice by multiple scattering inside the target foil. The mismatch in the charge sign assignment is inevitable at very low opening angles (due to limited spatial resolution in DC track extrapolation through the dipole magnet), but the sign of Q_T is not an objective of the experiment, since charge-conjugation symmetry is taken for granted in pion-pion interaction, and the contribution for this effect is well described by the Monte Carlo simulation, to be reported in Chapter (4).

Upstream tracks make use of the stereo angles of 4 GEM/MSGC and 2 SFD detectors, in conjunction with the TDC information from extrapolated X or Y SFD hits. As a consequence, they have a well defined time tag, which reduces the noise from out-of-time GEM/MSGC hits to a small amount.

The upstream track pairs are matched with DC tracks in order to determine the correct charge assignment. The Matching efficiency is uniform over the detector acceptance, and exceeds 95% everywhere [91, 92, 93, 95]. Time information is used as part of the matching procedure. The Pulse-height in the IH is calibrated with single and double upstream tracks. Double ionization signal is required in this detector to identify pion pairs when only a single unresolved track can be matched to two DC tracks.

Standard cuts for muon background rejection using the muon counters and pre-shower detector (PSH) are applied. The PSH pulses have been analysed to cross-check and improve the Cherenkov veto efficiency.

3.4 Monte Carlo Generators

The DIRAC collaboration has originally used two different numerical methods to describe the propagation of the atom pairs inside the target foil. One is based upon the resolution of the transport equations for atom propagation in discrete and continuum states [1, 49] and the other performs the same objective using step-by-step propagation using the Monte Carlo method [96, 97]. Both methods have been shown to be in excellent agreement, better than 1% [35].

Motivated by the above, the DIRAC collaboration has been using two simulation packages [96, 98] in order to calculate the pionium breakup probability for a given configuration of the apparatus, including the beam conditions. Although in this work we have used the DIPGEN generator [98], a comparison between them has been done. The numerical difference between the pionium breakup probability outputs is actually negligible, as shown in Fig. (3.1), where the pionium breakup probability versus momentum produced by the two Monte Carlos for a 98 μm Ni target are shown, for several lifetime hypotheses.

In previous works [91, 92] the input lab-frame pion momentum spectrum p was taken from real DIRAC data and a de-convolution by the spectrometer acceptance, calculated by the Monte Carlo, of the reconstructed prompt pair spectrum E as function of p and θ (angle with respect to the proton beam direction) had to be performed. The Monte Carlo generator described in [96] was used to produce a p, θ spectrum to describe real data. Fig. (3.1) shows those p and θ distributions.
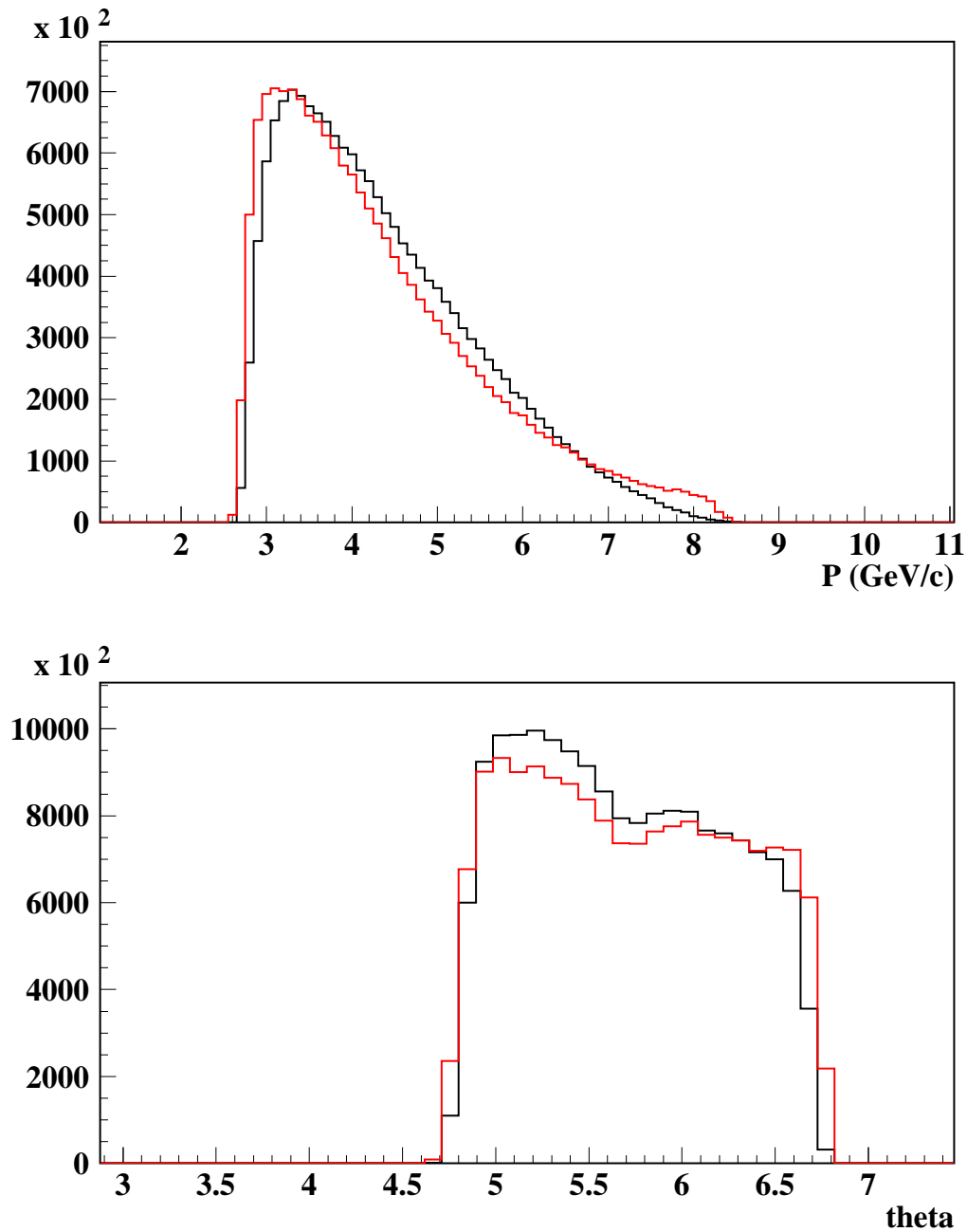
Figure 3.1: *p and θ distributions obtained from experimental prompt pairs (after subtraction of accidental pairs) are shown in black. Red lines correspond to the de-convoluted input spectrum for the Monte Carlo generator described in [96], as explained in the text.*
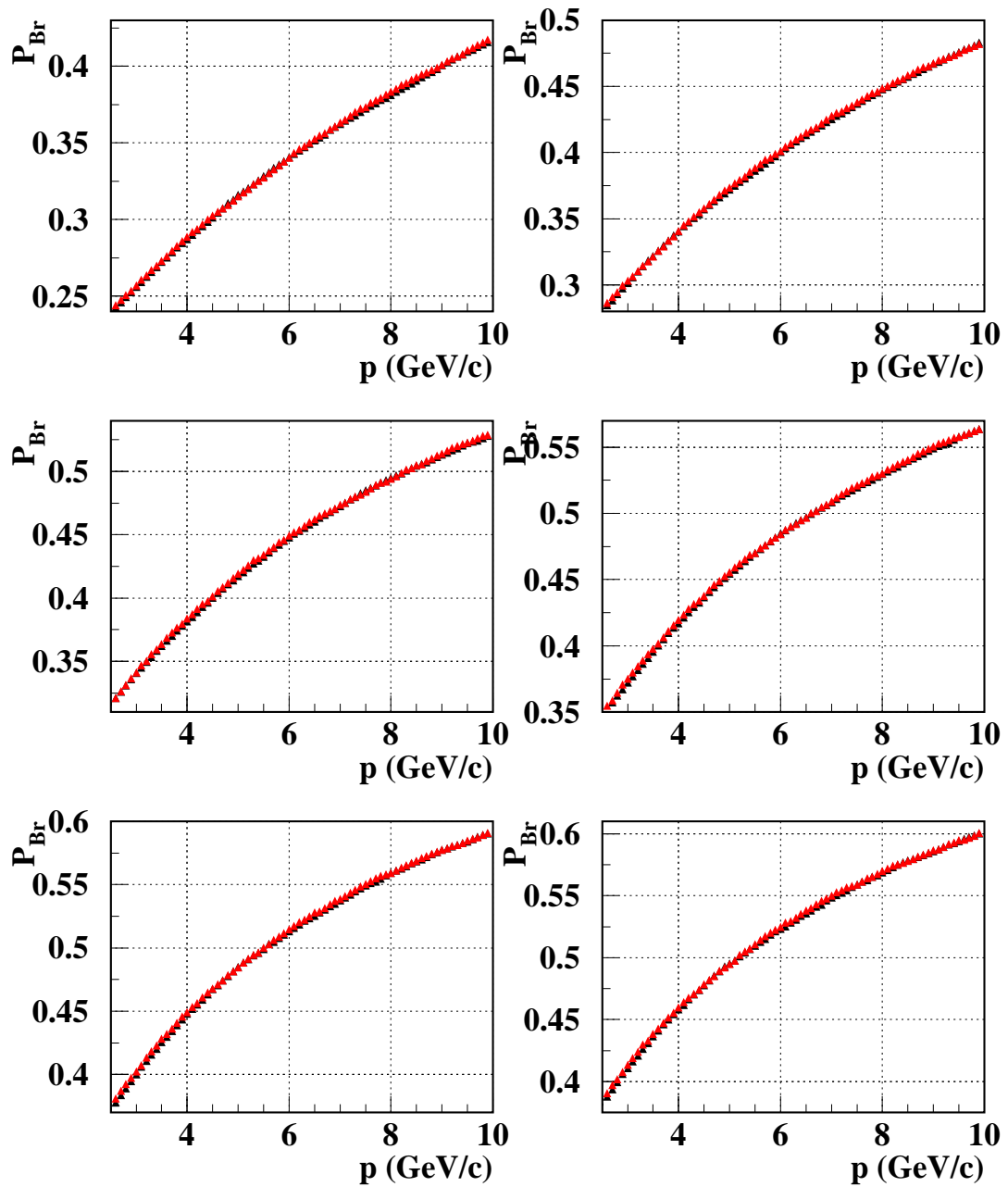
Figure 3.2: *Pionium breakup probability in a 98 μm Nickel target thickness versus pair momentum for several lifetime hypotheses. Black triangles represent the former Monte Carlo generator described in [96] whereas red triangles stand for the Monte Carlo generator used in the current analysis, described in [98]. From top to bottom and left to right, lifetime hypotheses: $\tau = 1.0$, 1.5, 2.0, 2.5, 3.0 and 3.2 fs. The agreement between both generators is excellent.*
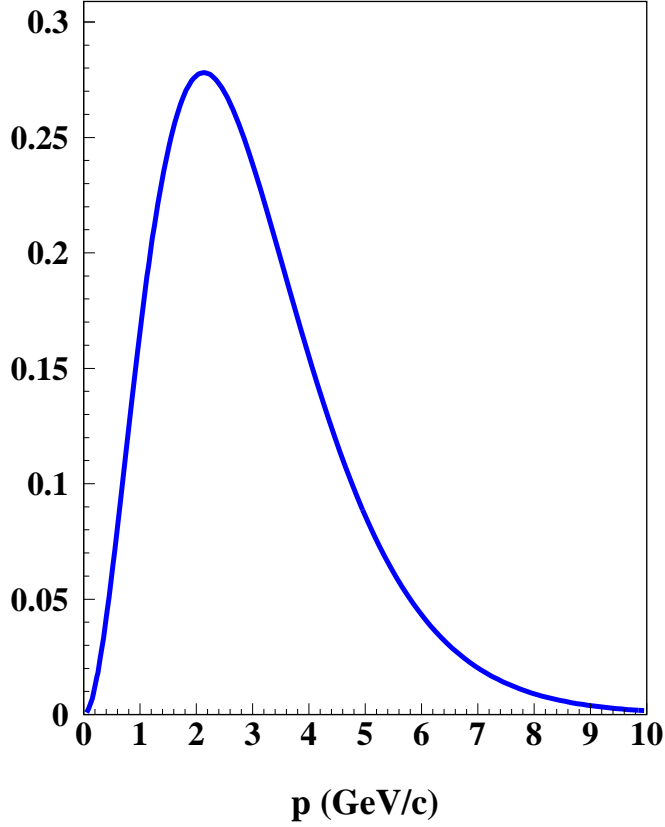
Figure 3.3: *p distribution used by the Monte Carlo generator employed in this analysis. The corresponding θ projection is uniform in (4.5°, 7.5°).*

The p function for the newer Monte Carlo generator is shown in Fig. (3.3). In comparison with the older Monte Carlo generator, which used a correlated two-dimensional (p, θ) function, the latter generator dissociates the dependence between p and θ by producing a p function uniformly distributed in the θ plane, to be corrected at a later stage of the analysis by applying some weigths to the distributions. The output of the Monte Carlo consists of a 50000 event file which contains the $\pi^+\pi^-$ pair position in the target and the (p_x, p_y, p_z) components of both pions momentum.

This kinematic file is introduced in the GEANT-DIRAC program [99] with standard geometry and detector files, but with modified average multiple scattering angle in the upstream region[1], to be described in Chapter 4 in this thesis.

---

[1]This was necessary to match the vertex distributions for real data and Monte Carlo. The multiple scattering angle in this region was increased in a 8%.

GEANT-DIRAC produces and propagates an event through the spectrometer, saving the information in a 50000 events buffer file.

In a later stage, the event reconstruction program, ARIANE, collects the buffer files created by GEANT-DIRAC and produces the detector digitizations which include the response of the detectors, hit generation, efficiences and detector resolutions, creating an n-tuple collection. It also performs the tracking reconstruction of the events after the digitization. N-tuples are processed with a program called *readnt* which applies weights in order to match the (p, θ) distributions between the real data and the Monte Carlo, consisting of a fraction between the real data shape and the Monte Carlo, building a (p, θ) distribution alike the real data.

One of the most important and celebrated features of the ARIANE program is the clusterization of the GEM/MSGC detector. The procedure for GEM/MSGC cluster patterning uses real data input to describe correlations between cluster total charge, micro-strip multiplicity and differential charge. Simulation of out-of-time noise hits in GEM/MSGC detectors is done by reproducing the experimentally observed characteristics of this background, namely:

- Existence of significant hit multiplicity correlations from plane to plane (4 detectors), which are encoded by specific look-up-tables determined from real data.

- Absence of space correlations between different planes in most of cases, once the two $\pi^+\pi^-$ triggering tracks are removed. This indicates that this background is essentially originated from wide angle tracks with respect to the beam direction.

- Presence of background with spatial correlated tracks. This background represents less than the 20% of the hit multiplicity distribution, and was introduced for the systematic error calculation, see section (6.7). The repercussion of this nasty background was expected to be important in the final pionium breakup measurement, but it was confirmed that its effect represents a minimal impact, demonstrating the high quality performance of the tracking.

In Fig. (3.4) we compare the observed GEM/MSGC hit multiplicity distributions for each detector with Monte Carlo simulation. Only hits (real or background) found within a momentum-dependent $\pm 3\sigma$ space window from a drift chamber track extrapolated to the upstream detector planes are retained. As it can be appreciated, the GEM/MSGC background is perfectly well described.
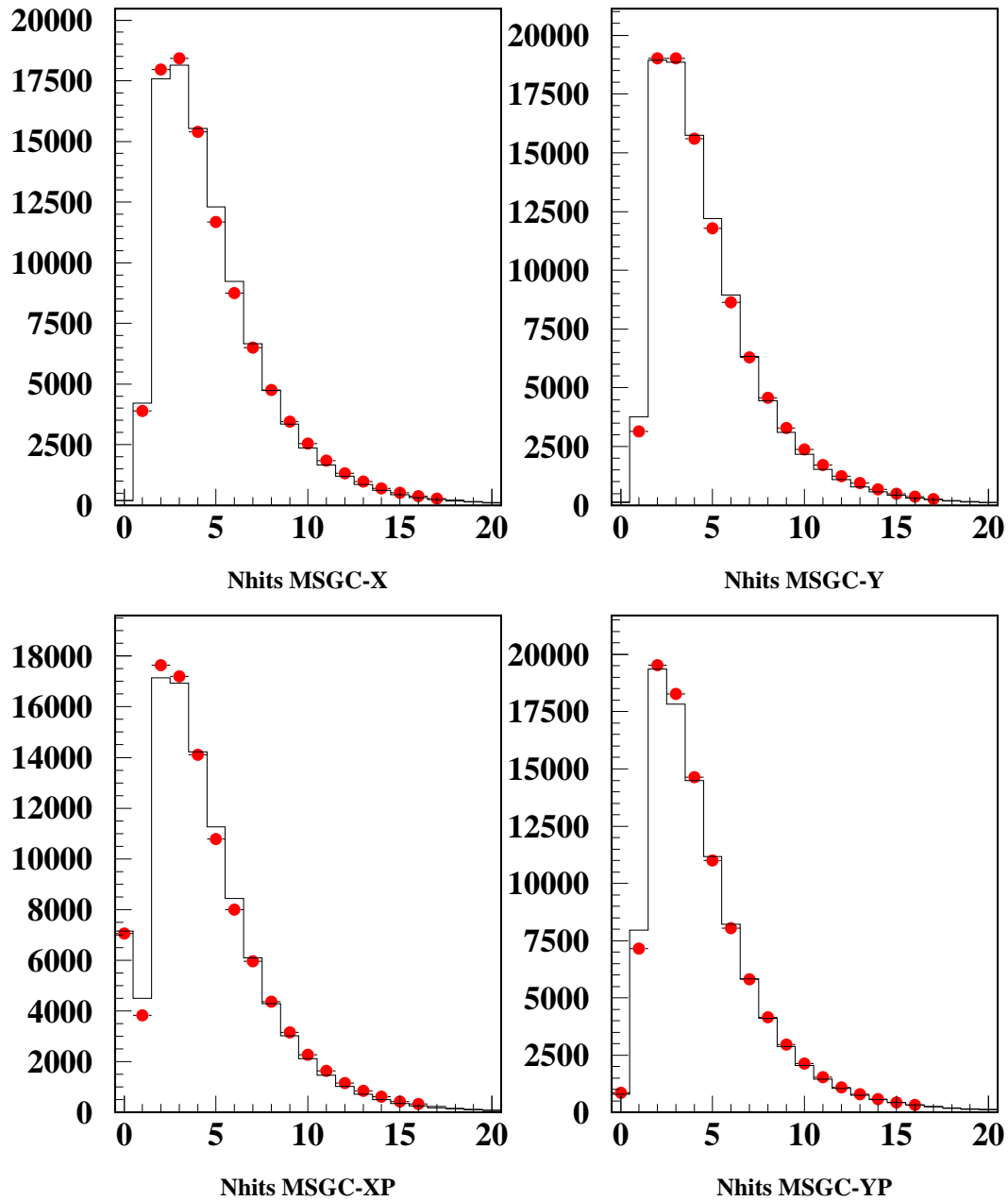
Figure 3.4: *Number of GEM/MSGC clusters found close to any of the drift chamber tracks, including the real signal pairs (dots), compared to Monte Carlo simulation (line). Detector ordering is X/Y (top left/right) and X'/Y' (bottom left/right).*

3.5 Monte Carlo Simulation

To achieve the most accurate parametrization of the Coulomb interaction down to very small values of Q, we have chosen Monte Carlo simulation as the most precise analysis procedure. In addition, 50% of the experiment DAQ was devoted to collect accidental pairs, which were used in preceeding analysis [91, 92] to perform trigger acceptance corrections to the Q_L spectrum. The present work includes a trigger simulation, so the acceptance corrections to the Q_L spectrum become unnecessary.

It should be understood that the use of Monte Carlo is entirely restricted to the description of the experimental resolution and the detectors efficiency, and by no means implies specific model assumptions about proton-nucleus physics. In particular, Coulomb interaction is described by the Coulomb enhancement of the Q-space wavefunctions, described in section (1.5).

Even with the excellent Time-Of-Flight resolution of the spectrometer, a non-Coulomb contamination remains in prompt-pair event selection. It consists of accidental pairs and other long-lifetime decays. Both are described by Monte Carlo, where pion pairs are simulated isotropically in their center-of-mass frame, and the Coulomb interaction is not accounted.

The lifetime determination performed in the works mentioned above only employed two kinds of Monte Carlo. One Monte Carlo was used to describe data from 2001 whereas the other Monte Carlo was used to interpret data from 2002 and 2003. In this work, real data were divided in five different sets, motivated by the two target thicknesses (94 and 98 μm) and two proton beam energies (20 and 24 GeV/c) configured in the DIRAC spectrometer. Three different Monte Carlo were utilized to describe the five data sets. Table (3.1) accounts for the real data and Monte Carlo sets used in this analysis.

Year	Target thickness	Beam Energy	Real Data	Monte Carlo
2001	94 μm	24 GeV/c	2001 94 μm	94 μm 24 GeV/c
2001	98 μm	24 GeV/c	2001 98 μm	98 μm 24 GeV/c
2002	98 μm	20 GeV/c	2002 20 GeV/c	98 μm 20 GeV/c
2002	98 μm	24 GeV/c	2002 24 GeV/c	98 μm 24 GeV/c
2003	98 μm	20 GeV/c	2003 20 GeV/c	98 μm 20 GeV/c

Table 3.1: *Different real data and Monte Carlo sets utilized in the pionium lifetime determination, encouraged by the two target thicknesses and beam energies installed in the experiment.*

3.6   Q-spectrum Analysis

A two-dimensional analysis of the $\pi^+\pi^-$ spectrum in the center-of-mass frame has been carried out, choosing the transverse $Q_T = \sqrt{Q_X^2 + Q_Y^2}$ and longitudinal $Q_L = |Q_Z|$ components of the center-of-mass momentum of the pion pair (with respect to the pair direction of flight Z) as independent variables. This analysis has been done independently for seven individual $600 MeV/c$ bins from 2.6 to 6.8 Gev/c of the pair laboratory-frame momentum p. The results will be presented in Chapter (5). Irrespective of the parameter variation strategy, or of the momentum definition followed in each case, the prompt two-pion spectrum in the (Q_T, Q_L) plane has been χ^2-analysed by comparison with a combination of the following input spectra:

- Monte Carlo describing the Coulomb final-state interaction by means of the Coulomb factor (labelled CC), using pion pair lab-frame momentum from prompt spectrometer data.

- Monte Carlo describing accidental coincidences taken by the spectrometer (labelled AC). It reproduces the uncorrelated non-Coulomb background in prompt events. Its laboratory momentum spectrum has been simulated according to that of true accidental pairs taken by the spectrometer. Its fraction has been determined from the Time-Of-Flight (TOF) spectrum in each momentum bin, and the values obtained are represented in Fig. (3.6).

- Monte Carlo describing non-Coulomb interacting $\pi^+\pi^-$ (labelled NC). It simulates pion pairs in which at least on of them is coming from a long-lived resonance. Such events are detected as time-correlated by the precision coincidence of the spectrometer. We assume they have a strictly isotropical distribution in their center-of-mass frame. Their lab-frame momentum spectrum is also taken from spectrometer data.

- The pionium Monte Carlo [98], calculated using the full description of the physics of the pionic atoms interactions with the target atoms. It is used to obtain the pionium spectrum and fit the observed deviation with respect to the continuum Coulomb background, constructed from the previous input (it is labelled AA)

The resulting number of events for each of the above samples is denoted by N_{CC}, N_{AC}, N_{NC} and N_{AA} respectively, with relative Monte Carlo type fractions α_1, α_2, α_3 and γ. N_{pr} represents the total number of prompt events in the

analysis, under the reference cuts $Q_T < 5 MeV/c$ and $Q_L < 15 MeV/c$. The double differential spectrum of prompt $\pi^+ \pi^-$ pairs N_{pr} is χ^2-analysed in the (Q_T, Q_L) plane by minimizing the expression:

$$\chi^2 = \sum_{ij} \frac{[M^{ij} - F_A^{ij} - F_B^{ij}]^2}{[M^{ij} + (\sigma_A^{ij})^2 + (\sigma_B^{ij})^2]} \tag{3.1}$$

where

$$M(Q_T, Q_L) = \left(\frac{d^2 N_{\mathrm{pr}}}{dQ_T dQ_L} \right) \Delta Q_T \Delta Q_L, \tag{3.2}$$

and the sum in (3.1) runs over a two-dimensional grid of $|Q_L| < 15$ MeV/c and $|Q_T| < 5$ MeV/c, with bin centers located at values (Q_T^i, Q_L^j) and uniform bin size $\Delta Q_T = \Delta Q_L = 0.5$ MeV/c. The F_A and F_B functions describe the pionium signal and the $N_{CC} + N_{AC} + N_{NC}$ three-fold background, respectively, defined as:

$$F_A(Q_T, Q_L) = \frac{N_{AA}^{rec}}{N_{AA}^{MC}} \frac{d^2 N_{AA}^{MC}}{dQ_T dQ_L} \tag{3.3}$$

and

$$F_B(Q_T, Q_L) = \frac{N_{CC}^{rec}}{N_{CC}^{MC}} \frac{d^2 N_{CC}^{MC}}{dQ_T dQ_L} + \frac{\omega_{AC} N_{pr}}{N_{AC}^{MC}} \frac{d^2 N_{AC}^{MC}}{dQ_T dQ_L} + \frac{N_{NC}^{rec}}{N_{NC}^{MC}} \frac{d^2 N_{NC}^{MC}}{dQ_T dQ_L} \tag{3.4}$$

σ_A and σ_B are their statistical errors. The analysis is based on the parametrization of F_A and F_B and the precise Monte Carlo simulation of the detector response.

ω_{AC} is the fraction of accidental background out of all prompt events. Subtraction of accidental pairs is performed by blocking the ω_{AC} parameter to the experimentally observed values, to be described in the next section. Minimization of the χ^2 over the entire (Q_T, Q_L) plane determines the non-Coulomb fraction N_{NC}^{rec}/N_{NC}^{MC}, and the atom fraction N_{AA}^{rec}/N_{AA}^{MC}. The total number of measured prompt events is restricted by the condition $N_{pr}(1 - \omega_{AC}) = N_{CC}^{rec} + N_{NC}^{rec} + N_A^{rec}$, and represents the overall Monte Carlo normalization, determined by the number of prompt events in the fitted range.

Once the previous fit has converged, we define the atom signal in each (i, j) bin as the difference between the prompt spectrum and the Monte Carlo with the pionium component (AA) removed. This two-dimensional signal, which reveals the excess with respect to the calculated Coulomb interaction enhancement, is analysed in detail in Chapter (5), where it is compared with the Monte Carlo prediction for atom production.

3.7   Accidental Pairs

The prompt region is defined by the Time-Of-Flight difference between the two arms of the spectrometer, $|\Delta t| \leq 0.5\ ns$, represented in Fig. (3.5). There is a contribution from all kind of pion pairs described in Chapter (1): atomic, Colulomb, non Coulomb and accidental pairs inside the prompt region. The contribution from the accidental pairs can be measured using the method to be described, which will allow us to fix the accidental contamination in the analysis fit, saving one free parameter.

To extract the fraction of accidental pairs present in the prompt region we have extrapolated the negative part of the Time-Of-Flight difference between $[-14, -4]\ ns$ to the $|\Delta t| \leq 0.5\ ns$ region. This is to avoid the positive part of the accidental region that contains contributions from protons.

The fraction of accidental pairs inside the prompt coincidence has been experimentally determined in ten momentum intervals, for each running period 2001, 2002 and 2003, separately, and the results are given in Table (3.2) and Fig. (3.6). It can be appreciated that the accidental contamination increases with the momentum, because the proton spectra produced by target fragmentation in the proton-nucleus interactions has a greater average momentum than the pion spectra, whose contribution becomes larger as the momentum increases.

The percentage of accidental contamination was incremented during 2002 and 2003 with respect to 2001. Fig. (3.6) does not represent the absolute fraction of accidental pairs, but the extrapolated accidental pairs in the prompt region, so this increment in the contamination cannot be explained in terms of the physics of the experiment. The discrepancy must be explained by means of different setup characteristics in 2001 and 2002-2003.
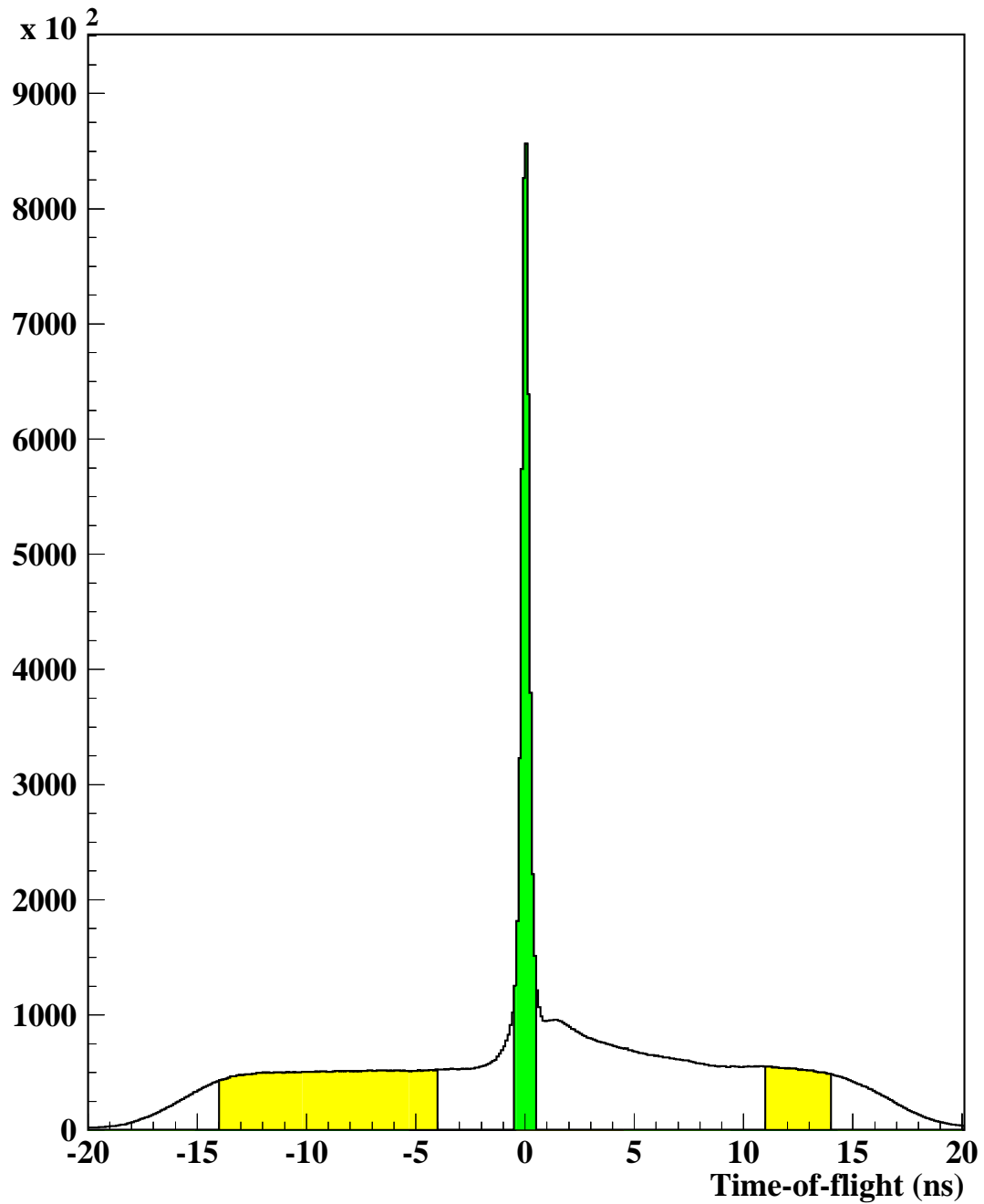
Figure 3.5: *Time difference between positive and negative particles from VH measurement. Prompt events are defined inside the* $[-0.5, 0.5]$ *ns window (green), and accidentals are selected from yellow coloured window in order to remove proton and kaon contamination (*$[-14, -4]$ *and* $[11, 14]$ *ns).*

	p (GeV/c)	% 2001	% 2002	% 2003
p_1	2.6 - 3.2	7.83 ± 0.07	12.25 ± 0.06	11.69 ± 0.11
p_2	3.2 - 3.8	8.86 ± 0.07	12.89 ± 0.07	12.28 ± 0.13
p_3	3.8 - 4.4	10.51 ± 0.07	13.43 ± 0.06	12.76 ± 0.10
p_4	4.4 - 5.0	11.52 ± 0.08	13.97 ± 0.06	13.32 ± 0.12
p_5	5.0 - 5.6	12.16 ± 0.09	14.51 ± 0.08	13.91 ± 0.15
p_6	5.6 - 6.2	12.81 ± 0.10	15.13 ± 0.09	14.60 ± 0.18
p_7	6.2 - 6.8	13.62 ± 0.14	16.09 ± 0.13	15.65 ± 0.24
p_8	6.8 - 7.4	14.62 ± 0.19	17.20 ± 0.18	17.38 ± 0.36
p_9	7.4 - 8.0	15.53 ± 0.27	18.26 ± 0.26	19.40 ± 0.57
p_{10}	8.0 - 8.6	16.25 ± 0.41	19.09 ± 0.42	20.30 ± 0.93

Table 3.2: *Accidental pair contamination inside the prompt coincidence, as determined from analysis of the TOF spectrum. Data are given for each datataking year.*
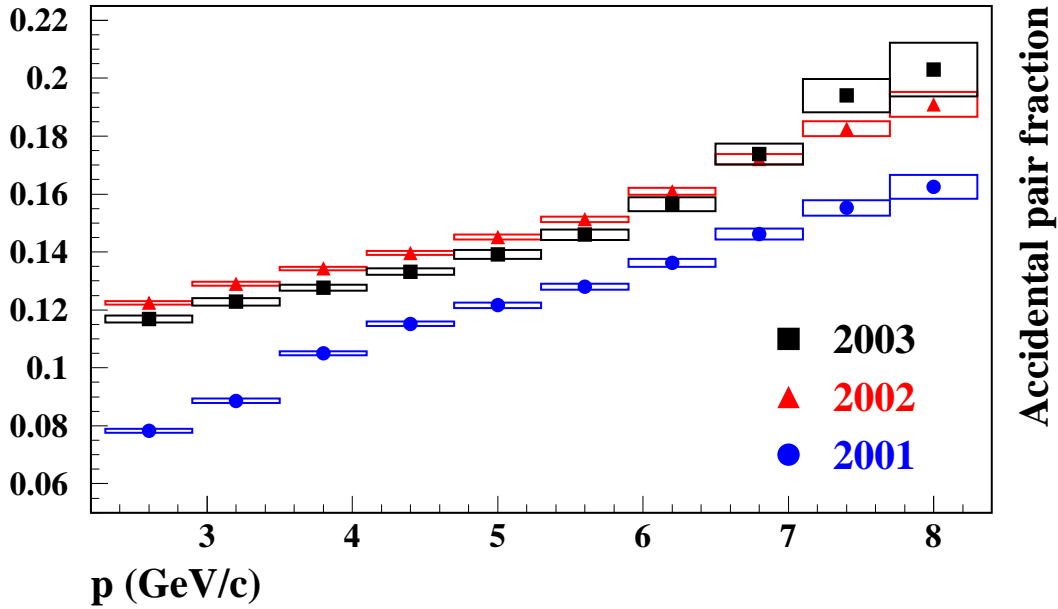
Figure 3.6: *Accidental pair contamination values extracted form Table (3.2), as function of pair momentum. The explanation of the larger fraction of accidental pairs present in the 2002-2003 prompt sample are explained in the text.*

The Vertical Hodoscope resolution remained approximately constant for the experiment's lifetime, unlike the proton beam energy, which was greater in 2002-2003 than in 2001. The more intensity, the larger accidental contamination. Partially, this can also be explained in terms of the better performance of the FPGA-based T3 trigger [62], used until 2001, as compared to the DNA/RNA T3 trigger [63, 81], used from 2002. The trigger conditions were degraded during 2002 and 2003, creating a excess in the accidental pairs accepted by the spectrometer, increasing the amount of accidental pairs outside the prompt region and leading to a overestimation of the accidental fraction when the extrapolation to the prompt region is done.

3.8 K-factors and Breakup Probability

The conversion from integrated atom production signal to breakup probability is done by means of the so-called K-factors, which are defined as follows.

Let us call $S_B(\Omega)$ the measured ratio between the number of atoms N_A and the number of Coulomb pairs N_C, both observed in the same kinematical region Ω of the (Q_T, Q_L) plane. This quantity can be converted into a measurement of the atom breakup probability P_{br}, because the number of atoms n_A produced in a given phase-space volume can be calculated analytically in quantum mechanics [49] according to :

$$K^{th} = \frac{n_A}{N_C} = 8\pi^2 Q_0^2 \frac{\sum_1^\infty \frac{1}{n^3}}{\int A_C(Q) d^3Q} \tag{3.5}$$

where the integral in the denominator extends over the desired Q-space volume. $Q_0 = \alpha M_\pi = 2p_B$ is twice the atom Bohr momentum, and n the pionium principal quantum number. For the sphere of radius $Q < Q_c$ the following expression is obtained:

$$K^{th}(Q_c) = \frac{n_A}{N_C} = \frac{\sum_1^\infty \frac{1}{n^3}}{\int_0^{Q_c/2p_B} \frac{kdk}{1-exp(-2\pi/k)}} \tag{3.6}$$

For a rectangular domain Ω in the (Q_T, Q_L) plane, the integration of the expression (3.5) in cylindrical coordinates provides the values given in Tables (3.3) and (3.4)

However, the actual K-factor which must be taken into account in the measurement (K^{exp}) differs from K^{th} due to experimental resolution [100, 101], which is a function of the domain Ω and can only be calculated using the Monte Carlo.

The breakup probability is then determined as:

$$P_{br} = \frac{S_B(\Omega)}{K^{exp}(\Omega)}$$

(3.7)

with the experimental K-factor defined in the following way:

$$K^{exp}(\Omega) = K^{th}(\Omega)\frac{\epsilon_A(\Omega)}{\epsilon_C(\Omega)}$$

(3.8)

where:

$$\epsilon_A(\Omega) = \frac{n_A^{rec}(\Omega)}{n_A^{gen}(\Omega)} \qquad \text{and} \qquad \epsilon_C(\Omega) = \frac{n_C^{rec}(\Omega)}{n_C^{gen}(\Omega)}$$

(3.9)

define the acceptance of the experimental apparatus as a whole for atoms and Coulomb pairs, respectively, in a given kinematical region Ω. The factors ϵ_A and ϵ_C are determined with high precision using Monte Carlo. They are ratios between reconstructed output and generated input.

For a given momentum interval, the measured values of P_{br} should not depend on the actual domain Ω which is chosen to perform the measurement, and this particular point will be studied in the following sections. The experimental K-factor values do however exhibit a momentum dependence, a legacy of the atomic and Coulomb efficiences, which we have analysed in detail.

Tables (3.3) and (3.4) show the theoretical and experimental K-factor values determined in the first ($2.6 \leq p \leq 3.2$ GeV/c) and seventh ($6.2 \leq p \leq 6.8$ GeV/c) bin interval, respectively, of the momentum-dependent fit analysis, to be described in Chapter (5). The momentum dependency on K^{exp} is quite clear.

$Q_T^{cut}(MeV/c)$	K^{theo}	ϵ_A	ϵ_C	K^{exp}
0.5	3.2181	0.0194	0.0669	0.9305 ± 0.0064
1.0	1.2380	0.0521	0.0916	0.7046 ± 0.0024
1.5	0.6996	0.0787	0.1029	0.5349 ± 0.0013
2.0	0.4673	0.0951	0.1098	0.4050 ± 0.0008
2.5	0.3426	0.1045	0.1142	0.3135 ± 0.0005
3.0	0.2660	0.1096	0.1167	0.2497 ± 0.0004
3.5	0.2147	0.1125	0.1182	0.2043 ± 0.0003
4.0	0.1781	0.1143	0.1191	0.1709 ± 0.0002
4.5	0.1509	0.1154	0.1195	0.1458 ± 0.0002
5.0	0.1299	0.1161	0.1191	0.1267 ± 0.0002
$Q_L^{cut}(MeV/c)$	K^{theo}	ϵ_A	ϵ_C	K^{exp}
0.5	0.4336	0.0742	0.1145	0.2811 ± 0.0006
1.0	0.2387	0.1041	0.1171	0.2123 ± 0.0003
1.5	0.1669	0.1132	0.1184	0.1596 ± 0.0002
2.0	0.1299	0.1161	0.1191	0.1267 ± 0.0002

Table 3.3: *Numerical values of K^{theo} and K^{exp} as defined in the text. Each row corresponds to a given rectangular cut in (Q_T, Q_L) plane, with $Q_T^{cut} = 5$ MeV/c and $Q_L^{cut} = 2$ MeV/c being the reference cut values. K^{theo} values are obtained by integration of Eq. (3.5) in cylindrical coordinates. Only K-factor values from the first momentum bin ($2.6 \leq p \leq 3.2$ GeV/c) of the 2001 94 μm data sample are shown. ϵ_A and ϵ_C are also shown for illustration.*

We do not aim to show all involved K-factors in the analysis, since the seven momentum bins of the analysis and the five data sets produce 35 different tables. These values have been taken into account in the determination of the breakup probability in Chapter (5).

$Q_T^{cut}(MeV/c)$	K^{theo}	ϵ_A	ϵ_C	K^{exp}
0.5	3.2181	0.0621	0.2258	0.8855 ± 0.0012
1.0	1.2380	0.1145	0.2155	0.6577 ± 0.0005
1.5	0.6996	0.1645	0.2310	0.4982 ± 0.0003
2.0	0.4673	0.2000	0.2437	0.3835 ± 0.0002
2.5	0.3426	0.2208	0.2557	0.2957 ± 0.0001
3.0	0.2660	0.2323	0.2622	0.2356 ± 0.0001
3.5	0.2147	0.2389	0.2670	0.1921 ± 0.0001
4.0	0.1781	0.2431	0.2701	0.1603 ± 0.0001
4.5	0.1509	0.2459	0.2729	0.1360 ± 0.0000
5.0	0.1299	0.2481	0.2751	0.1172 ± 0.0000
$Q_L^{cut}(MeV/c)$	K^{theo}	ϵ_A	ϵ_C	K^{exp}
0.5	0.4336	0.1557	0.2594	0.2602 ± 0.0001
1.0	0.2387	0.2206	0.2675	0.1969 ± 0.0001
1.5	0.1669	0.2412	0.2728	0.1475 ± 0.0000
2.0	0.1299	0.2481	0.2751	0.1172 ± 0.0000

Table 3.4: *Numerical values of K^{theo} and K^{exp} as defined in the text. Each row corresponds to a given rectangular cut in (Q_T, Q_L) plane, with $Q_T^{cut} = 5$ MeV/c and $Q_L^{cut} = 2$ MeV/c being the reference cut values. K^{theo} values are obtained by integration of Eq. (3.5) in cylindrical coordinates. Only K-factor values from the seventh momentum bin* ($\mathbf{6.2} \leq p \leq \mathbf{6.8}$ **GeV/c**) *of the 2001 94 μm data sample are shown. ϵ_A and ϵ_C are also shown for illustration.*

3.9 K^+K^- Contamination

The Coulomb interaction is much stronger for K^+K^- than for $\pi^+\pi^-$, at the same Q value. This is because of the different Bohr radius in the Coulomb wave function $(A_C(Q))$, 387 fm for the pionium and 109 fm for the K^+K^-. Although we expect a low level of K^+K^- contamination in the sample, an investigation in two steps was done:

- First we have determined the contamination fraction $r_K^+ = K^+K^-/\pi^+\pi^-$ at low pair momentum ($p = 2.9\ GeV/c$) to be $r_K^+ = (2.38 \pm 0.35) \times 10^{-3}$, using standard physics triggers[2], by means of the TDC information of upstream detectors (SFD and IH) together with the Vertical Hodoscopes TDC [102].

- Secondly, a new measurement was performed at higher momentum using Λ triggers and high precision Time-Of-Flight measurements from the Vertical Hodoscopes [103], which permitted us to compare the momentum derivative of r_K with the predicted by the UrQMD Monte Carlo, observing a very good agreement between them.

3.9.1   Measurement of r_K^+ at 2.9 GeV/c

The exclusive use of the Vertical Hodoscopes information to measure the ratio $r_K^+ = K^+K^-/\pi^+\pi^-$ is not appropriate, since the TOF detector does not allow mass discrimination. However, upstream tracks contain time information stored in the TDC's of the Scintillanting Fiber Detector and the Ionization Hodoscopes.

The time of flight Δt is measured between upstream detectors SFD (SFD-X and SFD-Y) and IH (IH-X_A, IH-X_B, IH-Y_A and IH-Y_B) and the Vertical Hodoscopes, defined as $\Delta t = t_{VH} - t_{ups}$, where the upstream time, t_{ups}, can be constructed by averaging N measurements among the 6 available detectors[3], $t_{ups} = (1/N)\sum_i t_i$.

The squared invariant mass M_i^2 associated to every upstream single detector i can be determined in terms of every individual time measurement $\Delta t_i = t_{VH} - t_i$:

---

[2]The 2001 Ni data sample was used to determine the K^+K^- contamination fraction

[3]In Ref. [72] it was reported that the IH-X_B detector has a wider TDC distribution and slightly different properties than the other hodoscopes. No effort was made to include this detector in the sunsequent analysis, in order to avoid any doubts.

$$M_i^2 = p^2 \left(\frac{c^2 \Delta t_i^2}{L^2} - 1 \right) \tag{3.10}$$

where p is the momentum associated to the track and L is the path length. The particle squared invariant mass M^2 is obtained by appropriate averaging the N individual M_i^2 measurements, $M^2 = (1/N) \sum_i M_i^2$.

The K^+K^- signal must be determined after a huge suppression of the $\pi^+\pi^-$ background, and two methods are explored. In both cases a kinematical cut 1.4 $< p < 1.5$ GeV/c is applied in every charged track.

- **Method A.** The method A uses the three IH detectors to perform a veto in the pion mass, and the measurement goes to the SFD detector. Different criteria $M_L^2 < M_i^2 < M_H^2$ in the lower M_L^2 cut were applied, to obtain first the pion squared invariant mass resolution, $R(x)$. Fig. (3.7) shows the kaon squared-mass, of about the same size as that observed for the pion. As expected, lowering the cut M_L^2 results in increasing pion background, and the opposite effect is observed by setting higher values of M_L^2. The K^+K^- signal is however not unnafected by the M_L^2 values, due to the acceptance variations implied by the pion veto.

Then, a maximum likelihood fit is performed to the entire mass spectra for 8 different choices of M_L^2, with a generic number of events N in the fit. The probability density for an event with mass M_i^2 is given by the expression:

$$L_i = (1 - \alpha) R(M_i^2 - M_\pi^2) + \alpha R(M_i^2 - M_K^2) \tag{3.11}$$

The maximization of the expression

$$\prod_{i=1}^{N} L_i = \prod_{i=1}^{N} (1 - \alpha) R(M_i^2 - M_\pi^2) + \alpha R(M_i^2 - M_K^2) \tag{3.12}$$

over the N events involved in the fit, as a function of α, provides the number of K^+K^- pairs $N(K^+K^-) = \alpha N$.
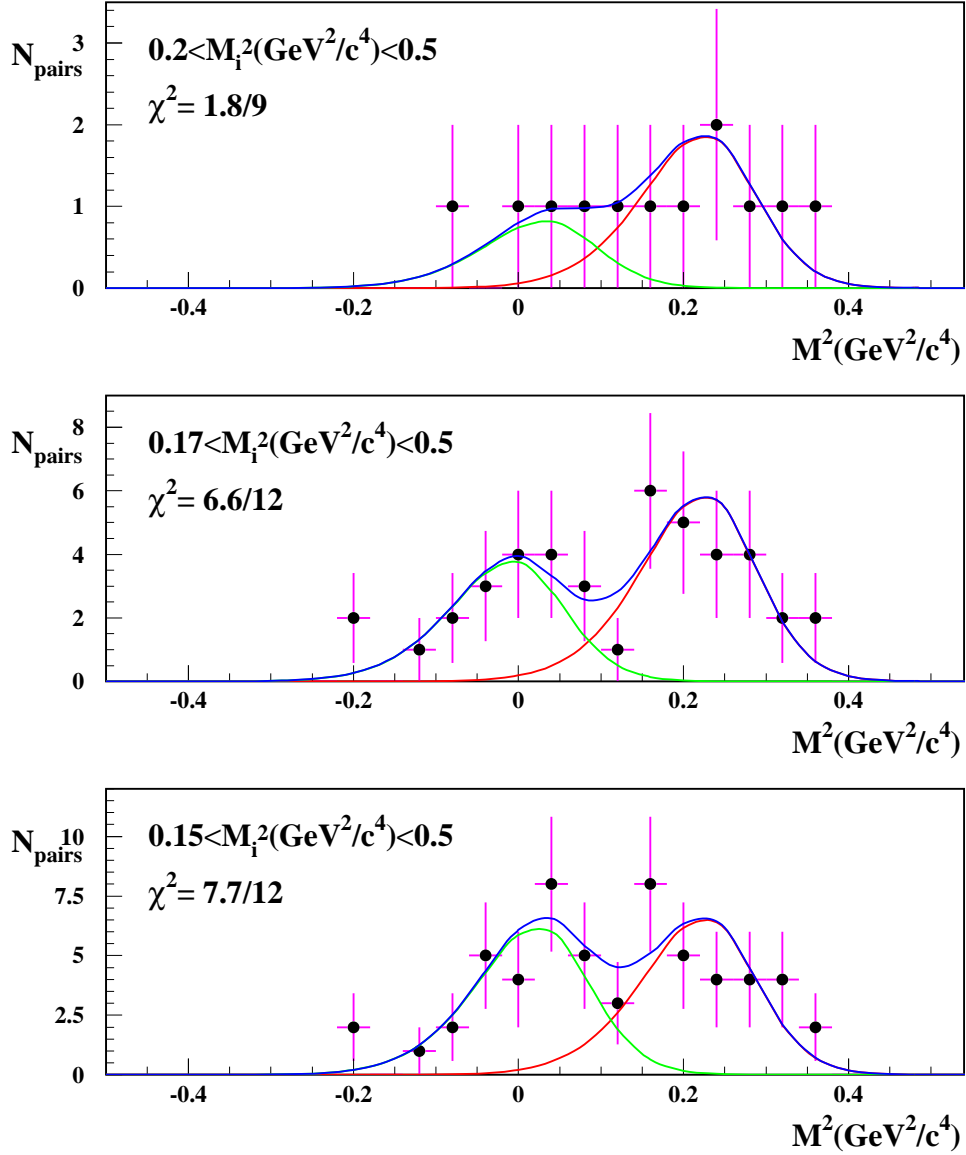
Figure 3.7: *Average squared invariant mass of particle pairs measured from TDCs of SFD X-Y according to expression (3.10). All individual hit measurements M_i^2 associated to any of the two upstream tracks in IH detectors have been restricted to the indicated limits $M_L^2 < M_i^2 < M_H^2$. The results of the maximum likelihood fit are shown in each case, indicating the progression of the $\pi^+\pi^-$ (green), K^+K^- (red) signals, and of the sum (blue), with decreasing lower limit M_L^2. χ^2 values are indicated only for reference.*

The kaon resolution function is not entirely contained within the interval (M_L^2, M_H^2), and the K^+K^- signal efficiency is then a calculable function of the lower limit M_L^2. Its parametrization is described by the acceptance probability $A(M_L^2)$, given by:

$$A(M_L^2) = \epsilon^{6-3s(1-s)^2-2[3s^2(1-s)]-3s^2]} \tag{3.13}$$

where $\epsilon = \int_{M_L^2}^{\infty} R(x)dx$, being s the average probability that both particles intersect the same IH slab, so, the last three terms in the exponential represent the probability of single, double or triple same-slab coindidences in the three active detectors, respectively. This exponent is accurately determined with real data, happening to be 5.14, which corresponds to $s = 0.30$.

Fig. (3.8) shows the function $A(M_L^2)$, which describes the K^+K^- signal found for the eight lower M_L^2 cuts, 0.2, 0.17, 0.15, 0.14, 0.13, 0.10, 0.08, 0 and -0.1 $(\text{GeV}^2/\text{c}^4)^4$. The plateau value corresponds to $N(K^+K^-) = 61 \pm 10$ events. Taking into account the total number of $\pi^+\pi^-$ pairs involved in this analysis, $N(K^+K^-)$ can be converted into the ratio $\epsilon_K = N(K^+K^-)/N(\pi^+\pi^-) = 0.238 \pm 0.035$ %, which is the K^+K^- contamination fraction calculated at low momentum.

---

[4]The upper limit, 0.5 GeV^2/c^4, remained constant in all this analysis.
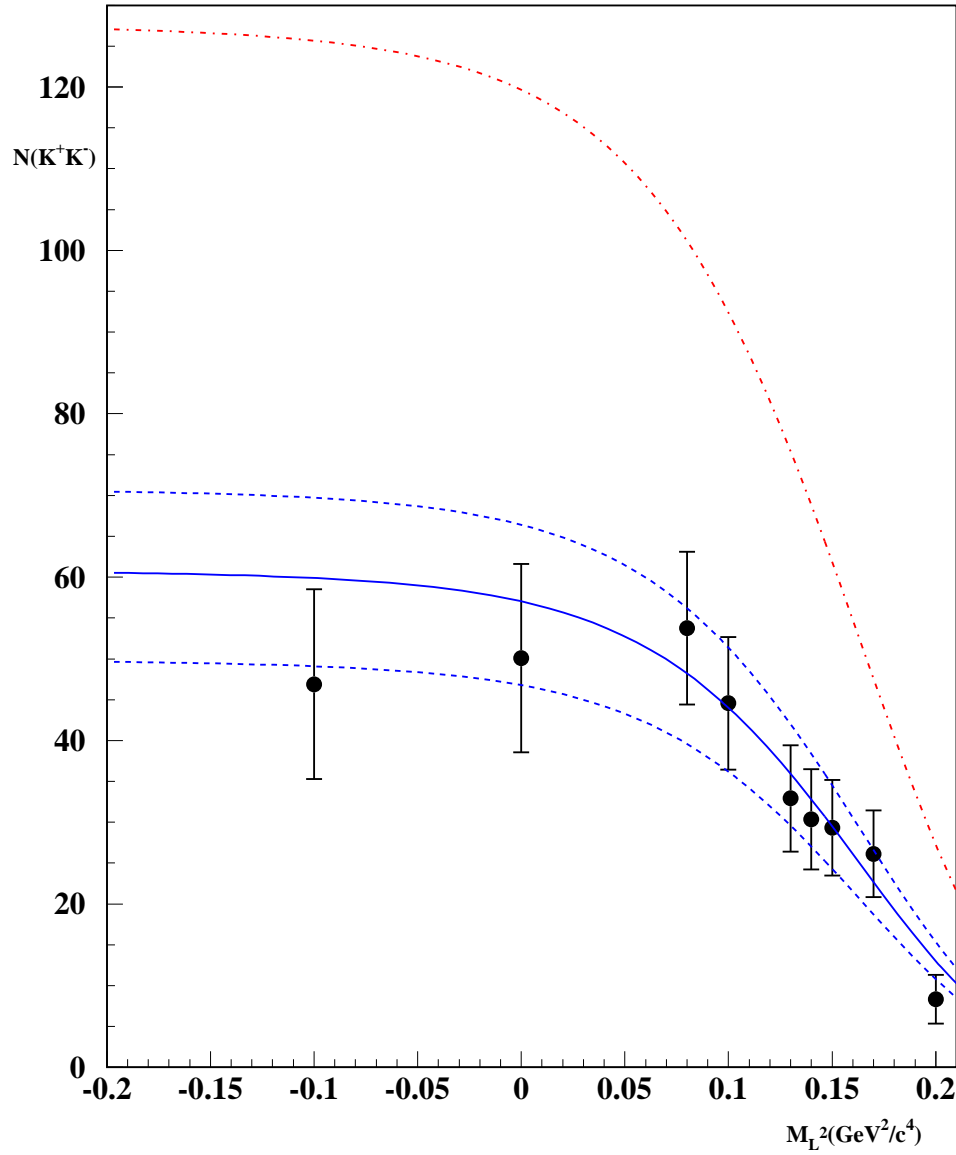
Figure 3.8: *Number of K^+K^- pairs determined from the maximum likelihood fit of the function (3.11), over the eight lower M_L^2 cuts, 0.2, 0.17, 0.15, 0.14, 0.13, 0.10, 0.08, 0 and -0.1 (GeV^2/c^4). The continuous line shows the function $A(M_L^2)$ multiplied by $N(K^+K^-) = 61$ events.*

- **Method B.** In this method, all five upstream detectors are used to perform an unbiased measurement, without a pion veto. This method is not so elaborated as the first one, and it confirms the contamination of K^+K^- of the former. A double parametrization of the pion resolution function is proposed in this method, given by $R(x) = Ae^{-(a_1|x|^2 + a_2|x|^3 + a_3|x|^4)}$ $(x \geq 0)$ and $R(x) = Ae^{-(b_1|x|^2 + b_2|x|^3 + b_3|x|^4)}$ $(x \leq 0)$, being $x = M_i^2 - M_\pi^2$.
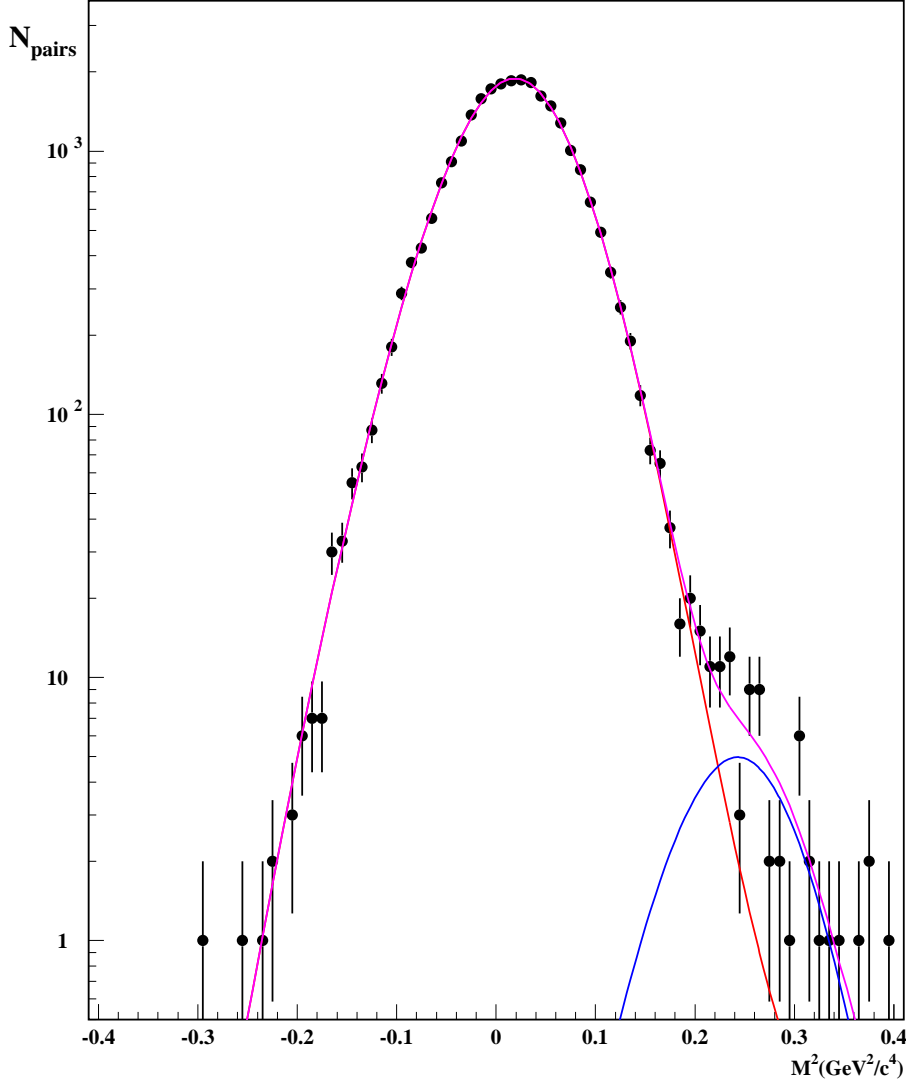
Figure 3.9: *Squared invariant mass calculated for pairs measured without pion veto, from the average of all upstream detectors tracks in IH and SFD. No attempt has been made to reduce the $\pi^+\pi^-$ background (red), which is described by the double parametrization described above. Fit results, indicated in Table (3.5), are shown for the K^+K^- signal (blue) and for the sum (purple).*

The squared invariant mass fit to this double parametrization produces the results summarized in Table (3.5). Fig. (3.9) shows the double parametrization applied to the squared invariant mass distribution. The fitted number of K^+K^- pairs is 65 ± 10, and is highly compatible with the value obtained in method A.

M_π	$0.0188 \pm 0.0014 \ GeV^2/c^4$
a_1	201 ± 18
a_2	-462 ± 181
a_3	511 ± 508
b_1	199 ± 8
b_2	-137 ± 46
b_3	-650 ± 92
α	0.9975 ± 0.0004
N_k	65 ± 10
$\epsilon_k(\%)$	0.253 ± 0.038
χ^2/ndf	$69.57 \ / \ 55$

Table 3.5: *Fit values obtained for the parametrization described above, obtained for the mass measurement without pion veto, using all IH and SFD upstream detectors, following method B, described in the text.*

3.9.2   Measurement of r_K^+ at High Momentum

The determination of the K^+K^- signal at higher values of momentum needs asymmetric triggers. In this way, the precise time-difference information provided by the TOF detector becomes useful for mass discrimination. The Lambda triggers are very well suited for this purpose [75, 56], being statistics the only problem, since these triggers only represent a small fraction of the normal DAQ runs. In order to maximize the amount of available data we have integrated the 2001, 2002 and 2003 samples.

The upstream mass is defined by expression (3.10), for each of the SFD (2) and IH (4) detector planes. In addition, the average upstream positive particle is defined mass as:

$$M_+^2 = \frac{\sum M_{i,+}^2}{N} \tag{3.14}$$

The event selection is done in the 1.2 GeV/c $< p_- <$ 1.6 GeV/c and 2.8 GeV/c $< p_+ <$ 4.0 GeV/c ranges, since the positive particle average momentum is significantly higher than the negative one, due to the Lambda trigger structure [56]. Protons are removed by the cut -0.2 $< M_+^2(GeV^2/c^4) <$0.5, whereas K^- identification is provided by requiring $0.015 < M_{i,-}^2(GeV^2/c^4) < 0.44$ for all upstream detectors[5].

These cuts play the role of a very strong pion veto, based upon the upstream Time-Of-Flight measurements only. Their effect is illustrated in Fig. (3.10) by showing as shaded area the event fractions retained in each case.
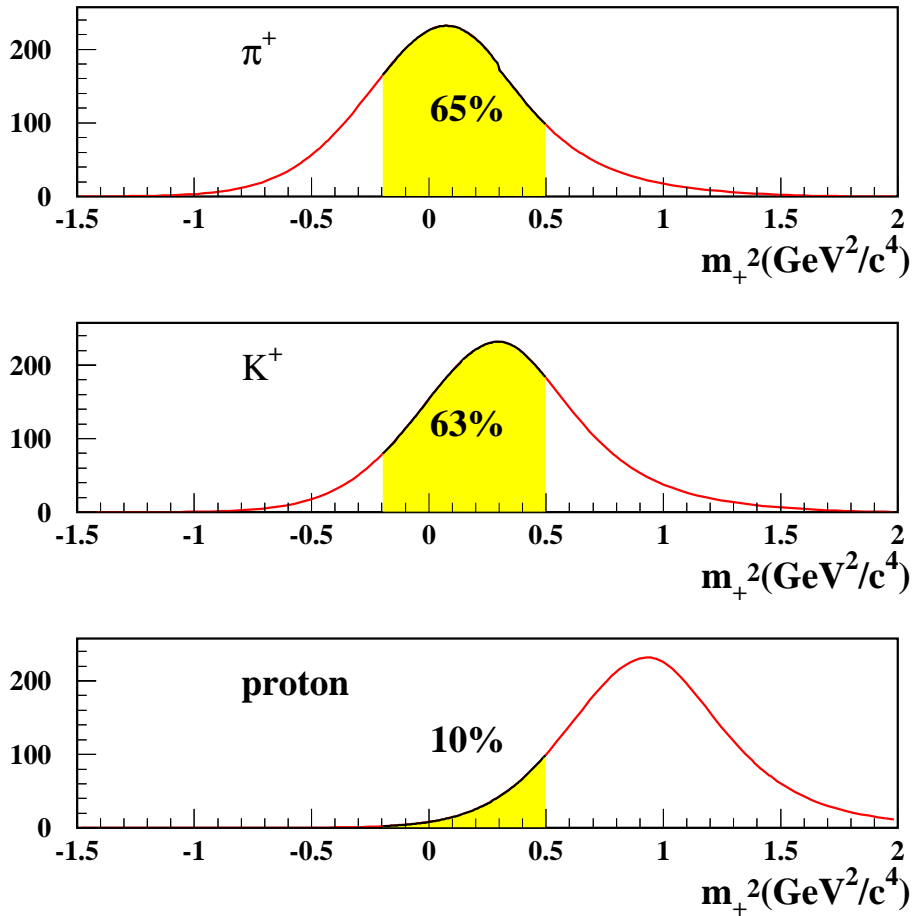
Figure 3.10: *Resolution function for the positive upstream squared mass M_+^2, obtained from a parametrization fitted to the experimental $\pi^+\pi^-$ data. The peak value has been displaced to three different mass hypotheses, in order to appreciate the effect of the cuts described in the text.*

---

[5]The upper limit for IH-X$_B$ is 0.7 GeV^2/c^4, since its different behaviour from all IH's, as reported in Ref. [72]

After the background suppression provided by the above cuts, we are now in position to analize the fine structure of the spectrum of the negative mass M_-^2, defined from the precision time-difference in the Vertical Hodoscopes, which is given by:

$$M_-^2 = p_-^2 \left[\left(\frac{L_+}{L_-} \sqrt{1 + \frac{M_K^2}{p_+^2}} - \frac{c\Delta t}{L_-} \right)^2 - 1 \right] \tag{3.15}$$

where the K^+ masss hipothesis in the opposite arm has now been chosen. The spectrum with full statistics is shown in Fig. (3.11), where four enhancements can be observed, which we attribute in principle to $\pi^+\pi^-$, K^-p, K^+K^-, and π^+K^- production. Please note that only the K^+K^- signal is seen at the correct mass hypothesis ($M_-^2 = M_K^2$), the others being shifted according to predictable deviations due to the positive particle time slewing. A more detailed analysis of this particular spectrum shows that the second peak is actually dominated by a background originated from a reflection of the negative upstream mass cuts, as we will see below, and that this is the reason for its broader structure.

The signal yield is analized by maximization of the following likelihood function:

$$L(x) = \sum_{\alpha=1}^{3} A_\alpha G_\alpha(x - x_{0\alpha}, \sigma_\alpha) + A_b G_b(x - x_{0b}, \sigma_b) + BP_4(x) \tag{3.16}$$

where $x = M_-^2$ and $G_\alpha(x)$ represent normalized Gaussian functions with peak value at $x = x_{0\alpha}$ and width σ_α describing the $\pi^+\pi^-$, K^+K^- and π^+K^- signals for $\alpha = 1, 2, 3$, respectively. Similarly $G_b(x)$ is a Gaussian describing the background broad structure in the neibourghood of the K^-p signal. An additional smooth background is described by the normalized fourth order polynomial $P_4(x) = (1 + \sum_{i=1}^{4} c_i x^i)/I_4$ where $I_4 = \int_{x_1}^{x_2} (1 + \sum_{i=1}^{4} c_i x^i) dx$ is the normalization integral. The signal event rates are then provided by the coefficients A_α.

The parameters $x_{0\alpha}$, σ_2 and σ_3 were determined independently, and remained fixed in the fit procedure. The rest (σ_1, σ_b, A_α, A_b, B,c_i) were left free. The location of the $x_{0\alpha}$ peaks was determined by selecting signal events under the peak with the correct mass hypothesis and projecting them into the uncorrect hypotheses, in order to evaluate the mass shift.

Table (3.6) and Fig. (3.11) show the fit results.
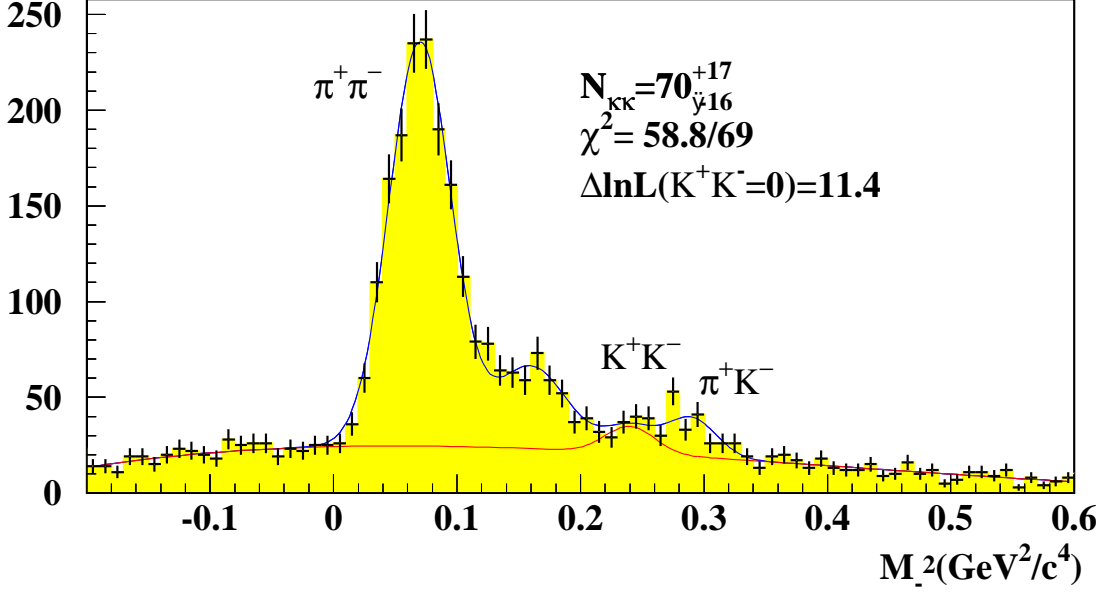
Figure 3.11: *Spectrum of squared negative mass M_-^2 measured with Vertical Hodoscopes under K^+ mass hypothesis, for the complete 2001, 2002 and 2003 proton-Nickel data sample with Lambda triggers. The maximum likelihood fit is explained in the text. The significance of the K^+K^- signal at average pair momentum $p = 4.8 GeV/c$ is indicated.*

Table 3.6: *Parameter setting in maximum likelihood fit to M_-^2 spectrum.*

Parameter	Value
$x^0_{\pi\pi}$	0.07
x^0_{KK}	0.24
$x^0_{\pi K}$	0.29
x^0_b	0.16
σ_{KK}	0.02
$\sigma_{\pi K}$	0.02

Parameter	Value
$\sigma_{\pi\pi}$	0.025
σ_b	0.029
$A_{\pi\pi}$	1327.2
A_{KK}	79.9
$A_{\pi K}$	101.8
A_b	311.8

Parameter	Value
B	1449.2
$c0$	0.5978
$c1$	0.3687
$c2$	-3.9717
$c3$	4.3075
$c4$	-1.3526

The number of K^+K^- pairs found by the fit are $N_{KK}^{obs} = 70^{+17}_{-16}$, and the total number of $\pi^+\pi^-$ pairs found when removing the $M_-^{2\,i}$ cuts is $N_{\pi\pi}^{obs} = 22942$. Both numbers need to be corrected for the acceptance.

The positive mass cut efficiency (see Fig. (3.10) top) is involved in the $\pi\pi$ case:

$$N_{\pi\pi} = N_{\pi\pi}^{obs} \times \frac{1}{\text{Eff}(\pi^+)} = 22942 \times \frac{1}{0.6514} = 35219 \tag{3.17}$$

whereas for N_{KK} both the positive (see Fig. (3.10) center) and negative mass cuts are subject to independent efficiency corrections. The final numbers are:

$$N_{KK} = N_{KK}^{obs} \times \frac{1}{\text{Eff}(K^+)} \times \frac{1}{\text{Eff}(K^-)} = 70 \times \frac{1}{0.6303} \times \frac{1}{0.5409} = 205 \tag{3.18}$$

so the measured contamination fraction at 4.8 GeV/c is:

$$r_{KK} = \frac{N_{KK}}{N_{\pi\pi}} = \frac{205}{35219} = 5.8 \times 10^{-3} \tag{3.19}$$

3.9.3   Comparison with UrQMD Monte Carlo

For a better understanding of the momentum dependence of the K^+K^- signal, the production of $K^\pm\pi^\mp$ and the semi-inclusive K^+K^- [103] were investigated in detail, and have been compared with a specific Monte Carlo model, the UrQMD [104]. As a result of our study, a very good agreement was found between our DIRAC data and UrQMD, particularly concerning the momentum dependence.

The basic approach has been to fully simulate the K^+K^- contamination as a function of the pair momentum, and include the simulated (Q_T, Q_L) spectrum in our standard χ^2-analysis, as a modification of the Coulomb $\pi^+\pi^-$ spectrum. Generation of K^+K^- pairs is achieved, in the center-of-mass frame, by means of the DIRAC atom pair generator (DIPGEN) [98] after modification of the Bohr radius in the Coulomb factor. Pairs are then boosted into the DIRAC laboratory frame, exploiting the input p distribution plotted in Fig. (3.3).

The prediction of the UrQMD Monte Carlo was evaluated by running 2049 million p-Ni events from the generator and selecting K^+K^- and $\pi^+\pi^-$ pairs with the cuts: $4.5^o < \theta < 7.0^o$, $1.3\ GeV/c < p_{+-} < 5.0\ GeV/c$ and $Q < 30 MeV/c$ in the $\pi\pi$ hypothesis, where θ is the angle between the vector sum of the particle momenta and the incoming proton direction and p_{+-} is the momentum of the positive or negative particle. The uncorrected curve was multiplied by an acceptance efficiency function determined separately after the GEANT-DIRAC processing of K^+K^- pairs, in order to take into account the $K^\pm$ lifetime effect in the spectrometer acceptance.

The UrQMD Monte Carlo prediction can be appreciated in Fig. (3.12) as a dotted line. At 2.9 GeV/c the r_K ratio result is 0.56 (after Coulomb correction), which is larger than the experimental value by a factor 2.7. We have however normalized the Monte Carlo to the experimental value at 2.9 GeV/c. We then see that very good agreement is found with respect to the data measured at 4.8 GeV/c. It seems that UrQMD describes precisely the cross-section dependence on the lab-frame momentum, although the magnitude of the strangeness ratio r_K is not reproduced correctly.
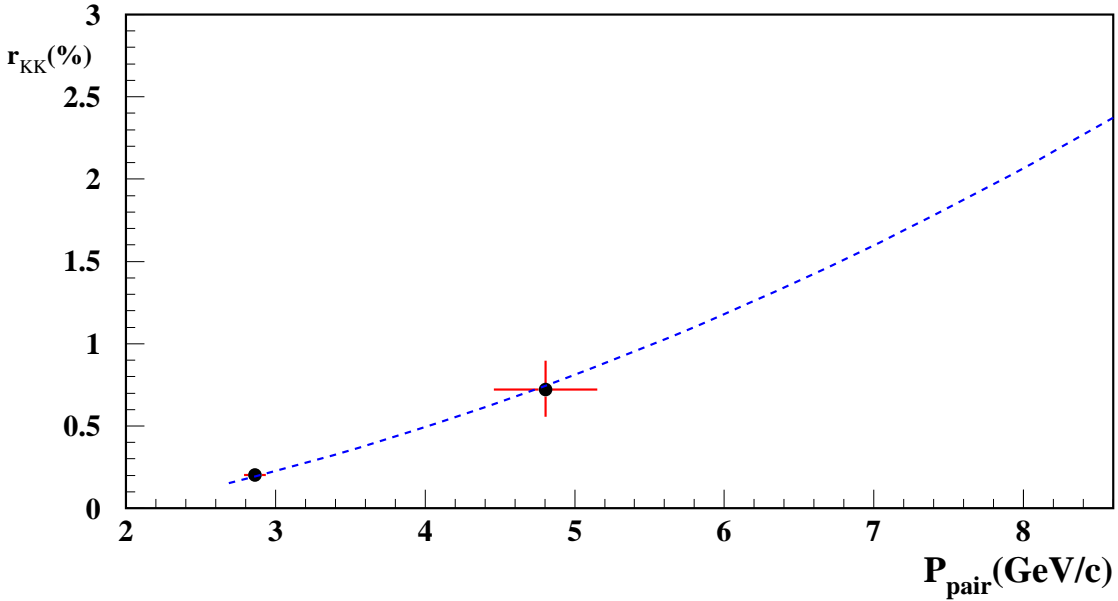
Figure 3.12: *Experimental measurements by DIRAC of the $K^+K^-/\pi^+\pi^-$ ratio r_K at two different values of the average pair momentum, 2.9 GeV/c and 4.8 GeV/c. The UrQMD Monte Carlo prediction multiplied by a factor 0.37 is shown as the dotted line.*

The Coulomb interaction has a different magnitude for K^+K^- and $\pi^+\pi^-$ pairs for a given kinematical domain, due to the different trigger structure and cuts applied in the analysis done at $p = 2.9$ GeV/c and $p = 4.8$ GeV/c. In addition, the standard pionium lifetime determination uses different kinematical cuts. A detailed study can be found in Ref. [103], where the average value of the Coulomb enhancement ($C_{\pi\pi}$ and C_{KK}) is defined for $\pi\pi$ and KK pair production cross sections.

The above investigation concludes that a correction factor that accounts for the ratio $R = C_{KK}/C_{\pi\pi}$ must be enforced to the K^+K^- contamination fractions obtained for $p = 2.9$ GeV/c and $p = 4.8$ GeV/c, resulting 0.845 and 1.23 respectively. In conclusion, we find that the contamination fractions relevant for pionium analysis are, at 4.8 GeV/c based upon the UrQMD Monte Carlo extrapolation, in agreement with the experimental data:

$$\frac{N_{KK}}{N_{\pi\pi}} = 5.8 \times 10^{-3} \times 1.23 = 7.2 \times 10^{-3} \tag{3.20}$$

and, at 2.9 GeV/c, according to the Coulomb-corrected experimental measurement:

$$\frac{N_{KK}}{N_{\pi\pi}} = 2.38 \times 10^{-3} \times 0.845 = 2.0 \times 10^{-3} \tag{3.21}$$

3.10   Summary

The analysis method and the pionium signal extraction from the Monte Carlo simulation has been described in this Chapter. Special attention has been paid to the Monte Carlo generator utilized for that purpose. We have discussed in detail the contribution from accidental pairs in the prompt $\pi^+\pi^-$ sample to be determined, together with the K^+K^- contamination in the Coulomb spectra.

Before tackling the final analysis, the Monte Carlo has to be optimized, together with the alignment of the spectrometer. Chapter (4) will deal with these questions, and in Chapters (5) and (6), respectively, we will report the analysis results and a complete systematic error description list involved in the determination of the pionium breakup probability.

Chapter 4

Analysis Improvements

This chapter describes all the new parametrizations introduced in the Monte Carlo to best describe the real data, introducing two main differences between the current analysis and the one presented in [92]:

- (a) The simulation of the trigger response.

- (b) The momentum smearing in the Monte Carlo.

These effects increase by a 5% the breakup probability of the pionium in a Nickel target. In addition, the suppression of the χ^2 cuts applied in the drift chambers provides a $\sim$30% statistics enlargement compared to the previous lifetime determination [92].

4.1 Alignment and Tracking

Before we can accomplish the Monte Carlo optimization of the present analysis, we need to perform some important modifications, related to the spectrometer alignment and the tracking routines, such as the Q_L alignment and the DC's track selection.

4.1.1 Drift Chambers Track Selection

One of the first stages for the off-line data selection is the track reconstruction, which includes a matching between upstream and downstream tracks. Very early software applied χ^2 cuts in the DC's track selection. This was motivated by the lower quality of the alignment of the DC tracks due to the difficulty to line up so many planes with different stero angles, and the need to improve the condition of the DC tracks, in order to select the most trustable ones.

The present analysis proposes some enhancements motivated by the fisrt-class status of the upstream tracking employed in previous works [91, 92], which has reached a notorious improvement in its quality. This revision was possible due to the utilization of the GEM/MSGC detector in such previous works, granting the withdrawal of the χ^2 cuts applied in the DC's, besides determining the validity of the previously rejected tracks. This allows to accumulate 30% more statistics, which represents 22000 atoms collected instead of the previous 17000, and a significant improvement in the statistical error.

4.1.2 Q_L Alignment

The power of the proposed analysis method underlies in description of the two-dimensional Q_T and Q_L spectra, which must be determined with the best precision. The calibration of these two distributions is a critical step, and specifically the Q_L alignment must be performed in an iterative way. The Q_L alignment is referred to the target position and must be accomplished assuming that the drift chambers are well aligned with respect to the upstream detectors.

To extrapollate the drift chambers tracks to the upstream region, using the magnet polynomials, the track momentum must be known. For this purpose, a point before the magnet is required to determine the momentum at first order. This vital point is the intersection between the beam and the target, which introduced in the track fit, helps the polynomials to trail the track inside the magnet, providing its momentum at first order. Later, the upstream detectors are exploited to give a correction to the entire track and its momentum.

In a very early stage the Q_L distribution is reconstructead without performing any alignment or correction. A transverse low Q_T cut is applied in order to enhance the Coulomb interaction in the longitudinal Q spectrum, and Q_L is plotted to check whether it is already aligned or not. Fig. (4.1) shows a non-aligned Q_L spectrum, where the Coulomb interaction is not peaked nor simmetrical at zero. This configuration does not fulfill the invariation under CP transformations, and therefore this motivated the callibration.

Q_L is reconstructed under the assumption of that every track points to the beam center in the target. As can be seen in Fig. (4.1), the Q_L peak is slightly displaced to the left and it is needed to relocate the beam center at the target by moving it some milimeters to the right. Finally, after some iterations, we get to a point on which we are pleased with the results, and Q_L is well aligned, as shown in Fig. (4.2).
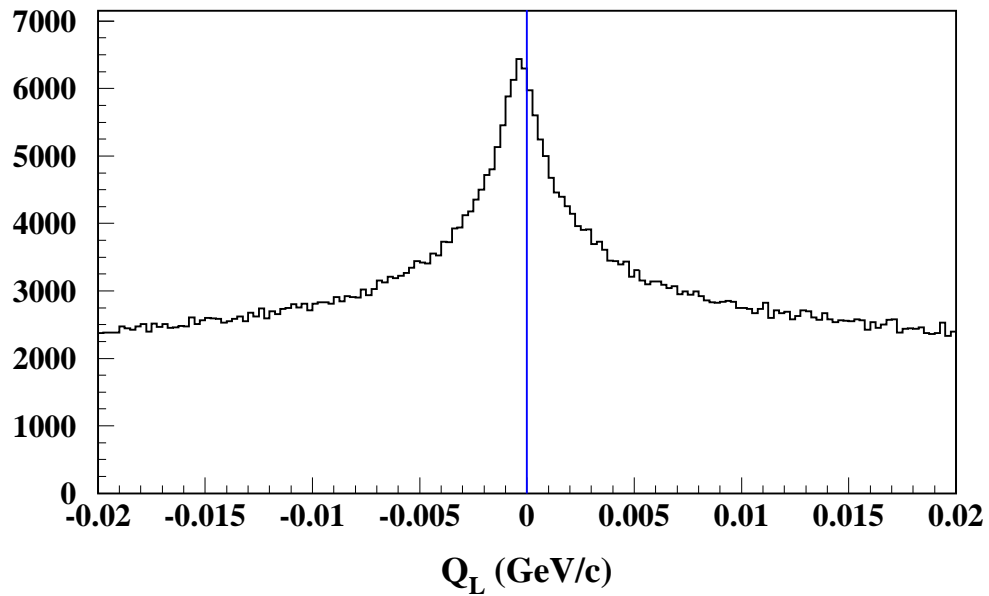
Figure 4.1: Q_L *distribution before the alignment. Please note the necessity of arrange the Q_L symmetry to assure the CP invariance, by means of peaking the Coulomb interaction at $Q_L = 0$.*
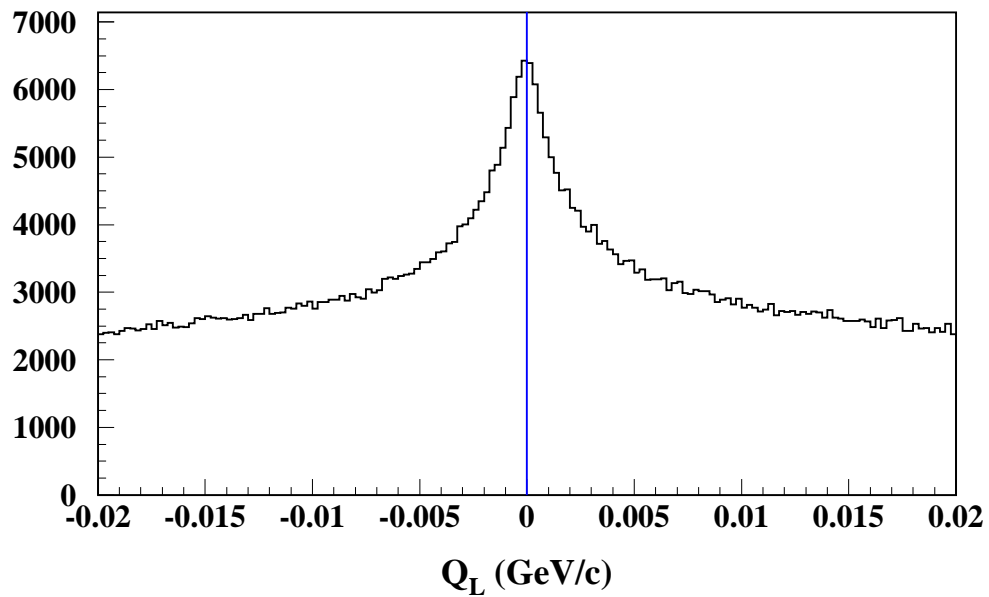
Figure 4.2: Q_L *distribution during the alignment. In this configuration Q_L seems to be properly aligned, but a more precise and detailed final correction as a function of the momentum must be performed to ensure, as much as possible, the symmetry in Q_L.*

A more detailed alignment is enforced to the Q_L distribution, to reach the optimum configuration which comes to guarantee the symmetry of Q_L. In this occasion, a momentum dependent correction must be directly enforced at the level of the *readnt* program, obtaining the desired symmetry in Q_L. Fig. (4.3) shows the final corrected version of the Q_L distribution, as employed in the current analysis.

All this procedure assumes that the drift chambers are well-aligned with respect to the upstream detectors. Otherwise the alignment of the drift chambers cannot be easily carried out by means of the four parameters that characterize their geometry and position: $x, y, tan\ x$ and $tan\ y$, which describe the relative position of the drift chambers and their inclination with respect to the beam direction. The alignment of the upstream detectors and the drift chambers can be accomplished by relocating the former *en masse*.
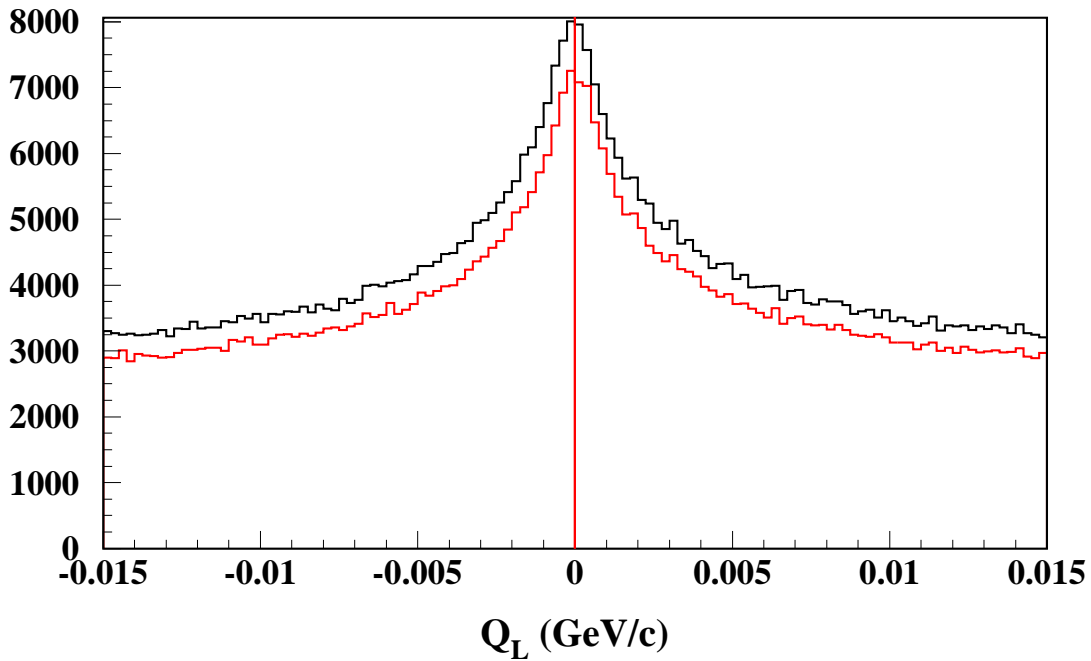
Figure 4.3: *Q_L distribution in an intermediary stage of the alignment (black histogram) and after the application of a momentum dependent correction in Q_L (red histogram). Please note the optimum Q_L symemtry level acquired, where CP invariance can be satisfied, after the Coulomb interaction is peaked at $Q_L = 0$.*

4.2 Monte Carlo Optimization

This work summarizes the most important and influential Monte Carlo features involved in the calculation of the pionium breakup probability in the DIRAC experiment. Some unprecedented aspects of this Monte Carlo are to be reported here, such as the momentum smearing applied in the Q_L resolution and the simulation of the trigger. Some other aspects were updated and their newest version is presented here, as the double track resolution.

4.2.1 Double Track Resolution

Straight-line tracks reconstructed in the upstream detectors are extrapolated to the IH in order to determine the slab intersected by the particle at each detector plane. The information provided by the ADC (pulse-height) and TDC is incorporated to the track, after application of several corrections, following reference [72], some of which depend upon the longitudinal coordinate along the counters.

Special attention is devoted at this point to single unresolved tracks[1] that can be matched to two DC tracks. It is neccesary to look for a double ionization signal in the IH detector in order to establish their two-particle nature. We say there is double ionization in one track when:

- The track is collapsed in the X projection and the IH-X_A and the IH-X_B show a calibrated pulse above threshold (~ 140 counts).

- The track is collapsed in the Y projection and the IH-X_A and the IH-X_B show a calibrated pulse above threshold (~ 140 counts).

- The track is doubly collapsed and the four IH planes show a calibrated pulse above threshold (~ 140 counts).

---

[1]We define a collapsed track in the X projection as a double track unresolved by the upstream planes GEM/MSGC-X, GEM/MSGC-XP and SFD-X; analogously for the Y projection. If the track is not resolved in both projections, then we say the track is doubly collapsed.

4.2.2   Optimization of the Peak Sensing Circuit in the SFD Detector

A delicate challenge to the DIRAC reconstruction procedure arises from the response of the Peak Sensing Circuit (PSC) electronics of the scintillation fiber detector [2]. The PSC algorithm provides efficient detection of double tracks from time correlated particle pairs (up to $\sim$5 ns time difference) when the relative distance between the two tracks is larger than the fiber column pitch. However, when adjacent fiber columns are crossed by two particles simultaneously, then the PSC algorithm leads to a suppression (by 20-40%) of the detected yield of double track events. In such cases a signal is detected for only one of two hit columns.
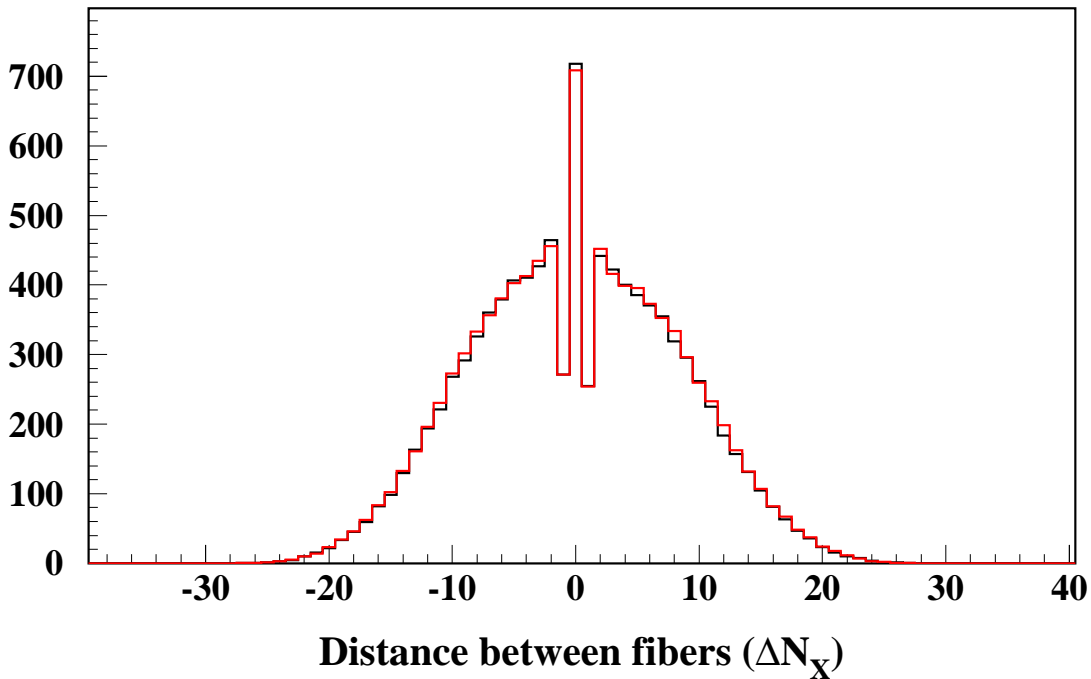
Figure 4.4: *Distance between adjacent fibers in the SFD-X detector, after the simulation of the PSC problem (red histogram) has coped with the real data dependence (black histogram. The overcrowded ($\Delta N = 0$) and the underpopulated regions ($|\Delta N| = 1$) are symptomatic of the PSC problem, showing the SFD detector inefficience for very close tracks.*

The distorsion caused by this effect in close-pair efficiency at small distances (below 3 mm) is largely diminished when the previously described GEM/MSGC upstream tracking is used, where only one SFD hit (in X or Y projection) is required to perform time tagging, the track being actually measured by GEM/MSGC hits having stereo angles.

The Monte Carlo needs to be optimized to simulate the correct amount of PSC present in the real data. When two hits cross the same slab in the SFD detector, there is a high probability to loose one of the two signals. This can be observed in Figs. (4.4) and (4.5), where the PSC simulation has coped with the real data dependence. Figs. (4.4) and (4.5) show the distributions in X and Y of the distance between the fibers in the scintillation fiber detector. The zero distance fiber $\Delta N = 0$ is overcrowded, whereas a distance between fibers of one unit is underpopulated, $|\Delta N| = 1$. These two features exhibit the detector inefficience.
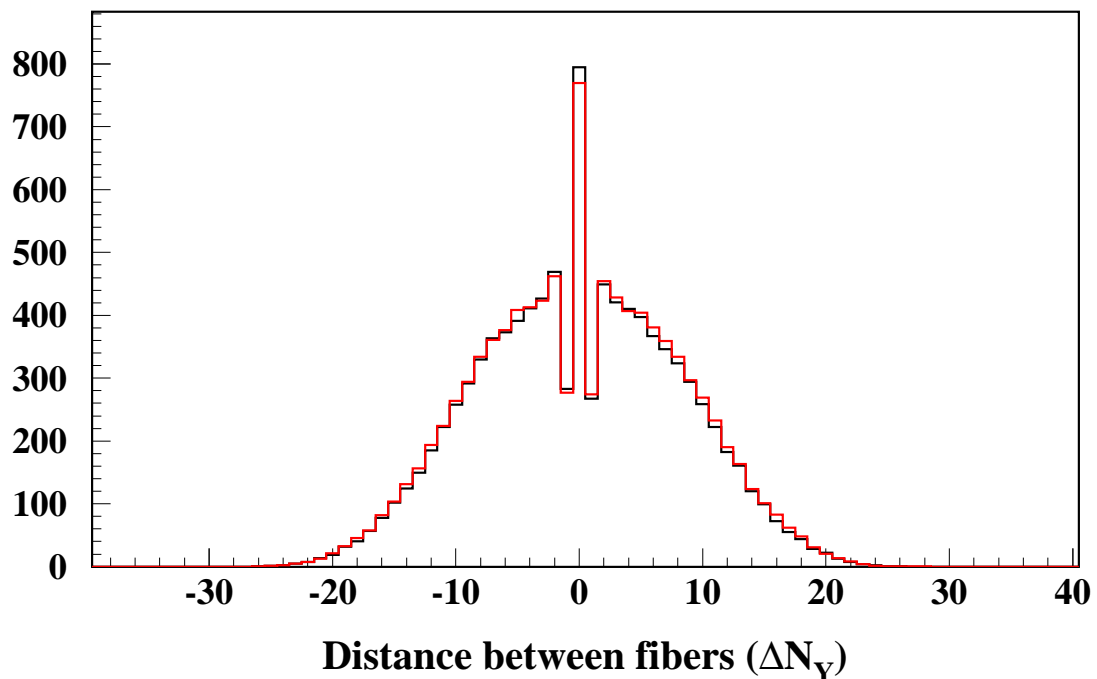
Figure 4.5: *Distance between adjacent fibers in the SFD-Y detector, after the simulation of the PSC problem (red histogram) has coped with the real data dependence (black histogram. The overcrowded ($\Delta N = 0$) and the underpopulated regions ($|\Delta N| = 1$) are symptomatic of the PSC problem, showing the SFD detector inefficience for very close tracks.*

4.2.3   Trigger Simulation

The simulation of the DIRAC trigger response constitutes one of the two principal differences of this thesis with the earlier works presented in [91] and [92], as well as the momentum smearing introduced in the momentum resolution, to be described in the next section.

The intention of the trigger simulation is to find out a possible bias in the Q_L and Q_T distributions, due to the performance of the trigger system employed in DIRAC. For this purpose we have used the 2002 T1 triggered data since this is the largest sample collected under the same conditions, with a postitive decision in the T1 trigger.

Figs. (4.6) and (4.7) show respectively the Q_L and $Q_{X,Y}$ distributions with and without the trigger simulation. Q_X and Q_Y are investigated here instead of Q_T because of the coplanarity selection properties of the T1 trigger, which introduces a slight dependence between Q_X and Q_Y at small Q_T values. The agreement between simulated and non-simulated spectra is quite good, and the discrepancy between them is at the percent level, to be reported below.
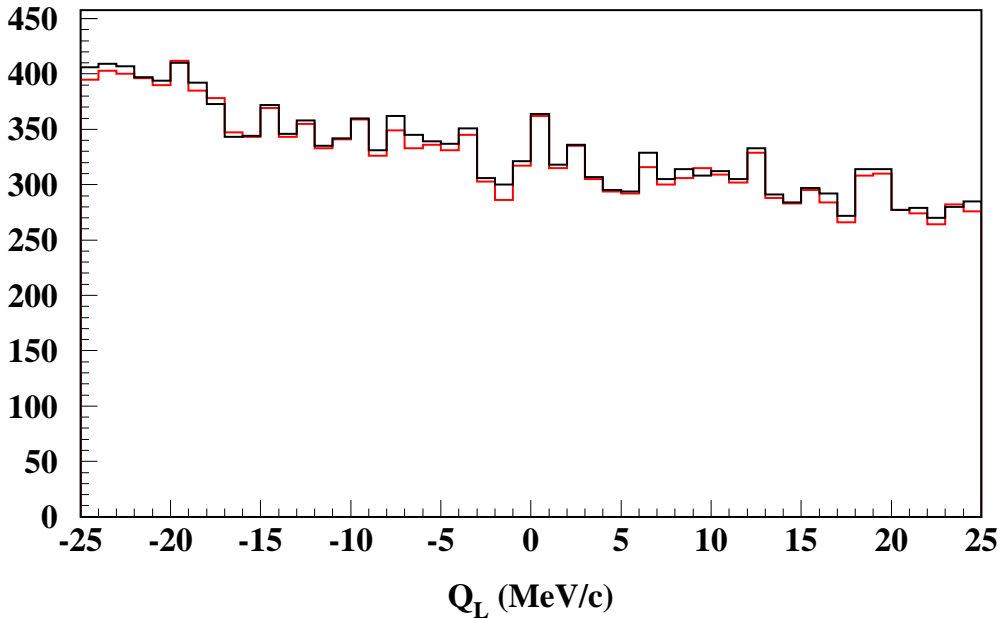
Figure 4.6: *Effect of the trigger simulation in the Q_L shape. The red histogram represents the Q_L distribution in which the simulation of the trigger response was not applied, whereas the black histogram displays the Q_L distribution after the inclusion of the trigger simulation. An excellent agreement between both distributions can be observed.*
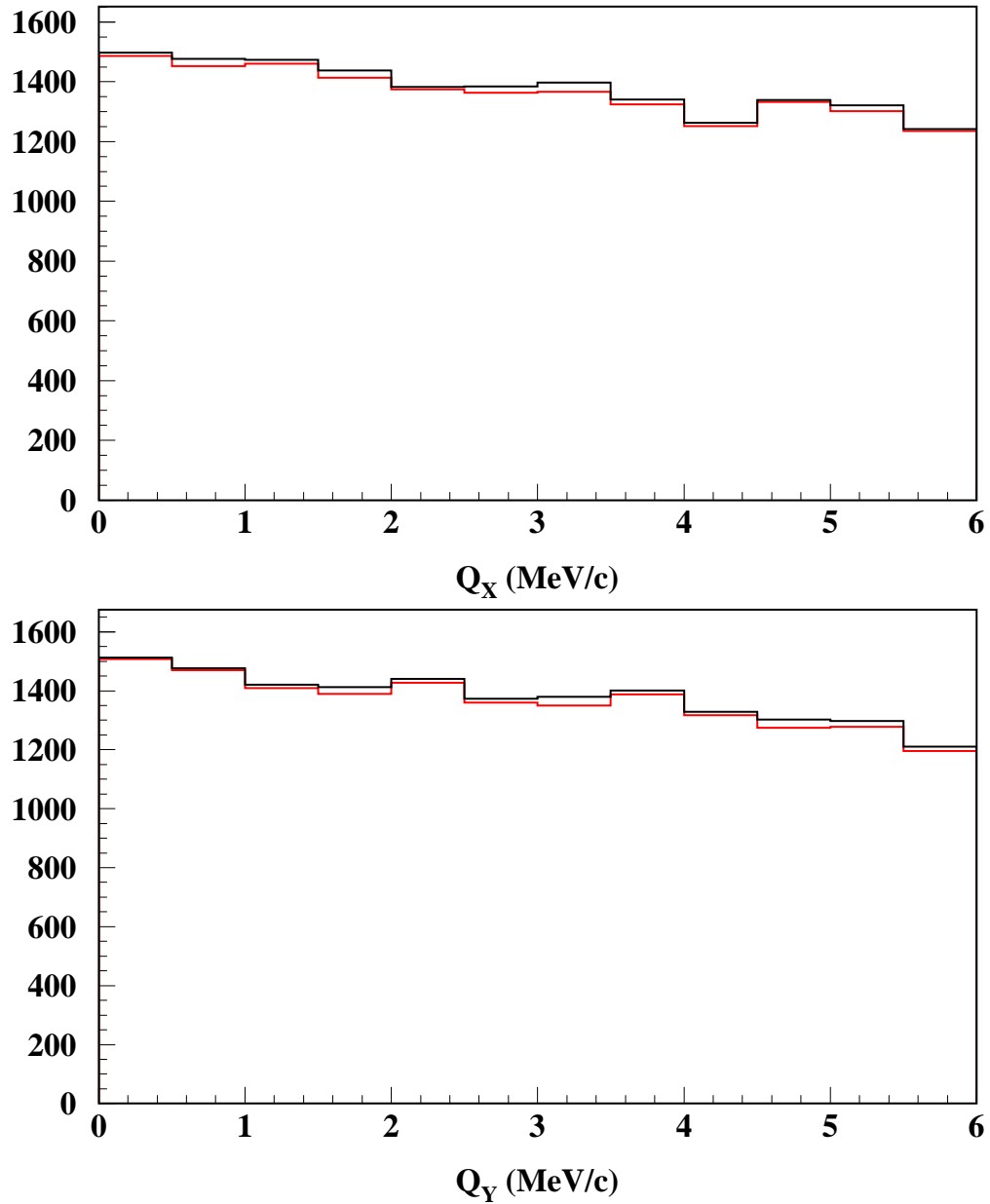
Figure 4.7: *Effect of the trigger simulation in Q_X and Q_Y. The red histogram represents the $Q_{X,Y}$ distributions in which the simulation of the trigger response was not applied, whereas the black histogram displays the $Q_{X,Y}$ distribution after the inclusion of the trigger simulation. The agreement is pretty good, as it can be appreciated.*

An efficiency study of the simulated and experimental triggers, dependent on Q_L, Q_X and Q_Y, was done. We have collected all runs in which the experimental trigger had a positive response and we have investigate how many of the simulated trigger runs were contained in this group. The result is that $\sim$98% of the simulated triggers was contained in the experimental sample, thus the experimental trigger efficiency is $\sim$98%. The $\sim$97% of the experimental triggers were contained in the simulated trigger sample, so the inefficiency of the trigger simulation is 3%. Figs. (4.8) and (4.9) shows the efficiency of the simulated and experimental triggers, and its dependency on Q_L and $Q_{X,Y}$, respectively. It can be observed that the simulated trigger efficiency is quite high, and its low inefficiency will play a role in the systematic error of the pionium breakup probability, to be studied in Chapter (6).
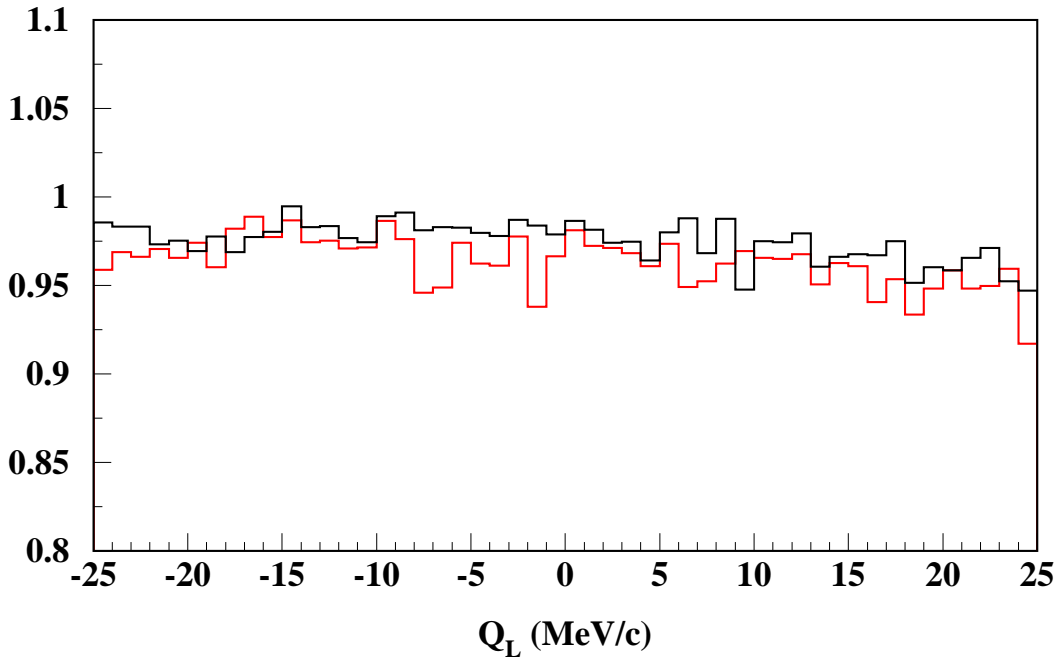
Figure 4.8: *Efficiency of the simulated and experimental triggers, as a function of Q_L. The red histogram corresponds to the experimental trigger efficiency, whereas the black histogram represents the trigger simulation efficiency. See text for further details.*
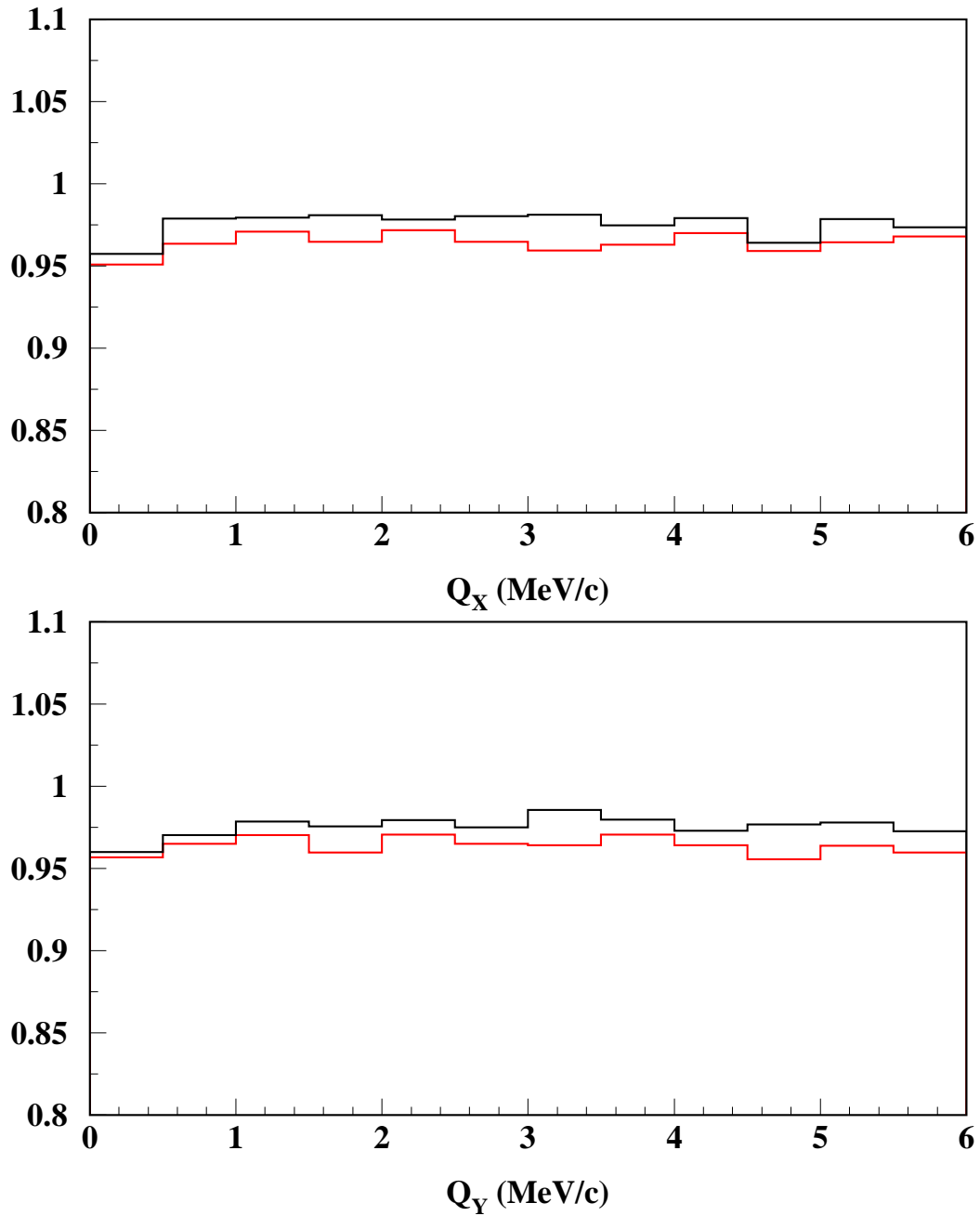
Figure 4.9: *Efficiency of the simulated and experimental triggers, as a function of Q_X and Q_Y. The red histogram corresponds to the experimental trigger efficiency, whereas the black histogram represents the trigger simulation efficiency. See text for further details.*

4.2.4   Momentum Smearing

The best tuning of the Monte Carlo is achieved when its resolution matches the real data, so it is indispensable to construct the Monte Carlo close to that resolution, whose longitudinal (Q_L) and transversal (Q_T) components of Q are mainly governed by the momentum resolution of the spectrometer and the multiple scattering in the target, respectively. Real $\Lambda \to p\pi$ events were analyzed in order to determine the momentum resolution of the DIRAC spectrometer ($\delta p/p$), parametrized with two coefficients, accurately determined using events at low decay angle.

The way to optimize the transversal resolution agreement is of increase or decrease the amount of matter present in the Monte Carlo simulation of each upstream detector. For the longitudinal resolution, the smearing in momentum is the method we have adopted, consisting of the introduction of a tiny (0.066%) Gaussian smearing term convoluted with the simulated momentum resolution function. The longitudinal component of Q is mainly determined by the drift chambers resolution, and in simulation terms, degrading their resolution in the Monte Carlo is utterly equivalent to introduce a tiny momentum smearing in the input momentum distribution.

4.2.4.1   Momentum Resolution with $\Lambda \to p\pi$ Events

The detection of the pionium signal over the background Coulomb pairs requires a satisfactory momentum resolution in the $\pi^+\pi^-$ center-of-mass frame, both in the longitudinal (Q_L) and transverse (Q_T) components. Q_L depends entirely on the magnitude of the pion momenta (p) in the laboratory frame at a very low pair opening angle θ. Resolution in p is essential for atom pair detection.

Meson resonances cannot be easily adopted as a calibration method due to the low Q acceptance of the DIRAC trigger, while lambda triggers happened to be adequate for these purposes. The first two slabs close to the beam direction of the TOF detector of the positive arm have been used to select the protons of the lambda decays, due to its kinematics, as can be appreciated in Fig. (4.10).

Lambda mass M_Λ can be exactly determined from the measured decay π^- (x) and proton (y) momenta and opening angle θ, by means of:

$$M_\Lambda^2 = M_p^2 + M_\pi^2 + 2\sqrt{M_\pi^2 + x^2}\sqrt{M_p^2 + y^2} - 2xy\cos\theta \qquad (4.1)$$

By squaring both sides of this equation a rotated hyperbola can be found, with a physical arm in the positive quadrant of (x, y) plane:
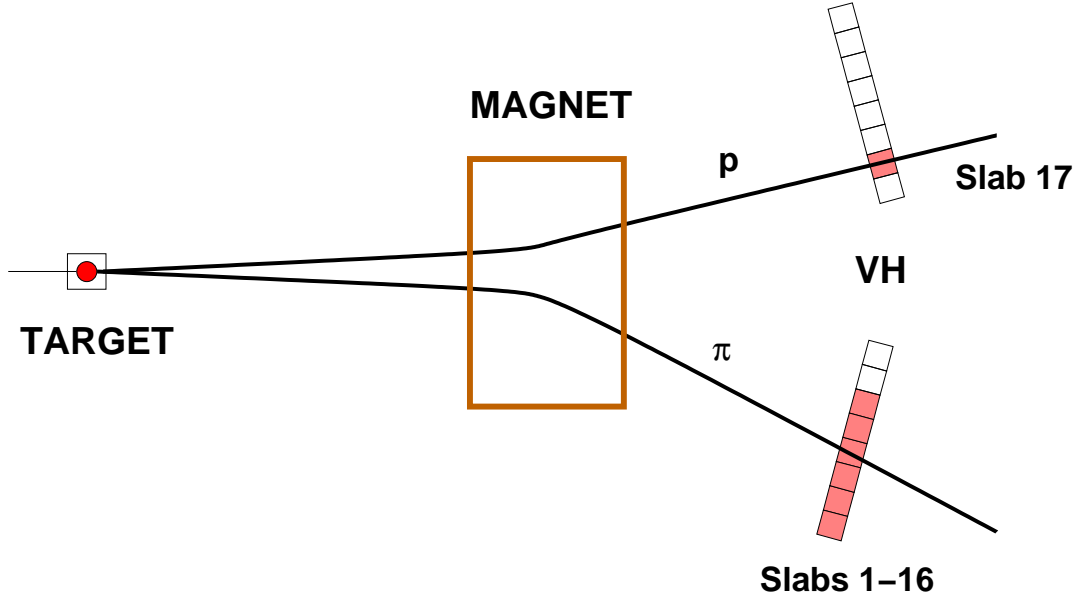
Figure 4.10: *Diagram of the lambda trigger employed in this phase of the ana-lysis. Due to the kinematics of the Λ decay, different slabs of the Vertical Ho-doscopes are used in the positive and negative arms.*

$$M_p^2 x^2 + M_\pi^2 y^2 + x^2 y^2 \sin^2\theta - \Delta^2 xy \cos\theta = K^2 \tag{4.2}$$

where $\Delta^2 = M_\Lambda^2 - M_p^2 - M_\pi^2$ and $K^2 = \left(\Delta^2/2\right)^2 - M_p^2 M_\pi^2$. For each positive value of the π^- momentum x, there are two positive solutions for the proton momentum y.

In the low-angle approximation ($\theta^2/2 \ll 1$), the lambda mass error δM_Λ is given by:

$$M_\Lambda{}^2 (\delta M_\Lambda)^2 = \left(\frac{x}{x_0} - \frac{y}{y_0}\right)^2 \left(y_0^2 (\delta x)^2 + x_0^2 (\delta y)^2\right) \tag{4.3}$$

where $x_0 = \sqrt{M_\pi^2 + x^2}$ and $y_0 = \sqrt{M_p^2 + y^2}$. δx and δy are the π^- and proton momentum errors, respectively. The lowest order finite angle correction to this expression arises from a term $+x^2 y^2 \theta^2 (\delta\theta)^2$. To make sense that (4.3) is exact at the percent level, a suitable upper cut on Q_T (actually a θ cut) must be done on lambda selection.

4.2.4.2   Selection of Lambda Events

The same upstream pattern recognition used for $\pi^+\pi^-$ prompt pair selection was required here to select lambda events. Consequently only tracks pointing to the beam intersection with the target within a 3σ resolution window in the transverse plane (XY) were reconstructed. This employment of the upstream pattern recognition causes a bias in lambda selection, favoring the enhancement of the signal at a short decay path, although we have decided to maintain the same tracking conditions as for $\pi^+\pi^-$, as far as possible. However some supplementary conditions are required for lambda triggers:

- A more restrictive time difference $t_1 - t_2$ between positive and negative tracks in the vertical hodoscope is applied, $0 < t_2 - t_1 < 1.3\ ns$.

- The point of closest approach between the two tracks is assigned to be the decay vertex, being $\mathcal{P}_v$ the probability of track intersection at that specific point. Only events with $\mathcal{P}_v$ larger than 1% are selected.

- A common track probability $\mathcal{P}_t$ is also defined as the sum of the two separated $\chi^2_{1,2}$ tracks, $\chi^2 = \chi_1^2 + \chi_2^2$. $\mathcal{P}_t$ is required to be larger than 1%.

The lambda invariant mass is then calculated according to expression (4.1), minding the error introduced in the vertex displacement, the parallax error in θ. Fig. (4.11) shows a scatter plot of individual track momenta (π^- and proton) versus the invariant mass reconstructed in the momentum range covered by our analysis. The mass projection of this scatter plot can be admired in Fig. (4.12), together with the average mass resolution extracted, resulting to be 0.338 $\pm$ 0.001 MeV/c^2.

Fig. (4.13) presents the selected lambda events in the (Q_L, Q_T) plane. As expected, they lay on a circular coronna whose width is determined by the mass resolution. To guarantee that the latter is only determined by the Q_L resolution, the exploitation of a cut $Q_T < 20\ MeV$ is sufficient, and in consequence the relation (4.3) is fulfilled.

4.2.4.3   Maximum Likelihood

We consider that the momentum error δp (for both pion and proton tracks) arises from the quadrature of two components, according to the expression:

$$(\delta p)^2 = (Ap)^2 + (Bp^2)^2 \tag{4.4}$$
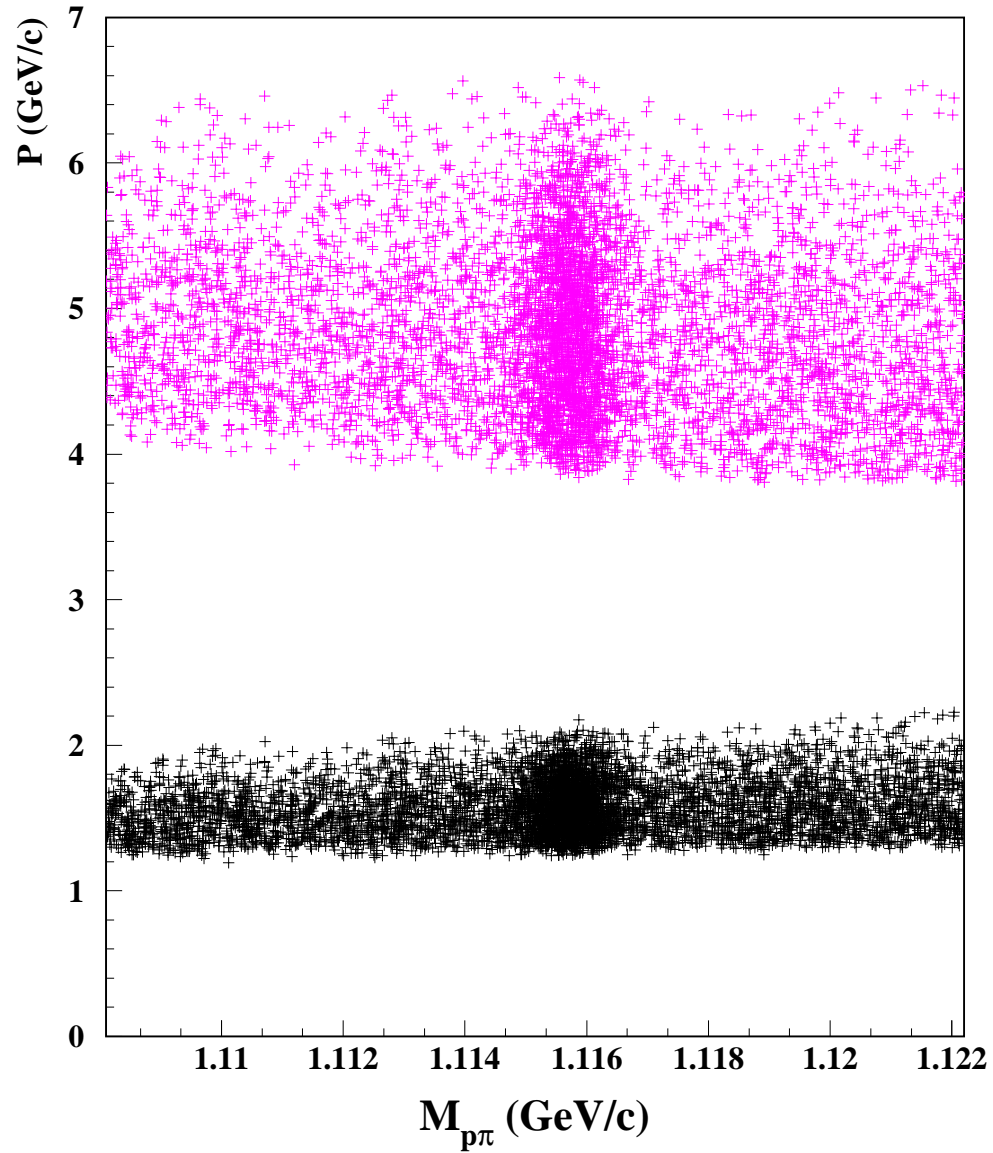
Figure 4.11: *Scatter plot representing the measured invariant mass (under $p\pi^-$ hypothesis) versus positive (pink colour) and negative (black) track momenta, for lambda triggers. A clear momentum gap can be appreciated, due to lambda decay kinematics and vertical hodoscope time cuts.*
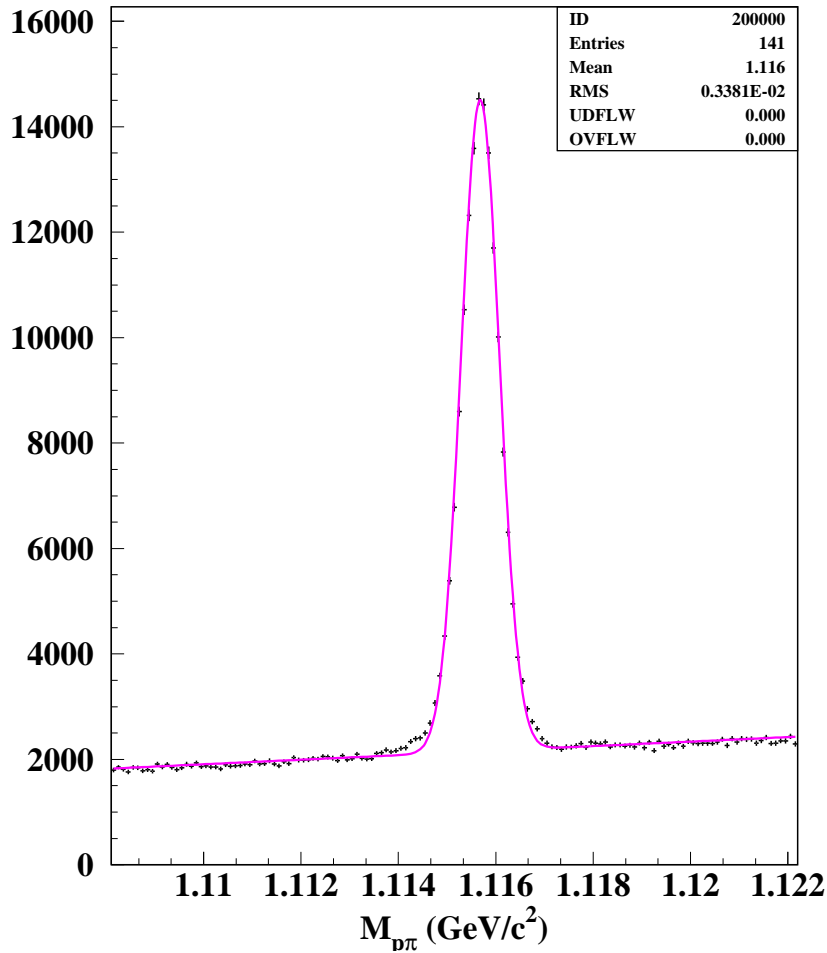
Figure 4.12: *Invariant mass spectrum obtained from the projection of the scatter plot in figure 4.11. A Gaussian fit with linear background is also shown for reference, with $\sigma = 0.338\ MeV/c^2$, and $M_{p\pi} = 1.1156\ GeV/c^2$.*

This momentum dependence arises from the assumption that multiple scattering error scales as $1/p$, whereas intrinsic detector resolutions are assumed to be momentum independent. The first term, proportional to p, depends on intrinsic tracking detector resolutions at both sides of the dipole (DC's, GEM/MSGC and SFD). The second term, proportional to p^2 receives contribution from the average material thickness of detector elements upstream and downstream the magnet.

As a consequence of the kinematics of lambda decays, the negative pion acquires a lower momentum than the average $\pi^+\pi^-$ prompt tracks in DIRAC physics triggers, whereas the proton momentum is higher than this average,
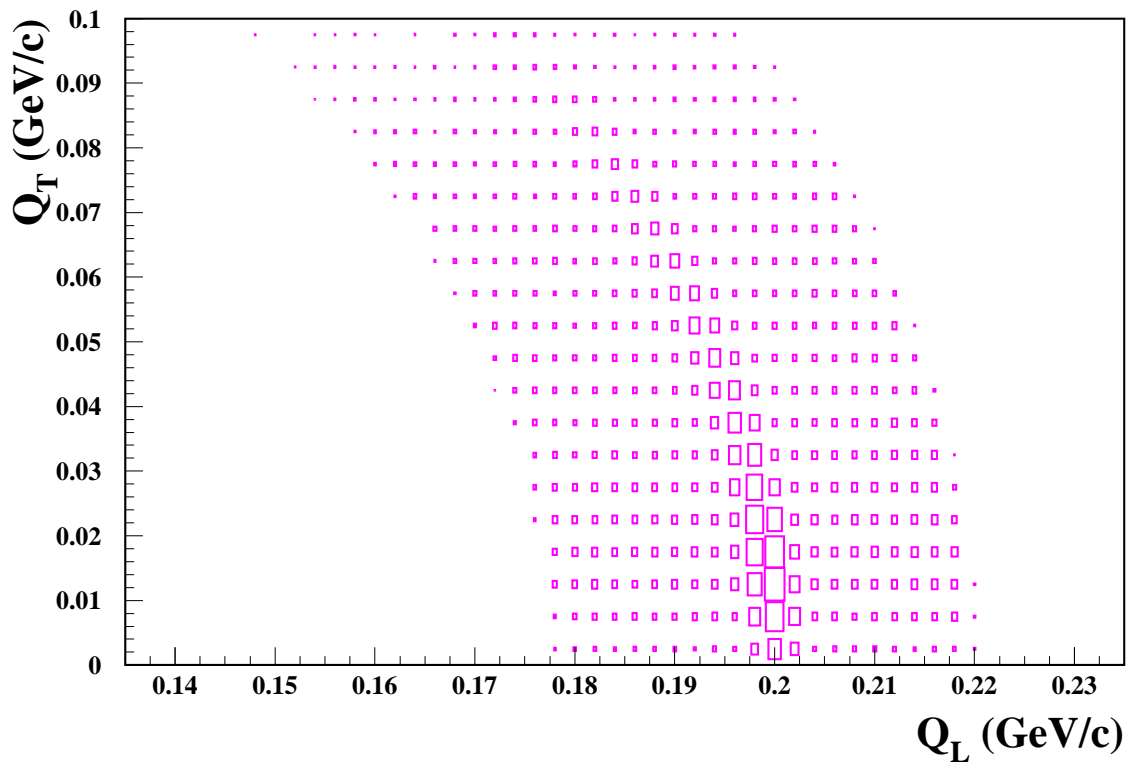
Figure 4.13: *Longitudinal (Q_L) versus transverse (Q_T) momentum in the lambda center-of-mass frame, with respect to its direction of flight. Lorentz transformation is done under $p\pi^-$ hypothesis. A mass cut $1114.0 < M_{p\pi}$ $(MeV/c^2) < 1116.5$ has been applied.*

as it can be appreciated in Fig. (4.11). This is almost the ideal situation[2] to perform a momentum analysis of the spectrometer resolution, specially if we use low angle pairs, with a topology as close as possible to that of the Coulomb $\pi^+\pi^-$ pairs.

The maximum likelihood method fits the expression (4.3) from a sample of lambda triggers which not only contains the signal but also introduces a non-resonant background, caused by the trigger noise.

---

[2]The pion and proton momentum is well separated but accordingly there is a region where the resolution cannot be directly measured, and it needs to be extrapolated.

Under the $p\pi^-$ hypothesis we define a two-dimensional likelihood function for a given event i, defined as a function of lambda mass M_i and the total momentum of the pair in the lab frame p_i, as follows:

$$\mathcal{L}_i = \alpha \frac{\mathcal{P}_N(p_i)}{S_N} \frac{G(M_i)}{S_G} + (1 - \alpha) \frac{\mathcal{P}_N(p_i)}{S_N} \frac{\mathcal{P}_B(p_i, M_i)}{S_B} \qquad (4.5)$$

where $\mathcal{P}_N(p) = 1 + a_1 p + a_2 p^2 + \dots$ is an nth order polynomial in p and $G(M)$ is a Gaussian function that describes the resonance:

$$G(M_i) = \exp\left(-\frac{(M_i - M_\Lambda)^2}{2(\delta M_i(A, B))^2}\right) \qquad (4.6)$$

where the error $\delta M_i(A, B)$ is given by the expression (4.3) evaluated at π^- (x_i) and proton (y_i) momenta of event i. The momentum uncertainty δp is given by (4.4) as a function of momentum, with identical A and B parameters for both particle types. The polynomial $\mathcal{P}_B(p, M)$ defines the background as a linear mass expression: $\mathcal{P}_B(p, M) = 1 + b_1 M + b_2 p$. The corresponding normalization integrals S_N, S_G and S_B must be calculated for each parameter choice, so that the likelihood function is normalized to unity in the domain $(p_1, p_2) \times (M_1, M_2)$, where $p_{1,2}$ are the lower and upper total momentum cuts (similarly $M_{1,2}$ for the invariant mass).

The maximum likelihood parameters are found minimizing the function:

$$-\ln \mathcal{L} = -\sum_{i=1}^{N} \ln \mathcal{L}_i(A, B, M_\Lambda, \alpha, a_k, b_l) \qquad (4.7)$$

where N represents the number of lambda triggers that enters the fit, and $\mathcal{L}_i$ is the likelihood function evaluated for event i described by the measured values x_i, y_i, M_i and p_i.

The overall likelihood $\mathcal{L}$ for N lambda events significantly increases when each measured proton momentum y_i is replaced in expression (4.3) for δM_i, by one of the hyperbolic solutions of equation (4.2), corresponding to the measured π^- momentum x_i. This is equivalent to take advantage of the lambda mass constraint in momentum scaling of δp (4.4), together with the fact that π^- momentum has always the smallest error.

A straightforward procedure is to determine first the a_k and b_l coefficients of the polynomials, by performing a fit to the background only. Once these parameters are fixed, M_Λ, α, A and B can be left free in the final fit. All minimizations were performed with the MINUIT program [105].

Table (4.1) summarizes the fit values obtained after minimizing the expression (4.7). Fig. (4.14) represents the graphical version of the formula (4.4), where the function $\delta p/p$ was constructed from the A, B values provided by the fit. These A and B values were obtained for real data, and two versions of the Monte Carlo were utilized to vrify the results, with and without smearing in momentum. For illustration we only show the 2001 Lambda data, accompanied with the 2001 94 μm 24 GeV/c Monte Carlo. The agreement is pretty good after the application of the momentum smearing.

Table 4.1: *Parameters obtained for the maximum likelihood fit to the experimental lambda sample of 2001, as defined in the text. Quoted errors correspond to variation of 0.5 units of the likelihood function.*

A	$(0.2728 \pm 0.0027) \times 10^{-2}$
B	$0.215^{+0.024}_{-0.023} \times 10^{-3}\ GeV^{-1}$
M_Λ	$1115.6 \pm 0.0001\ MeV/c^2$
α	0.529 ± 0.005
b_1	12.8 ± 1.9
b_2	-0.047 ± 0.009

a_1	-66.014 ± 0.048
a_2	36.205 ± 0.007
a_3	-7.3399 ± 0.0009
a_4	0.65470 ± 0.00002
a_5	-0.02176 ± 0.00001

Figure 4.14: *Relative momentum error $\delta p/p$ as function of track momentum. The red continuous line represents the parametrisation $\sqrt{A^2 + B^2 p^2}$ fitted to experimental lambda data. The yellow band represents $\pm 1\sigma$ variation of the parameters. Black dots indicate resolution of standard $\pi^+\pi^-$ Monte Carlo (only 2001 94 μm 24 GeV/c is shown here). Blue dots correspond to a Monte Carlo simulation with the introduction of a Gaussian smearing in momentum of 0.66×10^{-3} $[(GeV/c)^{-1}]$.*

4.2.4.4 Two Gaussian Method

The procedure to determine the suitable momentum smearing required for the Monte Carlo starts from the measurement of the lambda mass resolution for real data. The higher the accuracy in the determination of this lambda mass resolution, the better the measurement of the pionium breakup probability that can be achieved. In order to precisely determine the Lambda mass resolution, a two-Gaussian analysis method was performed, motivated by the asymmetry of the lambda mass distribution plotted in Fig. (4.12).

The left slope of the invariant mass is steeper than the right, because lambda events exhibit a finite decay path (around 8 cm) due to their lifetime, five orders of magnitude larger than pionium, which can only fly some few mm before breakup. This produces a bias in the pattern recognition, which underestimates the lambda decay angle by granting the target as their decay vertex. Although the real decay position is calculated in the lambda analysis, the bias in the pattern recognition is still present, yielding an asymmetric tail.

After reconstructing the lambda invariant mass from the expression (4.12) we define a F function to determine the resolution in the lambda mass, as follows:

$$F = \text{Pol} + G_1 + G_2 \tag{4.8}$$

being:

$$\text{Pol} = A_1 + A_2 x \tag{4.9}$$

$$G_1 = \frac{A_3}{\sqrt{2\pi}A_5} \exp\left(-\frac{1}{2}\frac{(x - A_4)^2}{A_5{}^2}\right) \tag{4.10}$$

$$G_2 = \frac{A_3 A_6}{\sqrt{2\pi}A_5 A_8} \exp\left(-\frac{1}{2}\frac{(x - A_4 - A_7)^2}{A_5{}^2 A_8{}^2}\right) \tag{4.11}$$

Pol is a linear polynomial which describes the background of the squared mass distribution. G_1 is a Gaussian function whose parameters A_3, A_4 and A_5 will determine the area embraced, the mean value and the width of the squared lambda mass or, in other words, its lambda mass value and resolution, whereas G_2 is introduced to account for the left slope of the squared mass distribution.

The G_2 parameters represent the ratio between the areas of the two Gaussian functions, the shift in the lambda mean value (with respect to the main Gaussian) and the ratio between both resolutions.

Once we have determined the parameters A_6, A_7 and A_8 for real data, we impose them to the Monte Carlo. We have used an iterative method to determine the suitable quantity of momentum smearing in the Monte Carlo, since its application has to be done at the n-tuple level, after introducing a very small correction in the momentum value, replacing the older momentum by the newer, as follows:

$$P \rightarrow P \left(1\ +\ 0.00066 \left[(GeV/c)^{-1}\right] P\right) \tag{4.12}$$

This can be done with relative simplicity and it is achieved when the lambda resolution is the same in the Monte Carlo and in the real data.

In Fig. (4.15) we can observe the Lambda mass distribution fitted with the two-Gaussians method, according to Eq. (4.8). The real lambda triggers were initially fitted to that 8-parameter fucntion, where A_5, A_6 and A_7 were enforced to the Monte Carlo without smearing in momentum (Fig. (4.15)) and to the Monte Carlo with a Gaussian smearing in momentum of 0.66×10^{-3} $[(GeV/c)^{-1}]$, the suitable option for this analysis (Fig. (4.16)). One should notice the optimal agreement in the lambda mass resolution obtained for this amount of momentum smearing and real data.

Note that the scale in Fig. (4.12) runs from 1.1081 to 1.1222 GeV/c^2 whereas in Figs. (4.15) and (4.16) runs from 81 to 222 GeV/c^2. This rescaling was done to obtain a better fit resolution in the lambda mass, since in the former case the fit produces a 1.1156 ± 0.0001 GeV/c^2 lambda mass, while in the second case, the lambda mass fit brings out a value 1115.689 ± 0.011 MeV/c^2, both obtained for Monte Carlo. This can be compared to the 1115.683 ± 0.006 MeV/c^2 value of the bibliography, showing the excellent agreement between them.

In summary, we have performed a lambda mass likelihood fit which produced a lambda mass value 1.1156 ± 0.0001 GeV/c^2 and a lambda mass resolution 0.338 ± 0.001 MeV/c^2. We also have accomplished a two-Gaussian χ^2 fit producing a lambda mass 1115.689 ± 0.011 MeV/c^2, with a resolution 0.324 ± 0.001 MeV/c^2. We have decided to adopt this latter method to determine the momentum smearing introduced in the Monte Carlo simulation, since it produces the best Monte Carlo description of the lambda mass distribution. In addition, it produces the best match of the lambda mass to the bibliography values.

χ^2/ndf	146.7 / 133
P1	281.0
P2	1.060
P3	0.1544E+05
P4	157.7
P5	3.244
P6	1.000
P7	-0.2046
P8	1.640

Real data witdh
0.324 MeV/c^2

$M_{p\pi}$ (0.1 MeV/c^2)

χ^2/ndf	176.6 / 133
P1	1470.
P2	4.222
P3	0.6128E+05
P4	156.9
P5	3.137
P6	1.000
P7	-0.2046
P8	1.640

Monte Carlo width
0.314 MeV/c^2

$M_{p\pi}$ (0.1 MeV/c^2)
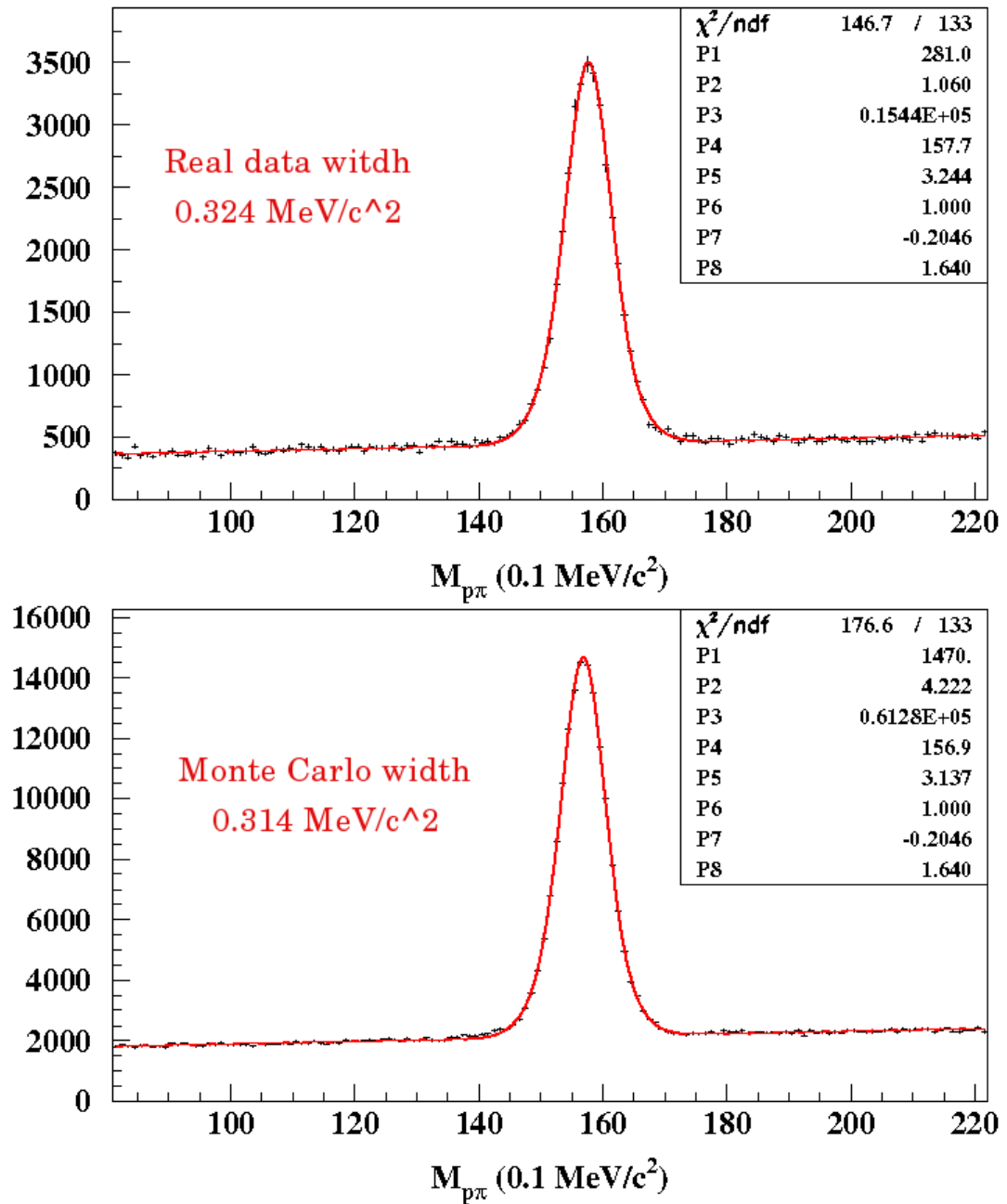
Figure 4.15: *Lambda mass distribution fitted following Eq. (4.8), where two Gaussian were used to determine the Lambda mass resolution. The upper figure corresponds to real data whereas the lower figure is the Monte Carlo without momentum smearing. Note the larger value of the Lambda mass resolution, parameter A_5, for real lambda triggers.*
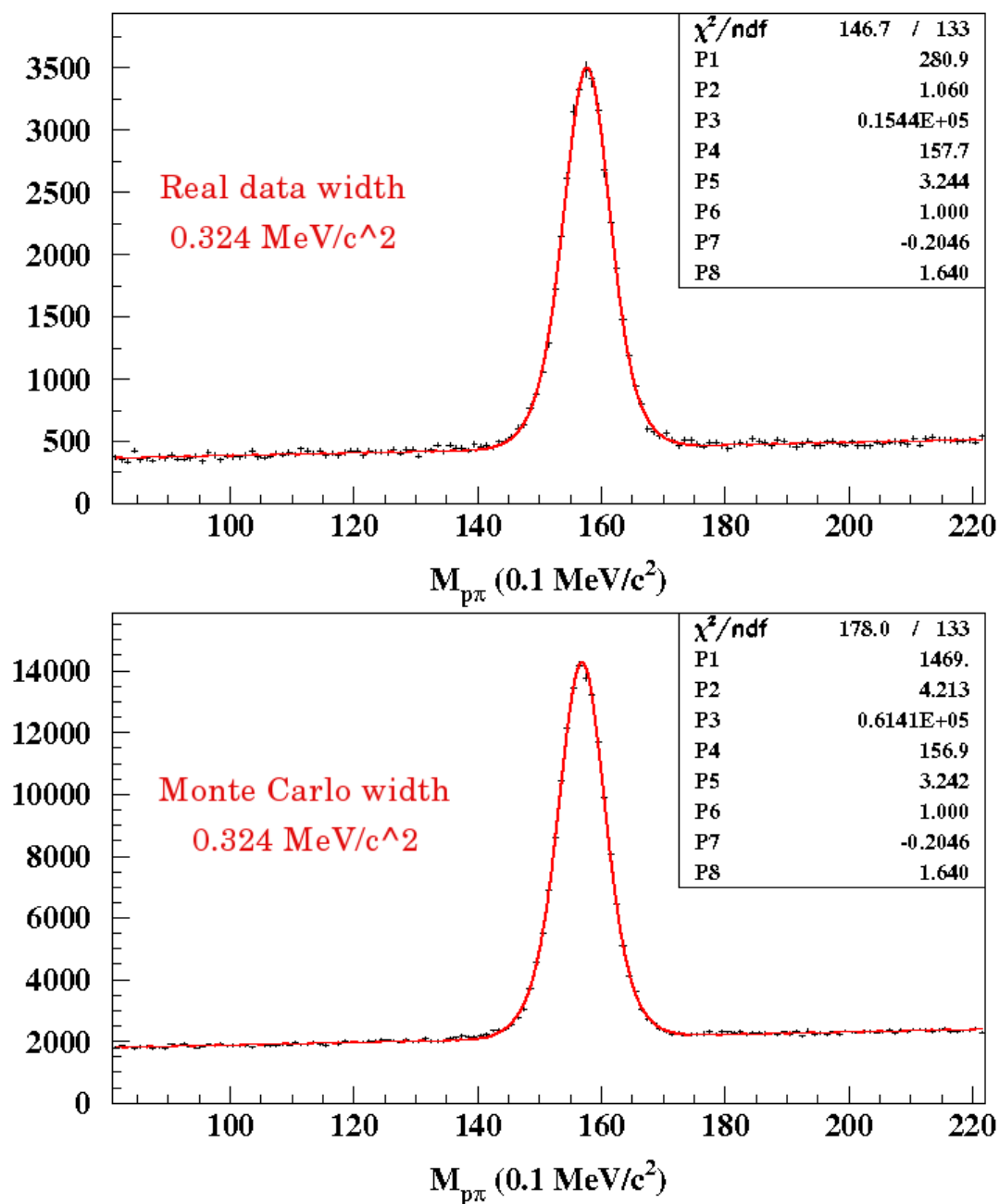
Figure 4.16: *Lambda mass distribution fitted following Eq. (4.8), where two Gaussian were used to determine the Lambda mass resolution. The upper figure corresponds to real data whereas the lower figure is the Monte Carlo with the suitable momentum smearing employed in this analysis. Please note that the same Lambda mass resolution is accomplished with this momentum smearing, corresponding to a convoluted 0.66×10^{-3} [(GeV/c)$^{-1}$] Gaussian smearing in the simulated momentum resolution distribution.*

4.3 Summary

In this Chapter we have discussed the improvements carried out in the frame of the alignment and tracking of the spectrometer, together with the Monte Carlo optimization. The Monte Carlo tuning has permitted us to get a better description of the former, including two very important enhancements, such as the momentum smearing and the simulation of the trigger, that were never been introduced before the present work.

The improvement of the analysis discussed in this Chapter allows us to obtain an optimal description of the experiment, providing the appropriate tools to perform an accurate breakup probability determination of the pionium, to be described in the following Chapter.

Chapter 5

Pionium Lifetime

5.1   Fit Method and Breakup Probabilities

The real data collected by the DIRAC spectrometer during 2001, 2002 and 2003 were splitted in five different sets, according to the different Nickel target thicknesses (94 and 98 μm) and to the proton beam intensities (20 and 24 GeV/c). Three separate Monte Carlo samples were employed to describe these five data sets, as summarized in Table (5.1).

Year	Target thickness	Beam Energy	Real Data	Monte Carlo
2001	94 μm	24 GeV/c	2001 94 μm	94 μm 24 GeV/c
2001	98 μm	24 GeV/c	2001 98 μm	98 μm 24 GeV/c
2002	98 μm	20 GeV/c	2002 20 GeV/c	98 μm 20 GeV/c
2002	98 μm	24 GeV/c	2002 24 GeV/c	98 μm 24 GeV/c
2003	98 μm	20 GeV/c	2003 20 GeV/c	98 μm 20 GeV/c

Table 5.1: *Different real data and Monte Carlo sets utilized in the pionium lifetime determination, justified by the two target thicknesses and beam energies installed in the experiment.*

We have split the $\pi^+\pi^-$ pair momentum in seven regular slices of 600 MeV/c from 2.6 to 6.8 GeV/c, which ensures for each bin that the non-linear contribution in the linear approximation of the breakup probability is negligible. The breakup probability is extracted from 35 independent fits corresponding to the seven slices of momentum and the five data sets, by minimizing the expression (3.1), which runs over a two dimensional grid of $|Q_L| < 15\ MeV/c$ and $|Q_T| < 5\ MeV/c$, with bin centers located at values (Q_T^i, Q_L^j) and uniform bin size $\Delta Q_T = \Delta Q_L = 0.5\ MeV/c$.

The only two free parameters in Eq. (3.1) are the number of detected atomic pairs (n_A^{rec}) and the fraction between non-Coulomb and Coulomb pairs $(N_{NC}^{rec}/N_{CC}^{rec})$. The total number of reconstructed pairs produces a constraint such that $N_{pr}(1 - \omega_{acc}) = N_{CC}^{rec} + N_{NC}^{rec} + n_{AA}^{rec}$, where ω_{acc} represents the fraction of accidental pairs present in the prompt sample.

Once the fit has converged, the atom signal is defined in each (i, j) bin as the difference between the prompt spectrum and the Monte Carlo with the pionium (AA) component removed (CC+NC). This two dimensional signal shows the excess with respect to the calculated Coulomb interaction enhancement background at very low Q_L and Q_T, which is the pionium spectrum.

$Q_T^{cut}(MeV/c)$	K^{theo}	ϵ_A	ϵ_C	K^{exp}
0.5	3.2181	0.0194	0.0669	0.9305 ± 0.0064
1.0	1.2380	0.0521	0.0916	0.7046 ± 0.0024
1.5	0.6996	0.0787	0.1029	0.5349 ± 0.0013
2.0	0.4673	0.0951	0.1098	0.4050 ± 0.0008
2.5	0.3426	0.1045	0.1142	0.3135 ± 0.0005
3.0	0.2660	0.1096	0.1167	0.2497 ± 0.0004
3.5	0.2147	0.1125	0.1182	0.2043 ± 0.0003
4.0	0.1781	0.1143	0.1191	0.1709 ± 0.0002
4.5	0.1509	0.1154	0.1195	0.1458 ± 0.0002
5.0	0.1299	0.1161	0.1191	0.1267 ± 0.0002
$Q_L^{cut}(MeV/c)$	K^{theo}	ϵ_A	ϵ_C	K^{exp}
0.5	0.4336	0.0742	0.1145	0.2811 ± 0.0006
1.0	0.2387	0.1041	0.1171	0.2123 ± 0.0003
1.5	0.1669	0.1132	0.1184	0.1596 ± 0.0002
2.0	0.1299	0.1161	0.1191	0.1267 ± 0.0002

Table 5.2: *Numerical values of K^{theo} and K^{exp} as defined in reference [106], obtained for our improved Monte Carlo simulation. Each row corresponds to a given rectangular cut in (Q_T, Q_L) plane, with $Q_T^{cut} = 5$ MeV/c and $Q_L^{cut} = 2$ MeV/c being the reference cut values. For simplicity, only values corresponding to the first momentum bin ($2.6 \leq p \leq 3.2$ GeV/c) of the 2001 94 µm data sample are shown. Atomic and Coulomb efficiences, ϵ_A and ϵ_C, defined in Eq. (3.9) are also shown for illustration.*

The breakup probability of the pionium P_{br} is then determined by means of the K-factors defined in (Eq. (3.7), (3.8) and (3.9)). Experimental K-factors were calculated for each of the five different sets of real data defined earlier, and are required in the P_{br} measurement.

Table (5.2) shows these calculated experimental K-factors involved in the breakup probability measurement. For the sake of simplicity, only K-factors corresponding to the first momentun bin of the analysis $(2.6 \le p \le 3.2 \text{ GeV/c})$ for the data sample 2001 94 μm are shown. The remaining thirty four tables are also employed to accomplish the total 35 momentum-dependent fits of the pionium breakup probability. The fit results are summarized in Tables 5.3, 5.4, 5.5, 5.6 and 5.7.

p (GeV/c)	P_{br}	Atom pairs	Coulomb pairs	χ^2/ndf
$2.6 - 3.2$	0.4546 ± 0.0455	1039 ± 90	17427 ± 378	$258/298$
$3.2 - 3.8$	0.4087 ± 0.0352	1369 ± 105	26200 ± 438	$285/298$
$3.8 - 4.4$	0.4350 ± 0.0399	1193 ± 97	21896 ± 402	$308/298$
$4.4 - 5.0$	0.4946 ± 0.0463	1036 ± 85	16913 ± 348	$266/298$
$5.0 - 5.6$	0.4439 ± 0.0554	666 ± 73	12256 ± 301	$281/298$
$5.6 - 6.2$	0.4507 ± 0.0662	463 ± 60	8443 ± 252	$404/298$
$6.2 - 6.8$	0.4087 ± 0.0841	254 ± 47	5106 ± 207	$325/298$

Table 5.3: *Breakup probabilities, number of atomic and Coulomb pairs and χ^2 of the fit calculated for seven momentum bins from 2.6 to 6.8 GeV/c for the 2001 94 μm sample.*

p (GeV/c)	P_{br}	Atom pairs	Coulomb pairs	χ^2/ndf
$2.6 - 3.2$	0.4239 ± 0.0753	382 ± 59	6990 ± 253	$294/298$
$3.2 - 3.8$	0.4857 ± 0.0629	622 ± 70	10088 ± 287	$345/298$
$3.8 - 4.4$	0.4762 ± 0.0682	510 ± 64	8514 ± 264	$273/298$
$4.4 - 5.0$	0.4762 ± 0.0747	405 ± 56	6912 ± 237	$327/298$
$5.0 - 5.6$	0.5132 ± 0.0896	307 ± 47	4894 ± 183	$293/298$
$5.6 - 6.2$	0.6043 ± 0.1234	232 ± 41	3213 ± 156	$325/297$
$6.2 - 6.8$	0.5432 ± 0.1628	108 ± 29	1656 ± 106	$300/290$

Table 5.4: *Breakup probabilities, number of atomic and Coulomb pairs and χ^2 of the fit calculated for seven momentum bins from 2.6 to 6.8 GeV/c for the 2001 98 μm sample.*

p (GeV/c)	P_{br}	Atom pairs	Coulomb pairs	χ^2/ndf
$2.6 - 3.2$	0.4257 ± 0.0587	561 ± 68	10185 ± 292	$302/298$
$3.2 - 3.8$	0.4615 ± 0.0490	887 ± 82	15220 ± 346	$301/298$
$3.8 - 4.4$	0.4914 ± 0.0538	799 ± 76	13077 ± 320	$316/298$
$4.4 - 5.0$	0.5289 ± 0.0654	613 ± 65	9376 ± 274	$286/298$
$5.0 - 5.6$	0.4710 ± 0.0733	394 ± 53	6927 ± 238	$345/298$
$5.6 - 6.2$	0.4901 ± 0.0895	285 ± 46	4836 ± 184	$324/298$
$6.2 - 6.8$	0.5578 ± 0.1394	163 ± 35	2400 ± 145	$302/297$

Table 5.5: *Breakup probabilities, number of atomic and Coulomb pairs and χ^2 of the fit calculated for seven momentum bins from 2.6 to 6.8 GeV/c for the 2002 20 GeV/c sample.*

p (GeV/c)	P_{br}	Atom pairs	Coulomb pairs	χ^2/ndf
$2.6 - 3.2$	0.4355 ± 0.0435	1100 ± 96	19395 ± 410	$281/298$
$3.2 - 3.8$	0.4216 ± 0.0352	1560 ± 115	29184 ± 488	$297/298$
$3.8 - 4.4$	0.3910 ± 0.0369	1243 ± 105	25470 ± 441	$292/298$
$4.4 - 5.0$	0.4751 ± 0.0444	1112 ± 92	19087 ± 374	$298/298$
$5.0 - 5.6$	0.4481 ± 0.0524	759 ± 78	13916 ± 332	$302/298$
$5.6 - 6.2$	0.5215 ± 0.0677	589 ± 66	9382 ± 280	$328/298$
$6.2 - 6.8$	0.6464 ± 0.1014	392 ± 51	5008 ± 222	$333/298$

Table 5.6: *Breakup probabilities, number of atomic and Coulomb pairs and χ^2 of the fit calculated for seven momentum bins from 2.6 to 6.8 GeV/c for the 2002 24 GeV/c sample.*

p (GeV/c)	P_{br}	Atom pairs	Coulomb pairs	χ^2/ndf
$2.6 - 3.2$	0.2489 ± 0.0655	211 ± 51	6514 ± 228	$323/298$
$3.2 - 3.8$	0.5155 ± 0.0678	566 ± 64	8679 ± 266	$339/298$
$3.8 - 4.4$	0.5890 ± 0.0764	529 ± 58	7189 ± 235	$294/298$
$4.4 - 5.0$	0.4839 ± 0.0809	338 ± 50	5696 ± 206	$291/298$
$5.0 - 5.6$	0.4636 ± 0.0939	237 ± 43	4225 ± 172	$271/297$
$5.6 - 6.2$	0.6477 ± 0.1351	198 ± 35	2544 ± 145	$308/295$
$6.2 - 6.8$	0.5594 ± 0.1553	105 ± 26	1562 ± 91	$255/289$

Table 5.7: *Breakup probabilities, number of atomic and Coulomb pairs and χ^2 of the fit calculated for seven momentum bins from 2.6 to 6.8 GeV/c for the 2003 20 GeV/c sample.*

5.2 Lifetime Calculation

The pionium lifetime calculation was performed using the 35-independent P_{br} values obtained above for the momentum-dependent analysis, together with the Monte Carlo predictions on the $P_{br}(p, \tau)$ functions.

A maximum likelihood fit was done where both statistical and systematical errors were taken into account in the maximization procedure. Up to now we only have dealt with the statistical error implicated in the pionium lifetime determination. In Chapter (6) the systematic errors involved in the pionium breakup probability calculation will be studied in detail. The likelihood maximization produces our final measurement of the pionium ground state lifetime:

$$\tau = \left(3.15^{+0.20}_{-0.19}\Big|_{\text{stat}}\right) \times 10^{-15} \ s. \tag{5.1}$$

Fig. (5.1) shows the maximun likelihood fit performed to determine the pionium lifetime, in which a combination of real data sets and Monte Carlo was utilized through the 35 independent breakup probability measurements mentioned in the previous section.
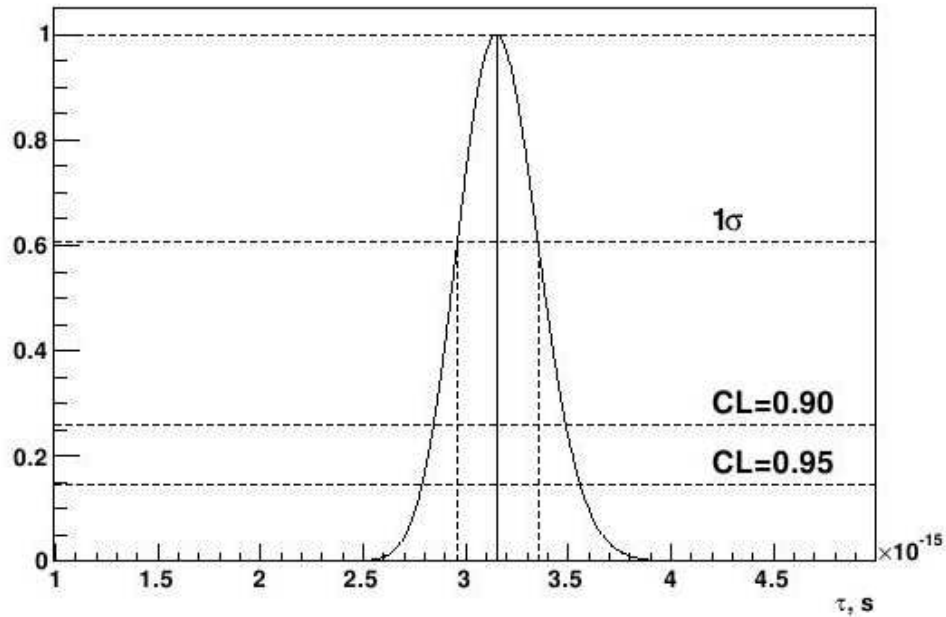
Figure 5.1: *Maximum likelihood fit carried out in the final pionium lifetime determination. The maximization of the likelihood produces a lifetime* $\tau = \left(3.15^{+0.20}_{-0.19}\Big|_{\text{stat}}\right) \times 10^{-15} \ s.$

A χ^2 test was done to cross-check the results. The DIPGEN generator was used to perform a full scanning in the lifetime, from 1.0 to 7.2 fs, using these functions as an input to the χ^2 analysis. For every hypothesis of lifetime, a χ^2 test to the 35 independent breakup probabilities was done. Fig. (5.2) illustrates the χ^2 values calculated for every lifetime hypothesis used in this analysis. A simple algorithm was used to find out the mininum χ^2 value, corresponding to the best fit of the pionium lifetime, resulting to be 25.85. To obtain the error committed, we performed one unit variation in the minimum χ^2 value, looking for the two lifetime hypotheses which satisfy $\chi^2 = 25.85 \pm 1$. This χ^2 test yields a lifetime value in perfect agreement with the one produced by the maximum likelihood fit:

$$\tau = (3.15 \pm 0.20|_{\text{stat}}) \times 10^{-15} \; s \qquad \text{with} \qquad \chi^2/\text{ndf} = 25.85/34. \qquad (5.2)$$
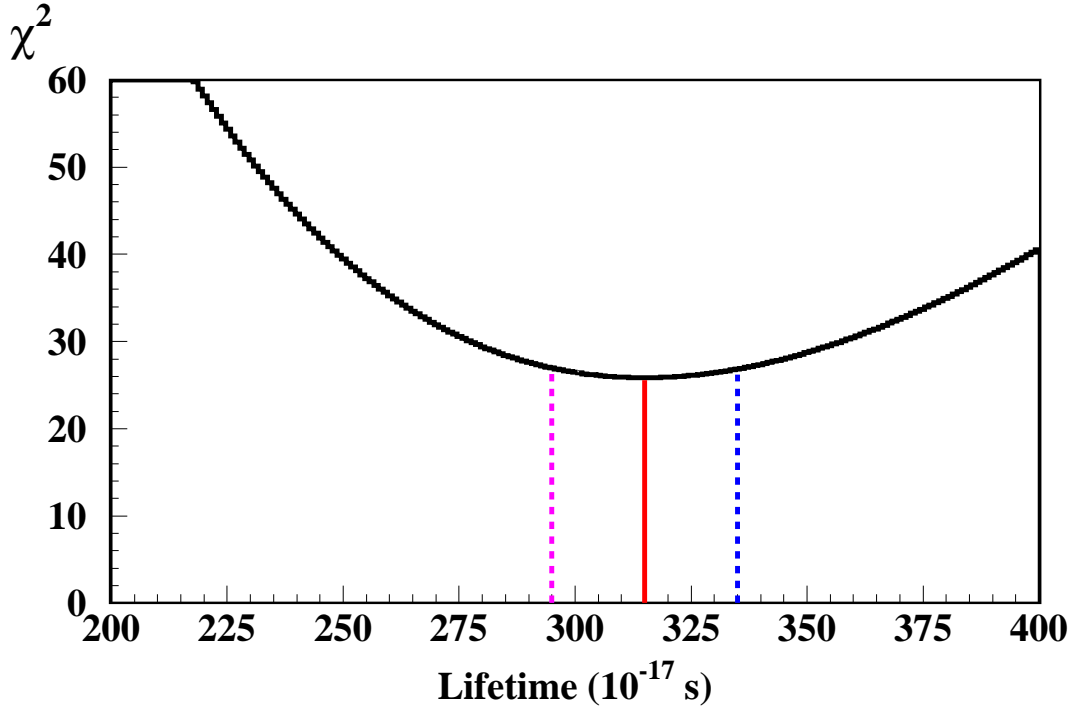
Figure 5.2: χ^2 *test imposed to the 35 independent breakup probabilities involved in the pionium lifetime determination. The curve shows the χ^2 values calculated for the input lifetime hypothesis described in the text. Red line represents the lowest χ^2 value (25.85/34.), whereas the dotted lines represent a ± 1 unit variation in the χ^2, to calculate the left (pink line) and right (blue line) error. The χ^2 test produces a lifetime value $\tau = 3.15 \pm 0.20 \; fs.*$

5.3 Graphical Fit Results

The 35 atomic spectra produced by the 35 independent fits described above were integrated in a common picture collection, only for visual purposes.

Figs. (5.3) and (5.4) show the Q_T and $|Q_L|$ projections of the experimental reconstructed prompt $\pi^+\pi^-$ spectrum, in comparison with the simulated Monte Carlo. The pionium signal emerges at small values of Q_T and $|Q_L|$ after subtraction of the Coulomb, non-Coulomb and accidental pairs, and can be directly compared with the atomic component of the Monte Carlo. The multiple scattering in the target affects the Q_T final shape, broadening the distribution.
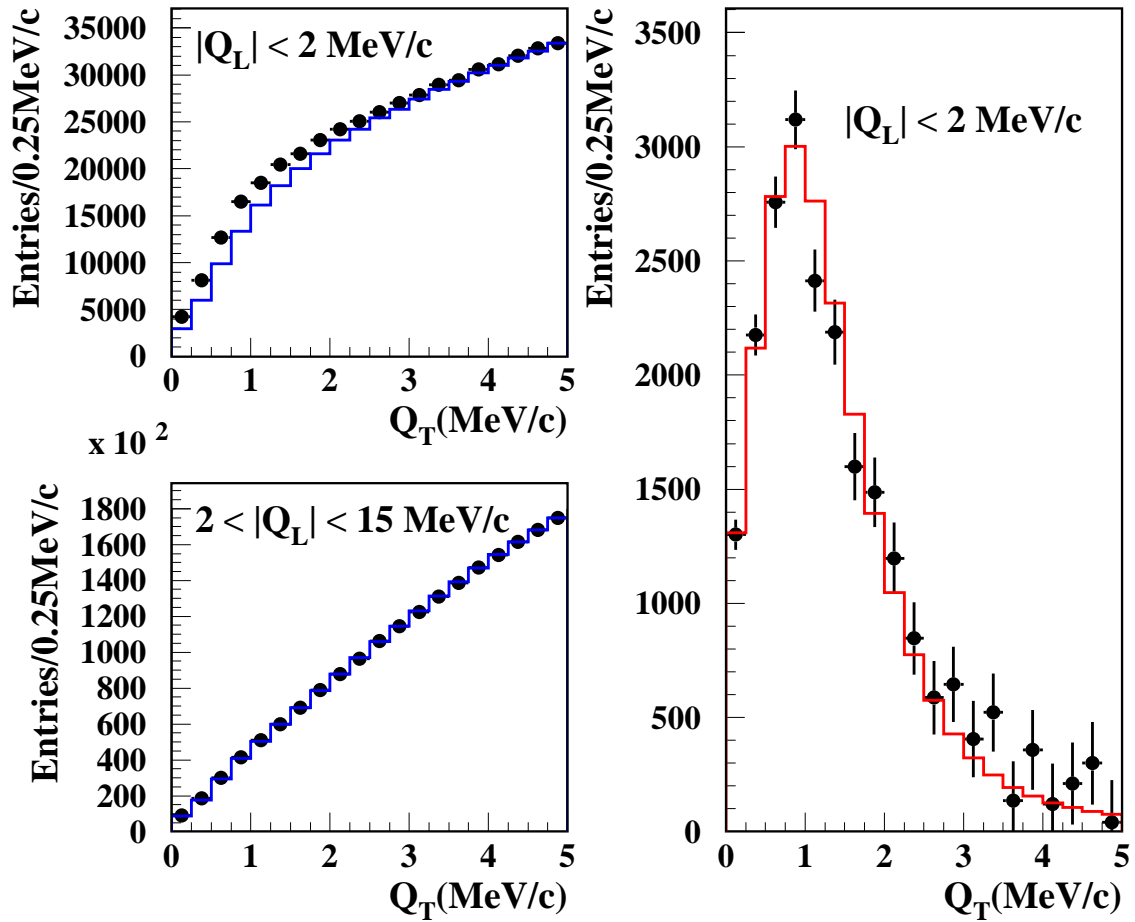
Figure 5.3: *Two-dimensional pionium signal projection onto Q_T. The data are shown separately for $Q_L < 2MeV/c$ (left top) and $Q_L > 2MeV/c$ (left bottom). The difference between prompt data (dots) and Monte Carlo (blue line), which corresponds to transverse pionium signal, is plotted (right) and compared with the pionium atom Monte Carlo (red line).*
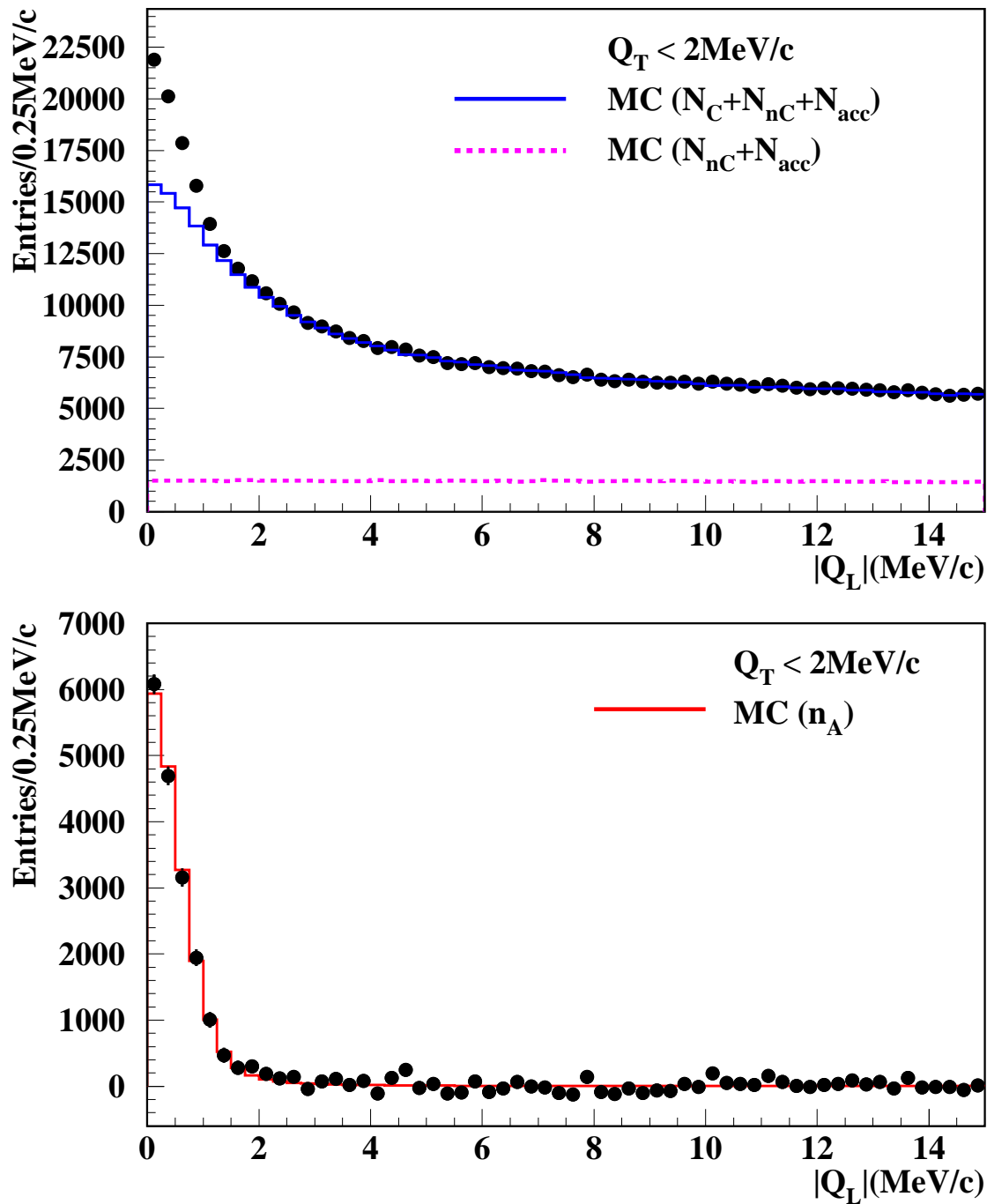
Figure 5.4: *Two-dimensional pionium signal projection onto $|Q_L|$. A more restrictive $Q_T < 2$ MeV/c cut with respect to the standard $Q_T < 4$ MeV/c has been applied to enhance the signal. The difference between prompt data (dots) and Monte Carlo (blue line), which corresponds to pionium signal, is plotted at the bottom, where the signal is compared with the pionium atom Monte Carlo (red line).*

Fig. (5.5) illustrates the two-dimensional Coulomb subtracted $\pi^+\pi^-$ correlation function in the $(Q_T, Q_L = |Q_Z|)$ plane, clearly showing the pionium signal.
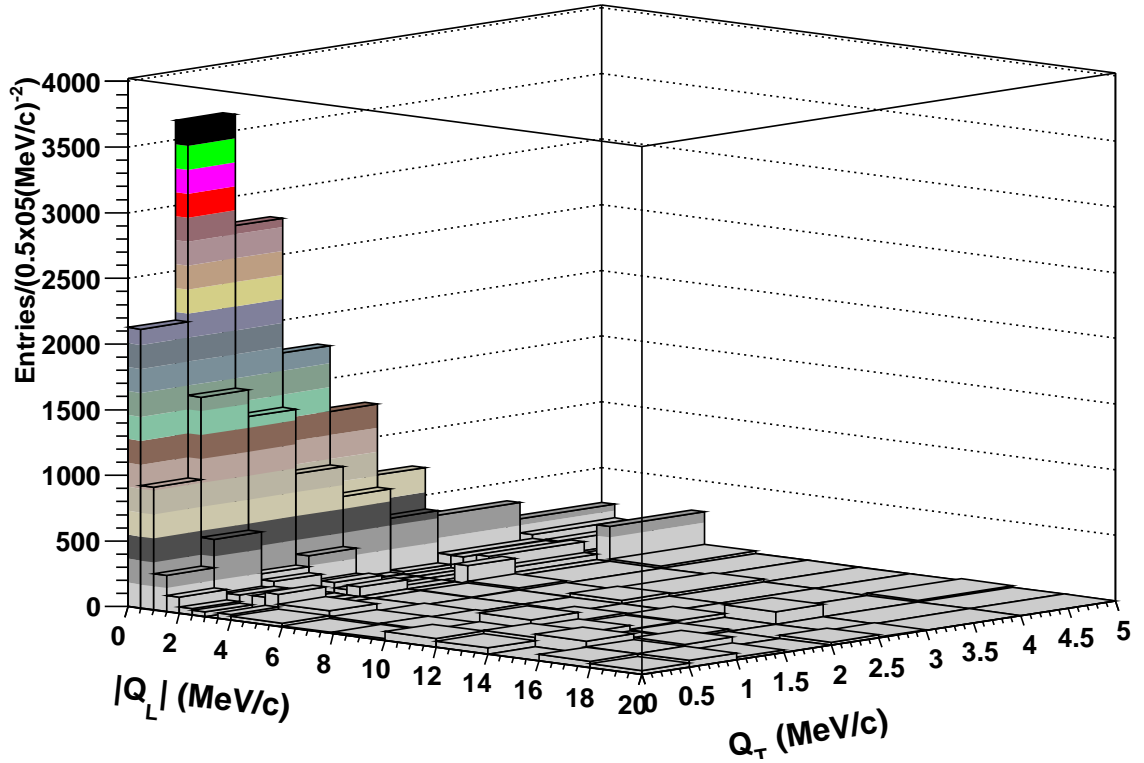
Figure 5.5: *Lego plot showing the pionium breakup spectrum in Ni in the $(Q_T, |Q_L| = |Q_Z|)$ plane, after subtraction of Coulomb, non-Coulomb and accidental background.*

Fig. (5.6) illustrates the two-dimensional Coulomb subtracted $\pi^+\pi^-$ correlation function in the $(Q_\perp, Q_L)$ plane, clearly showing the pionium signal. $Q_\perp$ is the signed projection of $\vec{Q}$ into a generic transverse axis; the azimuthal invariance is ensured here by the absence of polarization of the beam or the target. As it can be seen, the overall agreement between the experimental fit and the simulated spectra is excellent, over the entire (Q_L, Q_T) domain.
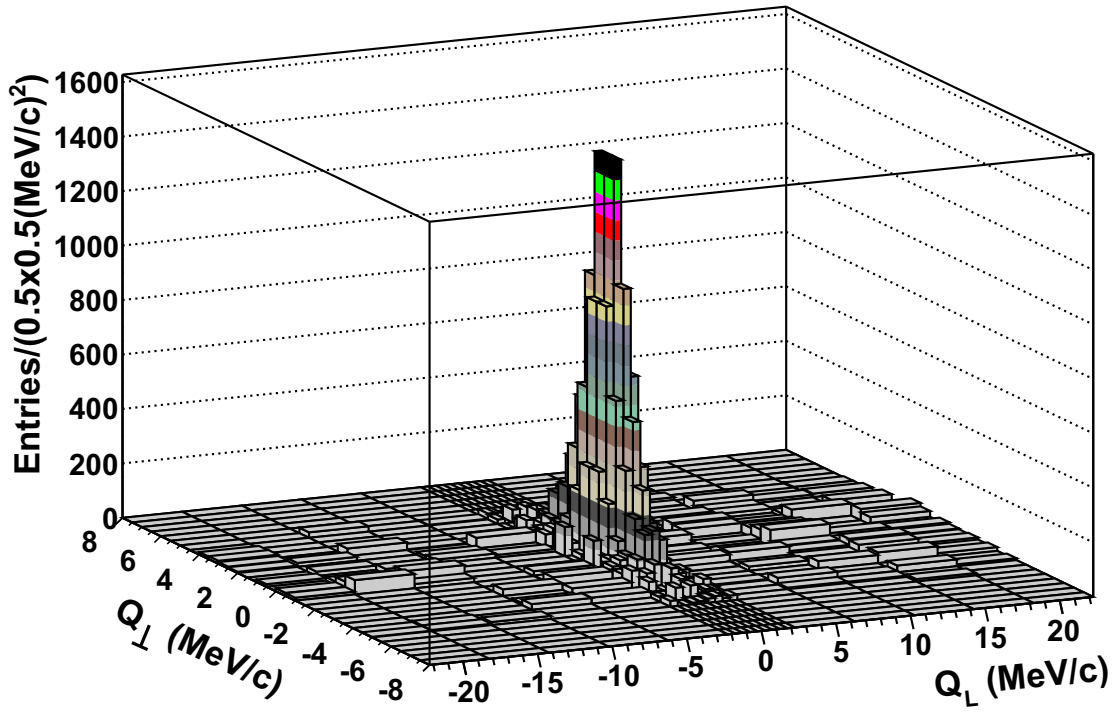
Figure 5.6:   *Lego plot showing the pionium breakup spectrum in Ni in the $(Q_\perp, Q_L)$ plane, after subtraction of Coulomb background. The transverse component, $Q_\perp = Q_T \cos\phi$, is defined as the product of the measured Q_T value times the cosine of a random azimuth. The azimuthal invariance is ensured by the absence of beam and target polarization.*

A slight increase of the measured breakup probability with increasing pionium momentum is observed in Fig. (5.7) (data points), which is a consequence of the longer decay path, and hence the greater breakup yield, expected at higher atom momenta. The continuous curve represents the predicted evolution of the breakup probability with pionium laboratory momentum, for the value of the pionium ground-state lifetime $\tau = 3.15 \times 10^{-15}$ s obtained from this analysis. This curve was constructed using the DIRAC pion pair generator [98] where the average target thickness was utilized, calculated by means of the expression:

$$\text{thick}_{\text{ave}} = 0.281 \times 93.8 \ \mu\text{m} + 0.719 \times 97.6 \ \mu\text{m} \tag{5.3}$$

where 0.281 and 0.719 are the fraction of data collected by the spectrometer corresponding to 94 (93.8) μm and 98 (97.6) μm, respectively.
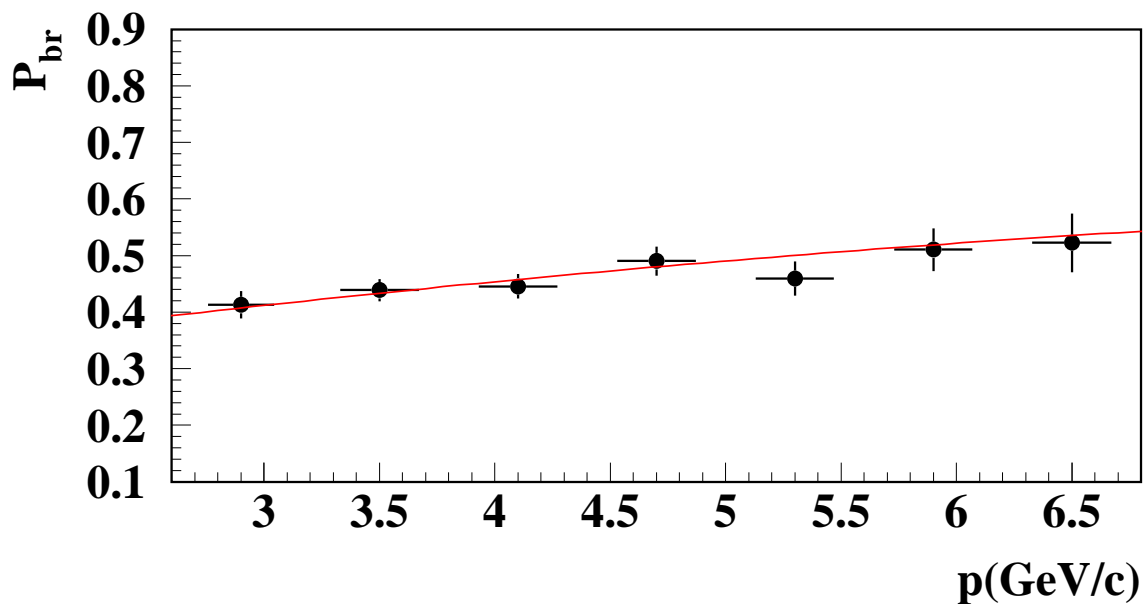
Figure 5.7: *The dependence of the measured breakup probability, averaged over all data sets, from the pionium laboratory momentum and the Monte Carlo prediction corresponding to the ground-state lifetime of $3.15 \times 10^{-15}s$ obtained from the best fit.*

The dependence of the pionium breakup probability on the specific choice of the integration domain $(Q_L, Q_T) \leq (Q_L^{cut}, Q_T^{cut})$ has been verified. The measured breakup probability, averaged over the data sets, is indeed very stable versus variations of the $|Q_L|$, Q_T integration limits as shown in Fig. (5.8).
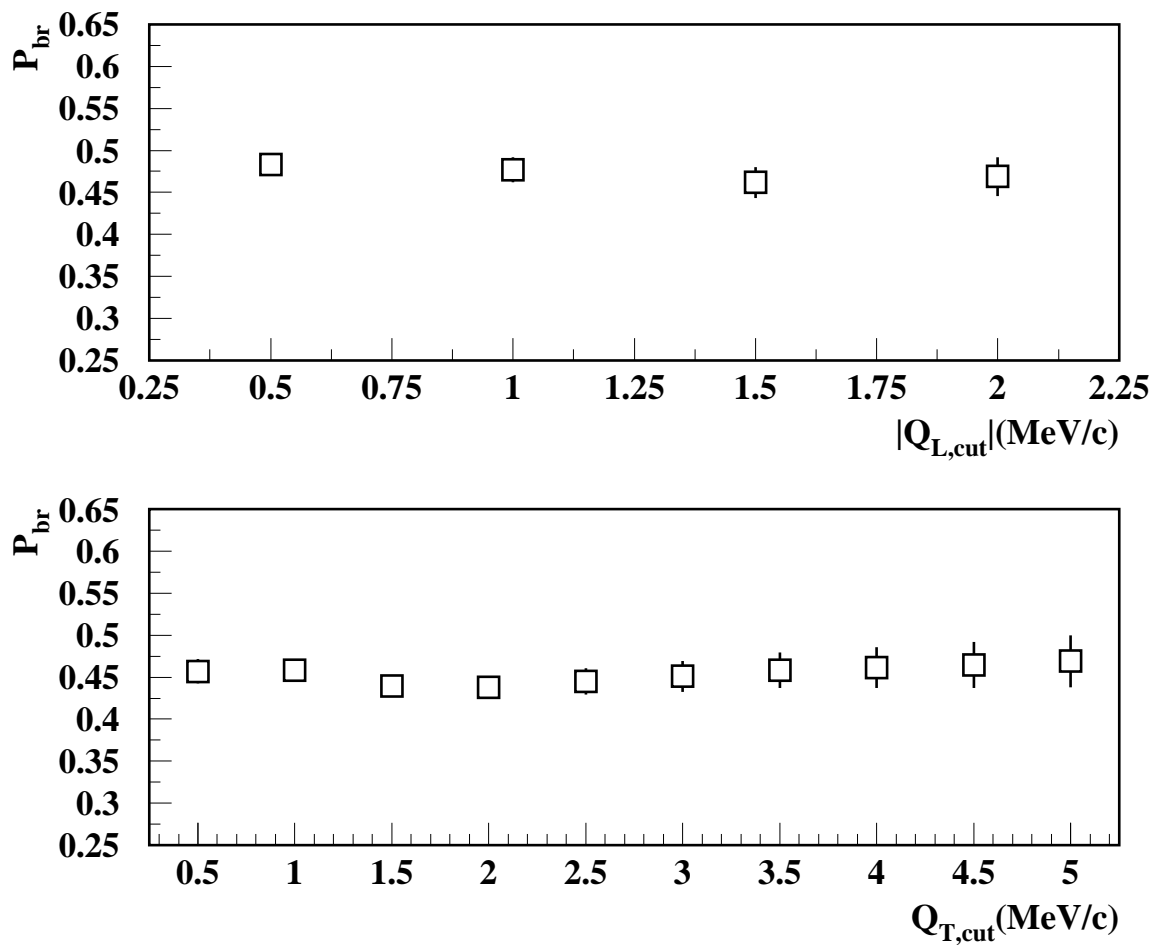
Figure 5.8: *Stability of the average breakup probability with respect to the $|Q_L|$ and Q_T upper limits of integration. Top: $|Q_L|$ upper cuts for $Q_T < 5$ MeV/c and bottom: Q_T upper cuts for $|Q_L| < 2$ MeV/c.*

5.4 Summary

The data collected by the DIRAC experiment were split into five different data sets, and the pionium breakup probability was calculated for each of them, using a momentum-dependent analysis. The breakup probability was shown to be stable under different choices of the upper limit in the integration region of the (Q_T, Q_L) spectrum.

The pionium lifetime calculation was undertaken utilizing a maximum likelihood fit, performed over 35-independent breakup probabilities, producing $\tau = (3.15^{+0.20}_{-0.19}) \times 10^{-15}$ s. A χ^2-analysis was also performed as a cross-check, resulting in $\tau = (3.15 \pm 0.20) \times 10^{-15}$ s.

The integrated sample of atomic pairs shows a perfect agreement with the longitudinal and transverse projections of Q predicted by the simulation, illustrating the soundness of the method to determine the pionium lifetime.

Chapter 6

Systematic Errors

This chapter will provide a complete description of the systematic errors involved in the breakup probability and in the pionium lifetime determination. The most important are the multiple scattering in the target, the relation between the breakup probability and the pionium lifetime and the momentum smearing. Some other important systematic errors are related to the Monte Carlo simulation, such as double track resolution or K^+K^- admixture. Finally, some systematic errors which were expected to be larger, happened to be quite small, such as the background hits in the upstream detectors or the trigger simulation.

As a general procedure, the systematic error assigned to the breakup probability of the pionium is computed as the difference in the breakup with and without the error or correction under study, then divided by $\sqrt{12}$, corresponding to a uniform distribution.

6.1   Multiple Scattering in the Target

The Q_T resolution is governed by the multiple scattering in the target, with additional minor contributions from multiple scattering in the upstream detectors. Since this is the largest source of systematic uncertainty, we have performed a equivalent measurement of the multiple scattering in a 100×25 mm^2 layer, with exactly the same composition to the Ni target, by placing it between the third and fourth modules of the DC detector, in the right arm of the spectrometer.

The procedure is to measure the multiple scatering angle in terms of the projected angle θ, just before and after the sample plane used in the analysis. The track before the plane is defined by DC-1 and DC-3 modules, whereas the

track reconstructed after the sample plane is defined by the intersection point of the first track and the DC-4 module. The first distribution corresponds to the intrinsic resolution of the DC detector, and the second has, in addition, the contribution from the multiple scattering in the sample plane. After a deconvolution method, the multiple scattering distribution can be extacted, as shows Fig. (6.1).
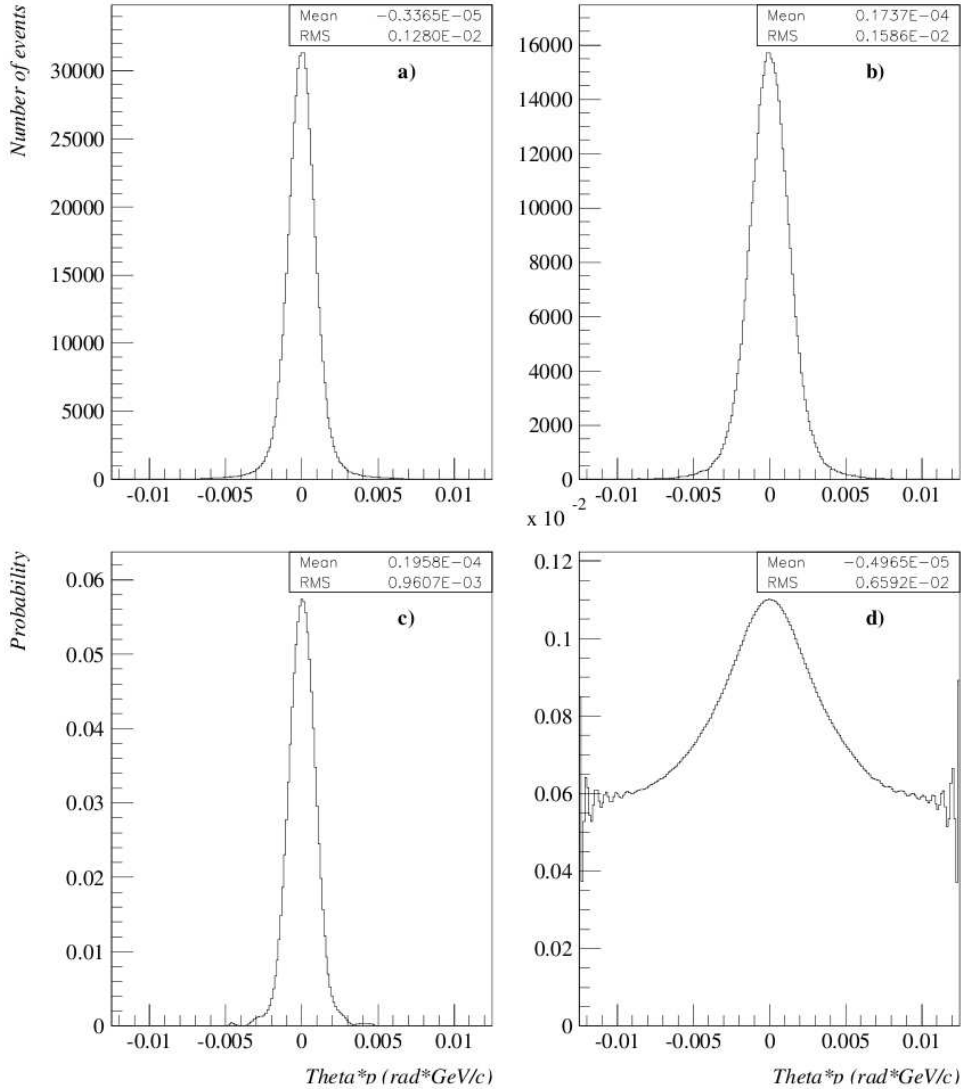
Figure 6.1: *Reconstructed tracks before and after the sample Ni plane introduced between DC-3 and DC-4 modules. The drift chamber resolution (a) can be deconvoluted from the distribution of particles which cross the Ni sample (b), thus extracting the multiple scattering (c) in the Ni sample, and its reconstruction distribution error (d).*

In a later stage, the experimental multiple scattering distribution in the Ni sample is fitted to a 3-Gaussian function [107], extracting the effective radiation length $X_0^* = 1.421$ cm, to be compared to the nominal standard value $X_0 = 1.42336$ cm. This 1% of discrepancy in the effective radiation length is assigned as the maximun uncertainty in the multiple scattering in the target. It should be noticed that this 1% uncertainty is an upper limit because not all pionium pairs traverse the whole target thickness.

The multiple scattering in the target is responsible of a ± 0.0077 deviation in the pionium breakup probability, being the largest source of systematic error in the pionium breakup probability calculation.

6.2 Trigger Simulation

The simulation of the trigger response together with the momentum smearing are the main features of the improved analysis presented here, which represent, at the Monte Carlo level, the main distintion from the previous works [91, 92]. They have played a conclusive role in the breakup probability determination, and in the subsequent lifetime measurement. The trigger simulation was extensively discussed in section (4.2.3).

A comprehensive simulation of the DIRAC trigger system was done. For the T1 runs collected in 2002, we have created an n-tuple collection with tags of experimental and simulated triggers, whose efficiency dependence on Q_L and Q_T is very similar. For the experimental trigger events, the efficiency of the simulated trigger was $\sim 98\%$, while for the simulated one, the fraction of positive decisions of experimental trigger is $\sim 97\%$.

The pionium breakup probability was calculated with and without the simulation of the trigger, obtaining a shift in the P_{br} of -0.016. The estimation of the systematic error due to the trigger simulation was accomplished through the relation $S = \pm| - 0.016| \times 0.03 = \pm 0.0005$, where 0.03 is the innacuracy of the simulated trigger. We expected that the simulation of the trigger could introduce one of the dominant systematic errors in the pionium lifetime determination, but finally it resulted to be the second smallest uncertainty.

6.3   Double Track Resolution

Double ionization criteria in the IH is required when the upstream tracking does not distinguish two separated tracks (in one projection, X or Y) due to the intrinsic detectors double track resolution or one of the tracks lost by inefficiency. If one single unresolved track that points to two DC tracks is found, a double ionization signal in the IH detector is required. A track is showing double ionization when the two intersected IH slabs presents a calibrated pulse above a determined threshold (140 counts) for the two projections (X and Y).
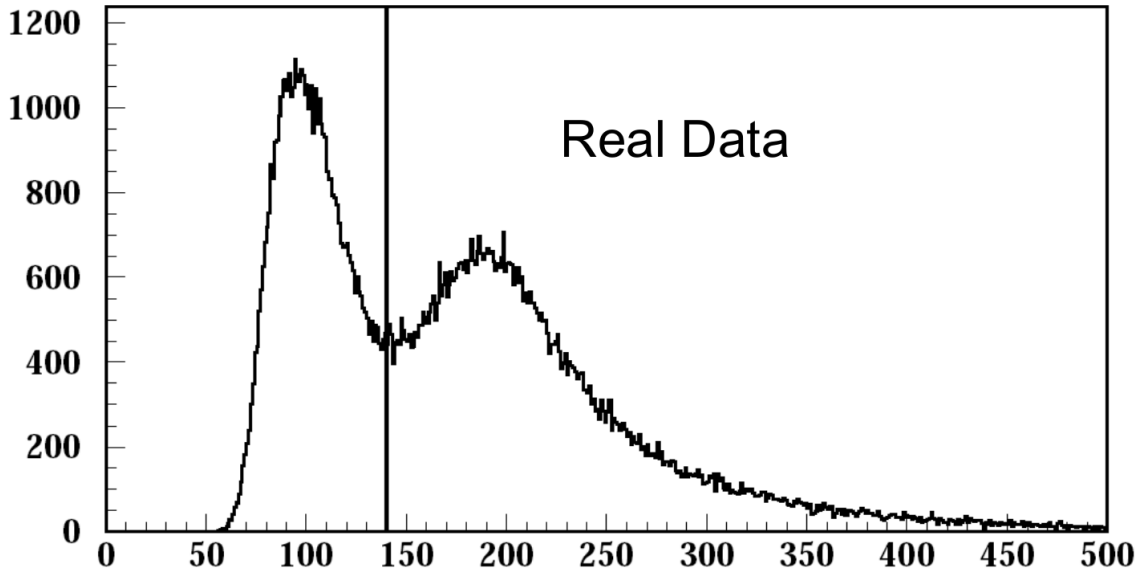
Figure 6.2: *Double ionization cut applied for real data. Single and double tracks are clearly separated by the cut.*

Fig. (6.2) shows the double ionization cut applied in real data. This cut separates the single and double ionization events detected by the Ionization Hodoscope. This cut is selected in order to remove the maximum number of single ionization events without loseing double ionization tracks. Attending to the collapse criteria described in section (4.2.1), when a track is collapsed in the X projection, a double cut is applied simultaneously in the IH-X_A and IH-X_B detectors, which only allows less than a 3% of single ionization signal contamination. The procedure is analogous for the Y projection.
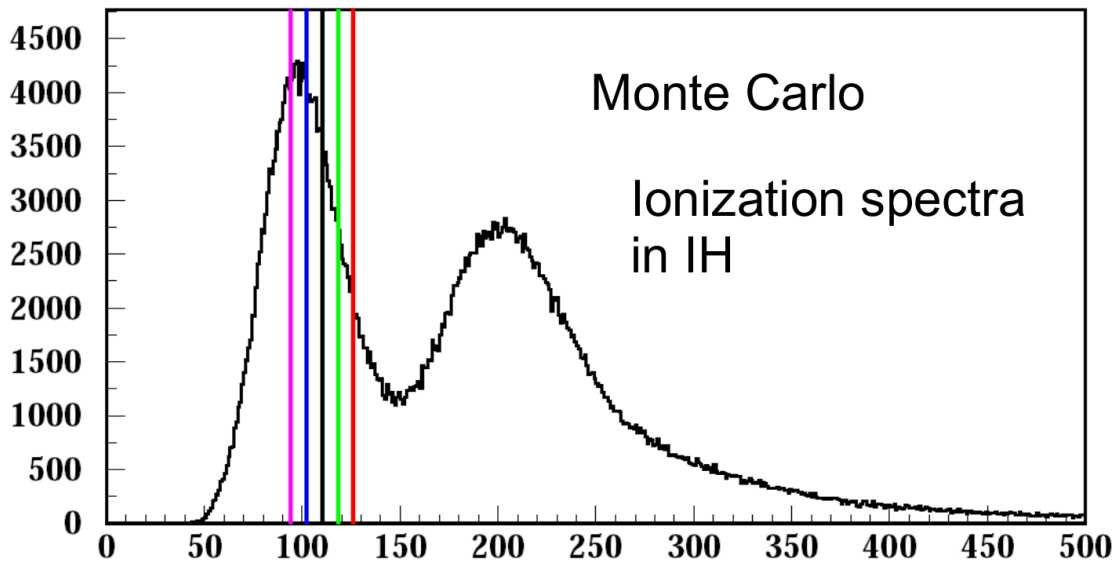
Figure 6.3: *Different double ionization cuts applied for Monte Carlo. Colors are in correspondence to the distinct P_{br} vs. Q_T^{cut} distributions plotted in Fig. (6.4); the black line corresponds to the double ionization cut applied for real data. Note the necessity to choose a Monte Carlo double ionization cut different from the one applied to the real data.*

At this point, the ratio between collapsed and non-collapsed tracks is calculated. If this double ionization cut is enforced directly to the Monte Carlo, the ratio between collapsed and non-collapsed tracks is not the same as for real data, so the Monte Carlo double ionization cut needs to be shifted to satisfy this collapse criterion, as can be observed in Fig. (6.3).

Several cuts were inspected for the Monte Carlo, and for all those tests the breakup probability of the pionium was calculated as a function of the Q_T cut applied, as shown in Fig. (6.4). It should be noticed that regardless of the different trends, all the curves essentially coincide at $Q_T = 5\ MeV/c$, where the breakup probability is calculated.
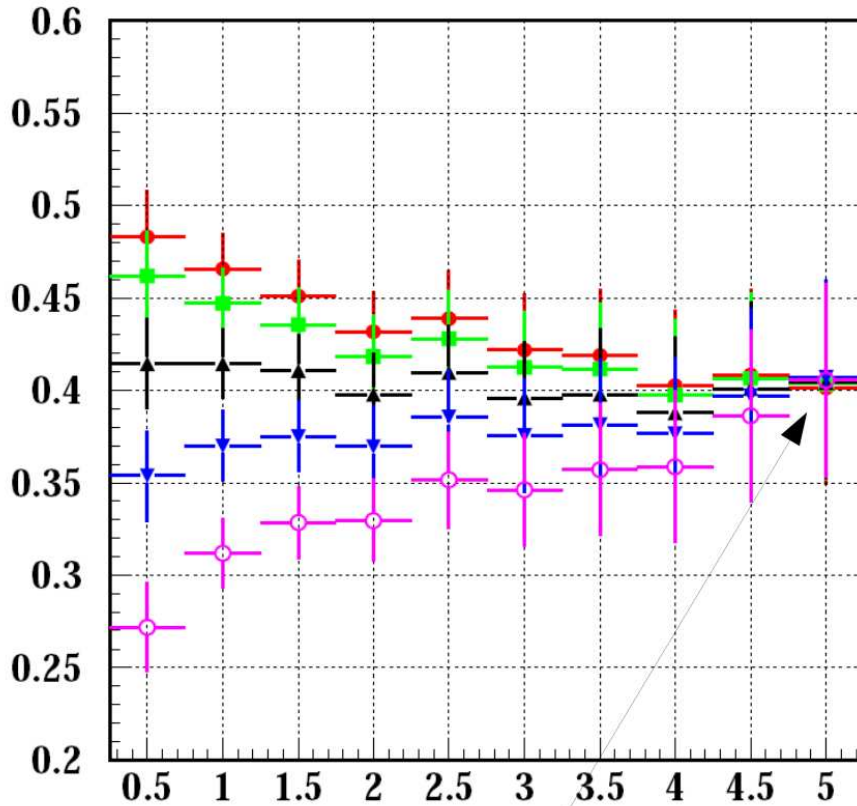
Figure 6.4: *Breakup probability versus Q_T^{cut} for different double ionization cuts applied in the Monte Carlo. Note that despite the different trends of the distributions, the only important matter is the breakup probability calculating point, $Q_T = 5\ MeV/c$.*

After performing the breakup probability calculation for the several choices of the double ionization cut shown in Fig. (6.4), it was decided to assign the systematic error associated in the following way. In the Monte Carlo, five different double ionization cuts were applied (94, 102, 110, 118, 126), being 110 the cut providing the same ratio between colapsed and non-colapsed tracks, for real data and Monte Carlo, and it was found that the maximum variation in the pionium breakup probability was 0.005. The variation in the cuts applied are very exaggerated (32 ADC counts) and are not realistic, since the ratio between collapsed and non-collapsed tracks varies too much. A more realistic variation of 9 ADC counts, which is still very strong, produces a variation in the break probability of $\pm$ 0.0014, adopted as the systematic error committed in the P_{br} determination.

6.4 K^+K^- Admixture

The K^+K^- contamination was studied in detail in Chapter (3). The percentage of this contamination in the prompt $\pi^+\pi^-$ sample was determined at low (2.9 GeV/c) and high (4.8 GeV/c) laboratory momentum values, although the former is much more constraining and reliable, due to the higher statistics obtained, to the detriment of the latter, which was performed with Λ triggers, instead of standard $\pi^+\pi^-$ triggers, much more numerous.

Fig. (3.12) illustrates the low momentum measurement as the most advisable value for the K^+K^- contamination, which is calculated within a relative 15% of uncertainty for 2.9 GeV/c ($r_K = (2.38 \pm 0.35) \times 10^{-3}$). The systematic error has been estimated by varying the K^+K^- contamination by $\pm 15\%$. This systematic error represents an uncertainty of ± 0.0011 in the pionium breakup probability.

6.5   Finite Size Correction

Coulomb pairs are generated using the theoretical Coulomb enhancement function of Eq. (1.11). This hypothesis assumes that the two pions of a Coulomb correlated pair are created at zero distance. Of course this is not true and the parametrization needs some corrections which receive the name of finite size correction.

The simulation performed in this analysis includes an option in the background generator, motivated by the work done in Ref. [50], which proposes a possible correction for $A_C(Q)$ of the order of $2 - 3\%$. This correction can be expressed by means of the following modified Coulomb enhancement function [108]:

$$A_C^{\text{fs}}(Q) = A_C(Q)(1.10017 - 0.0285((1 + (0.278 \cdot Q)^2)^{-0.421} - 1)) \qquad (6.1)$$

where fs denotes finite size and $A_C(Q)$ (1.11) is the theoretical Coulomb enhancement. The correction affects the Coulomb pair spectra by increasing higher Q while decreasing lower Q, which leads to a fit with more Coulomb pairs and fewer non-Coulomb pairs.

The implementation of this effect in the analysis was done in two steps. In the first stage the Coulomb correlated pair spectrum was produced, with the standard Coulomb factor definition. Secondly, the expression (6.1) was utilized to compute the corrected Coulomb spectrum, to obtain the ratio between both distributions, $\mathcal{R}$. Fig. (6.5) shows this ratio in the acceptance Q-range of the spectrometer. This ratio was used to correct the original Coulomb correlation pair function.
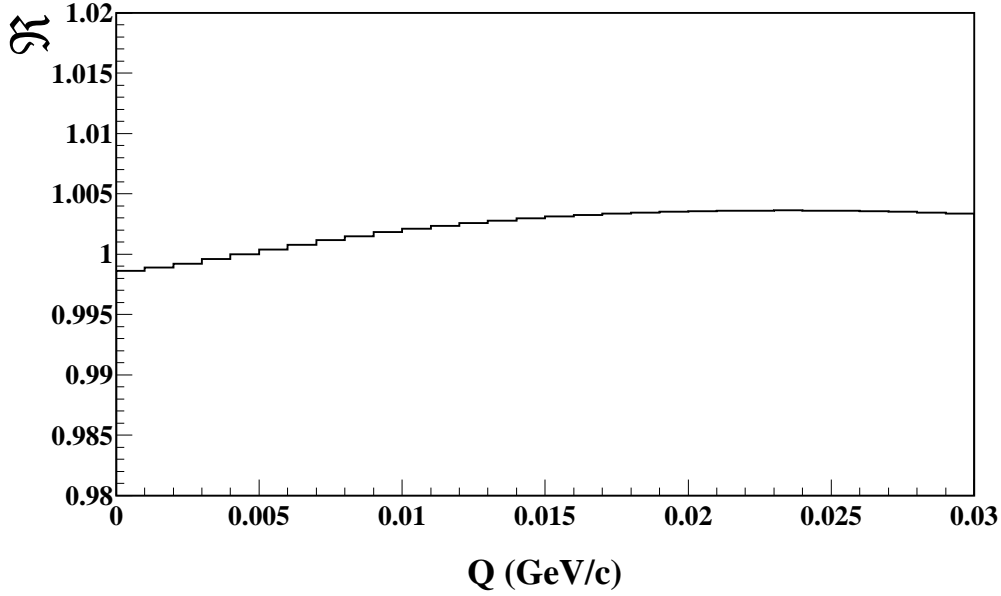
Figure 6.5: *Ratio between the standard Coulomb correlation function given by Eq. (1.11) and the corrected Coulomb factor proposed in [48], given by Eq. (6.1). Notice that the scale runs from 0.98 to 1.02. The average deviation from the unit accounts for a 0.099% .*

We have calculated the pionium breakup probability in the target without this improved treatment (P_{br1}) and we have also calculated it bearing in mind the finite size correction (P_{br2}). The systematic error appointed to this improvement was judged to be $\Delta P_{br} = (P_{br1} - P_{br2})/\sqrt{12}$, which means a systematic error of ± 0.0011 in the pionium breakup probability in Ni.

6.6 Momentum Smearing

The momentum smearing described in Chapter (4) was introduced in the Monte Carlo to match the reconstructed lambda mass resolution of the real data. In addition, we have obtained, with a very high precision level, a lambda mass measurement very close to the tabulated values, using a two-Gaussian fit method.

The impact of the momentum smearing in the pionium breakup probability was computed as the difference of the breakup probability calculated with and without momentum smearing. The following expression took care of the smearing in momentum, introduced in section (4.2.4):

$$P \rightarrow P \ (1 \ + \ 0.00066 \ [(GeV/c)^{-1}] \ P) \tag{6.2}$$

This difference resulted to be $+9 \times 10^{-3}$. In consequence, we have assigned this maximun deviation in the pionium breakup probability, divided by $\sqrt{12}$, as the systematic error committed, ± 0.0026, which represents the third largest systematic error associated to the breakup probability measurement.

6.7 Background Hits in the Upstream Detectors

The systematic error assigned to the background in the upstream detectors was calculated using two different Q_T and Q_L resolutions from Monte Carlo as a function of the pionium pair momentum:

$$Q_{L,T}^{Res}(i) = Q_{L,T}^{Rec}(i) - Q_{L,T}^{Gen}(i) \tag{6.3}$$

where $Q_{L,T}^{Res}$ are the resolutions as function of the momentum p, $Q_{L,T}^{Rec}$ are the $Q_{L,T}$ distributions reconstructed by the spectrometer, while $Q_{L,T}^{Gen}$ correspond to the $Q_{L,T}$ distributions after the target, both provided by the Monte Carlo. Index $i = 1, 2$ denotes a $Q_{L,T}^{Gen}$ distribution with a 20% of correlated background and without correlated background, respectively. Both distributions were generated in accordance with the real data hit multiplicity.

Uncorrelated background is created by the Monte Carlo by means of random hits generated in the upstream detectors. The correlated background generates tracks coming from the intersection point of the beam with the target, which go through the upstream detectors. Therefore, hits from these latter events are spatially correlated with the interaction point. In addition, requires the presence of hits in the scintillating fiber detector.

Using this two $Q_{L,T}^{Res}$ resolutions we have created a 2D $Q_{L,T}$ plot for atomic, Coulomb and non Coulomb pairs. The shift in the pionium breakup probability was calculated with and without correlated background, resulting to be very small, so we have decided to assign directly this difference to the systematic error associated to the background hits in the upstream detectors, which happens to be ±0.0001.

6.8   Target Impurity for 2001 94 μm

The effect in the breakup probability of the small impurity in the 94 μm Ni target foil from elements of lower Z values was calculated in Ref. [111]. This work was used to perform a small positive correction to the lifetime, and lead to a correction factor applicable to the relation between the pionium breakup probability and its lifetime, for each momentum bin of the analysis.

The target impurity affects only the relation between the breakup probability and the pionium lifetime, and its effect changes the relation P_{br}-τ in such a way that multiplying the obtained breakup probability by a factor 1.014 is completely equivalent to use directly the breakup probability measured with the correct P_{br}-τ relation.

In order to check a possible dependence of the P_{br} correction on the pair momentum p, a simulation was done using the propagation code [96] having Al as target foil material. The ratio between both corrected by the target impurity and the pure target P_{br}-τ relations, was plotted as function of p, and the observed slope was $0.05/GeV$. Given such small value, we consider a sufficiently good approximation to apply the same correction factor (1.014) in all momentum bins.

The systematic error associated to this correction happens to be ±0.0013, after calculating the breakup probability with and without the factor correction and dividing the shift in the breakup probability by $\sqrt{12}$, as corresponding to a uniform distribution.

6.9   Breakup Probability Dependence with Pionium Lifetime

The breakup probability dependence with the pionium lifetime τ carries with it an implicit systematic error which has been studied in extreme detail in several works by exactly solving the transport equations which describe the $\pi^+\pi^-$ pair excitations/de-excitation, breakup and annihilation for several target materials [109, 110], as well as by simulating the pionium propagation inside the target foil [35]. The precision reached by these calculations is at the level of 1% [27], producing a ± 0.0042 systematic error on the breakup probability for a lifetime $\tau = 3.15 \times 10^{-15}$ s.
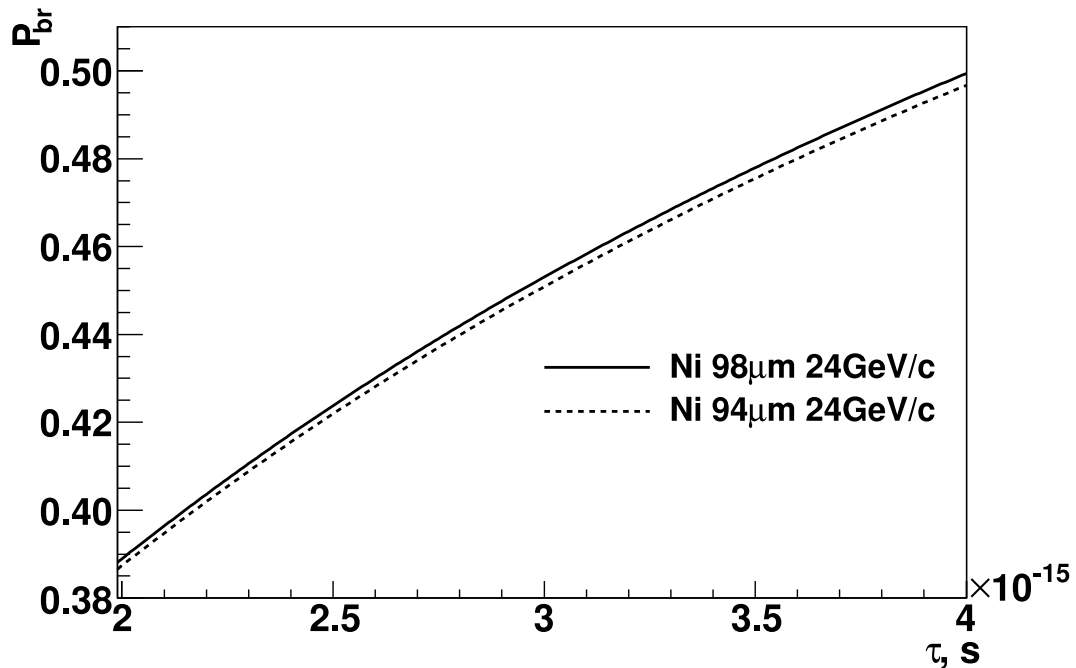
Figure 6.6: *Breakup probability function $P_{br}(\tau)$ dependence on pionium lifetime for the two target thicknesses employed in this analysis, 94 and 98 μm. For the sake of simplicity only the 24 GeV/c proton beam momentum is shown.*

A different function $P_{br}(\tau, p)$ must be used for each target due to the dependence of the breakup probability with the target thickness, as shown in Fig. (6.6). The functions $P_{br}(\tau, p)$ are further convolved with the experimental momentum spectra of the Coulomb pairs[1] inside the seven momentum bins of the analysis, ensuring that the non-linear dependence of the breakup probability with the laboratory momentum is practically negligible for each momentum bin.

---

[1]Coulomb pairs are taken from prompt pairs in the $\vec{Q}$ extrapolation region, where the pionium signal is not present, after the non-Coulomb contribution is subtracted from the prompt sample

6.10 Summary of Systematic Errors

The systematic errors involved in the breakup probability measurement that were studied in this chapter are summarized in Table (6.1). The overall systematic error was computed adding in quadrature the contributions from each considered source. This overall error is ± 0.0095, which must be propagated to the lifetime calculation, and combined with the statistical error from the fit described in Chapter (5).

Source of Systematic Error	P_{br} deviation
Multiple Scattering in the Target	± 0.0077
Dependence of P_{br} with Lifetime τ	± 0.0042
Momentum Smearing	± 0.0026
Double Track Resolution	± 0.0014
Target Impurity Correction for 2001 94 μm	± 0.0013
$K^+ K^-$ Admixture	± 0.0011
Finite Size Correction	± 0.0011
Simulation of the Trigger	± 0.0005
Background Hits in the Upstream Detectors	± 0.0001
Overall Systematic Error	± 0.0095

Table 6.1: *Summary of the systematic errors involved in the calculation of the pionium breakup probability studied in this chapter.*

Chapter 7

Summary and Conclusions

This work presents the new analysis method adopted to obtain the most accurate and updated pionium lifetime determination by the DIRAC experiment at CERN, and is summarized in Ref. [85]. The elimination of a restrictive cut in the DC detector has allowed to increase the statistics in more than 30% with respect to the preceding work done in 2008 [92], explained by the inclusion of events which were not considered previously.

The comparison between two Monte Carlo generators [96, 110] was done, demonstrating the equivalence between them. A brand-new simulation was implemented to improve the description of the pionium signal extracted from the spectrometer reconstruction. The new Monte Carlo was tuned with extra atributes that introduced corrections and improvements that had never been taken into account, such as the simulation of the trigger and the inclusion of the momentum smearing in the momentum resolution.

A rigorous reduction of the systematic errors involved in the breakup probability calculation was done. This, together with the statistical increment of 30% results in the most accurate pionium lifetime measurement in its ground state with a total uncertainty of $\sim$9%, where more than 22000 atoms were reconstructed by the spectrometer. This granted the determination of the $|a_0 - a_2|$ scattering lengths difference with a $\sim$4% precision.

Real data were divided in five different sets, depending on the data taking period. Each set was split in 7 laboratory momentum bins and a momentum dependent fit was done, producing 35 independent breakup probability values. A maximum likelihood fit was performed taking into account these 35 independent breakup probabilities and their statistical and systematic errors, yielding a lifetime of:

$$\tau = \left(3.15^{+0.20}_{-0.19}\bigg|_{\text{stat}} \ {}^{+0.20}_{-0.18}\bigg|_{\text{syst}}\right) \times 10^{-15} \ s \tag{7.1}$$

As a safety precaution, a χ^2 test was also performed to cross-check the lifetime obtained with the maximum likelihood method. This χ^2 analysis yielded a lifetime value practically identical to the obtained from the maximization of the likelihood, $\tau = (3.15 \pm 0.20) \times 10^{-15}$ s, which comes to reinforce the soundness of the result.

In our previous publication [6] we reported a pionium lifetime calculated without including the GEM/MSGC detector in the tracking routines:

$$\tau = \left(2.91^{+0.45}_{-0.38}\bigg|_{\text{stat}} \ {}^{+0.19}_{-0.49}\bigg|_{\text{syst}}\right) \times 10^{-15} \ s \tag{7.2}$$

where both statistical and systematic errors were significantly bigger than the errors reported in the present result. In spite of taking into account uncertainty sources previously unconsidered, we have reduced the systematic error by a factor of 1.7, demonstrating the supreme effort done on this matter during the last few years. The statistical error was also reduced by nearly a factor of 2, and finally, after squaring all systematic and statistical errors, the relative error, that in the earlier measurement accounted for 19%, has been reduced to less than 9%, hence by more than a factor of 2.

Putting this all together we obtain the final $\pi\pi$ scattering length difference:

$$|a_0 - a_2| = \left(0.2533^{+0.0080}_{-0.0078}\bigg|_{\text{stat}} \ {}^{+0.0078}_{-0.0073}\bigg|_{\text{syst}}\right) M_{\pi^+}^{-1} \tag{7.3}$$

This scattering length difference, compared with our previous published measurement [6]:

$$|a_0 - a_2| = 0.264^{+0.033}_{-0.020} \ M_{\pi^+}^{-1} \tag{7.4}$$

has reduced the systematic and statistical error by a factor 2.5, as can be seen in Fig. (7.1).

Our $|a_0 - a_2|$ determination is fully compatible with the one obtained by the NA48/2 experiment through the $K_{3\pi}$ and the K_{e4} decays. The $\pi\pi$ scattering lengths difference obtained with $K_{3\pi}$ decays is:

$$(a_0 - a_2)M_{\pi+} = 0.2571 \pm 0.0048 \text{ (stat)} \pm 0.0029 \text{ (syst)} \pm 0.0088 \text{ (theo)} \quad (7.5)$$

The measurements performed by the $K_{3\pi}$ and the K_{e4} experiments brought together yield a difference in the pion scattering lengths:

$$(a_0 - a_2)M_{\pi+} = 0.2639 \pm 0.0020 \text{ (stat)} \pm 0.0015 \text{ (syst)} \pm 0.0088 \text{ (theo)} \quad (7.6)$$

Our scattering length difference includes the theoretical uncertainties into the systematic error. Combining all the errors of the measurements in quadrature, we can finally compare the values obtained by DIRAC with the ones obtained by the NA48/2 Experiment. Table (7.1) and Fig. (7.1) summarize the $|a_0 - a_2|$ measurements performed by DIRAC and NA48/2, showing the excellent agreement between both experiments and ChPT. Also the world average can be computed obtaining $|a_0 - a_2|M_{\pi+} = (0.2581 \pm 0.0058)$.

$|a_0 - a_2|$ determination	$|a_0 - a_2| \times M_{\pi+}$	Combined error
ChPT	0.2650	$\pm$ 0.0040
DIRAC	0.2533	$\pm$ 0.0109
$K_{3\pi}$	0.2571	$\pm$ 0.0104
$K_{3\pi}$ & K_{e4}	0.2639	$\pm$ 0.0091
World Average	0.2581	$\pm$ 0.0058

Table 7.1: *Current values of $\pi\pi$ scattering lengths difference.*
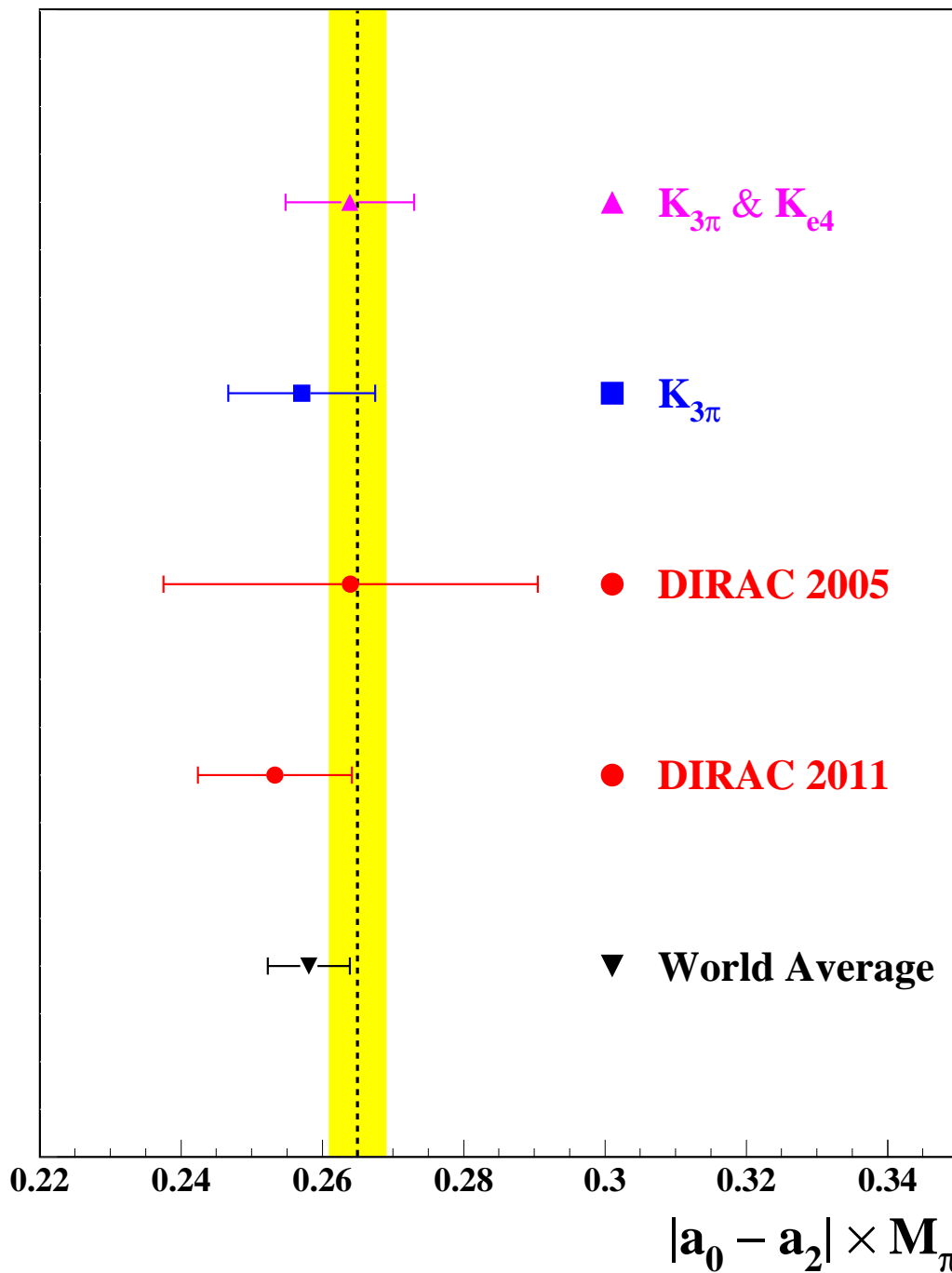
Figure 7.1: *Experimental values of $|a_0-a_2|$ obtained by DIRAC and by NA48/2. The dashed black line represents the standard Chiral Perturbation Theory prediction, and its error is depicted by the yellow band. The world average value was computed performing a mean value weighted by the individual errors involved in the calculation, involving the two values provided by the NA48/2 experiment and the DIRAC 2011 measurement.*

Appendix A

Criteria for pre-selection

1. One requires 1 or 2 DC-tracks fitted in each arm (i.e. events with multiplicities larger than 2 in either arm are rejected). When there are two tracks the earliest one —that most probably produced the trigger — is taken for further analysis.

2. For each DC-track the momentum is estimated and an extrapolation upstream is made in the SciFi planes, using a pre-defined approximation of the vertex at the target.

3. For each DC-track, one selects hits in each plane of the SciFi detector within a time window. This time window is of a range [-4,+4] ns about the expected time obtained by subtracting the Time-Of-Flight from the time measured by the corresponding slab in the Vertical Hodoscope (as selected in the DC tracking).

4. Hits are further selected in a space window [-D,+D] where D=(0.2cm + 4.8cm/p) with p in GeV/c. One requires at least 1 and at most 4 hits in this window for each plane. In case more than 4 hits are found, only the 4 closest to the center of the window are retained.

5. For each DC-track, a global fit procedure is done —Kalman filter— using SciFi hits (but not the assumed vertex). One keeps events with at least one track candidate per arm with a confidence level larger than 1% and a distance at the target level between the track and the assumed beam position smaller than 1.5 cm (more than 3 sigmas) in both X- and Y-projections.

6. In each SciFi plane, and for each arm, one counts the number of hits in a space window of range (essentially) [-1,+1] cm. The window center depends on the intersections of the track candidates with the SciFi plane considered and with the target plane. To avoid confused cases, with a high ambiguity level, events with too many hits in any of these windows are rejected. The upper limit is set at 4 hits.

7. Further one keeps only events with at most 3 hits in each plane or 4 in one plane and 2 in the other.

8. For each couple of track candidates (1 track per arm) an overall vertex-fit is made using the results and covariance matrices of individual track fits.

9. The relative momentum Q (twice the cms momentum) and its projections are calculated. Events for which at least one combination matches all the conditions $|Q_X| < 6$ MeV/c, $|Q_Y| < 6$ MeV/c and $|Q_L| < 45$ MeV/c are selected for a further analysis. These events are written out on file/tape in a format identical to that of the raw data (i.e. this is a direct copy, with minor additions).

The data reduction is expected to be large —a few % of the events retained— while not loosing significantly events of interest. This pre-selection would be done on all data taken so far, some 1.2×10^9 events, in a fairly short time lapse of about 3 weeks at CERN. Upstream tracking with GEM/MSGC will be left for a further processing of the selected data. If it turns out that this pre-selection is found to loose events, unduly, a new selection could be redone. The time spent for the original pre-selection would however have been beneficial to study many side effects such as, for example but not exhaustively, precise adjustments of IH thresholds and muon contamination.

Tests on the run 1588 (Autumn 1999) give the following passing rates for Pi-Pi triggers: 43% after step 1, 27% after step 5, 25% after step 7 and 2% after step 9. In terms of data (i.e. including the rejection of non $\pi\pi$ events) this pre-selection keeps about 1.5% of the 1999 data and 2% of the 2000 data. These numbers are rather crude and may strongly depend on the run conditions.

Criteria for Analysis

Some results will be made available for direct analysis as a by-product of the pre-selection. The following procedures are applied in addition to the pre-selection.

- If the time difference Δt between the 2 tracks, as measured by the Vertical Hodoscope slabs (using lengths of flight and pion mass assignments), is smaller than 0.5 ns the event is marked as "prompt". If Δt is in either ranges [-15,-5] ns or [7,17] ns the event is marked as "accidental". Other events are rejected.

- Protons in "prompt" events are rejected by requiring, in addition to the time cut defined above, an upper limit of 4.5 GeV/c on the momentum of the positive particle.

- Only one vertex-fit is considered, the best one based on confidence levels from track fits and subsequent vertex fit.

- The cuts on the projections of the relative momentum are as well tightened to: $|Q_X| < 5$ MeV/c, $|Q_Y| < 5$ MeV/c and $|Q_L| < 24$ MeV/c. For the events thus selected, a set of variables is stored via "ntuples" for later analysis.

List of Figures

List of Tables

Bibliography

[1] B. Adeva, et al., DIRAC proposal, CERN/SPSLC 95-1, SPSLC/P 284 (1994).

[2] B. Adeva et al. [DIRAC Collaboration], Nucl. Instr. Meth. A515 (2003) 467 [arXiv:hep-ex/0305022].

[3] F. Gomez et al. [DIRAC Collaboration], Nucl. Phys. Proc. Suppl. 96 (2001) 259.

[4] B. Adeva et al. [DIRAC Collaboration], J. Phys. G30 (2004) 1929 [arXiv:hep-ex/0409053].

[5] D. Goldin [DIRAC Collaboration], Int. J. Mod. Phys. A20 (2005) 321.

[6] B. Adeva et al., Phys. Lett. B619: 50-60, 2005. [arXiv:hep-ex/0504044].

[7] B. Adeva et al., Lifetime measurement of $\pi^+\pi^-$ and $\pi^\pm k^\mp$ atoms to test low energy QCD. Addendum to the DIRAC proposal, CERN-SPSC-2004-009 [SPSC-P-284 Add.4]

[8] J. Uretsky and J. Palfrey, Phys. Rev. 121 (1961) 1798

[9] H.-W. Hammer and J.N. Ng, Eur. Phys. J. A6 (1999) 115.

[10] S. Deser et al., Phys. Rev. 96 (1954) 774

[11] S. M. Bilenky et al., Yad. Fiz. 10 (1969) 812; (Sov. J. Nucl. Phys. 10 (1969) 469)

[12] H. Jallouli and H. Sazdjian, Phys. Rev. D58 (1998) 014011; Erratum: ibid. D58 (1998) 099901

[13] M. A. Ivanov et al., Phys. Rev. D58 (1998) 094024

[14] J. Gasser et al., Phys. Rev. D64 (2001) 016008; hep-ph/0103157

[15] A. Gashi et al., Nucl. Phys. A699 (2002) 732

[16] S. Weinberg, Physica A96, 327 (1979).

[17] J. Gasser and H. Leutwyler, Phys. Lett. B125 (1983) 325.

[18] G. Colangelo, J. Gasser, H. Leutwyler, Nucl. Phys. B603: 125-179, 2001.

[19] M. Knecht, B. Moussallam, J. Stern and N. H. Fuchs, Nucl. Phys. B457 (1995) 513 [hep-ph/9507319]; ibid. B471 (1996) 445 [hep-ph/9512404].

[20] L. Rosselet et al., Phys. Rev. D15 (1977) 547.

[21] S. Pislak et al., Phys. Rev. Lett. 87 (2001) 221801

[22] L. S. Dulian and A. M. Kotsinian, Yad. Fiz. 37 (1983) 137; (Sov. J. Nucl. Phys. 37 (1983) 78)

[23] S. Mrówczyński, Phys. Rev. A33 (1986) 1549

[24] S. Mrówczyński, Phys. Rev. D36 (1987) 1520; K. G. Denisenko and S. Mrówczyński, ibid. D36 (1987) 1529

[25] L. G. Afanasyev and A. V. Tarasov, Yad. Fiz. 59 (1996) 2212, (Phys. At. Nucl. 59 (1996) 2130)

[26] Z. Halabuka et al., Nucl. Phys. B 554 (1999) 86

[27] A. V. Tarasov and I. U. Khristova, JINR-P2-91-10, Dubna 1991

[28] O. O. Voskresenskaya, S. R. Gevorkyan and A. V. Tarasov, Phys. At. Nucl. 61 (1998) 1517

[29] L. G. Afanasyev, A. Tarasov and O. Voskresenskaya, J. Phys. G25 (1999) B7

[30] D. Yu. Ivanov, L. Szymanowski, Eur. Phys. J. A5 (1999) 117

[31] T. A. Heim et al., J. Phys B33 (2000) 3583

[32] T. A. Heim et al., J. Phys B34 (2001) 3763

[33] M. Schumann et al., J. Phys. B35 (2002) 2683.

[34] L. G. Afanasyev, A. Tarasov and O. Voskresenskaya, Phys. Rev. D65 (2002) 096001; hep-ph/0109208

[35] C. Santamarina et al., J. Phys B36 (2003) 4273

[36] L. G. Afanasyev et al., J. Phys B37 (2004) 4749.

[37] L. G. Afanasyev et al., Phys. Lett. B338 (1994) 478

[38] L. L. Nemenov, Yad. Fiz. 41 (1985) 980; (Sov. J. Nucl. Phys. 41 (1985) 629)

[39] M. Gell-Mann, R. J. Oakes and B. Renner, Phys. Rev. 175 (1968) 2195.

[40] S. Weinberg, Phys. Rev. Lett. 17: 616-621, 1966.

[41] J. Bijnens, G. Colangelo, G. Ecker, J. Gasser and M. E. Sainio, Phys. Lett. B374 (1996) 210 [hep-ph/9511397].

[42] J. Gasser and H. Leutwyler, Annals Phys. 158 (1984) 142.

[43] J. Gasser and H. Leutwyler, Nucl. Phys. B250: 517-538, 1985.

[44] S. Roy, Phys. Lett. 353 (1971).

[45] G. Colangelo, AIP Conf. Proc. 756, 60 (2005).

[46] H. Sazdjian, Phys. Lett. B490 (2000) 203 [hep-ph/0004226].

[47] A. D. Sakharov, Z. Eksp. Teor. Fiz. 18 (1948) 631.

[48] R. Lednicky, DIRAC Note 04-06 (2004).

[49] L. G. Afanasyev, Observation of $\pi^+\pi^-$ atoms, Ph. D. Thesis, JINR, Dubna (1997).

[50] R. Lednicky, J. Phys. G: Nucl. Part. Phys. 35 (2008) 125109.

[51] L. G. Afanasyev et al., Phys. Lett. B308 (1993) 200 L. G. Afanasyev et al., Phys. At. Nucl. 60 938 (1997). L. G. Afanasyev, O. O. Voskressenskaya, V. V. Yazkov, Communication JINR P1-97-306, Dubna, 1997.

[52] V. Fanti et al., Nucl. Instr. Meth. A574 433-471 (2007).

[53] O. Ferrando and J-Y. Hemery, CERN-PS Division, PS/ CA/ Note 97-16

[54] A. Lanaro, DIRAC Note 02-01 (2002).

[55] K. Hagiwara et al. (PDG), Phys. Rev. D66 (2002) 010001

[56] B. Adeva, A. Romero and O. Vázquez Doce, DIRAC Note 04-05 (2004).

[57] O. Gorchakov and C. Santamarina, DIRAC Note 04-01 (2004).

[58] O. E. Gorchakov et al., Yad. Fiz. 63 (2000) 1936; (Phys. At. Nucl. 63 (2000) 1847)

[59] L. G. Afanasyev et al. Nucl. Instr. Meth. A491 (2002) 376

[60] S. Vlachos, DIRAC Note 03-04 (2003).

[61] L. G. Afanasyev et al., Nucl. Instr. Meth. A479 (2002) 407

[62] M. Gallas, Nucl. Instr. Meth. A481 (2002) 222

[63] P. Kokkas et al., Nucl. Instr. Meth. A471 (2001) 358

[64] S. Vlachos, DIRAC Note 00-13 (2000).

[65] A. Kulikov, M. Zhabitsky, Nucl. Instr. Meth. A527 (2004) 591

[66] GEANT3 for DIRAC, version 2.63, unpublished, http://dirac.web.cern.ch/DIRAC/

[67] Analysis software package for DIRAC, unpublished

[68] T. Núñez Pardo de Vera, *Desarrollo de un detector de micropistas de gas para el experimento DIRAC*, Ph. D. Thesis, Universidad de Santiago de Compostela (1999).

[69] C. Buttner et al., Nucl. Instr. Meth. A409, 1-3, 79-83 (1998).

[70] V. Agoritsas et al., Nucl. Instr. Meth., A411, 17-30 (1998).

[71] A. Gorin et al., Nucl. Instr. Meth., A452, 280-288 (2000).

[72] V. Brekhovskikh, M. Jnabitski, A. Kuptsov, V. Lapshin, V. Rykalin, L. Tauscher, DIRAC Note 02-09 (2002).

[73] Millipore paper type HAWP pore size 0.45 made by MILLIPORE Corp., Bedford, Ma 01730 USA.

[74] L. Afanasyev, V. Karpukhin, Nucl. Instr. Meth. A492 351 (2002).

[75] B. Adeva et al., Nucl. Instr. Meth. A491 (2002) 41

[76] M. Bragadireanu et al., Nucl. Instr. Meth. A426, 254 (1999).

[77] A. Kuptsov, DIRAC report "DIRAC targets", 5 March 2005.

[78] M. Pentia, Gh. Caragheorgheopol, M. Ciobanu, D. Pop and C. Rusu (IAP). DIRAC Note 99-03 (1999).

[79] A. Lanaro, DIRAC Note 02-02 (2002).

[80] A. Kulikov, DIRAC Note 98-01 (1998).

[81] F.R. Leimgruber et al., NIM A365, 198 (1995).

[82] G.D. Badhwar, S.A. Stephens, R.L. Golden Phys Rev. D15, 820 (1977).

[83] A. Lanaro, DIRAC Note 01-01 (2001).

[84] DIRAC collaboration, Lifetime measurement of $\pi^+\pi^-$ and $\pi^\pm K$ atoms to test low energy QCD, CERN-SPSc-2004-009 (April 2004)

[85] B. Adeva et al., Determination of $\pi\pi$ scattering lengths from measurement of $\pi^+\pi^-$ atom lifetime, Physics Letters B 704 (2011) 24-29, arXiv:1109.0569.

[86] Garfield, package simulation of gaseous detectors, http://garfield.web.cern.ch/garfield/

[87] E. L. Garwin and A. Roder, Nucl. Instr. and Meth. 93 (1971) 593.

[88] J. Heintze et al., Nucl. Instr. and Meth. 138 (1976) 641.

[89] Y. Allkofer et al., Nucl. Instr. Meth. A 585 (2008) 212

[90] B. Adeva et al., Evidence for πK atoms with DIRAC, Physics Letters B 674 (2009) 11. (arXiv:0905.0101)

[91] O. Vázquez Doce, Ph. D. Thesis, *Study of Pionium Lifetime in pNi Collisions at p=24 GeV/c*, Universidade de Santiago de Compostela (2007)

[92] A. Romero, Ph. D. Thesis, *Precision Determination of the S-wave $\pi\pi$ isospin scattering length difference $|a_o - a_2|$ in the DIRAC experiment*, Universidade de Santiago de Compostela (2008)

[93] B. Adeva et al., DIRAC Note 03-08 (2003).

[94] D. Drijard, M. Hansroul, V. Yazkov, http://www.cern.ch/dirac/ariane.html

[95] B. Adeva et al., DIRAC Note 05-15 (2005).

[96] C. Santamarina, DIRAC Note 04-02 (2004).

[97] C. Santamarina, *Detección e Medida de Tempo de Vida Media do Pionium no Experimento DIRAC*, Ph. D. Thesis, Universidad de Santiago de Compostela (2001).

[98] M.V. Zhabitsky, DIRAC Note 07-11 (2007).

[99] P. Zrelov and V. Yazkov, DIRAC Note 98-08 (1998).

[100] C. Santamarina and C. P. Schutz, DIRAC Note 03-09 (2003).

[101] O. Gorchakov and V.V. Yazkov, DIRAC Note 05-01 (2005).

[102] B. Adeva et al., DIRAC Note 06-05 (2006).

[103] B. Adeva et al., DIRAC Note 07-02 (2007).

[104] UrQMD manual. http://th.physik.uni-frankfurt.de/˜ urqmd/

[105] F. James, http://wwwasdoc.web.cern.ch/wwwasdoc/minuit.minmain.html

[106] B. Adeva et al., DIRAC Note 06-03 (2006).

[107] A. Dudarev, V. kruglov, M. Nikitin, DIRAC Note 08-06 (2008).

[108] R. Lednicky and J. Smolik, private communication to the DIRAC collaboration mail list.

[109] O. E. Gorchakov et al., Yad. Fiz. 59 (1996) 2015; (Phys. At. Nucl. 59 (1996) 1942)

[110] M.V. Zhabitsky, Phys. At. Nucl. 71 (2008) 1040; arXiv:0710.4416 [hep-ph]

[111] A. Kuptsov, DIRAC report "DIRAC targets", 5 March 2005.

QUEEN - WE ARE THE CHAMPIONS
(Freddie Mercury - "News of the World, 1977)

I've paid my dues
Time after time
I've done my sentence
But committed no crime
And bad mistakes
I've made a few
I've had my share of sand
Kicked in my face
But I've come through
And I need to go on and on and on and on

We are the champions - my friend
And we'll keep on fighting till the end
We are the champions
We are the champions
No time for losers
'Cause we are the champions of the world

I've taken my bows
And my curtain calls
You've bought me fame and fortune
And everything that goes with it
I thank you all
But it's been no bed of roses no pleasure cruise
I consider it a challenge before the whole human race
And I ain't gonna lose
And I need to go on and on and on and on

We are the champions - my friend
And we'll keep on fighting till the end
We are the champions
We are the champions
No time for losers
'Cause we are the champions of the world